

# **Fatigue Behavior of Constructional Steels Subjected to Pitting Corrosion and Elevated Temperature**

**Doctoral Thesis**

by

**Siddharth Chauhan**

**(2018CEZ0002)**



**DEPARTMENT OF CIVIL ENGINEERING  
INDIAN INSTITUTE OF TECHNOLOGY ROPAR**

**May 2024**

# **Fatigue Behavior of Constructional Steels Subjected to Pitting Corrosion and Elevated Temperature**

A Thesis Submitted  
In Partial Fulfilment of the Requirements  
for the Degree of  
**DOCTOR OF PHILOSOPHY**

by  
**Siddharth Chauhan**  
(2018CEZ0002)



DEPARTMENT OF CIVIL ENGINEERING  
**INDIAN INSTITUTE OF TECHNOLOGY ROPAR**  
May 2024



*Fatigue Behavior of Constructional Steels Subjected to Pitting Corrosion and Elevated Temperature*

Copyright © 2024, Indian Institute of Technology Ropar

All Rights Reserved

DEDICATED  
TO  
FAMILY & FRIENDS

## Declaration of Originality

I hereby declare that the work which is being presented in the thesis entitled **Fatigue Behavior of Constructional Steels Subjected to Pitting Corrosion and Elevated Temperature** has been solely authored by me. It presents the result of my own independent investigation/research conducted during the time period from 23<sup>rd</sup> September 2021 to 30<sup>th</sup> November 2023 under the supervision of Dr. Muthulingam Subramaniyan, Assistant Professor, IIT Ropar and Dr. Aditya Singh Rajput, Assistant Professor, IIT Ropar. To the best of my knowledge, it is an original work, both in terms of research content and narrative, and has not been submitted or accepted elsewhere, in part or in full, for the award of any degree, diploma, fellowship, associateship, or similar title of any university or institution. Further, due credit has been attributed to the relevant state-of-the-art and collaborations (if any) with appropriate citations and acknowledgments, in line with established ethical norms and practices. I also declare that any idea/data/fact/source stated in my thesis has not been fabricated/ falsified/ misrepresented. All the principles of academic honesty and integrity have been followed. I fully understand that if the thesis is found to be unoriginal, fabricated, or plagiarized, the Institute reserves the right to withdraw the thesis from its archive and revoke the associated Degree conferred. Additionally, the Institute also reserves the right to appraise all concerned sections of society of the matter for their information and necessary action (if any). If accepted, I hereby consent for my thesis to be available online in the Institute's Open Access repository, inter-library loan, and the title & abstract to be made available to outside organizations.



Signature

Name: Siddharth Chauhan

Entry Number: 2018CEZ0002

Program: PhD

Department: Civil Engineering

Indian Institute of Technology Ropar

Rupnagar, Punjab 140001

Date: 23 May 2024

## Acknowledgments

I am deeply grateful to my esteemed supervisors, Dr. Muthulingam Subramaniyan and Dr. Aditya Singh Rajput, for their invaluable guidance and support throughout my doctoral journey. Their expertise, encouragement, and unwavering belief in my work were instrumental in shaping not only this thesis but also my professional development.

I am also thankful to my Doctoral committee members, Dr. Naveen James, Dr. Mitesh Surana, Dr. Reet Kamal Tiwari, and Dr. Prabir Sarkar, for their invaluable insights and constructive advice that enriched my research

I am indebted to the Material Behavior Research Laboratory, Department of Mechanical Engineering, IIT Ropar, and its supportive members for facilitating crucial experimental investigations related to my research. I express my gratitude to Dr. Samir Chandra Roy, Department of Mechanical Engineering, IIT Ropar, for his consistent guidance and support during the experimental phase of my research.

I acknowledge the essential resources provided by the Central libraries, including books and journals, that proved indispensable to my success.

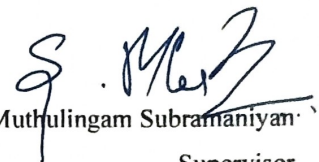
My appreciation extends to the staff members of the Central Workshop for their assistance in material preparation and to the technicians at the Central Research Facilities, IIT Ropar, for helping me in carrying out microstructural investigations for this research. I am deeply grateful to the staff of the Design Lab, Department of Mechanical Engineering, and the Centre for Design & Fabrication of Electronic Devices at IIT Mandi for their support.

Finally, a heartfelt gratitude to the Almighty and my family, especially my supportive mother, whose unwavering encouragement kept me motivated throughout this journey. This thesis is also dedicated to my brother, whose continuous support and presence were invaluable blessings.


## Certificate

This is to certify that the thesis entitled "**Fatigue Behavior of Constructional Steels Subjected to Pitting Corrosion and Elevated Temperature**", submitted by **Siddharth Chauhan (2018CEZ0002)** for the award of the degree of **Doctor of Philosophy** of Indian Institute of Technology Ropar, is a record of bonafide research work carried out under our guidance and supervision. To the best of my knowledge and belief, the work presented in this thesis is original and has not been submitted, either in part or full, for the award of any other degree, diploma, fellowship, associateship or similar title of any university or institution.

In our opinion, the thesis has reached the standard fulfilling the requirements of the regulations relating to the Degree.

  
Dr. Muthulingam Subramanian  
Supervisor

Department of Civil Engineering  
Indian Institute of Technology Ropar  
Rupnagar, Punjab 140001  
Date: 23 May 2024

  
Dr. Aditya Singh Rajput  
Supervisor

Department of Civil Engineering  
Indian Institute of Technology Ropar  
Rupnagar, Punjab 140001  
Date: 23 May 2024

## **Lay Summary**

The study investigated the combined effects of pitting corrosion and elevated temperatures on the low-cycle fatigue and high-cycle fatigue behavior of constructional steels. Understanding these combined effects is crucial for assessing the long-term durability and reliability of structures in aggressive environments. The experimental investigation involved subjecting steel specimens to corrosion and elevated temperatures. Subsequently, both low-cycle fatigue (LCF) and high-cycle fatigue (HCF) tests were conducted to evaluate the resulting changes in the material's fatigue behavior.

One of the focuses of the study was to quantify the changes in surface roughness induced by pitting corrosion and temperature variations. Surface parameters such as amplitude, spacing, and volume were measured to ascertain their impact on the mechanical properties of the steel. Through this analysis, the study was able to develop predictive models that establish correlations between surface topography features and the severity of corrosion and temperature exposure. These models offer valuable insights into how surface degradation progresses over time and its implications for fatigue failure. The study also proposes a framework for estimating fatigue life based on surface topography features. This framework provides engineers with a valuable tool for predicting the remaining useful life of steel components in corrosive and high-temperature environments. In addition to surface characterization, the study also investigates the microstructural changes occurring within the steel specimens subjected to pitting corrosion and elevated temperatures.

The study also proposes a precise analytical expression for the stress concentration factor, which accurately reflects the effect of corrosion penetration depth along the constructional steel bar's perimeter. The experimental investigations revealed critical insights into the LCF behavior of corroded constructional steel bars at elevated temperatures. The prediction models were developed to understand LCF behavior under the influence of pitting corrosion and elevated temperature. These models encompass various parameters and provide valuable tools for assessing structural integrity. The experimental investigations into high-cycle fatigue behavior demonstrated a significant reduction in fatigue life in constructional steel with multiple pit sites, correlating directly with the severity of corrosion and applied stress levels. Fractographic analysis of fracture surfaces provided further insights into the mechanisms governing crack initiation and propagation under the combined influence of corrosion and temperature. These findings offer crucial insights for engineering applications and structural integrity assessments, providing a foundation for developing effective strategies to mitigate fatigue-related failures in corroded steel structures.

## Abstract

The structural integrity of reinforced cement concrete (RCC) and steel structures is highly dependent on the fatigue performance of their constructional steel, especially in demanding environments like those subject to chloride contamination or fire exposure. These structures are exposed to repeated cyclic loading, including HCF induced by wind and traffic, and LCF arising from seismic activity or thermal cycling. Importantly, the combined effect of both cyclic loading and corrosion significantly accelerates material degradation, necessitating a comprehensive understanding of constructional steel fatigue behavior under such combined stressors. Surface topography, characterized by features like roughness and pits, significantly influences fatigue behavior. In this study, an accelerated corrosion technique was employed to induce localized pitting in the specimens. Moreover, experimental investigations, including microstructural examinations, were performed to quantify the surface roughness changes in reinforcing bars exposed to pitting corrosion and elevated temperatures of up to 700 °C. Predictive models are developed to relate these surface topographic parameters to the severity of corrosion and temperature exposure. Leveraging these models, a framework is proposed for estimating the high-cycle fatigue life of corroded reinforcing bars, providing valuable insights for structural health assessments and design optimization. Further, the study experimentally investigated the LCF behavior of reinforcing steel bars subjected to pitting corrosion and elevated temperatures. LCF tests were conducted under stress-controlled conditions with a maximum stress level of  $0.7 f_y$  and stress ratio of -1. Analysis of the resulting hysteresis loop revealed significant detrimental effects of both pitting corrosion and elevated temperature on the LCF performance of the steel specimens. An analytical expression for the stress concentration factor (SCF) based on the inverted Gaussian distribution of pitting corrosion penetration depth along the reinforcing bar's perimeter has been proposed. In addition, LCF behavior of medium-strength structural steel exposed to pitting corrosion and elevated temperatures was experimentally investigated using a symmetrical triangular waveform. LCF tests have been conducted with strain amplitudes of  $\pm 0.6\%$ ,  $\pm 0.8\%$  and  $\pm 1\%$ , with a strain ratio of -1. LCF tests at varied strain amplitudes revealed an expanding rhombus hysteresis with increasing temperature, accompanied by an 82% drop in fatigue life at 700°C. Analysis of corroded and uncorroded specimens under these conditions showed the influence of strain amplitude and temperature on cyclic life and energy dissipation. A Coffin-Manson model successfully quantified strain amplitude effects, with temperature-dependent coefficients predicted through an established power-law equation. Furthermore, the HCF tests on constructional steels with single and multiple pit sites confirmed a decrease in fatigue life with increased corrosion and stress levels. The developed fatigue  $S-N_f$  curve incorporating corrosion severity, offering valuable insights into the development of pitting corrosion in constructional steel.

**Keywords:** Constructional steel; LCF; HCF; Pitting corrosion; High-Temperature; Roughness Parameters; Microstructural investigation

# Table of Contents

Declaration	iv
Acknowledgements	v
Certificate	vi
Lay Summary	vii
Abstract	viii
List of Figures	xiii
List of Tables	xvii
Notations and Abbreviations	xviii
1 Introduction	
1.1 Background	1
1.2 Research objectives	2
1.3 Research scope	3
1.4 Research significance	4
1.5 Outline of thesis	4
2 Literature Review	
2.1 Introduction	7
2.2 Fatigue Process	8
2.3 Fatigue life prediction model	11
2.3.1 Model for fatigue crack nucleation life	11
2.3.2 Model for fatigue crack propagation life	13
2.4 Corrosion process	15
2.5 Fatigue failure of constructional steel	17
2.6 CorrosionFatigue failure of constructional steel	20
2.7 Effect of temperature exposure on properties of steel	23
2.8 High-temperature fatigue behavior of constructional steel	25
2.9 Surface roughness characteristics	27
2.9.1 Analysis of surface roughness	27
2.9.2 Techniques for Surface profile measurement	28
2.9.3 Surface roughness parameters	29
2.9.3.1 Amplitude parameters	29
2.9.3.2 Spatial parameters	32
2.9.3.3 Spacing parameters	33
2.9.3.4 Volume parameters	35
2.9.4 Effect of surface roughness on fatigue strength of steel	36
2.9.5 Effect of pitting corrosion on surface roughness of steel	38



2.9.6	Effect of temperature exposure on surface characteristics of steel	40
2.10	Fatigue life models	41
2.10.1	Stress based fatigue life model	41
2.10.2	Strain based fatigue life model	42
2.10.3	Energy based fatigue life model	43
2.11	Major conclusions from existing literature	45
2.12	Need for further research	46
3	Surface topography of high-ductile TMT steel rebar subjected to pitting corrosion and high temperature	49
3.1	Introduction	50
3.2	Experimental procedure	50
3.2.1	Material and specimen preparation	50
3.2.2	Corrosion protocol	51
3.2.3	Temperature exposure	52
3.2.4	3D corrosion surface morphology	53
3.3	Surface roughness parameters	55
3.3.1	Amplitude Parameters	55
3.3.1.1	Arithmetic mean height $R_a$	57
3.3.1.2	Root mean square height $R_q$	58
3.3.1.3	Total height $R_t$	58
3.3.1.4	Maximum peak height $R_p$ and maximum valley depth $R_v$ :	59
3.3.1.5	Skewness $R_{sk}$ and Kurtosis $R_{ku}$	61
3.3.2	Spacing parameters	64
3.3.3	Spatial parameters	67
3.3.4	Volume parameters	69
3.4	Microstructure investigation	78
3.5	Conclusions	
4	Fatigue life estimation of TMT rebar exposed to pitting corrosion and elevated temperature impacted surface topography	81
4.1	Introduction	82
4.2	Corrosion-fatigue life	83
4.3	Experimental procedure	83
4.3.1	Material and samples preparation	85
4.3.2	Pitting corrosion	90
4.3.3	Surface topography	95
4.4	Prediction models	97
4.4.1	Model development of $R_a$	101
4.4.2	Model development of $R_t$	104
4.4.3	Model development of $R_{10z}$	107
4.4.4	Model development of $R_{sm}$	

	4.4.5	Prediction of $k_t$ and $a_0$	109
	4.5	Fatigue life estimation	113
	4.5.1	Effect of $p_d^{\max}/w$	113
	4.5.2	Effect of $\eta_{\text{cri}}$	114
	4.6	Fatigue life estimation using prediction models	115
	4.7	Conclusions	119
5		LCF behaviour of pitting corroded high-strength TMT rebars exposed to high temperatures considering Gaussian morphology	
	5.1	Introduction	121
	5.2	Experimental work	122
	5.2.1	Material and specimen preparation	122
	5.2.2	Corrosion procedure	123
	5.2.3	Pits characterization	124
	5.2.4	Gaussian representation of pits	126
	5.3	SCF of inverted Gaussian model	127
	5.4	LCF experiment	132
	5.4.1	Test procedure	132
	5.4.2	Hysteresis behaviour	133
	5.4.3	Variation in $N_{f, \text{exp}}$	137
	5.4.4	Energy dissipation capacity	140
	5.5	SED approach	144
	5.5.1	Pit sensitivity function	147
	5.5.2	Variation of average SED	149
	5.5.3	Pit opening angle	150
	5.5.4	Evaluation of $N_{f, \text{est}}$	151
	5.6	Fractographic analysis	153
	5.7	Conclusions	158
6		Effects of High Temperature and Strain Amplitude on LCF Behavior of pitting Corroded Killed E350 BR Structural Steel	
	6.1	Introduction	159
	6.2	Materials and methods	160
	6.2.1	Specimen preparation	160
	6.2.2	Corrosion experiment	161
	6.2.3	Pit Geometry evaluation	162
	6.2.4	Corrosion depth distribution	163
	6.3	Analytical stress concentration factor	165
	6.4	Fatigue Experiment	167
	6.4.1	Testing procedure	167
	6.4.2	Cyclic response	168
	6.4.2.1	Hysteresis behaviour	168
	6.4.2.2	Variation in peak stress	169

6.4.2.3	Stress softening	170
6.4.2.4	Variation in plastic strain	171
6.4.2.5	Variation in modulus	172
6.4.3	Variation in $N_{f, \text{exp}}$	173
6.4.4	Relation between $\varepsilon_a$ and $\exp N_{f, \text{exp}}$	175
6.4.5	Total dissipated energy density	177
6.4.6	Strain energy density approach	179
6.4.6.1	Analytical model	180
6.4.6.2	Pit sensitivity factor	182
6.4.6.3	Pit opening angle	184
6.4.6.4	Variation of $\Delta \bar{w}$	185
6.4.6.5	Estimation of $N_{f, \text{est}}$	186
6.5	Conclusions	189
7	High-cycle fatigue behaviour of structural steel subjected to multiple pitting corrosion under elastic stress conditions	
7.1	Introduction	191
7.2	Materials and test arrangements	192
7.2.1	Specimen preparation	192
7.2.2	Corrosion procedure	192
7.2.3	Characterization of Pitting corrosion	193
7.2.4	Fatigue testing	194
7.3	Fatigue testing results	195
7.3.1	$S_r$ - $N_{f, \text{exp}}$ development based on fatigue data	195
7.3.2	Relation between fatigue life and maximum stress levels	196
7.4	Fractography analysis	197
7.5	Conclusions	199
8	Conclusions and recommendations	
8.1	Introduction	201
8.2	Research conclusions and contributions	201
8.3	Recommendations for future work	204
	Bibliography	205
	List of publications from thesis	215

## List of Figures

Figure 2.1 Typical loading cycles: (a) fully reverse loading; and (b) tension-tension loading .....	9
Figure 2.2 Stages of fatigue failure .....	9
Figure 2.3 Formation of slip band and development of extrusions and subjected to cyclic load .....	10
Figure 2.4 The progression from stage I to stage II fatigue .....	11
Figure 2.5 Development of stage I and stage II fatigue crack growth .....	11
Figure 2.6 Crack propagation curve for fatigue propagation .....	13
Figure 2.7 Representation of profile elements distribution as per (ISO 21920–2:2021) .....	34
Figure 2.8 Illustration of volume parameters .....	35
Figure 2.9 Log-log plot of the generalized S– $N_f$ curve for wrought steel .....	42
Figure 2.10 A typical hysteresis loop.....	43
Figure 3.1 Experimental setup: (a) preparation of specimen; and (b) accelerated corrosion.....	51
Figure 3.2 Elevated temperature exposure .....	52
Figure 3.3 Typical corroded pit: a) original cleaned specimen; (b) 3D laser scan image; (c) corroded pit geometry; and (d) corroded pit length .....	53
Figure 3.4 Non-contact 3D optical profiler .....	55
Figure 3.5 Surface topography of corroded pits.....	56
Figure 3.6 Surface roughness amplitude parameters.....	57
Figure 3.7 Variation of $R_a$ with corrosion time and temperature .....	57
Figure 3.8 Variation of $R_q$ with corrosion time and temperature .....	58
Figure 3.9 Distribution of $R_t$ with corrosion time and temperature.....	58
Figure 3.10 Variation of maximum peak height and maximum valley depth with corrosion time and temperature: (a) $R_p$ ; and (b) $R_v$ .....	59
Figure 3.11 Variation of $R_{sk}$ with corrosion time and temperature .....	60
Figure 3.12 Relation of $R_{ku}$ with corrosion time and temperature.....	60
Figure 3.13 Variation of $\sqrt{area_R}$ with corrosion period and temperature.....	64
Figure 3.14 Illustration of autocorrelation function .....	64
Figure 3.15 Relation of $R_{al}$ with temperature and corrosion period .....	65
Figure 3.16 Illustration of power spectral density function .....	66
Figure 3.17 Variation of $\lambda_{max}$ with corrosion time and temperature .....	67
Figure 3.18 Variation of volume parameters with corrosion time and temperature: (a) $R_{vmp}$ ; (b) $R_{vme}$ ; (c) $R_{vvc}$ ; and (d) $R_{vvv}$ .....	68
Figure 3.19 Optical microscope investigation.....	70
Figure 3.20 Optical micrographs: (a) and (b) 25 °C; (c) 400 °C; (d) 500 °C; (e) 600 °C; and (f) 700 °C .....	70
Figure 3.21 Fractographic images of uncorroded specimens: (a) 25 °C; (b) 400 °C; (c) 500 °C; (d) 600 °C; and (e) 700 °C .....	72
Figure 3.22 EDS of uncorroded specimen .....	73
Figure 3.23 Fractographic images of corroded pits: (a) 25 °C, 10 min; (b) 25 °C, 20 min; (c) 25 °C, 30 min; (d) 400 °C, 10 min; (e) 400 °C, 20 min; (f) 400 °C, 30 min; (g) 500 °C, 10 min; (h) 500 °C, 20 min; (i) 500 °C, 30 min; (j) 600 °C, 10 min; (k) 600 °C, 20 min; (l) 600 °C, 30 min; (m) 700 °C, 10 min; (n) 700 °C, 20 min; and (o) 700 °C, 10 min.....	75
Figure 3.24 EDS of corroded pits: (a) 10 min; (b) 20 min; and (c) 30 min.....	76

Figure 4.1 A schematic of surface topographic feature parameters.....	83
Figure 4.2 Experiment: (a) sample preparation; and (b) accelerated corrosion setup .....	84
Figure 4.3 Corroded pit: (a) sample; (b) 3D laser scan image; and (c) geometry .....	85
Figure 4.4 Experimental data and trends based on flipped Gaussian model .....	87
Figure 4.5 3D surface topography of corroded pits .....	91
Figure 4.6 SEM images of pitting corroded samples: (a) S1_P1; (b) S4_P1; S4_P1; (c) S7_P1; (d) S10_P1; (e) S13_P1; (f) S2_P1; (g) S5_P1; (h) S8_P1; (i) S11_P1; (j) S14_P1; (k) S3_P1; (l) S6_P1; (m) S9_P1; (n) S12_P1; and (o) S15_P1.....	94
Figure 4.7 EDS spectrum of corroded pits: (a) 10 min; (b) 20 min; and (c) 30 min .....	95
Figure 4.8 Comparison between experimental and predicted values of $\sqrt{R_a}$ .....	98
Figure 4.9. Residual plots for $\sqrt{R_a}$ model: (a) histogram; (b) normal probability–probability; (c) standardized residual–predicted value.....	100
Figure 4.10 Sensitivity analysis for $\sqrt{R_a}$ model.....	100
Figure 4.11 Comparison between experimental and predicted values of $\sqrt{R_t}$ .....	102
Figure 4.12. Residual plots for $\sqrt{R_t}$ model: (a) histogram; (b) normal probability–probability; (c) standardized residual–predicted value.....	103
Figure 4.13 Sensitivity analysis for $\sqrt{R_t}$ model.....	104
Figure 4.14 Comparison between experimental and predicted values of $R_{10Z}$ .....	105
Figure 4.15. Residual plots for $R_{10Z}$ model: (a) histogram; (b) normal probability–probability; (c) standardized residual–predicted value.....	106
Figure 4.16 Sensitivity analysis for $R_{10Z}$ model.....	107
Figure 4.17 Comparison between experimental and predicted values of $\sqrt{R_{sm}}$ .....	108
Figure 4.18. Residual plots for $\sqrt{R_{sm}}$ model: (a) histogram; (b) normal probability–probability; (c) standardized residual–predicted value.....	109
Figure 4.19 Sensitivity analysis for $\sqrt{R_{sm}}$ model .....	109
Figure 4.20. Residual plots for $F_s$ model: (a) histogram; (b) normal probability–probability; (c) standardized residual–predicted value.....	110
Figure 4.21 Comparison of experimental values of $F_s$ with prediction model and Equation 4.23 ...	111
Figure 4.22 Variations in $a_0$ : (a) $a_0$ Vs $p_d^{max}/w$ ; (b) $a_0$ Vs $\eta_{cri}$ .....	112
Figure 4.23 Effect of $p_d^{max}/w$ on $N_f$ : (a) $R(0.1)$ and $S_m(0.5f_y)$ ; (b) $R(0.4)$ and $S_m(0.5f_y)$ ; (c) $R(0.1)$ and $S_m(0.8f_y)$ .....	114
Figure 4.24 Effect of $\eta_{cri}$ on $N_f$ : (a) $R(0.1)$ and $S_m(0.5f_y)$ ; (b) $R(0.4)$ and $S_m(0.5f_y)$ ; (c) $R(0.1)$ and $S_m(0.8f_y)$ .....	115
Figure 5.1 Test specimen: (a) prepared sample; and (b) geometry (unit: mm) .....	123
Figure 5.2 Corrosion experiment: (a) sample preparation; and (b) accelerated corrosion.....	124
Figure 5.3 Illustrative 3D image of a specimen: (a) 3D laser scan; and (b) pit morphology and dimensions .....	125
Figure 5.4 Regression analysis of corrosion data using inverted Gaussian function.....	126
Figure 5.5 Variation of SCF based on the analytical model.....	131
Figure 5.6 Numerical analysis of SCF: (a) 3D laser scan image; (b) FE mesh; (c) stress distribution in the specimen; and (d) stress distribution in the corrosion pit...	132
Figure 5.7 Fatigue testing .....	134
Figure 5.8 Hysteresis curves: (a) UC_25_1; (b) UC_400_1; (c) UC_500_1; (d) UC_600_1; (e) UC_700_1; (f) C_25_1; (g) C_400_1; (h) C_500_1; (i) C_600_1; (j) UC_700_1; (k) UC_25_3; (l) UC_500_3; (m) UC_700_3; (n) C_25_3; (o) C_500_3 and (p) C_700_3 .....	135-136

Figure 5.9 Effect of high temperatures: a dimensionless comparison of $N_{f,T}^{\max} / N_{f,25}^{\max}$ .....	139
Figure 5.10 Variation of $N_{f, \exp}$ with temperature .....	140
Figure 5.11 Relation between stiffness and $N_{f, \exp}$ .....	140
Figure 5.12 Variation of energy dissipation capacity and number of cycles to failure .....	143
Figure 5.13 Influence of high temperatures: a dimensionless comparison of $W_T^{\max} / W_{25}^{\max}$ .....	143
Figure 5.14 Relation between $W_t$ and temperature .....	144
Figure 5.15 Variation of $W_t$ with $N_{f, \exp}$ : (a) uncorroded specimens; and (b) corroded specimens ....	144
Figure 5.16 Gaussian pit: reference system, stress components, and control volume .....	147
Figure 5.17 Variation of $P_s(T)$ with temperature .....	149
Figure 5.18 Variation of $\Delta \bar{w}$ with temperature .....	150
Figure 5.19 Variation of normalized index with Gaussian pit opening angle .....	151
Figure 5.20 Relation between average SED and $N_{f, \exp}$ .....	151
Figure 5.21 Comparison between experimental and estimated value of $N_f$ .....	152
Figure 5.22 Fractographic analysis of fracture surface: (a) corrosion pit; (b) failure surface; (c) C_25_1; (d) C_400_1; (e) C_400_3; (f) C_500_1; (g) C_500_3; (h) C_600_1; (i) C_700_1; and (j) C_700_3 .....	156
Figure 5.23 EDS spectrum of the corroded specimens. ....	157
Figure 6.1 Specimen for fatigue testing (unit: mm) .....	161
Figure 6.2 Corrosion experimental setup .....	161
Figure 6.3 3-D image of a specimen (a) 3D laser scan; and (b) pit morphology and dimensions ....	162
Figure 6.4 Experimental data and trends based on inverse Gaussian model .....	164
Figure 6.5 Numerical analysis of SCF: (a) 3D laser scan image, FE mesh, stress distribution in the corrosion pit; and (b) stress distribution in the specimen .....	167
Figure 6.6 Hysteresis curves: (a) UC_25 $\pm 0.6\%$ ; (b) UC_25 $\pm 0.8\%$ ; (c) UC_25 $\pm 1.0\%$ ; (d) UC_700 $\pm 0.6\%$ ; (e) UC_700 $\pm 0.8\%$ ; (f) UC_700 $\pm 1.0\%$ ; (g) UC_25 $\pm 0.6\%$ ; (h) UC_25 $\pm 0.8\%$ ; (i) UC_25 $\pm 1.0\%$ ; (j) UC_700 $\pm 0.6\%$ ; (k) UC_700 $\pm 0.8\%$ and (l) UC_700 $\pm 1.0\%$ .....	168
Figure 6.7 Variation of peak stress amplitude with $N_{f, \exp}$ .....	170
Figure 6.8 Variation of $K_\sigma$ with $N_{f, \exp}$ : (a) $\varepsilon_a = 0.6\%$ ; and (b) $\varepsilon_a = 1.0\%$ .....	171
Figure 6.9 Variation of $\varepsilon_p$ with $N/N_{f, \exp}$ : (a) $\varepsilon_a = 0.6\%$ ; (b) $\varepsilon_a = 0.8\%$ ; and (c) $\varepsilon_a = 1.0\%$ .....	172
Figure 6.10 Variation of $E_t$ with $N_{f, \exp}$ .....	173
Figure 6.11 Effect of high temperatures: a dimensionless comparison of $N_{f,T} / N_{f,25}$ .....	174
Figure 6.12 Relation between $N_{f, \exp}$ and temperature .....	175
Figure 6.13 Relation between $\varepsilon_a$ and $2N_{f, \exp}$ .....	176
Figure 6.14 Relation between coefficients and temperature .....	177
Figure 6.15 Effect of high temperatures: a dimensionless comparison of $\bar{W}_{t,T} / \bar{W}_{t,25}$ .....	178
Figure 6.16 Relation between $\bar{W}_{t, \exp}$ and temperature .....	179
Figure 6.17 Gaussian pit: reference system, stress components, and control volume .....	180
Figure 6.18 Variation of $P_s(T)$ with temperature .....	183
Figure 6.19 Variation of normalized index with Gaussian pit opening angle .....	184
Figure 6.20 Variation of $\Delta \bar{w}$ with temperature .....	186
Figure 6.21 Relation between average SED and $N_{f, \exp}$ .....	187
Figure 6.22 Comparison between experimental and estimated value of $N_f$ .....	187
Figure 7.1 Fatigue testing specimen (unit: mm) .....	192
Figure 7.2 Specimen with corrosion pit: (a) single pit; (b) multiple pits .....	193
Figure 7.3 HCF test setup .....	195
Figure 7.4 $S_r$ - $N_f$ curves for corroded E350 structural steel .....	196

Figure 7.5 Relation between fatigue life and maximum stress levels.....	197
Figure 7.6 Fractographic images of corroded pits: (a) SC_1; (b) SC_2 (c) SC_3; (d) SC_4; (e) DC_1; (f) DC_2; (g) DC_3; and (h) DC_4.....	199

## List of Tables

Table 2.1 Fitting parameters (Hua et al. 2022).....	27
Table 3.1 Material chemical composition .....	50
Table 3.2 Mechanical properties of Fe 500D steel rebar .....	50
Table 3.3 Result summary of corrosion pit geometry .....	54
Table 3.4 Values of profile element based parameters.....	63
Table 4.1 Fatigue crack growth properties .....	83
Table 4.2 Result summary of corrosion pit geometry from 3D laser scanning.....	89
Table 4.3 Curve fitting parameters of flipped Gaussian model.....	90
Table 4.4 Values of surface topographic feature parameters .....	96
Table 4.5 Pearson correlation matrix for $R_a$ .....	99
Table 4.6 Pearson correlation matrix for $R_t$ .....	103
Table 4.7 Pearson correlation matrix for $R_{10z}$ .....	105
Table 4.8 Pearson correlation matrix for $R_{sm}$ .....	108
Table 4.9 Pearson correlation matrix for $F_s$ .....	111
Table 4.10 Comparison between predicted and experimental values of $N_f$ .....	118
Table 5.1 Chemical composition of Fe 500D specimen (in wt.%) .....	123
Table 5.2 Mechanical properties of Fe 500D.....	123
Table 5.3 Summary of corrosion pit geometry from 3D laser scanning .....	125
Table 5.4 Fitting parameters of inverted Gaussian model.....	127
Table 5.5 Stress concentration factor for inverted Gaussian model.....	130
Table 5.6 $N_{f, \text{exp}}$ of specimens exposed to different temperatures.....	139
Table 5.7 $W_t$ of specimens exposed to different temperatures .....	142
Table 5.8 Parameters for the stress distributions of Gaussian model.....	148
Table 5.9 Comparison between experimental $N_{f, \text{exp}}$ and estimated $N_{f, \text{est}}$ of specimens .....	152
Table 6.1 Chemical composition of E350 (in wt. %). .....	160
Table 6.2 Mechanical properties of E350 .....	161
Table 6.3 Result summary of corrosion pit geometry using 3D laser scanning.....	163
Table 6.4 Regression parameter values from the inverse Gaussian model .....	164
Table 6.5 Stress concentration factor for inverted Gaussian model.....	166
Table 6.6 Test result summary of $N_{f, \text{exp}}$ and $\bar{W}_{t, \text{exp}}$ values .....	174
Table 6.7 Regression coefficients used to find the relation between $N_{f, \text{exp}}$ and $T$ .....	175
Table 6.8 Regression coefficients and exponents used in fatigue model.....	176
Table 6.9 Regression coefficients used to find the relation between $\bar{W}_{t, \text{exp}}$ and $T$ .....	179
Table 6.10 Parameters for the stress distributions of Gaussian model.....	182
Table 6.11 Regression coefficients used to find the relation between $P_s(T)$ and $T$ .....	183
Table 6.12 Regression coefficients used to find the relation between $\Delta\bar{W}$ and $T$ .....	185
Table 6.13 SED approach for comparison between $N_{f, \text{exp}}$ and $N_{f, \text{est}}$ of specimens .....	188
Table 7.1 Chemical composition of E350 (in wt. %). .....	192
Table 7.2 Mechanical properties of E350 .....	192
Table 7.3 Result summary of corrosion pit geometry .....	194
Table 7.4 Result summary of fatigue testing.....	197



## Notations and Abbreviations

$a$	Crack size ( $\mu\text{m}$ )	ACF	Autocorrelation function
$a_0$	Initial crack length ( $\mu\text{m}$ )	DC	Direct current
$a_f$	Final crack size ( $\mu\text{m}$ )	HCF	High-cycle fatigue
$a_{sc}$	Critical crack size ( $\mu\text{m}$ )	HV	Vickers hardness
$A$	Fatigue ductility coefficient	LCF	Low-cycle fatigue
$A_m$	Minimum cross-sectional area ( $\text{mm}^2$ )	MA	Micro alloyed
$A_n$	Initial cross-sectional area ( $\text{mm}^2$ )	MLR	Multiple linear regression
$C'$	Fatigue toughness coefficient	PSB	Persistent slip bands
$C$ and $m$	Fatigue crack growth parameters	PSD	Power spectral density function
$da/dn$	Rate of crack growth	$PV$	Principal value in Cauchy sense
$d_i$	Semi-minor length of slip band ( $\mu\text{m}$ )	RCC	Reinforced cement concrete
$\tilde{d}$	Inclusion depth ( $\mu\text{m}$ )	SCF	Stress concentration factor
$\text{erfi}$	Imaginary error function	SED	Strain energy density
$E$	Modulus of Elasticity (MPa)	SEM	Scanning electron microscopy
$E_1^e$	Elastic strain energy (MPa)	SIF	Stress intensity factor
$f_{ACF}$	Autocorrelation function	TMT	Thermo-mechanically treated
$f_{PSD}$	Power spectral density function ( $\mu\text{m}^3$ )	ULCF	Ultra-low cycle fatigue
$f_y$	Yield strength of the material (MPa)	VHCF	Very-high cycle fatigue
$F_s$	Factor dependent on surface topographic parameters ( $\mu\text{m}$ )		
$G$	Shear modulus (MPa)		
$G_i$	Shear modulus at inclusion (MPa)		
$I_1$	Integral depends on notch opening angle		
$k$	inverse slope		
$k_f$	Fatigue notch factor		
$k_t$	Stress Concentration factor		
$k_t^{\text{Fe}}$	SCF obtained from FE analysis		
$K_{IC}$	Fracture toughness ( $\text{MPa m}^{1/2}$ )		
$K_\sigma$	Cyclic softening factor		
$l$	Pit length (mm)		
$\bar{K}$	Cyclic strength coefficient		
$l_e$	Sampling length of the profile (mm)		
$l_i$	Semi-length the slip band ( $\mu\text{m}$ )		
$m_0$	initial mass of the specimen (g)		
$m_c$	Mass of the corroded specimen (g)		

$m'$	Fatigue toughness exponent
$n$	Stress state
$\bar{n}$	Cyclic strain hardening exponent
$N/N_{f, \text{exp}}$	Relative number of cycles to failure
$N_{\text{ci}}$	Crack initiation life
$N_{\text{cp}}$	Crack propagation life
$N_{\text{f}}$	Number of cycles to failure
$2N_{\text{f}}$	Number of reversals to failure
$N_{\text{f}, T}$	Number of cycles to failure at T °C
$N_{\text{f}, 25}$	Number of cycles to failure at 25 °C
$N_{\text{f}, \text{est}}$	Estimated cycles to failure
$N_{\text{f}, \text{exp}}$	Experimental cycles to failure
$N_{\text{r}}$	Reference cycles to failure
$p$ and $r$	Material ratio (%)
$p_{\text{d}}$	Corrosion pit depth (mm)
$p_{\text{d}}^{\text{max}}$	Maximum depth of corroded pit (mm)
$P_{\text{f}}$	Fatigue pit factor
$P_{\text{s}}$	Pit sensitivity function
$q$	Factor depends on notch opening angle
$q'$	Fatigue notch sensitivity factor
$r$ and $\phi$	Local coordinates
$r_0$	Distance between the origin of the coordinate system and pit tip (mm)
$R$	Stress ratio
$R_{\text{a}}$	Arithmetic mean height (μm)
$R_{\text{al}}$	Autocorrelation length (mm)
$R_{\text{c}}$	Radius of control volume (mm)
$R_{\text{cp}}$	Mean profile element height (μm)
$R_{\text{cq}}$	Standard deviation of profile (μm)
$R_{\text{cx}}$	Maximum profile element height (μm)
$R_{\text{ku}}$	Kurtosis
$R_{\text{p}}$	Maximum peak height (μm)
$R_{\text{pc}}$	Peak count parameter (μm)
$R_{\text{q}}$	Root mean square height (μm)
$R_{\text{sk}}$	Skewness
$R_{\text{sm}}$	Mean profile element spacing (mm)
$R_{\text{smq}}$	Standard deviation of profile element spacings (mm)

$R_{\text{smx}}$	Maximum profile element spacing (mm)
$R_v$	Maximum valley depth ( $\mu\text{m}$ )
$R_{\text{vmc}}$	Core material volume ( $\text{mm}^3/\text{mm}^2$ )
$R_{\text{vmp}}$	Hill material volume ( $\text{mm}^3/\text{mm}^2$ )
$R_{\text{vvc}}$	Core void volume ( $\text{mm}^3/\text{mm}^2$ )
$R_{\text{vvv}}$	Dale void volume ( $\text{mm}^3/\text{mm}^2$ )
$R_t$	Total height ( $\mu\text{m}$ )
$R_{10z}$	Ten-point height ( $\mu\text{m}$ )
$S$	Stress amplitude (MPa)
$S_e$	Fatigue strength (MPa)
$S_m$	Mean stresses (MPa)
$S_r$	Stress range (MPa)
$S_r-N_f$	Fatigue curve
$S_{\text{max}}$	Maximum applied stress levels
$T$	Temperature ( $^{\circ}\text{C}$ )
$T_{\Delta w}$	Scatter index
$w$	Corrosion Pit width (mm)
$W$	Energy dissipation capacity per loop (kN mm)
$W_s$	Fracture energy (MPa)
$W_{t, SED}$	Total strain energy density ( $\text{MJ}/\text{m}^3$ )
$W_t$	Total energy dissipation capacity
$W_t$	Total energy dissipation capacity at $T^{\circ}\text{C}$ (kN mm)
$W_{25}$	Total energy dissipation capacity at $25^{\circ}\text{C}$ (kN mm)
$\bar{W}_e$	Total elastic dissipated energy density (MPa)
$\bar{W}_p$	Total plastic dissipated energy density (MPa)
$\bar{W}_t$	Total dissipated energy density (MPa)
$\bar{W}_{T,\text{exp}}$	Experimental total dissipated energy density at $T^{\circ}\text{C}$ (MPa)
$\bar{W}_{25,\text{exp}}$	Experimental total dissipated energy density at $25^{\circ}\text{C}$ (MPa)
$\bar{W}_{t,\text{exp}}$	Experimental total dissipated energy density (MPa)
$Y$	Shape Factor
$z$	Vertical deviation from mean line (mm)
$F$	Fourier Transform
$H$	Hilbert Transform
$\alpha$	Fatigue ductility exponent
$2\alpha$	Notch opening angle (degrees)

$\beta$	Fatigue ductility coefficient
$\Delta K$	Stress intensity range
$\Delta K_{th}$	Threshold stress intensity factor
$\Delta \sigma$	Stress range of each cycles (MPa)
$\Delta \sigma_{N_{f,exp}/2}$	Stress range of $N_{f,exp}/2$ (MPa)
$\Delta \bar{w}$	Average SED (MJ/m <sup>3</sup> )
$\Delta \epsilon$	Total strain range
$\Delta \epsilon_e$	Elastic strain range
$\Delta \epsilon_p$	Plastic strain range
$\Delta \sigma$	True stress amplitude (MPa)
$\Delta \tau$	Shear stress amplitude (MPa)
$\epsilon_a$	Total strain amplitude
$\epsilon_{max}$	Maximum plastic-strain amplitude
$\epsilon_{min}$	Minimum plastic-strain amplitude
$\epsilon_p$	Plastic-strain
$\eta_{cri}$	Critical cross-sectional area loss (%)
$\eta_{max}$	Maximum corrosion degree (%)
$\theta$	Angle subtended between bar center and circumferential point
$\kappa$	Geometry constant
$\lambda_{max}$	Dominant wavelength (mm)
$\lambda_1$	Williams' eigen value
$\mu_m$	Maximum corrosion degree (%)
$\pi$	pi
$\rho$	Profile valley radius ( $\mu\text{m}$ )
$\varsigma$	Dummy variable
$\sigma_{max}$	Maximum stresses (MPa)
$\sigma_m$	Mean stress (MPa)
$\sigma_{min}$	Minimum stresses (MPa)
$\sigma_n$	Nominal stress (MPa)
$\sigma_{nn}$	normal stress for mode I loading (MPa)
$\sigma_p$	Peak stress (MPa)
$\sigma_{p,w}$	Predicted fatigue limit (MPa)
$\sigma_t$	Fracture stress (MPa)
$\sigma_\phi, \sigma_r$ and $\tau_{r\phi}$	Stress components in local coordinates (MPa)
$\tau_f$	Frictional shear stress (MPa)
$\tau_0$	Octahedral shear strength (MPa)

$\omega_{\max}$	Dominating spatial frequency
$\bar{a}$	Factor depends on notch opening angle
$\Omega$	Area of control volume (mm <sup>2</sup> )
$\sqrt{area_R}$	Equivalent defect size (mm)

## 1.1 Background

Steel, an integral material in engineering, is characterized by its inherent versatility and widespread application. Evolving from wrought iron and cast iron, steel exhibits exceptional mechanical properties, including high elasticity, ductility, weldability, and malleability. Its carbon content lies between wrought iron and cast iron. The most common types of steel used in construction today are reinforcing steel bars, structural steel, plain carbon steel, mild steel, etc. Notably, the hot-rolled, deformed high-strength bars are increasingly favored for concrete reinforcement due to their economic advantage over traditional mild steel. Their growing popularity has spurred numerous studies on their behavior within concrete members. Structural steels, offering a broad range of steel shapes and forms, constitute the framework for buildings, bridges, and other structures. While steel possesses remarkable properties, it's crucial to acknowledge its vulnerability to fatigue (Sherman, 1975).

The fatigue phenomenon, recognized in the early 1800s with cracking in railroad bridge components arises from repeated cyclic loading (Bokůvka et al., 2002). As construction has progressed, so have instances of fatigue-related failures in various components. The coupled action of cyclic stress and corrosive environments, manifesting as corrosion-fatigue, significantly compromises the integrity of structural members. This combined phenomenon has cardinally led to numerous catastrophic events, such as the sudden collapse of the Point Pleasant Silver Bridge, claiming 46 lives. The investigations concluded that the phenomenon occurred due to the failure induced by the corrosion-fatigue of the steel reinforcement bars constituting the bridge (Bullard et al., 2012). The 2018 collapse of the Majerhat Bridge in Kolkata cannot be attributed solely to individual occurrences of corrosion and fatigue. Instead, the combined action of these two mechanisms likely played a significant role in the ultimate failure. The combined phenomenon of corrosion-fatigue significantly accelerates steel degradation in RCC structures.

Pitting, acting as a stress raiser, promotes early-fatigue crack nucleation and growth. Cracks further exacerbate chloride ingress, increasing the corrosion rate and the crack propagation normal to the tensile stress (Otieno et al., 2010). This interdependent phenomenon drastically reduces the fatigue life of structural components. Understanding the steel behavior under corrosion-fatigue is crucial, as pitting reduces the local cross-section, amplifies the stress, and weakens the mechanical properties of the steel. Examples include older RCC bridges with traffic loads and seismic zones with high-stress reversals, both prone to premature rebar failure due to the combined action of corrosion and fatigue. Under the combined influence of the

## **Fatigue Behavior of Constructional Steels Subjected to Pitting Corrosion and Elevated Temperature**

corrosion–fatigue, the damage of the steel is dominated by the pitting corrosion rate during the initial stage, however, with time, the fatigue crack rate increases and the pitting corrosion rate decreases substantially (Liu et al., 2018).

Not only, the reinforcing steel but structural steel is also degraded due to the continuous effect of the corrosion–fatigue phenomenon. Studies have shown that seawater can deteriorate structural steel at a rate of 0.13 mm per year, with pit growth rates reaching ten times than the critical value (Gaythwaite, 1981). Further, the fatigue strength can plummet by a factor of 2–3 in the marine environment (Vosikovsky & Tyson, 1986). Thus, it is important to study in detail the behavior of constructional steels subjected due to the corrosion–fatigue behavior. It is well established that surface topography significantly influences steel's mechanical and physical properties (Jacobs et al., 2022). Parameters like surface roughness plays crucial role in various applications, including friction and fatigue.

Several natural and anthropogenic disasters may also prove to be detrimental in the service life of RCC structure once such crucial occurrence is fire generated from both natural and anthropogenic sources. Moreover, the offshore structures can also succumb to fire disasters. However, after the fire, a structure may not collapse, but nevertheless it is significant to evaluate its performance during service. The structure after sustaining the fire may be subjected to cyclic stress such as it may experience earthquake due to which LCF is induced. Therefore, understanding the fatigue behaviour of steel after exposure to temperature is of great importance. Unfortunately, research investigating the combined impact of pitting corrosion and elevated temperatures on fatigue strength of steel is limited (Abar et al., 2015).

The present research highlights the critical need for in–depth research on the behavior of constructional steel under the combined influence of pitting corrosion fatigue and elevated temperatures. Such research holds immense potential for enhancing the safety and longevity of our infrastructure, protecting lives and safeguarding investments.

### **1.2 Research objectives**

The combined influence of pitting corrosion and elevated temperatures on the fatigue behavior of constructional steels poses significant challenge for maintaining the structural integrity and safety of buildings and infrastructure. Consequently, there has been a surge of interest within the research community to investigate these combined effects of on constructional steel. While previous research has focused on the uniform corrosion of steel bars and evaluated their fatigue performance, limited studies have made an attempt to understand the behavior of reinforcing steel bars exposed to elevated temperatures and pitting corrosion under stress and strain–controlled loading conditions. Various researchers have developed predictive equations to evaluate the fatigue performance of constructional steel subjected to fire focusing

on the damage of the structural members affected by fatigue at elevated temperatures. Studies on the microstructural investigations of fatigue crack initiation and propagation in non-corroded steel bars have been conducted, but there is a lack of microstructural investigations of fatigue crack initiation and growth in corroded steel bars under high temperatures. Additionally, the fatigue behavior of construction steels with multiple pit sites remains unexplored. These research gaps have motivated the need for a comprehensive experimental investigation into the fatigue behavior of constructional steel, and based on the test results, predictive equations have been proposed to consider the effect of pitting corrosion and elevated temperature exposure. The objectives of the thesis have been presented as follows:

1. To experimentally investigate the surface roughness characteristics of thermo-mechanically treated (TMT) reinforcing steel bars subjected to pitting corrosion and elevated temperature along with microstructural examinations.
2. To propose a comprehensive framework for estimating the fatigue life of reinforcing steel bars, considering the combined influences of pitting corrosion and changes in surface topography due to elevated temperatures.
3. To experimentally examine the LCF behavior of pitting-corroded high-strength reinforcing steel bar under combined stress-controlled loading and elevated temperatures.
4. To experimentally investigate the LCF behavior of structural steel subjected to pitting corrosion and elevated temperature exposure under strain-controlled loading condition.
5. To experimentally investigate the HCF behavior of constructional steels subjected to pitting corrosion at multiple sites under room temperature and elastic stress condition.

### **1.3 Research scope**

1. The study employed an accelerated corrosion process that did not consider various factors known to influence steel corrosion under natural exposure conditions, such as water-binder ratio, cement composition, concrete cracks, oxygen presence, relative humidity, and temperature.
2. The study focusses on short-term fatigue behavior and may not fully captures the long-term durability or performance of constructional steel under prolonged exposure to pitting corrosion and high temperatures.
3. The average SED approach might not fully account for all factors affecting fatigue behavior, such as microstructural changes, residual stresses, and environmental effects.



## **1.4 Research significance**

The research presents a comprehensive investigation into the fatigue response of constructional steel subjected to the effects of pitting corrosion and elevated temperatures. By quantifying the changes in the surface roughness and the surface topographic feature parameters of steel reinforcing bars exposed to these conditions, the study provides essential insights into how surface characteristics influence fatigue behavior. The development of predictive models relating surface topographic feature parameters with corrosion level severity and temperature exposure establishes a robust framework for estimating the high cycle fatigue life of corroded reinforcing bars. Additionally, utilizing the parameters, this study also presents prediction models for a surface topographic feature variable in terms of SCF and defect size parameter.

Moreover, fatigue tests are conducted on both corroded and non-corroded high-strength high-ductile reinforcing bars under elevated temperatures enable a detailed analysis of the material's LCF strength under stress-controlled conditions. Based on experimental observations, including fractographic analysis of fracture corroded specimen at elevated temperature the study proposes a model for the distribution of pitting corrosion penetration depth and derives an analytical expression for the SCF and compared with the finite element (FE) analysis. Furthermore, through experimental investigations of LCF tests on corroded and non-corroded structural steel under strain-controlled conditions, the study utilizes a fatigue model to quantify the influence of strain amplitude on the number of cycles to failure. Microstructural investigation and morphology of the fractured surface of corroded and as well as corrosion-free structural steel specimens at different temperature exposures and at different strain-controlled conditions has been carried out. The study furthermore, extends to HCF behavior in constructional steel with multiple pit sites, by investigating the impact of corrosion level and maximum stress levels on the fatigue properties of structural steel along with the resulting macroscopic and microscopic morphological changes in structural steel specimens.

Overall, this research significantly advances our understanding of fatigue mechanisms in constructional steel under combined influence of pitting corrosion and elevated temperature exposure, contributing to the development of safer and more resilient infrastructure through enhanced design, assessment, and maintenance methodologies.

## **1.5 Outline of the thesis**

This thesis is presented in eight chapters. The first chapter provides the foundation for the research, covering the background of fatigue behaviour of the constructional steel under the combined effect of pitting corrosion and elevated temperature, objectives, research scope, and its significance. Chapter 2 presents a comprehensive literature review on the combined effects of corrosion and elevated temperature on the fatigue behavior of constructional steel, covering

fundamental fatigue processes, electrochemical corrosion mechanisms, and the severe impact of pitting corrosion on fatigue life. The study explores into the influence of temperature exposure, particularly post-fire, on steel fatigue, highlighting a gap in the experimental studies. Additionally, the review examines the critical role of surface characteristics of the constructional steel, such as pitting-induced surface roughness, and its correlation with fatigue strength. By summarizing these interconnected factors, the literature review underscores the importance of understanding the complex interactions between corrosion, fatigue, elevated temperature, and surface characteristics for ensuring the structural integrity and longevity of RCC and steel structures. Finally, the chapter identifies and discusses the existing research gaps within the current state-of-the-art.

Chapter 3 undertakes the experimental investigation to reveal the surface roughness characteristics of thermo-mechanically treated reinforcing bar subjected to pitting corrosion and elevated temperatures. The surface topography of the steel subsurface is seriously impacted by the pitting corrosion and elevated temperature exposure. This study presents the results of surface characteristics of the reinforcing bar exposed to pitting corrosion and elevated temperature.

Chapter 4 presents the novel and comprehensive framework for estimating the fatigue life of TMT reinforcing steel bars considering the combined action of pitting corrosion and elevated temperature impacted surface topography has been presented. A combination of experimental and numerical methods has been used in designing the framework. The framework is further validated using experimental data available in the literature.

Chapter 5 experimentally investigates the LCF behavior of pitting-corroded high-strength reinforcing steel bars at elevated temperatures. It proposes models for pitting corrosion and stress concentration factor, conducts fatigue tests on corroded and uncorroded specimens. The study utilizes average SED approach for fatigue life assessment of reinforcing steel bars and the study also develops predictive equations for key fatigue parameters correlated with temperature.

Chapter 6 covers the combined effect of pitting corrosion and elevated temperature exposure on the LCF behavior in structural steel. The study develops predictive models and evaluate the key parameters for both corroded and uncorroded specimens. Additionally, a fatigue model based on strain amplitude and cycles to failure quantifies the LCF response to these combined stressors.

Chapter 7 deals with the investigation of the HCF behavior of constructional steel subjected to single pitting corrosion as well as multiple pitting corrosion at room temperature under elastic stress conditions. The study provides an essential basis for assessment of the HCF properties of corroded constructional steel servicing in harsh environments such as chloride-contaminated.

## **Fatigue Behavior of Constructional Steels Subjected to Pitting Corrosion and Elevated Temperature**

Chapter 8 concludes the research by presenting a concise summary of key findings and conclusions. It also incorporates suggestions for future research work.

#### 2.1 Introduction

This chapter thoroughly review literature on the corrosion fatigue behavior of constructional steel. The various stages of fatigue processes, including microscopic and macroscopic damage, are comprehensively reviewed. Subsequently, the electrochemical corrosion process, involving metal oxidation and reduction, is thoroughly examined. Corrosion, an electrochemical phenomenon, involves the loss of electrons from metal atoms, resulting in positive charges (oxidation). These liberated electrons then combine with nearby atoms or adjacent substances (reduction). Under specific conditions, the transfer of electrons from the anodic region to the cathodic region may accelerate. Corrosion is categorized based on conditions such as galvanic, pitting, crevice, corrosion fatigue, and stress corrosion, or on the basis of electrochemical processes.

Corrosion of constructional steel emerges as a significant cause for the degradation of engineering structures. An estimated annual expenditure of approximately \$40 billion, constituting about 4% of the total economy, is allocated to the maintenance and repair of corroding structures in India. Chloride-induced corrosion poses a critical threat to the residual life and load-carrying capacity of RCC and steel structures. In corrosion fatigue scenarios, pitting corrosion acts as a substantial stress raiser, giving rise to numerous fatigue cracks that propagate across material grains. As these cracks grow, fatigue life diminishes due to accelerated corrosion-fatigue conditions.

The fatigue properties of constructional steel after exposure to temperature are thoroughly discussed further. The impact of fire on the service performance of structures, particularly those utilizing structural steel, is a critical concern. Elevated temperatures during a fire event significantly reduce the strength properties of steel. Although a post-fire steel structure may not immediately collapse, accurately evaluating its remaining serviceability is crucial for ensuring public safety and minimizing potential infrastructure failures. Limited studies have focused on post-fire mechanical properties, limited experimental studies have been conducted to comprehend the fatigue behavior of steel after exposure to temperature. A comprehensive literature review is presented to examine the effects of temperature exposure on the mechanical properties of steel, its impact on fatigue properties, and the influence of heating on microstructure.

Pitting corrosion at elevated temperatures remarkably affects the surface characteristics of steel, potentially reducing its mechanical performance, especially in terms of fatigue behavior.

## Fatigue Behavior of Constructional Steels Subjected to Pitting Corrosion and Elevated Temperature

The fatigue life of steel is heavily dependent on its surface characteristics, where fatigue cracks typically initiate from geometric discontinuities or corrosion pits, controlled by cyclic deformations higher than the average. Since fatigue failure generally initiates at the material surface, it is essential to comprehend the effect of surface roughness characteristics on the fatigue properties of steel. Focusing on the relationship between surface roughness and fatigue strength, this review also explores the detailed effects of varying exposure temperatures on the surface characteristics of steel.

### 2.2 Fatigue process

ASTM E-1823-21 defines fatigue as “the process of progressive localized permanent structural change occurring in a component subjected to conditions that produce fluctuating stresses and strains at some point or points and that may culminate in cracks or complete fracture after a sufficient number of fluctuations”. Since fatigue has a detrimental effect on the material, it is important to understand the mechanism and its associated effects.

There are different types of cyclic loading encountered. A schematic illustration of fatigue loading has been depicted in Fig. 2.1. Reverse cyclic loading has been illustrated in Fig. 2.1 (a). This type of loading is used in testing of material where maximum and minimum stresses are equal in magnitude. The material is loaded first from zero stress to maximum positive stress and then reverse loading start falling back to zero to maximum negative stress. After sufficient cycles, microscopic crack will initiate first, the crack initiation starts from the discontinuities or any kind of surface defect present. With the accumulation of further cycles, the cracks increase in size until the complete separation of the material takes place. Other type of fluctuating stress generally encountered is where the mean stress is applied on the top of minimum or maximum stress. The minimum stress may not be equal to the maximum stress as shown in Fig. 2.1 (b). The cyclic loading is composed of: (i) cyclic stress amplitude; and (ii) cyclic stress range. The cyclic stress range is the difference between the maximum stress ( $\sigma_{\max}$ ) and minimum stresses ( $\sigma_{\min}$ ) present in the cycle given by Equation 2.1:

$$\sigma_r = \sigma_{\max} - \sigma_{\min} \quad (2.1)$$

The cyclic stress amplitude is half of stress range in a cycle:

$$S = \frac{\sigma_{\max} - \sigma_{\min}}{2} = \frac{\sigma_r}{2} \quad (2.2)$$

Mean stress is algebraic sum of minimum and the maximum stress present in the cycles represented as:

$$\sigma_m = \frac{\sigma_{\max} + \sigma_{\min}}{2} \quad (2.3)$$

Stress ratio is expressed as:

$$R = \frac{\sigma_{\min}}{\sigma_{\max}} \quad (2.4)$$

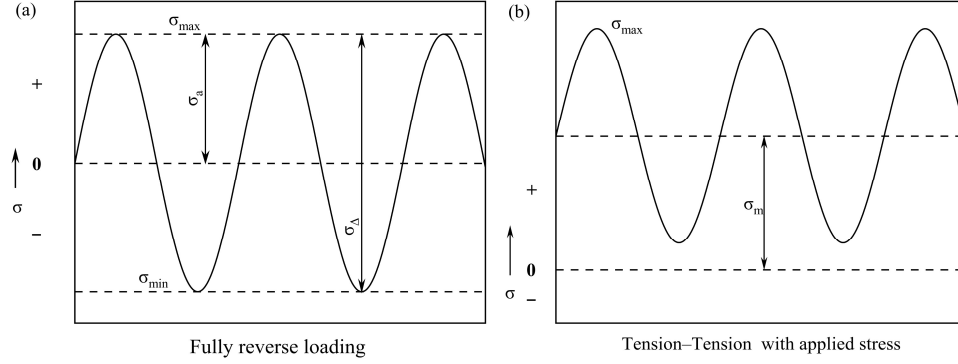


**Fig. 2.1** Typical loading cycles: (a) fully reverse loading; and (b) tension–tension loading.

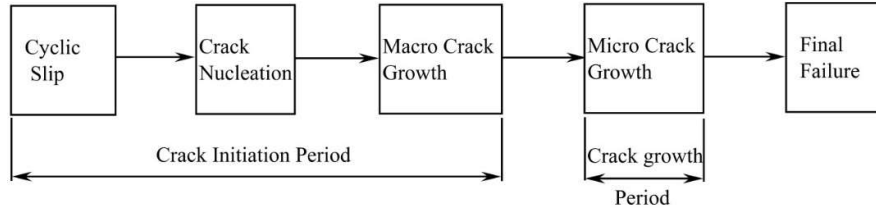


**Fig. 2.2** Stages of fatigue failure (Campbell, 2012).

The different stages of fatigue crack growth, from initiation to final fracture, are illustrated in Fig. 2.2 as follows: (i) Stage I involves the crack initiation period, characterized by the onset of damage induced by cyclic loading, resulting in crack initiation and nucleation; (ii) Stage II represents the crack propagation phase; and (iii) Stage III involves the sudden and complete failure of the cross-section.

**Crack initiation:** Generally, the fatigue crack nucleates and propagates in the region where the material contains any damage, corrosion pits, scratches or localized geometric discontinuities. Fatigue crack initiation and propagation are primarily attributed to cyclic slip mechanisms. Fatigue failure typically occurs at stress amplitudes significantly lower than the material's yield strength. (Schijve, 2009). When the material is subjected to cyclic loading the crack nucleates and tends to grow along the plane of maximum shear stress, leading to the generation of persistent slip bands (PSB) (Lee, 2005). These slip bands are the results of fine slip movements which are build up systematically and is of order of few nanometers. The accumulated strains in the PSB are more than 100 times than the adjoining material. The

## Fatigue Behavior of Construction Steels Subjected to Pitting Corrosion and Elevated Temperature

backward and forward motion of the slip bands leads to extrusion and intrusion of the surface, which ultimately, forms crack on the surface. Fig. 2.3 illustrates the formation of intrusion and extrusion of the surface during crack initiation (Campbell, 2012). Initially, the crack propagates parallel to the slip bands, approximately at a 45° angle to the maximum principal stress direction, with a propagation rate typically less than 1 nanometer (nm) per cycle. As the crack length increases sufficiently to develop a plastic zone at the crack tip, the crack plane changes its orientation to become perpendicular to the principal stress, transitioning into Stage II crack, as depicted in Fig. 2.4.

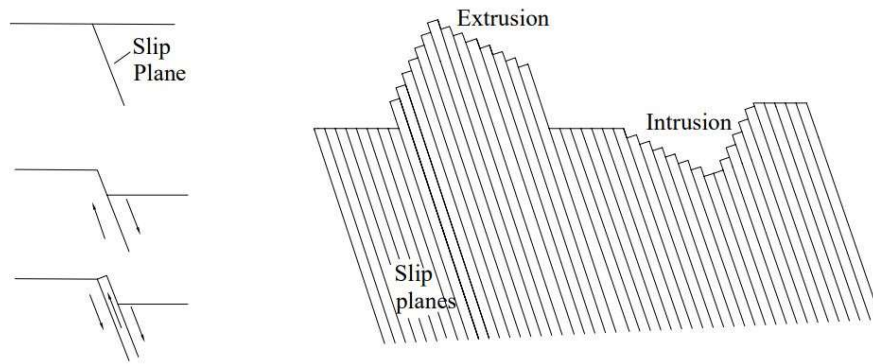


**Fig. 2.3** Formation of slip band and development of extrusions and intrusion subjected to cyclic load (Campbell, 2012).

**Crack propagation:** When the stage I crack changes its direction Stage II crack growth occurs and propagates normal to the principal stress. The plateaus are generally, normal to the tensile stress as shown in Fig. 2.4 (Lee, 2005). Crack propagation often produces the striations marks which are finely space parallel marks, generally formed perpendicular to the crack propagation direction. Each striation mark is the result of a single cyclic stress, and the spacing of these marks depends on the applied loading (Campbell, 2012). Two types of striation marks are observed: ductile and brittle types (Pelloux, 1969). Ductile striation marks are generally common type whereas; brittle type striations are generally the results of corrosion environment. When the crack growth rate is more, the striation marks became rough and develop wavy texture. Due to the development of the plastic zone at the crack tip secondary crack is developed. As the secondary crack grow and propagates a combination of secondary striations are developed and often difficult to distinguish from the combination of slip bands and slip lines (Campbell, 2012).

The size of crack initiation can be evaluated using linear elastic fracture mechanics for smooth specimen (Dowling et al., 1999) as :

$$a_0 = \frac{1}{\pi} \left( \frac{\Delta K_{th}}{S_e} \right)^2 \quad (2.5)$$

where  $a_0$  is the initial crack length ( $\mu\text{m}$ ),  $\Delta K_{th}$  is the threshold stress intensity factor ( $\text{MPa m}^{1/2}$ ) and  $S_e$  is the fatigue strength of the material (MPa).

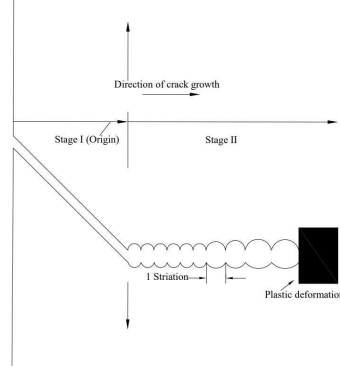


**Fig. 2.4** The progression from stage I to stage II fatigue (Campbell, 2012).

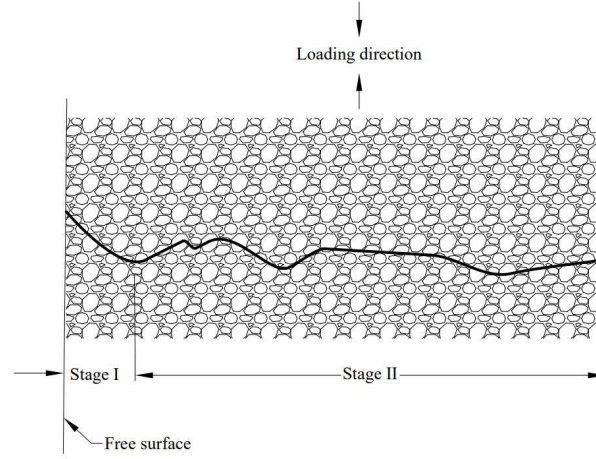


**Fig. 2.5** Development of stage I and stage II fatigue crack growth (Stephens et al., 2000).

The fatigue crack initiates at the surface and propagates across numerous grains (Fig. 2.5), which is controlled mainly by shear strain and shear stress and then the crack grows in the irregular zigzag direction perpendicular to the loading direction controlled mainly by the maximum tensile stress. Most of the fatigue crack grows across the boundaries of the crack i.e. transcrystalline. However, some crack develop intercrystalline propagating along grain boundaries and depends on the loading condition and material type (Stephens et al., 2000).

## 2.3 Fatigue life prediction model

### 2.3.1 Model for Fatigue crack nucleation life:

A dislocation model has been proposed by Tanaka and Mura (1981) to estimate the fatigue crack initiation life. The development of plastic deformation inside the PSB is modeled by using dislocation dipoles, which are layered systematically at the grain boundary. In the simplest form of the model the fatigue crack initiation life ( $N_{ci}$ ) is given as:



$$N_{ci} = \frac{AW_i}{(\Delta\tau - 2\tau_f)^2} \quad (2.6)$$

where  $\Delta\tau$  is the local shear stress range (MPa),  $W_i$  is the accumulated strain energy in the dislocation, and  $\tau_f$  is the frictional stress required to counteract the movement of dislocations. Whereas, the function  $A$  depends on the initial crack type and the properties of the material (Zhou et al., 1989).

$$A = \begin{cases} \frac{2G}{d_i} & \text{crack nucleates along the grain boundary} \\ \frac{4G}{\pi(1-\nu)d_i} & \text{crack nucleates along PSB} \\ \frac{4G(G+G_i)l_i^2}{G_i(l_i+d_i)^2 a_i} & \text{crack nucleates along the inclusion interface} \end{cases} \quad (2.7)$$

$G$  is the shear modulus of the material (MPa),  $G_i$  is the shear modulus of the inclusion (MPa),  $l_i$  is the length of the slip band ( $\mu\text{m}$ ),  $d_i$  is semi-minor length of slip band area ( $\mu\text{m}$ ),  $\nu$  is Poisson's ratio and  $a_i$  is the initial size of fatigue crack ( $\mu\text{m}$ ). However, in the theory proposed by Mura and Nakasone (1990) the friction shear stress is equal to half of the fatigue strength  $\sigma_f$ , that is at stress range of less than  $2\tau_f$  no fatigue crack nucleate. The relationship between the stress amplitude  $S$  and  $\Delta\tau$  is expressed as (Wang et al., 2001):

$$\Delta\tau = \left(\frac{\sqrt{2}}{3}\right)S \quad (2.8)$$

Utilizing the Von-Mises yielding criteria, i.e. when the shear stress on the octahedral plane is more than the octahedral shear strength  $\tau_0$  yielding occurs in a material:

$$\tau_0 = \left(\frac{\sqrt{2}}{3}\right)f_y \quad (2.9)$$

where  $f_y$  is the yield strength of the material (MPa). The frictional shear stress and the strain energy accumulated is expressed as follow (Wang et al., 2001):

$$\tau_f = \frac{1}{2} \left(\frac{\sqrt{2}}{3}\right) \sigma_f = \frac{\tau_0}{2} \quad (2.10)$$

since, frictional shear stress is half of the fatigue limit at a specific stress ratio. The fracture energy is obtained by:

$$W_s = \frac{\Delta K_{th}}{E} \quad (2.11)$$

$\Delta K_{th}$  for ferrite–pearlite and martensitic steel is expressed as (Barsom, 1974):

$$\Delta K_{th} = 7.03(1 - 0.85 R) \quad (2.12)$$

The fatigue crack initiation life is evaluated using the Equation 2.6–2.12 expressed as (Wang et al., 2002):

$$N_{ci} = \frac{9 \Delta K_{th}^2 G}{2 E (S - S_e)^2 a_0} \quad (2.13)$$

### 2.3.2 Model for Fatigue crack propagation life:

Fatigue crack growth from initial crack size ( $a_0$ ) to critical crack size ( $a_c$ ) with respect to cycles to failure are shown in Fig. 2.6.

In the region I,  $\Delta K_{th}$ , is at lower end of  $\Delta K$  range and the crack growth rate is nil at region I.  $\Delta K$  is the stress intensity range which is expressed as (Campbell, 2012):

$$\Delta K = \Delta K_{max} - \Delta K_{min} \quad (2.14)$$

In the region II, the rate of crack growth ( $da/dn$ ) can be related to  $\Delta K$  approximately linearly in the log–log plot and lie in the range of  $10^{-6}$ – $10^{-3}$  in./cycle (Bannantine et al., 1990).

Paris and Erdogan (1963) postulated that under fatigue loading conditions, the crack growth rate remains stable within the Stage II regime. They proposed an equation known as the "Paris equation," which follows a power–law relationship and is expressed as:

$$\frac{da}{dn} = C(\Delta K)^m \quad (2.15)$$

where  $C$  and  $m$  are fatigue crack growth parameters which is related to the fatigue loading condition, material variable, and temperature.

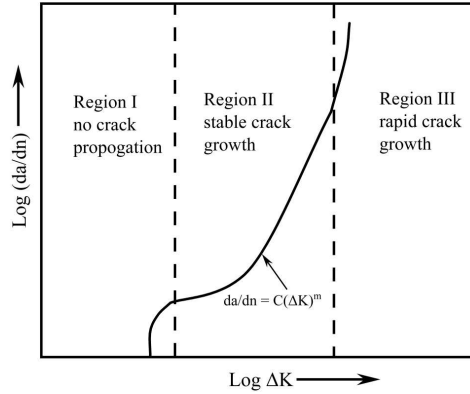


**Fig. 2.6** Crack propagation curve for fatigue propagation (Campbell, 2012)

## Fatigue Behavior of Constructional Steels Subjected to Pitting Corrosion and Elevated Temperature

The Paris law can be used to evaluate the cycles to failure as (Bannantine et al., 1990; Campbell, 2012):

$$\Delta K = \Delta K_{\max} - \Delta K_{\min} = Y\sigma_{\max}\sqrt{\pi a} - Y\sigma_{\min}\sqrt{\pi a} = Y\sigma_r\sqrt{\pi a} \quad (2.16)$$

where  $Y$  depends on the geometry of the specimen, in case of large plate with a small crack at edge loaded in tension  $Y=1.12$ . The Paris law is expressed as substituting  $\Delta K$  into Equation 2.15:

$$\frac{da}{dn} = C(Y\sigma_r\sqrt{\pi a})^m \quad (2.17)$$

$$dn = \frac{da}{C(\Delta K)^m} \quad (2.18)$$

Integrating the above equation gives:

$$n_f = \int_0^{n_f} dn = \int_{a_i}^{a_f} \frac{da}{C(\Delta K)^m} \quad (2.19)$$

Substituting the value of  $\Delta K$  and rearranging  $n_f$  is expressed as:

$$n_f = \int_{a_i}^{a_f} \frac{da}{C(Y\sigma_r\sqrt{\pi a})^m} = \frac{1}{C\pi^{0.5m}(\sigma_r)^m} \int_{a_i}^{a_f} \frac{da}{Y^m a^{0.5m}} \quad (2.20)$$

However, the Paris equation doesn't take into account the effect of  $R$ . In order to utilize the stress ratio the above equation has been modified as (Forman et al., 1967):

$$\frac{da}{dn} = \frac{C(\Delta K)^m}{(1-R)K_{IC} - \Delta K} \quad (2.21)$$

where  $K_{IC}$  is the fracture toughness of the material ( $\text{MPa m}^{1/2}$ ). The final crack size needs to be determined in the above equation. The material will ultimately fail when the applied stress ( $\sigma$ ) exceeds some critical value ( $\sigma_c$ ). Thus, at  $\sigma_c$  or  $\sigma_{\max}$  there exists some critical value of  $K$  which is called  $K_{IC}$  and it is the material ability to resist brittle fracture when crack is already accommodated within it.

$$K_{IC} = Y\sigma_c\sqrt{\pi a_f} \quad (2.22)$$

Therefore, from the above equation the final crack size can be expressed as (Bannantine et al., 1990; Campbell, 2012; Lee, 2005):

$$a_f = \frac{K_c^2}{\pi Y^2 \sigma_{\max}^2} \quad (2.23)$$

In region III, unstable crack growth rate can be observed due to the material approach toward the fracture toughness. In many fractures analysis for material this region is ignored since, failure due to overload occurs. The crack propagation life,  $(N_{cp})$ , in a material can be estimated using the analytical solution of Paris law integral given as (Wang et al., 1999):

$$N_{cp} = \frac{a_0^{\left(1-\frac{m}{2}\right)} - a_{sc}^{\left(1-\frac{m}{2}\right)}}{C S^m \kappa_1^m \pi^{\frac{m}{2}} \left(\frac{m}{2} - 1\right)} + \frac{a_{sc}^{\left(1-\frac{m}{2}\right)} - a_f^{\left(1-\frac{m}{2}\right)}}{C S^m \kappa_2^m \pi^{\frac{m}{2}} \left(\frac{m}{2} - 1\right)} \quad (2.24)$$

where  $a_{sc}$  is defined as the critical crack size,  $a_f$  is the final failure crack size,  $\kappa_1 = 0.5\sqrt{\pi}$  and  $\kappa_2 = 1$ . Typically, the number of cycles required for crack growth from  $a_0$  to  $a_{sc}$  is significantly higher than the cycles needed to advance from  $a_{sc}$  to  $a_f$ . Consequently,  $N_{cp}$  can be expressed as (Wang et al., 1999):

$$N_{cp} = \frac{a_0^{\left(1-\frac{m}{2}\right)}}{C S^m \kappa_1^m \pi^{\frac{m}{2}} \left(\frac{m}{2} - 1\right)} \quad (2.25)$$

## 2.4 Corrosion process

ASTM G193–2022 describe corrosion as “the degradation of the material and its properties generally a metal by involving chemical or electro–chemical reaction with its environment”. Since, corrosion has detrimental effects on the material, it is necessary to know its mechanism and its effect on the material. Generally, the extraction of metals from their ore requires considerable amount of energy; however, with the passage of time the metal reacts with atmosphere and tend to revert backs to its ground state. Metals such as steel has thermodynamically instability and with time it reacts with the environment and tends to return to its natural condition i.e. by forming iron oxide or rust this process involve release in energy, known as corrosion. Corrosion involves the sum of two half reactions, anodic reaction and cathodic reaction. The metal which is corroding undergoes oxidation (anodic reaction) i.e. capable of generating electrons while, electron–consumption species undergoes the cathodic reaction (reduction). The cathodic reaction is dependent on the pH near the surface of the steel and also on oxygen availability (Hansson, 1984). In order to ensure charge balance, the rate of consumption and production of electron must be same i.e. both oxidation and reduction must occur at same time and rate. General anodic reaction is of form:

## Fatigue Behavior of Constructional Steels Subjected to Pitting Corrosion and Elevated Temperature



The primary cathodic reaction that contributes to metal corrosion is typically expressed as:



*Corrosion due to chloride ingress:* One of the primary causes of the pitting corrosion of the reinforcing steel bar in RCC members and structural steel is the presence of the chloride ions of sufficient concentration. When enough concentration of chloride ions reaches the reinforcing steel bar they causes breakdown of the passive film on the surface of the steel reinforcing bars initially formed due to the presence of sufficient concentration of soluble sodium, calcium and potassium oxides (Montemor et al., 2003). In the presence of water these oxides form hydroxides which make a high alkaline environment. This high alkalinity environment creates the passive layer around the surface of reinforcing bar (Elsener et al., 2003). Pitting corrosion is a localized break down of the passive film form on the surface of the metals resulting in active disintegration or dissolution of the metal (Frankel, 1998). The Chloride ions can infiltrate to the concrete through various sources. These chloride ions interfere with the alkalinity of the porous solution when diffused into concrete, thereby reducing the pH of the pore solution. The Chloride ions intruding steel surface results in decomposition of the passive film and leads to the formation of the soluble by-products i.e., ferrous chloride ( $\text{FeCl}_2$ ). The ferrous chloride has the tendency to get dissolve in the porous solution from the surrounding, liberating chloride ions in order to cause more decomposition.



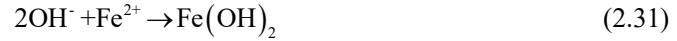
After the breakdown of passive layer, pits are formed and iron dissolves into the porous solution leading to release of electrons.



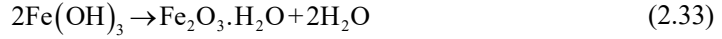
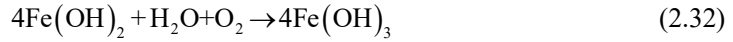
Ferrous ions ( $\text{Fe}^{2+}$ ) positively charged present at the anode passes into the solution while the negatively charged ions ( $2\text{e}^-$ ) reached to the cathode through porous solution. Hydroxyl ions are formed by the absorption of water and oxygen to form cathodic reaction.



since, metals are not thermodynamically stable, and tend to get back to its natural form under the normal atmospheric conditions i.e. hydroxyl or oxides by the release of the energy. Therefore, the ferrous hydroxide is formed by the reaction of ferrous ions with hydroxyl ions.



This is further converted to rust by oxidation.



Corrosion of the reinforcing steel bar is one of the most common failures in RCC structures, widely accepted as the main factor affecting their service life. The essential components required for corrosion, including multiple metals with differing energy levels, an electrolytic solution, and a metallic connection, are present in RCC structures. The reinforcing bars contain many locations with various energy levels, and the pores of the concrete contain oxides that react with water to form hydroxides, creating a protective alkaline environment with a pH greater than 12.5 (Tuutti, 1982). Pitting corrosion, characterized as an autocatalytic or self-catalytic reaction, promotes further pit growth once initiated. Palsson and Mirza (2002) reported that as the cross-sectional area of reinforcement diminishes to 50% due to pitting corrosion, the behavior of the reinforcing bar transitions from ductile to brittle. Stewart (2004) and Stewart and Al-Harthy (2008) identified pitting corrosion as causing a significant reduction in the structural reliability of reinforced concrete elements compared to uniform corrosion. The high alkalinity in the micropores of concrete allows the formation of a passive film on the surface of the rebars (Poupard et al., 2006), with the reinforcing steel bar providing the necessary metallic connection for the corrosion process. Darmawan and Stewart (2007) observed a shift from plastic to brittle failure in steel reinforcement due to pitting corrosion, which is particularly notable in members subjected to flexure, carrying potentially serious consequences. Detection of pitting corrosion poses challenges as the formed products often cover the pits. Consequently, chloride-induced corrosion is considered more severe than uniform corrosion.

## 2.5 Fatigue failure of constructional steel

RCC bridges, under increased traffic loads from economic expansion, become more susceptible to fatigue damage. Sudden steel bar failures in RCC structures, marked by localized concrete crack propagation, result from cyclic stress surpassing the fatigue limit, crucial in RCC bridge failures. Investigating reinforcing bar fatigue under cyclic loading holds theoretical and practical significance. Similarly, road networks, bridges, and offshore structures, facing cyclic loading from operational loads, require assessment of steel bar HCF properties. For instance, offshore structures endure over  $10^7$  cycles of stress reversal within a 30-year lifespan, while highway bridges with a 50-year expectancy may experience traffic-induced stress reversals exceeding  $3 \times 10^8$  cycles (Tilly, 1979). Stress reversal's, high frequency and low magnitude

## **Fatigue Behavior of Constructional Steels Subjected to Pitting Corrosion and Elevated Temperature**

emphasize HCF's importance, especially in developing countries like India undertaking extensive infrastructure projects. Investigating HCF is crucial to ensure the intended design lifespan of these structures. Seismic events induce LCF loading in reinforcing steel, confirmed by studies like Sheng and Gong's analysis of the Tangshan earthquake (Sheng and Gong, 1997). Recognizing LCF's pivotal role in assessing seismic response, extensive research focuses on characterizing the LCF properties of rebars and structural steels. Reinforced concrete buildings are composite structures where brittle materials like concrete provide compressive support, and steel rebar reinforces tensile capacity and managing high-strain cyclic loads during earthquakes. The rebar acts as a resilient skeleton, redistributing seismic forces, and crucially, the entire building's integrity relies on its ability to withstand fatigue-inducing seismic demands, allowing for occupant evacuation time. Investigating the LCF behavior of rebar, indicating resilience under repeated seismic loading, becomes a crucial step in validating and optimizing seismic design for structural integrity and occupant safety. Paul et al. (2014) investigated the HCF and LCF behavior of micro-alloyed (MA) and 500 steel grade TMT rebars. HCF tests were conducted using a 100 kN servo-hydraulic testing machine with a test frequency of 30 Hz, maintaining a constant stress ratio of 0.2. LCF tests were performed at a strain rate of 0.001/sec. The stress range versus the number of cycles to failure was plotted for both type of steel revealing that at higher stress levels, HCF strength curves for TMT and MA rebars closely aligned, diverging at lower stress levels. MA rebar demonstrated significantly higher strength at lower stress ranges. Throughout tested stress ranges, HCF strength consistently surpassed that of TMT rebar. Stress amplitude versus the number of cycles curves for LCF with various strain amplitudes showed minimal cyclic hardening for both rebars, similar to HCF. A comparison of strain amplitude versus fatigue life indicated that, like HCF life, LCF life for MA rebar exceeded those of TMT rebar. The difference in LCF life diminished as the strain amplitude increased.

Hawileh et al. (2010) conducted an experimental investigation to assess the LCF behavior and characteristics of two distinct steel reinforcing bars: BS 460B and BS B500B. This study experimentally evaluates the LCF resistance BS 460B and BS B500B reinforcing bars with different values of strain ratios and propose models for prediction of their fatigue life based on plastic-strain and total-strain amplitudes. Strain controlled fatigue test has been conducted at room temperature. Steel samples, experiencing maximum strains within the range of 3% to 10%, under varied strain ratios with values set at -1, -0.5, and 0. The LCF test reveals that the hysteresis loops expand with increasing strain amplitude, resulting in a larger area under the hysteresis loop and, consequently, greater energy dissipation. Additionally, it is observed that the energy dissipation per loop (damping level) is higher for strain ratio of -1 compared to strain ratio of -0.5 and strain ratio of 0. Moreover, the log-log curves are plotted between the total

strain amplitude and the number of cycles to failure based on the Coffin–Manson equation, expressed as:

$$\varepsilon_p = \frac{\varepsilon_{p,\max} - \varepsilon_{p,\min}}{2} = \beta (2N_f)^\alpha \quad (2.34)$$

where  $\varepsilon_p$  is the plastic-strain amplitude;  $\varepsilon_{p,\max}$  and  $\varepsilon_{p,\min}$  are the maximum and minimum plastic-strain  $\beta$  is the fatigue ductility coefficient.  $2N_f$  represents the number of reversals to failure ( $N_f$  is the number of cycles to failure) and  $\alpha$  is an empirical constant known as the fatigue ductility exponent. However, Koh and Stephens (1991) have modified Coffin–Manson equation to relate the total strain amplitude with fatigue life, as expressed below:

$$\varepsilon_a = \beta (2N_f)^\alpha \quad (2.35)$$

It has been observed that the  $\beta$  ranges between 0.207 and 0.602 while  $\alpha$  ranges between -0.54 and -0.74 for the study. With an increase in strain ratio from -0.5 to 0 at the same strain amplitude, the number of cycles to failure rises for both BS 460B and BS B500B reinforcing bar specimens. The proposed models exhibit higher accuracy in predicting fatigue life at high strains (low number of cycles) compared to low strains (high number of cycles). The study also reveals that at low total strain values (high number of cycles), the mean strain ratio significantly impacts the material's fatigue life. The simpler empirical models Equation 2.34 and 2.35 demonstrate better predictive capabilities for the experimental data holding true for both steel types and all investigated strain ratio values. Qian et al. (2010) experimentally investigated the HCF and very-high-cycle fatigue (VHCF) properties of 40Cr structural steel. The Specimens were smooth hour-glass-shaped with a minimum section diameter of 3 mm. The specimen surfaces were mirror polished. The fatigue tests were conducted at a frequency of 52.5 Hz in room temperature. The stress ratio was maintained at -1. The notched specimens were employed in this study also have an hour-glass shape but feature a V-notch at the reduced section. The fatigue  $S_f$ – $N_f$  curves depicting the fatigue behavior of smooth and notched specimens reveals that the fatigue failure occurred at a cycle of  $7.1 \times 10^8$ , indicating the potential risk associated with considering the conventional fatigue limit as the VHCF limit. In the case of smooth specimens, the  $S_f$ – $N_f$  curve exhibits a stepwise pattern. A consistently declining curve was obtained for notched specimens. For a given fatigue life, the fatigue notch sensitivity factor  $q'$  was calculated using the following equation:

$$q' = \frac{k_f - 1}{k_t - 1} \quad (2.36)$$



## **Fatigue Behavior of Constructional Steels Subjected to Pitting Corrosion and Elevated Temperature**

where  $k_f$  is the ratio of fatigue strength for smooth specimens to the fatigue strength for notched specimens. Fatigue tests on notched specimens revealed a continuously decreasing  $S_r-N_f$  curve. Scanning electron microscopy (SEM) analysis, identifying multiple crack initiation sites predominantly on the specimen surface, indicating that fatigue cracks primarily originate from the surface under fatigue conditions. The fatigue life depends on the inclusion's depth  $\tilde{d}$  ( $\mu\text{m}$ ), and the study propose the following correlation between fatigue life and inclusion depth:

$$N_f = 1.96 \times 10^5 \tilde{d}^{2.4} \quad (2.37)$$

### **2.6 Corrosion–Fatigue failure of constructional steel**

Corrosion exerts a detrimental influence on the fatigue behavior of constructional steel used in concrete and steel structures. Apostolopoulos and Papadopoulos (2007) have investigated both the tensile and LCF behavior of corroded reinforcing steel bar of grade S400S. The specimens for tensile and LCF tests were corroded using the salt spray method, utilizing 5 % of NaCl solution and corroded for duration of 10, 20, 30, 45, 60 and 90 days respectively. The corrosion damage has been measured using the gravimetric mass loss technique. LCF test were performed at a constant low strain amplitude of  $\pm 1\%$  and it has been recorded that, there has been sufficient reduction in number of cycles to failure with increases in mass loss percentage. A 47% of reduction occurred at 3% mass loss. The total dissipated energy density, reflecting earthquake–related energy absorption, decreased with higher corrosion levels. Evaluation of maximum force (tensile and compressive) per fatigue cycle showed that the maximum tensile force dropping from about 37 kN to approximately 32.5 kN after the initial 150 fatigue cycles for uncorroded material, remaining stable until approaching failure. The crucial role of reinforcing steel in withstanding tensile loads highlighted changes in anticipated displacements and structural static design after initial fatigue cycles, particularly pronounced in the case of corroded reinforcement. The maximum tensile force diminished to around 27.5 kN, remaining relatively constant until the final stages before failure, which occurred at a significantly smaller number of cycles. In the work performed by Apostolopoulos (2007) the LCF behavior of reinforcing steel bar of grade S500s at constant strain amplitude of  $\pm 1\%$ ,  $\pm 2.5\%$  and  $\pm 4\%$  and at frequency of 1 Hz under the impact of corrosion has been investigated. The specimens were corroded, using accelerated corrosion method in salt spray environment. The corrosion damage significantly influences the number of cycles to failure. With the increasing exposure time, a consistent decrease in cycles to failure is observed. Notably, at a low strain levels of  $\pm 1\%$ , a more substantial reduction in service life (50.3% for 90 days of accelerated salt spray corrosion) is evident compared to  $\pm 2.5\%$  and  $\pm 4\%$  where the reduction stabilizes at less than 20%.

The capacity to bear maximum loads diminishes under fatigue loading, with a more pronounced reduction evident in corroded specimens. Consequently, in the context of aging RCC structures located in seismically active regions, one should not anticipate a sustained constant load-bearing capability beyond a certain service life. The LCF characteristics on TMT rebar at room temperature has been conducted by Paul et al. (2014) on machined TMT bar specimen under strain controlled at a strain rate of  $10^{-3}$  /sec with strain amplitude of 0.3%, 0.5%, 0.75%, 1.0% and 1.5% and stress-controlled condition and 50 MPa/sec at constant stress rate, with stress amplitude of 400 MPa, 450 MPa and 500 MPa. Notably, negligible cyclic softening (reduction in stress amplitude with increasing cycles) occurs at higher strain amplitudes (e.g., 1.5%, 1.0%). Conversely, distinct cyclic softening is observed at lower strain amplitudes (e.g., 0.3%, 0.5%). Two key factors contribute to the TMT rebar's shorter fatigue life: (a) stress concentration arising from the presence of transverse ribs; and (b) the presence of tempered martensite on the outer surface. Fatigue life is closely linked to surface properties, and the presence of martensite is believed to be detrimental to fatigue performance.

Nakamura and Suzumura (2013) conducted an experimental investigation into the impact of corrosion on the fatigue strength of galvanized steel wires. The study subjected steel wires with varying levels of corrosion to fatigue testing under both dry and wet conditions. Measurements of surface roughness and pit depth were taken on corroded wires, revealing a correlation between the level of corrosion and the size of pits. The deepest pits, measuring up to 0.56 mm in depth, were concentrated in smaller areas, while shallower pits (<0.4 mm) were more dispersed. Cyclic loading tests were conducted on wire specimens with artificial pits with stress range of 400 MPa. These results confirm the lowest fatigue strength for notched pits due to stress concentration at the sharp edge. The SCF around pits were evaluated using strain gauges and FE analysis. The analysis confirmed that higher stress concentration for sharper and shorter triangular pits, whereas lower concentration for round pits. The study shows that deeper and sharper corrosion pits significantly reduce the fatigue strength of bridge wires. The study highlights the critical importance of early detection and mitigation strategies when corrosion pits are still shallow.

Fernandez et al. (2015) conducted cyclic fatigue tests to evaluate the fatigue performance of 10 mm and 12 mm reinforcing steel bars, investigating both corroded and uncorroded conditions. The tests were carried out under stress-controlled loading. The specimens exhibited a yield strength of 500 MPa. Pitting corrosion was induced using a direct current (DC) power supply, and fatigue tests were conducted at a frequency of 15 Hz with stress ranges of 150 MPa, 200 MPa, and 300 MPa. The results indicated that ultimate and yield stress were highly dependent on corrosion levels, and mechanical properties decreased with increasing corrosion degree. The study emphasized that the greater influence of pit depth compared to pit

## Fatigue Behavior of Constructional Steels Subjected to Pitting Corrosion and Elevated Temperature

length on the fatigue behavior of steel. Higher corrosion degrees lead to a significant reduction in fatigue life, with number of cycles to failure decreasing rapidly as corrosion levels increased. Overall, a negative exponential adjustment accurately captured the decline in fatigue life of corroded specimens compared to uncorroded specimen. An attenuation rate was observed as stress levels decreased, highlighting a consistent behavior across all the specimens regardless of the applied stress range. The study concluded that steel reinforcement corrosion has a limited impact on fatigue life at very low corrosion degrees, but a substantial reduction becomes evident as corrosion intensifies.

A surface defect model has been proposed by Chen et al. (2018) to estimate the fatigue life of corroded reinforcing steel bar. The smooth standard specimen utilized in this study is derived from lathe-processed hot-rolled ribbed steel bars having yield strength of 455 MPa with a 20 mm diameter. The original steel bar's outer layer is removed. HCF test has been performed on corroded specimen under stress-controlled loading at stress ratio of 0.1 with a frequency of 20 Hz. The maximum stress levels are set to be  $0.5 f_y$ ,  $0.6 f_y$ ,  $0.7 f_y$  and  $0.8 f_y$ . Accelerated corrosion method using the impressed current, has been adopted as the pre-corrosion technique in this study. The corrosion degree has been evaluated on the basis of minimum cross section in the corroded pit section rather than on the mass loss percentage of the specimen and is evaluated using Equation 2.38:

$$\eta_{\max} = 1 - A_m / A_n \quad (2.38)$$

where  $\eta_{\max}$  is the maximum corrosion degree,  $A_m$  is the minimum cross-sectional area at the pit location and  $A_0$  is the initial cross-sectional area of the rebar. The cross-section geometry of the corroded pit has been measured using a high resolution 3-dimensional laser technique. The study established relationship on the basis of surface defect crack evaluated under HCF condition with maximum corrosion degree and the aspect ratio of the corrosion pit i.e. the ratio of depth and width of the corroded pit. The total fatigue life has been determined using Equation 2.24 and the equivalent defect size has been evaluated further, organize into two categories based on the observed crack initiation mode (single- and multi-crack initiation cases). The least square method is employed in order to establish the relation between the surface defect size with maximum corrosion degree and the aspect ratio of the corroded pit. The equivalent surface defect model has been expressed by Equation 2.39:

$$\ln a_0 = \begin{cases} 19.06\eta_{\max} - 12.40(p_d^{\max} / w) - 20.72 & \text{single-crack initiations} \\ 25.48\eta_{\max} - 3.97(p_d^{\max} / w) - 22.50 & \text{multi-crack initiations} \end{cases} \quad (2.39)$$

The fatigue behaviour of high-strength steel Q460D and Q550E under corrosion has been experimentally investigated by (Liu et al., 2021). An electrochemical accelerated method has been utilized. Corrosion level has been determined using the mass loss percentage as:

$$\mu_m = \frac{(m_0 - m_c)}{m_0} \times 100 \quad (2.40)$$

where  $\mu_m$  is the designed mass loss percentage,  $m_0$  is the initial mass of the specimen and  $m_c$  is the mass of the corroded specimens. A 3D laser scanner (accuracy 29  $\mu\text{m}$ ) characterized the corrosion morphology. Fatigue testing was conducted on electro-hydraulic servo fatigue testing equipment with a stress ratio of 0.1 was used for all cycles. Load-controlled tests were conducted using a sinusoidal loading curve with 8 Hz frequency for Q460D and 6 Hz for Q550E and six stress levels are designed based on the maximum stress levels ranged from 0.42 to 0.7 times the ultimate strength of the non-corroded steels. Upon specimen failure, the cyclic load value, failure cycle, and fracture details were recorded. The study employed a power exponential  $S - N_f$  to model the fatigue failure process in corroded specimens. This equation  $N_f$  to  $S$  on a double logarithmic scale, forming a linear relationship with slope ( $n$ ) and intercept ( $B$ ) is expressed as:

$$\log N_f = B - n \log S \quad (2.41)$$

The following Equation 2.42 for Q460D steel and Equation 2.43 for Q550E steel has been proposed in the study to estimate the fatigue life of the test specimens based on the maximum cross-sectional loss ratio and the fatigue stress amplitude.

$$\log N_f = 0.1261\mu_m + 22.692 - (0.0638\mu_m + 7.9959)\log S \quad (2.42)$$

$$\log N_f = 0.1261\mu_m + 22.692 - (0.0638\mu_m + 7.9959)\log S \quad (2.43)$$

where  $\mu_m$  lies in the range of 0 to 48%.

## 2.7 Effect of temperature exposure on properties of steel

Fire poses a significant risk to building structures, impacting their safety. While RCC structures are generally less susceptible to progressive collapses due to concrete protection on steel rebars, overall material and structural performance can degrade after exposure to the fire conditions. The degradation of steel rebar mechanical properties is a crucial factor. Experimental investigations was conducted by Raj et al. (2016) to analyse the effects of elevated temperatures and exposure durations on the mechanical and metallographic properties of TMT bars.

## **Fatigue Behavior of Constructional Steels Subjected to Pitting Corrosion and Elevated Temperature**

Specimens, extracted from 25 mm diameter Fe500 steel bars conforming to IS 1786:2008 standards. The steel bars were subjected to heat treatment with two main parameters: peak temperature and soaking period. Heating was done in an electric furnace, with temperatures ranging from 250 °C to 950 °C and soaking periods from 10 to 240 minutes. A thermocouple ensured precise temperature control within  $\pm 4^\circ\text{C}$ . After heating, specimens cooled in ambient air, with rapid initial cooling to around 200 °C within 20 minutes, followed by a slower cooldown to room temperature in about an hour. Though direct heating was used, real-world scenarios in reinforced concrete structures may differ due to factors like cover concrete protection or fire extinguishing materials. The test procedure involved evaluating mechanical properties and microstructure. Mechanical properties like yield stress and ultimate tensile strength were tested using a universal testing machine. Microstructural examination utilized an optical microscope and hardness of the steel specimens was measured using a standard Vickers microhardness test on polished surfaces. The study found that TMT bars experienced significant damage above 500 °C, with potential yield strength, ultimate strength and elongation ratio losses of up to 50% and 30%, respectively. Elongation at failure increased by 66% with higher peak temperatures. Microstructural changes were observed, including tempered martensite at 250 °C and spheroidization of cementite at 500 °C. Heating upto 750 °C eliminated the outer martensitic rim, transforming the cross-section into ferrite and austenite. Exposure to 950 °C resulted in a uniform ferrite-pearlite microstructure, coarser than the structure exposed to 750 °C.

The effects of elevated temperatures on reinforcing steel properties has been experimentally investigated by Tariq and Bhargava (2021). Super ductile TMT rebars (8 mm to 20 mm) with a yield strength of 540 N/mm<sup>2</sup> and minimum ductility of 18% underwent accelerated corrosion to achieve precise mass loss. Subsequently, specimens were heated to various temperatures exposure (250 °C, 550 °C, 800 °C, and 950 °C), reaching steady-state before cooling for tensile testing to failure. The study shows a slower, steady decline in mechanical properties between 250 °C and 550 °C, followed by a rapid drop in the temperature range of 550 °C–950 °C. The reduction in yield strength and ultimate strength is primarily influenced by corrosion at moderate temperatures (25 °C –550 °C) and elevated temperatures (550 °C–950 °C). The findings emphasize the deterioration of mechanical properties due to corrosion-temperature combinations affecting critical parameters such as yield strength, ultimate tensile strength, modulus of elasticity, and elongation at failure in rebars. Stress-strain behavior changes are attributed to combined macro and microstructure damage. Corrosion-induced deterioration is followed by temperature-induced microstructure alterations. Exposure to temperatures above 600 °C triggers changes in microstructure, including coarser spheroidal particles and alterations in ferrite distribution. TMT bars' residual mechanical behavior is significantly influenced by the grain size and distribution of ferrite across the cross-section. The tensile strength tends to

decrease with an increase in ferrite grain size. Changes in key mechanical properties result from alterations in the martensitic, bainite transition zone, and ferrite–pearlite core followed by variations in grain size and dislocation density due to exposure to elevated temperatures. When subjected to marine conditions, steel undergoes continuous corrosion. The proliferation of offshore structures for transporting and storing combustible oil and gas reserves poses a risk of leakage, leading to potential explosions or fires. Aging offshore steel structures, when exposed to fire, can result in catastrophic accidents. A study by Ren et al. (2020) examined the mechanical characteristics of corroded marine steel after temperature exposure. Corrosion was induced using a salt spray technique with durations ranging from 0 to 384 hours. The steel's elastic modulus, ultimate tensile strength, and yield strength decreased with increasing corrosion duration. The steel's residual strength at 900 °C was only 20–50% compared to that at 500 °C. Fracture morphology analysis of the corroded specimen exposed to high temperatures revealed larger and deeper dimples, indicating substantial plastic deformation. The microstructures of the specimens exposed to 500°C reveal a banded structure. These bands consist of alternating white and black regions corresponding to concentrated areas of ferrite and pearlite, respectively.

## **2.8 High–temperature fatigue behavior of constructional steel**

Fires pose a common threat to both RCC and steel structures, with temperature variations influenced by factors like combustible type, ventilation, fire duration, and structural member location, resulting in significant temperature uncertainty. Constructional steel in structures may experience temperatures exceeding 800 °C (Kodur et al., 2004). Assessing the post–fire mechanical performance of steel bars is crucial to determine whether a structure, surviving a fire without collapsing, can safely continue in service, requires maintenance, or should be demolished (Wang et al., 2015). Additionally, structures that withstand fires may encounter subsequent challenges, including potential earthquakes during future service. In seismic events, both structural and reinforcing steels face cyclic loads, particularly LCF. Thus, a comprehensive understanding of the post–fire fatigue properties of constructional steel is vital for evaluating the fatigue resistance of structures. In an experimental investigation on the LCF behavior of Q690 high–strength structural steel at elevated temperatures heating up to 900 °C followed by room temperature cooling conducted by Hua et al. (2022). LCF tests at room temperature featured varied strain amplitudes of 0.8%, 1.0%, 1.5%, and 2.0%, with a constant fatigue strain ratio of 0.1. A triangular wave pattern with a consistent strain rate of 0.01 strain/s and a constant fatigue strain ratio of -1 was followed in the study. The hysteresis curves displayed effective energy dissipation, with exposure temperatures up to 700 °C minimally affecting the hysteretic curve. However, in the temperature range of 700 °C to 900 °C, increasing exposure temperature gradually reduced specimen strength, resulting in a fuller hysteretic curve due to increased plastic strain. Stress and strain coefficients illustrated distinct stages of initial softening

## Fatigue Behavior of Constructional Steels Subjected to Pitting Corrosion and Elevated Temperature

(hardening), stable behavior, and final softening. The study investigates the influence of exposure temperature and fatigue strain amplitude on the stress–strain behavior of post–fire Q690 steel subjected to LCF loading. A selected fatigue model quantifies the correlation between  $\varepsilon_a$  and  $N_f$ , revealing a decrease in  $N_f$  with increasing  $\varepsilon_a$  and is expressed using Equation 2.44 as:

$$\varepsilon_a = \beta (2N_f)^\alpha \quad (2.44)$$

where  $\varepsilon_a$  is the total strain amplitude. The negative relation between  $\varepsilon_a$  and  $N_f$  was observed, indicating that the impact of exposure temperature on the  $\varepsilon_a$  vs.  $N_f$  can be effectively quantified using Equation 2.44. The ultra–low cycle fatigue (ULCF) tests on Q690 high–strength structural steel conducted by Hua et al. (2022), employing strain ratios of  $-1$  and three fatigue strain amplitudes (3%, 4%, and 5%). Fire effects were simulated using an electric furnace with a heating rate of 15 °C/min in the temperature range of (600 °C– 900 °C). A 20–minute constant temperature stage post–heating ensured uniform specimen temperature distribution, followed by room temperature cooling. Metallographic analysis revealed structural changes, such as the transition from flake to granular pearlite at temperatures above 600 °C. The fatigue test recorded load and deformation, enabling the calculation of stress and strain. Hysteresis curves at various temperatures and  $\varepsilon_a$  exhibited a shuttle shape, indicating good energy dissipation. Stable hysteresis curves, representing 50% fatigue life, showed minor shape changes with exposure temperature. Structural changes after cooling from 600 °C increased dislocation resistance, extending fatigue life. Total energy dissipation density ( $\bar{W}_T$ ) values mirrored  $N_{fT}$  trends. Prediction formulas expressed by Equations 2.45 and 2.46 effectively quantified the exposure temperature's impact on  $N_{fT}$  and  $\bar{W}_T$ . Coefficients were determined by numerical fitting, demonstrating that  $N_{fT}$  and  $\bar{W}_T$  decrease with rising exposure temperatures. The predicted results aligned well with test data, supporting the formulas' effectiveness in predicting the ULCF performance of Q690 HSS after exposure to elevated temperatures.

$$N_{fT} = (at^2 + bt + c)N_{f25} \quad 600^\circ\text{C} \leq t \leq 900^\circ\text{C} \quad (2.45)$$

$$W_T = (dt^3 + et^2 + ft + g)W_{25} \quad 600^\circ\text{C} \leq t \leq 900^\circ\text{C} \quad (2.46)$$

where  $a, b, c, d, e, f$  and  $g$  are the fitting parameters and is summarized in Table 2.1.

**Table 2.1** Fitting parameters (Hua et al. 2022).

$\varepsilon_a$ (%)	$a$	$b$	$c$	$d$	$e$	$f$	$g$
3	$2.2 \times 10^{-6}$	$-4.3 \times 10^{-3}$	3.04	—	$-3.0 \times 10^{-6}$	$-3.3 \times 10^{-3}$	0.219
4	$-6.7 \times 10^{-6}$	$8.0 \times 10^{-3}$	-1.18	$-8.0 \times 10^{-8}$	$-1.7 \times 10^{-4}$	-0.12	29.58
5	—	$-3 \times 10^{-3}$	2.678	—	—	-0.003	2.54

## 2.9 Surface roughness characteristics

ISO 4287 (1996) defines surface as a partition that separates an entity from the surrounding medium. A surface can be treated as the transformation region from one state of material to another whereas; topography refers to the physical characteristics to describe the surface. The surface topography analysis is concerned primarily with description of surface with respect to its features. The understanding of the surface geometry can be used to establish the performance of the material or components during its service life. The methodology by which surface description can be achieved is the characterization. The surface therefore, refers to the boundary and the topography refers to the surface description. Various techniques of characterization can be used to describe the surface such as geometric, statistical visual (Mainsah et al., 2001).

### 2.9.1. Analysis of surface roughness:

Surface texture is the random or repetitive deviation from the geometrically perfect surface that forms a three-dimensional surface topography. Surface texture comprises of: (i) waviness or (macroroughness); (ii) roughness includes nano-and microroughness; (iii) flaws; and (iv) lay (Bhushan, 2013). The shortest wavelength or the highest frequency component of concern on a surface represents the surface roughness (Mainsah et al., 2001). The formation of nano roughness and microroughness involves the deviation in the surface due to short wavelength and this include the features that are inherent to the production process. The presence of nano roughness and microroughness is characterized by the formation of dale or valleys, which are also the local minima and the hills or asperities which is local maxima. The hills and valleys are of varying spacing and amplitudes. The asperities in the surface profile refer to the peak in two dimensions, whereas summits in three dimensions in surface map (Bhushan, 2013). All surfaces are treated as rough. It is initial-point from where wear, friction, and other surface aspects has been emerged (Whitehouse and Archard, 1970). Waviness is characterized by the surface fluctuations of long wavelength or lower frequency and is referred as macroroughness. Waviness results due to the material deflection, heat treatment or vibration. If the spacing of the irregularities is greater than the sampling length of roughness it is referred to as waviness. Flaws



are the unexpected, unwanted and unintentional interference in the surface texture. Whereas, lay is used to describe the direction of the prevailing surface pattern (Bhushan, 2013).

### **2.9.2 Techniques for Surface profile measurement:**

Measurement of surface profile can be achieved by measuring the line over the surface and defining that line as a function of height mathematically, with  $z(x)$  as the lateral displacement. Cartesian coordinate system is utilized for measurement where,  $x$  axis is the direction of line, and  $z$  axis lies in the direction outward from the material to the surrounding medium. The various techniques for the surface profile measurements have been described below:

**Stylus method:** Contact-type stylus instrument is the most popular and widely used instrument to evaluate two-dimensional surface roughness measurement. The profile measurement from the contact type stylus instrument is achieved by moving the stylus in traverse direction across the surface along the evaluation length. ISO 21920-2:2021 defines the evaluation length as the length along the  $x$  axis used for characterization of geometrical features within the limited-scale profile. The evaluation length should be of sufficient length such that the surface roughness can be well represented statistically also it shouldn't be long enough such that waviness is also included as roughness (Whitehouse, 2002). The movement of the stylus traversing is detected by the instrument detector. The signal is recoded by amplifying and then converting it digitally. In the past, it was assumed that only some significant information can be evaluated such as average roughness or root mean square of the profile (Peklenik, 1967). However, slope distribution, height distribution, power spectral distribution are also possible using contact stylus instrument in more digital and analogue technique as reported by Whitehouse and Archard, (1970). The contact-type method has advantage as: it is easy to operate, in situation where sample is covered with oil and dirt or in case of dark environment such that it is difficult for non-contact profiler to take measurement in such case the contact type stylus instrument is the best choice. However, certain disadvantage can't be neglected as it is difficult for the contact-type stylus to exactly detect the correct shape of the irregularities (peaks or valleys) if the width is less than the tip radius. Other disadvantages are the gradual tear and wear of the stylus after certain usage time and may leave scratches on the sample to be measure.

**Interferometry:** The optical instrument which utilizes the principle of interference of light is referred as interferometer (Steel, 1985). The optical interferometer compares the location of two points in space between the measured and the reference path of light. The optical interferometer consists of a beam splitter, a light source, a detector, a test surface and a reference surface. A sinusoidal phase modulating interferometer has been proposed by Ge and Kobayashi (2006) which is real time measurement of surface profile characterization. The instrument

consists of an electric system and an optical interferometer, first the light rays are collimated by the lens and the light rays are splitted into two interference beams by the beam splitter. One beam serves as the reference beam which is reflected by piezoelectric transducer attached to the modulate phases while, the other beam served as the measurement beam reflected by an object. The interference of the two beams creates an interference signal which is imaged on a high-speed image sensor. After processing the signal and demodulation of phase signal the surface profile as well as the distribution phase of surface measured can be obtained. The advantage of interferometry is the high vertical resolution which can go to 0.1nm. The interferometry covers a larger portion with a high resolution which can go to 0.1nm vertically. The disadvantage is that the material to be measure should be of good reflectivity and the instrument is sensitive to vibration and therefore should be placed on vibration-absorbing table.

### 2.9.3 Surface roughness parameters:

Roughness parameters are widely divided into: amplitude, spacing volume and hybrid related parameters. The height parameter and the spacing parameters are the prevailing parameters since these features are more related to the functional parameters. Most of the surface finish parameters in the 1970, relate only the height parameters and not the spacing information in the profile (Whitehouse, 2002). Surface roughness assessment typically involves measuring profile curves and extracting relevant characteristics and quantities. These extracted features serve as criteria for evaluating the surface's texture. Standards EN ISO 4287 and EN ISO 5436 previously defined parameters and values for quantifying surface roughness. However, these standards have been replaced by the series of newer standards: ISO 21920-1, ISO 21920-2, and ISO 21920-3.

#### 2.9.3.1 Amplitude parameters:

Arithmetic mean height ( $R_a$ ): It is the most extensively used roughness parameter and it is the absolute average deviation of the surface points from the mean line over the evaluation length  $l_e$  (mm). The evaluation length has been explained in the previous section. Consider  $z(x)$  which is measured from the mean line then  $R_a$  is expressed as per Equation 2.47 (ISO 21920-2:2021). From the definition of  $R_a$  it is not possible to describe whether the prevailing deviation are valleys or peaks.

$$R_a = \frac{1}{l_e} \int_0^{l_e} |z(x)| dx \quad (2.47)$$

Root mean square height ( $R_q$ ): It represents the standard deviation of the surface height distribution about the mean line. This parameter is more sensitive than  $R_a$  to large deviation

## Fatigue Behavior of Constructional Steels Subjected to Pitting Corrosion and Elevated Temperature

with respect to the mean line (Gadelmawla et al., 2002).  $R_q$  is expressed using Equation 2.48 as (ISO 21920–2:2021):

$$R_q = \sqrt{\frac{1}{l_e} \int_0^{l_e} z^2(x) dx} \quad (2.48)$$

Maximum peak height ( $R_p$ ) : As per (ISO 21920–2:2021), it is defined as the maximum height of the asperity from the mean line.

Maximum valley depth ( $R_v$ ) : As per (ISO 21920–2:2021), it is defined as the maximum depth of the lowest valley from the mean line.

$R_p$  and  $R_v$  has important application from tribological point of view, as damage of the surface may be done by few height of asperities whereas, the valleys influence the fluid retention and flow (Bhushan, 2013).

Total height ( $R_t$ ) : It is evaluated by summing the deepest valley to the highest peak of the surface topographic profile. It is expressed as (ISO 21920–2:2021):

$$R_t = \max_{x \in X} (z(x)) - \min_{x \in X} (z(x)) \quad (2.49)$$

Ten–point height ( $R_{10z}$ ) : It represents the summation of five–point pit depth and five–point peak height. The five–point pit depth is defined as the arithmetic mean of five highest pit depths whereas; five–point peak height is the arithmetic mean of five largest peak heights. Mathematically it is defined as (ISO 21920–2:2021):

$$R_{10z} = R_{5p} + R_{5v} \quad (2.50)$$

Many other parameters have also been evaluated in the past such as ( $R_{3z}$ ) which is the distance between the third highest peak height and the third lowest pit depth. Mean of the third point height: which is the average of five third point height. This parameter is extensively used in Japan (Gadelmawla et al., 2002; Whitehouse, 2002) expressed as:

$$R_{3z} = \frac{1}{5} \left( \sum_{i=1}^5 R_{3zi} \right) \quad (2.51)$$

Mean of maximum height ( $R_m$ ) : It is the average of all deepest valley to the highest peak heights within the sampling length. It is expressed as:

$$R_{\text{m}} = \frac{1}{n} \left( \sum_{i=1}^n R_{\text{ti}} \right) \quad (2.52)$$

The reason for adopting the average values is to reduce the effect of unwanted or unrepresentative valleys or peaks which occurs occasionally that may give incorrect value when adopted singly.

Skewness and kurtosis: The skewness ( $R_{\text{sk}}$ ) is related to the degree of the symmetry of the waveform, whereas kurtosis is related to the sharpness or bluntness of the surface profile (Whitehouse, 2002). Skewness of the profile refers to the third central moment of amplitude probability density function. (Gadelmawla et al., 2002). The skewness is sensitive to the occurrence of peak heights and deeper pits. The profile has zero skewness if same amount of peaks and valleys are present. A positive skewness represents the profile with high peaks and low valleys with respect to mean line and a negative skewness is represented by the high valleys or deep pit and low peaks above the mean line. The skewness depends whether the bulk of material of the sample is concentrated more i.e. above the mean line or below the mean line (Gadelmawla et al., 2002). Mathematically, skewness is expressed as (ISO 21920–2:2021):

$$R_{\text{sk}} = \frac{1}{R_{\text{q}}^3} \frac{1}{l_{\text{e}}} \int_0^{l_{\text{e}}} z^3(x) dx \quad (2.53)$$

Kurtosis ( $R_{\text{ku}}$ ) is the fourth central moment of amplitude probability density function. A value of kurtosis is  $< 3$  the kurtosis distribution is said to be platykurtic and represent few valleys and few maximum peaks i.e. almost equal distribution of heights. A value of kurtosis is  $> 3$  the kurtosis distribution is said to be leptokurtic if the profile has many high peaks and low valleys. Mathematically, kurtosis is represented as:

$$R_{\text{ku}} = \frac{1}{R_{\text{q}}^4} \frac{1}{l_{\text{e}}} \int_0^{l_{\text{e}}} z^4(x) dx \quad (2.54)$$

Autocorrelation function and power spectral density function: The concept of autocorrelation function (ACF) and power spectral density function (PSD) are based on random process theory (Mainsah et al., 2001). ACF and PSD require implementation of the Fourier transforms. The collection of infinite number of random variables correspond to a random process, for a specific  $x$  and  $y$ , if  $z(x, y)$  is defined as a random variable then the accumulation of all random variable constitutes random process. Surface topography often constitutes the real random process. The auto correlation function treated as a random process can be expressed as (Mainsah et al., 2001):

$$R_t(x, y; \tau_x, \tau_y) = M \left[ \left( z(x, y) - m_z(x, y) \right) \left( z(x + \tau_x, y + \tau_y) - m_z(x, y) \right) \right] \quad (2.55)$$

where  $M [ ]$  represent the ensemble average and  $m_z(x, y)$  is the ensemble mean,  $m_z(x, y)$  is given by the following equation as:

$$m_z(x, y) = M \left[ \left( z(x, y) \right) \right] = \int_{-\infty}^{+\infty} \int_{-\infty}^{+\infty} z(u, v) p_z(u, v; x, y) du dv \quad (2.56)$$

### 2.9.3.2 Spatial parameters:

Spatial parameters describe the texture of a pit surface, such as randomness and homogeneity. The most commonly used spatial parameters are autocorrelation length ( $R_{al}$ ) and dominant wavelength ( $\lambda_{max}$ ). The autocorrelation function ( $f_{ACF}$ ) is used to find the correlation of a profile with a shifted (by  $t_x$ ) version of itself. The autocorrelation function returns a value between  $-1$  and  $+1$ , with a value of  $0$  denoting no correlation and a value of  $+1$  representing perfect correlation. The function  $f_{ACF}$  is given as (ISO 21920–2:2021):

$$f_{ACF}(t_x) = \frac{\frac{1}{l_e - |t_x|} \int_{l_0}^{l_0 + l_e - |t_x|} (z(x) - \bar{z})(z(x + t_x) - \bar{z}) dx}{\frac{1}{l_e} \int_0^{l_e} (z(x) - \bar{z})^2 dx} \quad (2.57)$$

where  $\bar{z}$  is the arithmetic mean of the profile  $z(x)$  over the evaluation length  $l_e$ .

$$l_0 = \{x \in R \mid \max(0, -t_x) \leq x \leq \min(l_e, l_e - t_x)\}.$$

$|t_x| < l_e$  is the spatial shift.

The power spectral density function ( $f_{PSD}$ ) can be used to analyze the random nature of the pit surface topography. A pit surface topography comprises of sequences of sine waves with varying amplitude and frequency and  $f_{PSD}$  represent a measure of amplitude of each of the harmonic component for a given frequency and direction.  $f_{PSD}$  is derived mathematically by squaring the Fourier transform of the pit surface profile  $z(x)$  of evaluation length  $l_e$ . It is given as (ISO 21920–2:2021):

$$f_{\text{PSD}}(p) = \frac{\left| \int_0^{l_c} z(x) e^{-i2\pi px} dx \right|^2}{l_c} \quad (2.58)$$

### 2.9.3.3 Spacing parameters:

The spacing parameters are used to evaluate the horizontal feature of the surface deviation. These parameters are evaluated corresponding to the profile element. A profile element represents the valleys and peaks adjacent to each other in the surface profile. The spacing parameters are evaluated with respect to the profile element. A profile element represents peak and valley adjacent to each other in pit topography. A typical representation of profile elements distribution is shown in Fig. 2.7, where  $X_{s,i}$  and  $Z_{t,i}$  represent spacing and height of the  $i^{\text{th}}$  profile element, respectively. The spacing parameters include: mean profile element spacing ( $R_{\text{sm}}$ ), maximum profile element spacing ( $R_{\text{smx}}$ ), standard deviation of profile element spacings ( $R_{\text{smq}}$ ), mean profile element height ( $R_c$ ), maximum profile element height ( $R_{\text{cx}}$ ), standard deviation of profile element heights ( $R_{\text{cq}}$ ), and peak count parameter ( $R_{\text{pc}}$ ). While  $R_{\text{sm}}$  (mm),  $R_{\text{smx}}$  (mm), and  $R_{\text{smq}}$  (mm) represent the mean, maximum, and standard deviation of profile element spacings,  $X_s$ ,  $R_c$  ( $\mu\text{m}$ ),  $R_{\text{cx}}$  ( $\mu\text{m}$ ), and  $R_{\text{cq}}$  ( $\mu\text{m}$ ) represent the mean, maximum, and standard deviation of profile element heights,  $Z_t$ . Finally,  $R_{\text{pc}}$  ( $\mu\text{m}$ ) is referred to as the peak count parameter, which is the number of mean spacings of profile elements per unit length. The following spacing parameters are expressed as per (ISO 21920–2:2021):

Mean profile element spacing: It is the mean of the profile element spacing  $X_s$  expressed as:

$$R_{\text{sm}} = \frac{1}{n_{\text{pe}}} \sum_{i=1}^{n_{\text{pe}}} X_{s,i} \quad (2.59)$$

Maximum profile element spacing: It is the maximum of the profile element spacing  $X_s$  expressed as:

$$R_{\text{smx}} = \max_{i=1, \dots, n_{\text{pe}}} X_{s,i} \quad (2.60)$$

Standard deviation of profile element spacings: It refers to the standard deviation of the profile element spacing  $X_s$  expressed as:

$$R_{smq} = \sqrt{\frac{1}{n_{pe} - 1} \cdot \sum_{i=1}^{n_{pe}} (X_{s,i} - R_{sm})^2}, n_{pe} > 1 \quad (2.60)$$

Mean profile element height: It is the mean value of profile element height  $Z_t$ , calculated as:

$$R_{cp} = \frac{1}{n_{pe}} \cdot \sum_{i=1}^{n_{pe}} Z_{t,i} \quad (2.62)$$

Maximum profile element height: It refers to the maximum value of the profile element height  $Z_t$ , calculated as:

$$R_{cx} = \max_{i=1, \dots, n_{pe}} Z_{t,i} \quad (2.63)$$

Standard deviation of profile element heights: It refers to the standard deviation of the profile element height  $Z_t$  expressed as:

$$R_{eq} = \sqrt{\frac{1}{n_{pe} - 1} \cdot \sum_{i=1}^{n_{pe}} (Z_{t,i} - R_c)^2}, n_{pe} > 1 \quad (2.64)$$

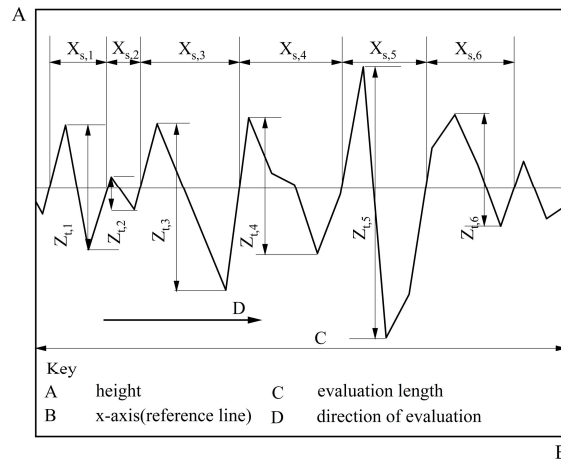


**Fig. 2.7** Representation of profile elements distribution as per (ISO 21920-2:2021).

Peak count parameter: It is the mean spacing of profile element per unit length evaluated as:

$$R_{pc} = \frac{L}{R_{sm}} \quad (2.65)$$

Where  $n_{pe}$  is the total number of profile elements, and  $L$  represents the default evaluation length (taken as 1 mm).

### 2.9.3.4 Volume parameters:

Volume parameters are classified as functional parameters within the discipline of surface tribology. They assist in examining the surface characteristics of mechanical components concerning frictional wear resistance and fluid retention capacity. However, in the present investigation, these parameters are used to describe the volumetric distribution of metal on the pit surface. The volume parameters are assessed using the Abbott–Firestone curve, commonly known as a material ratio curve. It is a plot that depicts metal ratio distribution from the highest hill to the lowest dale on the corrosion pit profile (Whitehouse, 2002). A typical curve is shown in Fig. 2.8. It identifies four different regions, each designating a volume parameter, namely hill material volume ( $R_{vmp}$ ), core material volume ( $R_{vmc}$ ), core void volume ( $R_{vvc}$ ), and dale void volume ( $R_{vvd}$ ). For a particular height range and material ratio  $p$ ,  $R_{vmp}$  measures the metal volume in pit peaks. It is expressed as (ISO 21920–2:2021):

$$R_{vmp}(p) = R_{vm}(p) \quad (2.6)$$

where

$$R_{vm}(p) = K \int_0^p (R_{cm}(r) - R_{cm}(p)) dr \quad (2.67)$$

$R_{vm}(p)$  is the material volume at a given  $p$  and has a unit of  $\text{mm}^3/\text{mm}^2$  and  $K$  ( $\text{ml}/\text{m}^2$ ) is a factor used for unit conversion. The hill material volume is assessed for a value of  $p$  equal to 10% in line with (ISO 21920–2:2021).

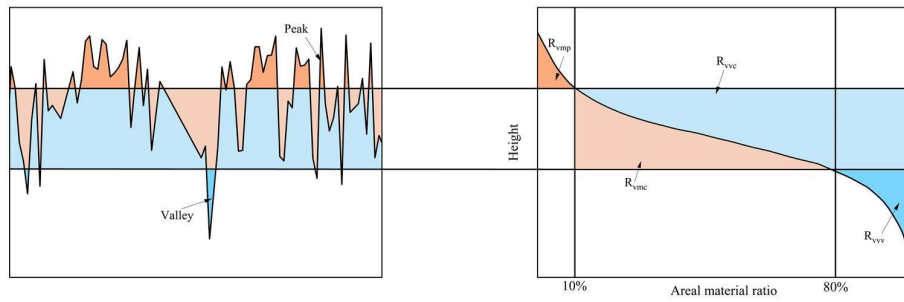


**Fig. 2.8** Illustration of volume parameters.

The volume parameter,  $R_{vmc}$ , calculates the change in volume of the metal in pit between two material ratios,  $p$  and  $r$ . Note that the default value of  $r$  is 80% (ISO 21920–2:2021).

$R_{vmc}$  is given by (ISO 21920–2:2021):

$$R_{vmc}(p, r) = R_{vm}(r) - R_{vm}(p), \quad p \leq r \quad (2.68)$$



## Fatigue Behavior of Constructional Steels Subjected to Pitting Corrosion and Elevated Temperature

The core void volume parameter,  $R_{vvc}$ , represents the change in void volume between the material ratios  $p$  and  $r$ . It is given as (ISO 21920–2:2021):

$$R_{vvc}(p, r) = R_{vv}(r) - R_{vv}(p), p \leq r \quad (2.69)$$

where

$$R_{vv}(p) = K \int_p^1 (R_{cm}(p) - R_{cm}(r)) dr \quad (2.70)$$

$R_{vv}(r)$  ( $\text{mm}^3/\text{mm}^2$ ) is the volume of voids at  $r$ .

Finally,  $R_{vvv}$  refers to the void volume in the pit surface for a given  $r$ . Note that the value of  $r$  is taken as 80%.  $R_{vvv}$  given as (ISO 21920–2:2021):

$$R_{vvv}(r) = R_{vv}(r) \quad (2.71)$$

### 2.9.4 Effect of surface roughness on fatigue strength of steel:

Failure due to fatigue originates at the surface of material. The surface condition thus becomes one of prevailing factor influencing material fatigue strength. It became necessary to relate the total fatigue life of the component under different roughness condition. Generally, an increase in surface roughness leads to increase in coefficient of friction and decrease in the fatigue performance of the material (Taylor, 1988). Bayoumi and Abdellatif (1995) have studied the influence of roughness parameters on the fatigue life of aluminum alloy. The study thoroughly investigated the role of surface finish on fatigue life of the component. The study reveal that amplitude parameters have a very strong influence on the fatigue endurance strength. The fatigue endurance strength reduces as the height parameters of the surface roughness profile are increased. The Percentage increase in the parameters of  $R_a$ ,  $R_p$ ,  $R_v$  and  $R_t$  will lead to an increase in the specimen vulnerability to the initiation of micro cracks and also affect the propagation of crack. The ratio of fatigue crack initiation life  $N_{ci}$  and crack propagation life  $N_{cp}$  is affected severely with increase in  $R_a$  values. The ratios lie between 0.8 to 0.97. The fatigue endurance stresses are related to the roughness parameters given by equation below:

$$\sigma_a = 248.42 - 45.2 \left( \frac{R_a}{2} \right)^2 + 20.3 \left( \frac{R_q}{2} \right)^2 \quad (2.72)$$

$$\sigma_a = 252.30 - 57.7 \left( \frac{R_p}{7} \right)^2 + 29.3 \left( \frac{R_p}{7} \right)^2 \quad (2.73)$$

$$\sigma_a = 252.80 - 63.5 \left( \frac{R_t}{15} \right) + 35.2 \left( \frac{R_z}{15} \right)^2 \quad (2.74)$$

From, Equation 2.72–2.74 it can be seen that the endurance stress is related to the surface roughness parameters. In an experimental investigation conducted on the effect of surface roughness on LCF life of SS 304 heated at 593 °C by Maiya and Busch (1975) the specimens were heated and then soaked prior to LCF test. The LCF test were conducted at strain–controlled loading condition and it has been observed that with increase in surface roughness the number of cycles for crack initiation severely decreases. The effect of surface roughness on number of cycles to crack initiation has been expressed using Equation 2.75. The study reported that the surface roughness might have an effect to crack propagation in the early growth stage, however, the effect is not considered significant. The relation between the crack initiation life and surface roughness is expressed as:

$$N_{ci}(R) = 1012 R^{-0.21} \quad (2.75)$$

Surface roughness serves as small notch, and the increases in the surface roughness causes enhancement of stress concentration which leads to premature initiation of crack and decrease in the fatigue strength of the material. The surface roughness causes the crack initiation at stress level much lower than yield strength of the material. From the SEM examination crack are always initiated at the base of the scratch marks (Itoga et al., 2003). The predicted fatigue limit of the specimen has been related to the equivalent defect size by the following equation proposed by Murakami and Endo (1994) as :

$$\sigma_{p,w} = \frac{1.43(HV + 120) \left[ (1 - R) / 2 \right]^\gamma}{\left( \sqrt{area_R} \right)^{1/6}} \quad (2.76)$$

where  $\sigma_{p,w}$  is the predicted fatigue limit of the specimen in (MPa).  $\sqrt{area_R}$  ( $\mu\text{m}$ ), is the equivalent defect size, projected on the principal area. HV is the Vickers hardness of the specimen ( $\text{kgf/mm}^2$ ) and  $\gamma$  depends on hardness value which is equal to  $\gamma = 0.226 + HV \times 10^{-4}$

However, Murakami (1997) has used the  $\sqrt{area_R}$  parameter to the periodic surface notch for simulating the surface roughness and proposed evaluation method for  $\sqrt{area_R}$  periodic notches. The stress intensity factor (SIF), for periodic surface crack is given as:

$$K_c = Y \sigma \sqrt{\pi a} \quad (2.77)$$

## Fatigue Behavior of Constructional Steels Subjected to Pitting Corrosion and Elevated Temperature

where  $a$  is the depth of the notch ( $\mu\text{m}$ ), the depth and pitch of the notch has a strong influence on the SIF, i.e. SIF decreases due to the interference between the cracks, the maximum value of SIF along the surface of crack as a function of  $\sqrt{area_R}$  parameter is given as (Murakami, 2002)

$$K_c = 0.65\sigma\sqrt{\pi\sqrt{area_R}} \quad (2.78)$$

Using the Equation 2.77 and 2.88,  $\sqrt{area_R}$  which is equivalent defect size can be obtained by equating to the equivalent value of  $\sqrt{area_R}$  for periodic crack expressed as:

$$\sqrt{area_R} = (Y/0.65)^2 \times a \quad (2.79)$$

Murakami (2002) has plotted the variation between the  $\sqrt{area_R}/2b$  and the parameter  $a/2b$  where,  $a$  is the depth of the notch ( $\mu\text{m}$ ),  $2b$  is the pitch of the notch ( $\mu\text{m}$ ) and it has been found that at  $a/2b = 0.195$ ,  $\sqrt{area_R}$  reaches a maximum value and for most of the value of  $a/2b$ ,  $\sqrt{area_R}$  is almost constant. In order to estimate the equivalent defect size  $\sqrt{area_R}$  the following model has been proposed:

$$\frac{\sqrt{area_R}}{2b} = 2.97\left(\frac{a}{2b}\right) - 3.51\left(\frac{a}{2b}\right)^2 - 9.74\left(\frac{a}{2b}\right)^3, \quad \text{for } \frac{a}{2b} \leq 0.195 \quad (2.80)$$

$$\frac{\sqrt{area_R}}{2b} \approx 0.38, \quad \text{for } \frac{a}{2b} > 0.195 \quad (2.81)$$

Since the surface topography, is very irregular and uneven, it can be considered as a series of surface notches, where the depth of notch  $a$  is equivalent to  $R_t$  and  $2b$  equivalent to  $R_{sm}$  in Equation 2.80 and 2.81.

### 2.9.5 Effect of pitting corrosion on surface roughness of steel:

The effect of surface roughness on the artificially corroded structural steel has been investigated by Qin et al.(2016) along with its effect on macro mechanical properties on steel. The surface topographic features have been studied using 3–dimensional surface topography. The surface topographic features were examined using three–dimensional surface topography analysis. Observations from surface topography revealed that during the initial stage of corrosion, only a portion of the test sample exhibited severe corrosion. However, as the exposure time to corrosion increased, larger and deeper pits were formed. In the former stage of corrosion, pits develop further along with secondary pits and corrosion turning into more uniform. The

surface topographic results reveal that with increase in corrosion percentage from 1.5 % to 18 % the arithmetic mean height and root mean square height increase by a factor of 4.5 and 4.0 respectively. The above results shows that the corrosion percentage has strong influence on roughness parameters. Similarly, surface characteristics on the corroded structural steel has been studied by Xia et al. (2021) using salt spray accelerated corrosion technique and the corrosion duration has been takes as 30, 70, 110, 150, 250, 310, 370, and 440 days. Surface topographic parameters have been evaluated using a non-contact type 3-d optical profiler. The study observed that initial stage of corrosion is characterized by the pitting corrosion and with the duration of corrosion, deeper pits along with bulges appeared on the surface of steel which further expands and more corrosion products get layered making the surface rougher. In an investigation carried out by Jia et al. (2021) on the surface topographic feature parameters based on ISO 25178-2:2012 in high strength steel, the steel specimens were artificially corroded. ... 3-dimensional surface roughness parameters have been evaluated. The ratio of mass loss of the specimen has been calculated and linear model has been proposed in order to relate it with the roughness parameters as:

$$S_p = A + B\mu_m \quad (2.82)$$

where  $S_p$  is the roughness parameters.  $A$  and  $B$  are the fitting parameters. The results reveal that the corroded specimens resulted in rougher surface and with increase in mass loss due to corrosion the height parameter has been risen up. As the mass loss ratio increases from 1.89 % to 13 % the total height difference of the corroded surface increase from 117.89  $\mu\text{m}$  to 247.90  $\mu\text{m}$ . The study also evaluates the stress concentration factor using FEM models by evaluating the ratio of maximum von misses stress to the control stress. The SCF has found to be increased with the corrosion duration i.e. at 1.0 from uncorroded state of the specimen to 1.15 at corrosion duration of 160 days.

The effect of atmospheric corrosion on surface roughness of the carbon steel has been experimentally conducted by Surnam and Oleti (2018). It has been observed that the average corrosion loss increases with the exposure time following a bilogarithmic trend. The value of  $R_a$  increases with the corrosion loss due to the effect of the surface degradation of steel specimen. The surface becomes more of an irregular and with bumpy characteristics. At the starting of the corrosion process the corrosion attack is more of a localized form with the formation of some inordinately high valleys and peaks but with the passage of time the surface is covered with rust and becomes more porous. Further corrosion progresses inside theses pores and the surface profile develops more of a Gaussian type. Regarding the spacing parameters, the corrosion loss has less effect on  $R_{sm}$ , but as the pit size increases with the corrosion loss the

## **Fatigue Behavior of Constructional Steels Subjected to Pitting Corrosion and Elevated Temperature**

peak counts reduce due to the formation of new small pits along with the growing pits with exposure time. Increasing in the pit size leads to increase in the roughness volume parameter i.e. core void volume also increases as the exposure to corrosion is increased. Thus, duration of corrosion exposures has a strong influence on the surface characteristics of the material.

### **2.9.6 Effect of temperature exposure on surface characteristics of steel:**

Under the exposure of elevated temperature, i.e., where the steel is subjected to fire the surface characteristics of the steel surface are affected significantly by the oxidation process. As, we have seen in the previous section that at an exposure temperature of 500 °C or more the steel undergoes considerable microstructural changes. Several studies in the past have studied the effect of exposure temperature on the surface roughness of steel. For instance, Jo et al. (2017) have explore the effect of temperature (10–200 hrs.) on surface roughness of steel. The SEM studies reveal the presence of oxide layer on the surface of steel with exposure temperature of 300 °C for 10 h, which is composed mainly of magnetite layer ( $\text{Fe}_3\text{O}_4$ ). However, with increase in exposure temperature of about of 600 °C for 5 h the surface of the steel is covered with thicker oxide layer which is composed of thick inner wustite layer ( $\text{FeO}$ ) and thicker outer magnetite layer. The formation of oxide layer due to thermal exposure results in increase in surface roughness parameter i.e. the value of  $R_a$  increases from 0.011  $\mu\text{m}$  at room temperature to 0.6  $\mu\text{m}$  at 600 °C for 5 h temperature duration. Kumar et al. (2010) has investigated the effect of surface roughness parameters on thermal exposure of Ti6Al4V alloy at temperature greater than 500 °C and compared with the untreated specimen. The study reveals that due to the presence of oxide layer the value of  $R_a$ ,  $R_t$  and  $R_q$  increases from 0.15  $\mu\text{m}$ , 0.80  $\mu\text{m}$  and 0.19  $\mu\text{m}$  for untreated specimen to 0.60  $\mu\text{m}$ , 4.05  $\mu\text{m}$  and 0.750  $\mu\text{m}$  for specimen exposed to 800 °C This increase is attributed to the accelerated outward growth of the oxide layer with rising temperature and exposure duration. The growth mechanism of this oxide layer, characterized by its porous and stratified structure, further contributes to the increase in surface roughness parameters. Omidbakhsh et al.(2013) conducted experimental studies on Ti–4Al–2V alloy. Surface roughness of the heat–treated specimen was measured using a mechanical profiler. It has been observed that at a temperature of (450 °C –600 °C) the value of  $R_a$  don't change considerable, However, at a temperature 700 °C for exposure duration of 1 h,  $R_a$  value increases linearly from 0.02  $\mu\text{m}$  for untreated specimen to 0.13  $\mu\text{m}$  because of the presence of thick oxide scale comprises of considerable amount of cracks along with multilayers covered all over the specimen. The skewness of the specimen changes from positive to negative in temperature range of (450 °C –600 °C) signifying the profile valleys are covered with oxides, However, at exposure temperature of 700 °C for of 1 h duration the condition is reverse skewness changes to negative due to rough morphology with irregular oxide scales. Significant changes in kurtosis from higher

value to about three or lesser have been recorded which signifies that surface morphology changes from spiky to bumpy one. This observation, suggested that the temperature exposure resulted in change in surface morphology and causes increase in average roughness.

## 2.10 Fatigue life models

### 2.10.1 Stress based fatigue life model:

The stress–life ( $S-N_f$ ) method is based on the Wöhler (or  $S-N_f$ ) curve, which plots the alternating stress applied to a material against the number of cycles it can withstand before failure.  $S-N_f$  data is typically presented on a log–log plot, with the mean of the data points represented by the  $S-N_f$  line. Some materials exhibit an endurance limit or fatigue limit ( $S_e$ ), below which the material exhibits infinite life. The fatigue ratio is defined as the ratio of the endurance limit to the ultimate strength of a given material ( $f_u$ ). Most steels have a fatigue ratio of 0.5. The relationship between endurance limit and ultimate strength can be expressed as  $S_e = 0.5f_u$  (Bannantine et al., 1990).

In the absence of specific fatigue data for a particular material, an estimation of the  $S-N_f$  curve can be made. One approach involves assuming the alternating stress level ( $S_{1000}$ ) corresponding to a lifespan of 1000 cycles is 90% of the ultimate tensile strength. Connecting this point with the estimated fatigue limit on a log–log plot defines the estimated  $S-N_f$  design line as illustrated in Fig. 2.9. Alternatively, a power–law relationship can be used to model the  $S-N_f$  curve for steel. This can be expressed as (Bannantine et al., 1990):

$$S = 10^a N_f^b \quad (2.83)$$

Where the exponents,  $a$  and  $b$  of the  $S-N_f$  curve are determined as:

$$b = -\frac{1}{3} \log_{10} \frac{S_{1000}}{S_e} \quad (2.84)$$

$$a = \log_{10} \frac{(S_{1000})^2}{S_e} \quad (2.85)$$

The equation that expresses fatigue life in relation to alternating stress is expressed as follows:

$$N_f = 10^{-a/b} S^{1/b} \quad (\text{for } 10^3 < N_f < 10^6) \quad (2.86)$$

When the estimates for  $S_{1000}$  and  $S_e$  are made

$$S_{1000} \approx 0.9f_u \text{ and } S_e \approx 0.5f_u \quad (2.87)$$

The  $S-N_f$  curve is expressed as (Bannantine et al., 1990):

$$S = 1.62 f_u N_f^{-0.85} \quad (2.88)$$

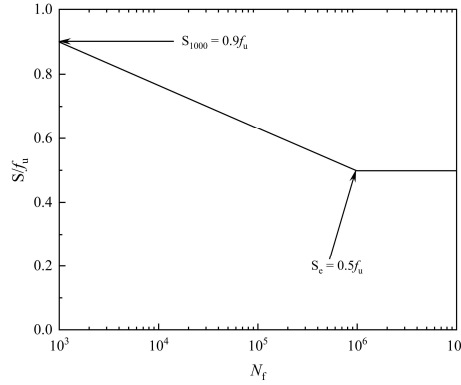


**Fig. 2.9** Log–log plot of the generalized  $S$ – $N_f$  curve for wrought steel (Bannantine et al., 1990).

### 2.10.2 Strain based fatigue life model:

Monotonic stress–strain curves have been conventionally used to determine design parameters for limiting stresses in engineering structures and components under static loading. Similarly, fatigue curves, representing the material's behavior under repeated loading, are crucial for assessing the durability of structures and components under cyclic loading conditions. When a material experiences cyclic inelastic loading, its response takes the form of a hysteresis loop, as illustrated in Fig. 2.10. The total width of the loop represents the total strain range ( $\Delta \varepsilon$ ), while the total height corresponds to the total stress range ( $\Delta \sigma$ ) can be expressed as (Bannantine et al., 1990):

$$\Delta \varepsilon_r = \frac{\Delta \varepsilon}{2} \quad (2.89)$$

where  $\Delta \varepsilon_r$  is the strain amplitude and the stress amplitude can be expressed as:

$$S = \frac{\Delta \sigma}{2} \quad (2.90)$$

The total strain which is the sum of elastic and plastic range can be expressed as:

$$\frac{\Delta \varepsilon}{2} = \frac{\Delta \varepsilon_e}{2} + \frac{\Delta \varepsilon_p}{2} \quad (2.91)$$

Using the Hooke's law Equation 2.91 can be expressed as:

$$\frac{\Delta \varepsilon}{2} = \frac{\Delta \sigma}{2E} + \frac{\Delta \varepsilon_p}{2} \quad (2.92)$$

Basquin, (1910) established a critical observation regarding fatigue behavior as the stress–life data could be represented linearly on a log–log scale. This finding, known as the Basquin

equation, provides a convenient method for engineers to analyse fatigue strength. Specifically, by utilizing the true stress amplitude, which accounts for material hardening during cyclic loading, the relationship between applied stress and fatigue life can be expressed as a linear equation in the log–log domain (Bannantine et al., 1990):

$$\frac{\Delta\sigma_a}{2} = \sigma_f (2N_f)^\gamma \quad (2.93)$$

where  $\left(\frac{\Delta\sigma_a}{2}\right)$  is the true stress amplitude,  $\sigma_f$  is the fatigue strength coefficient and  $\gamma$  is the fatigue strength coefficient.

However, (Coffin Jr, 1954) and (Manson, 1953) observed that the plastic strain life data could be linearized on log–log coordinates, and the relationship between plastic strain and fatigue life can be expressed by a power law function as follows:

$$\frac{\Delta\varepsilon_p}{2} = \beta (2N_f)^\alpha \quad (2.94)$$

Using the Equation 2.92 and 2.94 the total strain can be expressed as:

$$\frac{\Delta\varepsilon}{2} = \frac{\Delta\sigma}{2E} + \beta (2N_f)^\alpha \quad (2.95)$$

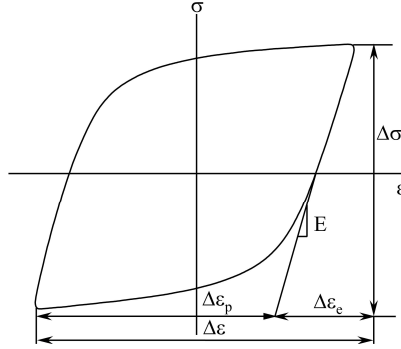


**Fig. 2.10** A typical hysteresis loop (Bannantine et al., 1990).

Using the Equation 2.93 the total strain can also be expressed as (Bannantine et al., 1990):

$$\frac{\Delta\varepsilon}{2} = \frac{\sigma_f (2N_f)^\gamma}{2E} + \beta (2N_f)^\alpha \quad (2.96)$$

Equation 2.96 is the basis of strain life method and is term as the Strain–life relation.

### 2.10.3 Energy based fatigue life model:

Energy based fatigue life model: The energy–based approach proposes that component failure occurs when the energy generated per cycle reaches a critical threshold. This approach



## Fatigue Behavior of Constructional Steels Subjected to Pitting Corrosion and Elevated Temperature

can be divided into two components: elastic strain energy density ( $\Delta W_e$ ) and plastic strain energy density ( $\Delta W_p$ ). While  $\Delta W_e$  is a valuable indicator for HCF damage, for the LCF loading scenario considered here,  $\Delta W_p$  is widely accepted as the primary representation of the component's damage behavior (Lee et al., 2008). Generally, the Ramberg–Osgood equation (Ramberg and Osgood, 1943) is used to model the material's stress–strain curve given by the expression as:

$$\bar{W}_p = \Delta \varepsilon_e + \Delta \varepsilon_p = \frac{\Delta \sigma}{2} + 2 \left( \frac{\Delta \sigma}{2\bar{K}} \right)^{1/\bar{n}} \quad (2.97)$$

where,  $\bar{K}$  is the cyclic strength coefficient and  $\bar{n}$  is the cyclic strain hardening exponent. The plastic strain energy density can be calculated by integrating the stress–strain curve over the plastic strain range. This is mathematically represented by Equation 2.98 as (Morrow, 1965):

$$\bar{W}_p = \int \Delta \sigma d\Delta \varepsilon = 2 \int_0^{\Delta \varepsilon_p} \Delta \sigma d\Delta \varepsilon - \Delta \sigma \Delta \varepsilon \quad (2.98)$$

Using the Equation 2.97 and 2.98 can be expressed as (Morrow, 1965):

$$\bar{W}_p = \frac{1-\bar{n}}{1+\bar{n}} \Delta \sigma \Delta \varepsilon_p = 2 \frac{1-\bar{n}}{1+\bar{n}} \Delta \sigma \left( \frac{\Delta \sigma}{2\bar{K}} \right)^{1/\bar{n}} \quad (2.99)$$

The elastic strain energy density ( $\bar{W}_e$ ) can be expressed as:

$$\bar{W}_e = \frac{1}{2} \left( \Delta \sigma \Delta \varepsilon - 2 \frac{1-\bar{n}}{1+\bar{n}} \Delta \sigma \left( \frac{\Delta \sigma}{2\bar{K}} \right)^{1/\bar{n}} \right) \quad (2.100)$$

The total strain energy density ( $\bar{W}_t$ ) can be expressed as:

$$\bar{W}_t = \bar{W}_e + \bar{W}_p = \frac{\Delta \sigma \Delta \varepsilon_p}{1+\bar{n}} + \frac{\Delta \sigma \Delta \varepsilon_e}{2} \quad (2.101)$$

$\bar{W}_t$  exhibits a power–law relationship with the number of cycles to failure. This relationship is similar to the Coffin–Manson equation commonly used in LCF analysis and can be expressed as (Halford, 1966):

$$\bar{W}_t = C' (N_f)^{m'} \quad (2.102)$$

where the total strain energy density ( $\bar{W}_t$ ) is referred as the fatigue toughness.  $C'$  is the fatigue toughness coefficient and  $m'$  is the fatigue toughness exponent. The value of  $C'$  and  $m'$  can be estimated by fitting the model to the experimental data using a least–squares method.

There is a positive correlation between total strain energy density and number of cycles to failure. This behavior can be attributed to the increased total energy required to initiate and propagate cracks at lower total strain amplitude. This, in turn, leads to lower plastic strain amplitude (Callaghan et al., 2010). Notably, lower  $\bar{W}_p$  implies less energy being absorbed by microstructural defects like dislocations, slip bands, and inclusions, which typically facilitate crack initiation and growth.

## 2.11 Major conclusions from existing research

- i. Numerous studies in the past have predominantly focused on the assessment of fatigue performance in steel bars subjected to uniform corrosion. Uniform corrosion uniformly affects the entire surface area of the bar, leading to a gradual reduction in cross-sectional area. In contrast, pitting corrosion induces localized attack, resulting in the formation of deeper and narrower cavities, which can significantly affect the structural integrity of the material.
- ii. The fatigue performance of corroded steel bars exhibits a notable decrease in fatigue life with increasing levels of corrosion. This decline can be attributed to the formation of pits and cracks caused by corrosion, which act as stress concentrators. These localized areas of high stress promote crack initiation and propagation under cyclic loading conditions, ultimately reducing the fatigue life of the material.
- iii. While microstructural investigations of fatigue crack initiation and propagation in steel bars have been extensively studied for non-corroded specimens, limited attention has been given to for corroded steel bars. This gap in research hinders a comprehensive understanding of the mechanisms underlying fatigue failure in corroded steel.
- iv. The combined impact of pitting corrosion and temperature exposure may substantially affect the surface topographical characteristics of steel. Consequently, these features can have a substantial impact on the fatigue performance of the steel. However, there is a scarcity of studies examining the combined effects of pitting corrosion and temperature on surface topography. Notably, parameters such as arithmetic mean height, total height, and ten-point height of surface topographic features exhibit strong correlations with fatigue stress concentration factors.
- v. Elevated temperatures influence the mechanical properties of steel bars. Experimental studies show significant reductions in yield and ultimate strength beyond critical thresholds. Microstructural changes like tempered martensite and cementite spheroidization contribute to this degradation. After exposure to fire conditions, constructional steel experiences changes in stress and strain properties under cyclic loading. Studies, shows reduced fatigue life under cyclic loading at elevated

## **Fatigue Behavior of Constructional Steels Subjected to Pitting Corrosion and Elevated Temperature**

- temperatures. Predictive formulas have been developed to quantify the impact of exposure temperature on fatigue life accurately.
- vi. Limited studies have explored the behavior of reinforcing steel bars and structural steel under LCF loading conditions in the presence of pitting corrosion and elevated temperatures. Understanding the interaction between these factors is crucial for developing the fatigue life prediction model for the constructional steel.
  - vii. The stress-based model offers a basic fatigue life estimation based on stress levels but lacks accuracy for materials without an endurance limit or under complex loading. In contrast, the strain-based model provides more precise predictions, especially for low-cycle fatigue, but requires material-specific constants. Meanwhile, the energy-based model assesses cumulative energy absorption per cycle, offering valuable insights into crack behavior, particularly useful for low-cycle fatigue and complex loading scenarios.

### **2.12 Need for further research**

Based on the literature review conducted many scopes of addressing several research gaps present in the existing literature have been recognized.

- i. The impact of elevated temperatures on the fatigue performance of pitting-corroded constructional steel is substantial; however, there exists a notable research gap regarding the fatigue behavior of constructional steels under the combined influence of pitting corrosion and elevated temperatures. This lack of understanding poses a significant challenge for ensuring the long-term safety and serviceability of large-scale infrastructure exposed to harsh environments.
- ii. The literature review reveals the substantial influence of both pitting corrosion and temperature on the surface topology of the steel, potentially affecting its fatigue performance. Consequently, it is necessary to investigate the combined impacts of pitting corrosion and temperature exposure on steel bar surface topography and fatigue performance. Experimental investigation to quantify changes in surface roughness parameters and their correlation with fatigue stress concentration factors.
- iii. Current research on fatigue life estimation of steel bars often neglects the combined influence of pitting corrosion severity and elevated temperature. This omission limits the accuracy and applicability of existing models. To address this gap, a comprehensive framework is needed that incorporates the synergistic effects of both corrosion and temperature on fatigue behavior. This framework should explicitly consider the impact of surface topographic features parameters.

- iv. The fatigue damage growth of structural steel is significantly affected by the elevated temperatures. Predictive equations have been developed for evaluating the fatigue performance of constructional steel subjected to fire. Limited studies in the past have made attempts to understand the LCF behavior of constructional exposed to elevated temperature and pitting corrosion under stress and strain-controlled loading conditions.
- v. Studies have extensively examined the microstructural aspects of fatigue crack initiation and propagation in non-corroded steel bars. However, there remains a significant gap in systematic and dedicated investigations addressing these phenomena in corroded steel bars exposed to high temperatures.
- vi. To accurately predict fatigue life in corroded steel at elevated temperatures, refinement of existing models is essential. For the strain-based approach, it is imperative to quantify the effects of corrosion and temperature-dependent material properties. Additionally, employing the energy-based approach provides valuable insights into fatigue damage accumulation by considering both elastic and plastic strain energy densities. This approach offers a comprehensive understanding of fatigue damage accumulation in corroded steel bars subjected to elevated temperatures.
- vii. The fatigue behavior of construction steels with multiple pit sites remains largely unexplored. Investigating how the presence of multiple pits influences fatigue performance is essential for assessing the structural integrity and durability of steel components in corrosive environments.

These research gaps motivated for comprehensive experimental investigation on the fatigue behavior of constructional steel and on the basis of test results predictive equations are proposed to consider the effect of pitting corrosion and elevated temperature exposure.



## Chapter 3

# Surface topography of high-ductile TMT steel bar subjected to pitting corrosion and high temperature

---

### 3.1 Introduction

Concrete reinforcement using hot-rolled deformed high-strength bars is becoming more common due to its economic advantage over conventional mild steel reinforcing bars. Their increased usage has prompted many researchers to investigate their behavior in concrete members. Accordingly, since poor fatigue properties have been a significant disadvantage of high-strength steels, the research on the fatigue performance of high-strength reinforcing bars has garnered much attention. Fatigue starts when the applied load is high enough to cause plastic deformation at the highest stress location in the bar and damage accumulates on repeated cyclic application of the load eventually leading to the formation of a crack. The crack lengthens on continuation of cyclic loads until the stress on the bar is high enough to cause its sudden fracture.

Corrosion of steel rebars is a serious problem that affects the structural performance of RCC structures. Pitting corrosion, a form of highly localized loss of cross-sectional area, is of particular concern as this provides sites for fatigue crack initiation and has been observed to be responsible for the nucleation of fatigue-induced cracks in various steels. Numerous structures such as offshore platforms, bridges, chimneys, bunkers, silos, and towers constructed close to the marine environment or exposed to de-icing salts experience corrosion and cyclic stress and are therefore highly susceptible to fatigue damage accumulation. Consequently, their failure is governed by the fatigue failure of the reinforcing bars in the majority of cases. During cyclic loading, corroded pits act as stress raisers, increasing the surface stress level, similar to notches on the metal surface. From this perspective, fatigue is a surface-sensitive process, and the metal's ability to withstand cyclic loading depends on its surface roughness.

The corroded surface morphology and microstructure of steel could be critically impacted in the situations of elevated temperature or direct fire exposure. Considerable changes in the microstructure such as appearance of carbide particles are seen in specimens heated to 500 °C or higher. At temperatures between 600 °C and 700 °C, hematite-dominated oxide scales form in various locations on steel surface and are noticeably thinner. Moreover, at 600 °C, the scale is rather thick where it is still in touch with the iron, but it is very thin where that contact has been lost. The formation of cracks and localized stress concentrations can also be attributed to the volume increase caused by the magnetite to hematite transition. The impacted surface topography could drastically reduce the structural performance of the steel bars, specifically concerning its fatigue behaviour. This study undertakes experimental investigations, including microstructural examinations, to explore the surface roughness characteristics of TMT

## Fatigue Behavior of Constructional Steels Subjected to Pitting Corrosion and Elevated Temperature

reinforcing bars subjected to pitting corrosion and elevated temperature. Based on the analysis of results, this study discusses potential strategies for mitigating the adverse effects of pitting corrosion and elevated temperature on surface roughness. Further, the practical implications of the study are also presented.

### 3.2 Experimental procedure

#### 3.2.1 Material selection and specimen design:

The steel specimens used in this study are prepared from the hot-rolled high-strength, deformed TMT ductile reinforcing bar of grade Fe 500D commercially available, confirming to IS 1786:2008. The chemical composition of steel and its mechanical properties as such received from the manufacturer are given in Tables 3.1 and 3.2, respectively. As in the Table 3.1, CEQ refers to Carbon Equivalent, which is used to assess the weldability of the steel. IS 1786:2008 recommends a CEQ value below 0.53% and 0.42% for steel with and without micro-alloy/low alloys for improved weldability. The outer ribbed layer of steel is removed by lathe processing and is polished to achieve a bright mirror-finish surface.

**Table 3.1** Material chemical composition.

Chemical composition	C	S	P	Mn	Fe	CEQ
Specimen	0.2%	0.020%	0.033%	0.88%	98.86%	0.34%

**Table 3.2** Mechanical properties of Fe 500D steel rebar.

Yield strength (MPa)	Tensile strength (MPa)	Tensile strength/Yield strength	Elongation (%)	Youngs modulus (MPa)
560	645	1.15	22	$2.1 \times 10^5$

Note that the outer ribbed layer of steel, which is composed of longitudinal and transverse ribs, exhibits non-uniform surface roughness. In the current study, the outer ribbed layer of the steel has been removed to achieve a uniform surface roughness. Final specimens are 10 mm diameter and 100 mm long. A total of 15 such specimens are prepared and subjected to pitting corrosion.

#### 3.2.2 Corrosion protocol:

The surface roughness parameters are determined on 30 accelerated corrosion pits. The impressed current technique is used for inducing pitting corrosion in the specimen. There are a total of 15 specimens, each measuring 100 mm in length, 10 mm in diameter, and featuring two

pit sites spaced 50 mm apart. The following steps are adopted for conducting the test as shown in Fig. 3.1 (a) and (b): (i) two polyethylene-insulated electrical wires are connected to each end of the specimen; (ii) with the exception of two marked pit locations, each having a diameter of 5 mm, the entire sample surface is wrapped with insulating tape; (iii) a hot melt glue is used to seal the wire's ends firmly; (iv) in a tray filled with 5% NaCl solution, the specimen (functioning as an anode) and stainless steel (working as a cathode) are fully immersed; and (v) each specimen is subjected to electrochemical accelerated corrosion using an external DC power source with a constant impressed current of 0.5 A for three different time intervals –10, 20, and 30 min. After corrosion is complete, the sample is removed from the pan and thoroughly cleaned with deionized water.

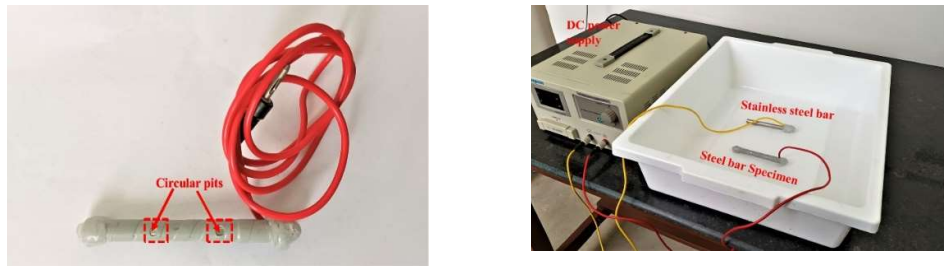


**Fig. 3.1** Experimental setup: (a) preparation of specimen; and (b) accelerated corrosion.

In accordance with ISO 8407:2021, the sample is placed for 10 min in a chemical solution containing 500 ml of hydrochloric acid, 500 ml of water, and 3.5 g of hexamethylenetetramine to remove the corrosion products formed at the pit sites during the corrosion process. Following a washing with water and ethanol (99% pure alcohol by weight), the specimen is dried fully before being stored in a desiccator. Note that, the accuracy of the corrosion protocol to replicate real-world conditions was ensured through rigorous methods. This includes using corrosive agents that closely match the chemical composition and aggressiveness of real-world environments, precise control over environmental variables such as temperature, humidity, and oxygen concentration to emulate actual conditions, and conducting extensive exposure tests to assess corrosion kinetics.

### 3.2.3 Temperature exposure:

In order to examine the effect of temperature on surface roughness parameters, the corroded specimens are exposed to high temperatures as shown in Fig. 3.2. Twenty-four of the thirty corroded pits are heated in a muffle furnace at a rate of 10 °C/min to various target temperatures (i.e., 400 °C, 500 °C, 600 °C, and 700 °C). In order to achieve uniform heating, the specimens with pits were soaked for 20 min inside the furnace after reaching target temperatures.



## Fatigue Behavior of Constructional Steels Subjected to Pitting Corrosion and Elevated Temperature

Note that, numerous studies have used similar target temperatures on steel in order to simulate fire exposure scenarios (Ren et al., 2020; Sk et al., 2017; Tariq & Bhargava, 2021). Specimens are then allowed to cool down to room temperature inside the furnace. The samples are then removed from the furnace and mechanically cleaned with an ultrasonic cleaner having a 2-liter tank capacity, operating at 70 W and operating at a frequency of 40 kHz. The samples are placed individually in the ultrasonic basket and then agitated ultrasonically in the ethanol for 10 min at room temperature. Finally, all the samples are thoroughly dried and kept in a desiccator for further analysis.



**Fig. 3.2** Elevated temperature exposure.

### 3.2.4 3D corrosion surface morphology:

The corrosion pit depth, length and width of specimens are measured at room temperature using a high-resolution three-dimensional (3D) laser scanner. The specimen's entire surface geometry is captured throughout the scanning process with a scan density of 5 million points per scan at an accuracy of 10  $\mu\text{m}$  and with the field of view fixed at 100 mm. The 3D light scanner collects and processes millions of data points in the x, y, and z dimensions to produce a point cloud – a precise virtual representation of the whole specimen geometry. The point clouds are then further processed, allowing the creation of the side view by aligning each point with the central axis of the rebar specimen. To generate cross-sectional images, planes transverse to the longitudinal axis are inserted. By following this process, specimens' geometry including pits are recreated. Fig. 3.3 (a)–(d) shows a specimen and its 3D image reconstructed from a 3D laser scan.

The dimensions of the corrosion pits, exposure temperatures and corrosion time measured for all specimens (i.e. SP1–SP15) are summarized in Table 3.3. As observed, for a given temperature, the pit depth increases with corrosion time by four-fold for 20 min; but only by five-fold for 30 min. This indicates that corrosion intensity decreases with time. Such behaviour results from the development of corrosion products, which reduce the diffusion of iron ions away from the surface of steel rebar. Additionally, the anode to cathode area ratio is reduced (Vu & Stewart, 2000). This observation is consistent with Galvele's hypothesis, which asserts that the product of corrosion intensity and pit depth is constant. Thus, as pit depth increases, corrosion intensity decreases (Galvele, 1981). As shown in Table 3.3, the pit depths do not show appreciable changes with rising temperatures for a given corrosion time. Further, the length and width of pits show marginal deviation from their original intended dimension of 5 mm.

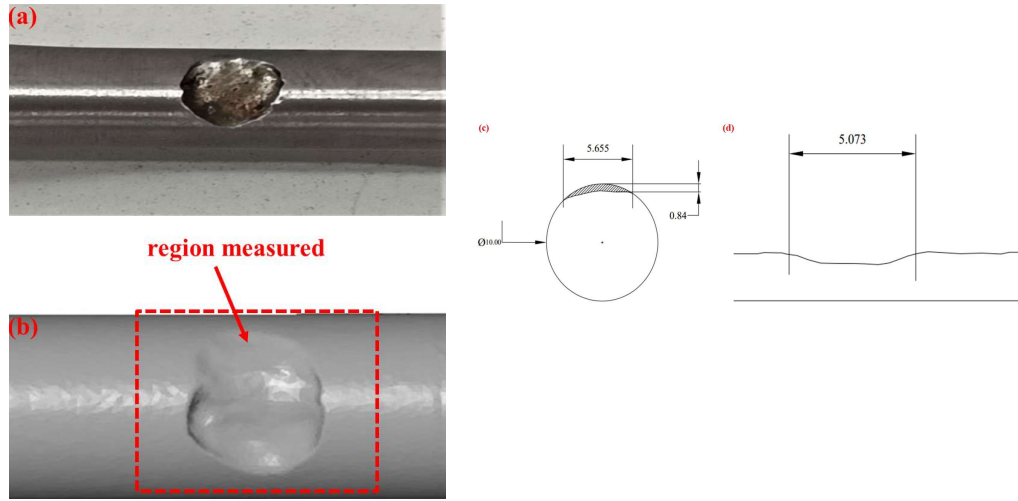


**Fig. 3.3** Typical corroded pit: a) original cleaned specimen; (b) 3D laser scan image; (c) corroded pit geometry (unit: mm); and (d) corroded pit length. (unit: mm).

The critical cross-sectional area loss ( $\eta_{\text{cri}}$ ), particularly for examining corrosion fatigue behavior, is one of the most frequently used parameters to quantify the severity of pitting corrosion. It is expressed as:

$$\eta_{\text{cri}} = (1 - A_{\text{m}} / A_{\text{n}}) \times 100\% \quad (3.1)$$

where  $A_{\text{m}}$  and  $A_{\text{n}}$  represent the specimen's minimum and nominal cross-sectional areas ( $\text{mm}^2$ ), respectively. The values of  $\eta_{\text{cri}}$  for various combinations of corrosion time and temperature are also provided in Table 3.3. As it can be observed,  $\eta_{\text{cri}}$  values fall within 5% for 10 min of exposure, are higher than 5% but less than 10% for 20 min of corrosion, and exceed 10% for 30 min of corrosion time.

**Table 3.3** Result summary of corrosion pit geometry.

Specimen	Temperature (°C)	Corrosion time (min)	Pit geometry from 3d laser scanning			
			Depth (mm)	Width (mm)	Length (mm)	$\eta_{cri}$ (%)
SP1_PIT1	25	10	0.193	5.105	5.183	2.609
SP1_PIT2	25	10	0.208	5.340	5.353	2.763
SP2_PIT1	400	10	0.221	5.134	5.571	3.245
SP2_PIT2	400	10	0.265	5.132	5.009	3.112
SP3_PIT1	500	10	0.300	6.444	6.556	3.848
SP3_PIT2	500	10	0.421	5.297	6.409	3.900
SP4_PIT1	600	10	0.619	7.204	5.383	4.237
SP4_PIT2	600	10	0.620	5.334	5.788	4.137
SP5_PIT1	700	10	0.692	5.223	6.918	4.554
SP5_PIT2	700	10	0.692	5.540	5.71	4.494
SP6_PIT1	25	20	0.724	5.195	5.582	6.865
SP6_PIT2	25	20	0.796	5.270	5.796	6.558
SP7_PIT1	400	20	0.812	5.350	5.785	7.181
SP7_PIT2	400	20	0.837	6.649	5.513	7.234
SP8_PIT1	500	20	0.842	6.034	5.073	7.772
SP8_PIT2	500	20	0.844	5.655	5.317	7.603
SP9_PIT1	600	20	0.922	5.181	6.015	8.434
SP9_PIT2	600	20	0.923	5.184	6.33	8.484
SP10_PIT1	700	20	0.939	6.293	5.753	8.876
SP10_PIT2	700	20	0.973	5.721	6.05	8.803
SP11_PIT1	25	30	0.969	5.224	6.509	10.065
SP11_PIT2	25	30	0.987	5.157	5.465	10.669
SP12_PIT1	400	30	1.043	8.062	5.714	10.865
SP12_PIT2	400	30	1.131	6.229	5.298	11.641
SP13_PIT1	500	30	1.141	6.253	5.162	11.234
SP13_PIT2	500	30	1.258	6.947	5.394	11.857
SP14_PIT1	600	30	1.263	5.246	5.968	11.995
SP14_PIT2	600	30	1.348	6.707	5.803	12.547
SP15_PIT1	700	30	1.459	6.709	5.135	13.184
SP15_PIT2	700	30	1.581	6.579	5.590	13.609

Accordingly, these ranges can be categorized into the three pitting corrosion levels: mild, moderate, and severe. It is emphasized here that the three corrosion durations used in the experiment are not random but preferentially selected to achieve the desired three corrosion levels.

### 3.3 Surface roughness parameters

The 3D surface analyses of all specimens were performed using a non-contact 3D optical profiler (Model: BRUKER Contour GT-K) as shown in Fig. 3.4. The profiler utilizes white light interferometry to evaluate surface geometry. Employing a laser beam of 1  $\mu\text{m}$  diameter, the specimens are scanned using a lens having 5X magnification and 25 mm back scan length. The specimens are positioned on a moveable platform with corroded pit facing profiler light source. Corrosion pits and normal surfaces are scanned each three times in longitudinal and transverse directions: once along the center and once on each side equidistant from the center. The 2D roughness parameters are independently computed from the obtained data of each scan and then the average value of each parameter is calculated.

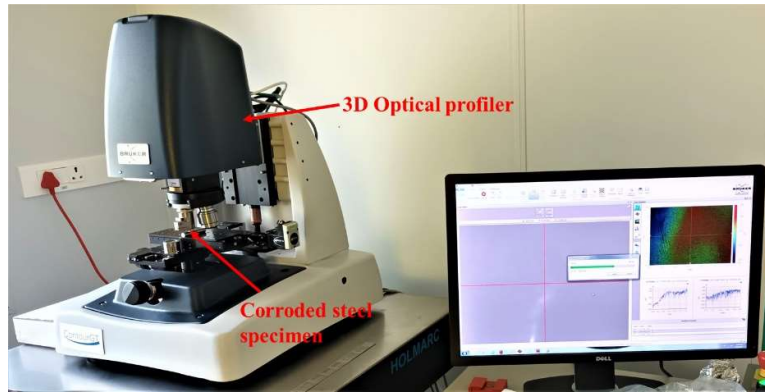


**Fig. 3.4** Non-contact 3D optical profiler.

#### 3.3.1 Amplitude Parameters:

The surface topography is best characterized by the amplitude parameters. They are used to measure the surface deviations' vertical characteristics. Fig. 3.5 (a)–(h) shows the general surface topography of a pit. As can be observed, a typical profile consists of a random distribution of pit/surface peaks and valley points as shown in Fig. 3.6.

##### 3.3.1.1 Arithmetic mean height ( $R_a$ ):

It measures average absolute deviation of the pit/surface points from the mean line over a sampling length.  $R_a$  ( $\mu\text{m}$ ) is expressed using Equation 2.47 given in section (2.9.3.1). Fig. 3.7

## Fatigue Behavior of Constructional Steels Subjected to Pitting Corrosion and Elevated Temperature

shows the variation of  $R_a$  with corrosion time and temperature. At room temperature, a significant difference in  $R_a$  values between corroded and uncorroded samples is seen, increasing upto ten times. When temperature rise is taken into account, this difference grows even more, upto a factor of 12.6. It can also be seen that for a given corrosion time and in reference to room temperature,  $R_a$  increases as the temperature rises. There is a substantial rise in  $R_a$  values by factors of upto 1.3, 1.2, 1.4, and 1.9, respectively, for uncorroded specimens, 10 min–, 20 min–, and 30 min–exposed pits. Additionally, at a given temperature, it is seen that  $R_a$  increases by a factor of upto 1.8 as corrosion time increases in the case of corroded samples. In general, an increase in corrosion duration results in a rise of valleys and peaks. It is important to note here that raising  $R_a$  shortens the metal's fatigue.

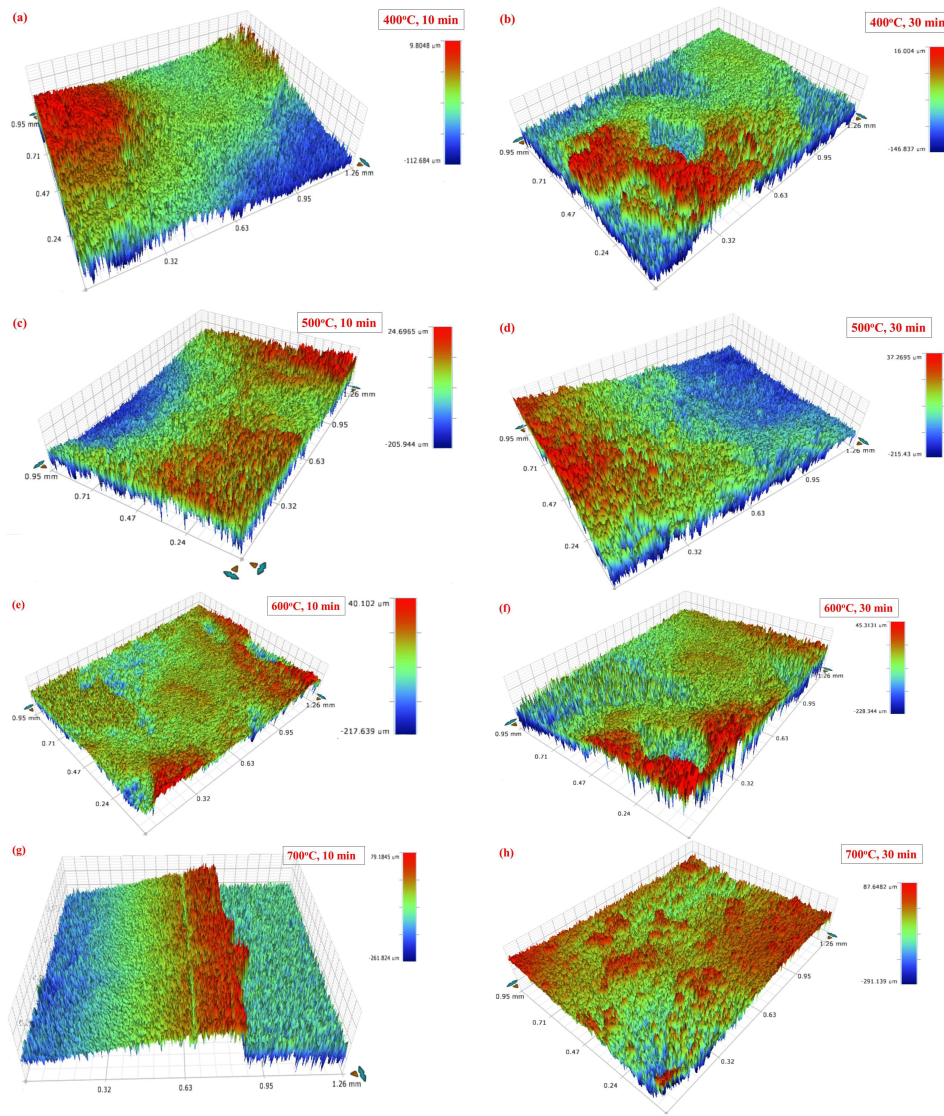


**Fig. 3.5** Surface topography of corroded pits.

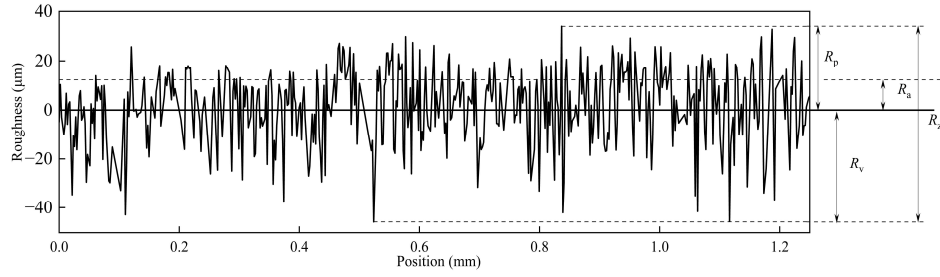


**Fig. 3.6** Surface roughness amplitude parameters.

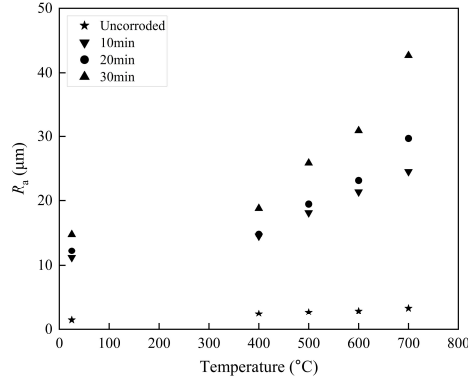


**Fig. 3.7** Variation of  $R_a$  with corrosion time and temperature.

### 3.3.1.2 Root mean square height ( $R_q$ ):

This variable represents root mean square deviation of a pit/surface points about a mean line. Since the random profiles have both positive and negative values, this parameter has more relevance. It is a dispersion parameter for characterizing  $R_a$  and comparable to standard deviation of heights. It is expressed by Equation 2.48 given in section (2.9.3.1). The variation in  $R_q$  ( $\mu\text{m}$ ) with temperature and corrosion time is shown in Fig. 3.8. With corrosion time,  $R_q$  values at a given temperature rise by a minimum of 11% to a maximum of upto 58%. While the values of  $R_q$  likewise rise with temperature at a given corrosion time, but by a minimum and maximum factor of 2.4 and 16.2, respectively. These drastic changes in  $R_q$  indicate an increase in surface topology unevenness brought about first by the corrosion process itself and followed by the heat treatment. During the process of pitting corrosion, after pit nucleation, pit growth occurs due to considerable differences in constantly changing surface areas between the two differently reacting surface regions. Whereas, due to the linear kinetics of oxidation, surface roughness significantly increases on increasing temperature.

## Fatigue Behavior of Constructional Steels Subjected to Pitting Corrosion and Elevated Temperature

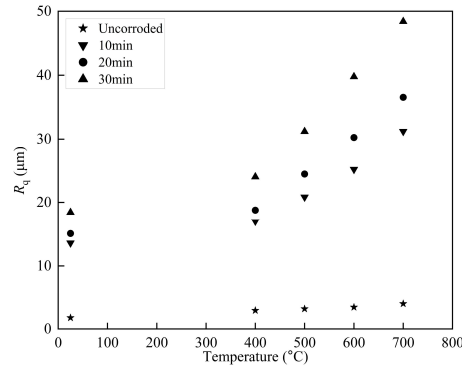


**Fig. 3.8** Variation of  $R_q$  with corrosion time and temperature.

### 3.3.1.3 Total height ( $R_t$ ):

The total height parameter is calculated by adding the highest peak value to the deepest valley value of a pit/surface topographic profile. It is expressed by Equation 2.49 given in section (2.9.3.1). Fig. 3.9 shows the distributions of  $R_t$  ( $\mu\text{m}$ ) with corrosion duration and temperature. For uncorroded samples, an increase in temperature from 25 °C to 700 °C causes an increase in  $R_t$  value by 57%, from 6.29  $\mu\text{m}$  to 9.87  $\mu\text{m}$ . However, for a given corrosion time,  $R_t$  increases nearly double from 25 °C to 700 °C for corroded samples. In contrast, continuous corrosion exposures at a given temperature cause increase in  $R_t$  by at least 8% and as much as 49%. While at a constant temperature, prolonged corrosion exposures cause increase in  $R_t$  of at least 8% and as much as 49%. These trends indicate a significant surface topography change due to corrosion and oxidation during pitting and heat treatment.

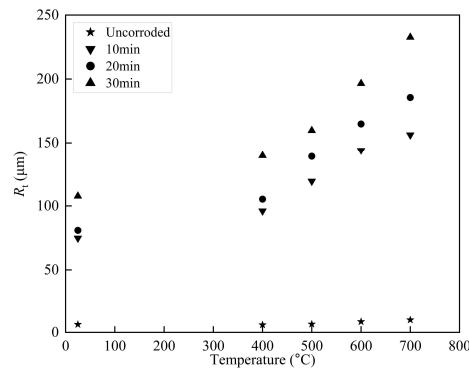


**Fig. 3.9** Distribution of  $R_t$  with corrosion time and temperature.

### 3.3.1.5 Maximum peak height ( $R_p$ ) and maximum valley depth ( $R_v$ ):

The maximum peak height and maximum valley depth has been explained in section (2.9.3.1). Fig. 3.10 (a) illustrates the variations in  $R_p$  ( $\mu\text{m}$ ) with corrosion duration and



temperature. In the case of uncorroded samples, elevating the temperature from 25 °C to 700 °C results in a 56% increase in  $R_p$  value, ranging from 2.97  $\mu\text{m}$  to 4.64  $\mu\text{m}$ . Conversely, for corroded samples, a constant corrosion duration leads to an approximately 2.5-fold increase in  $R_p$  from 25 °C to 700 °C. Moreover, continuous corrosion exposure at a fixed temperature results in increase in  $R_p$  from 12% to 64%. Simultaneously, with the progression of corrosion duration,  $R_v$  values at a constant temperature exhibit a minimum increase of 21% and a maximum increase of up to 58% (Fig. 3.10 (b)). Additionally, for a given temperature,  $R_v$  experiences a rise of at least 10% and up to 58% as corrosion time extends from 10 minutes to 30 minutes. These trends indicate a significant surface topography change due to corrosion and oxidation during pitting and heat treatment.

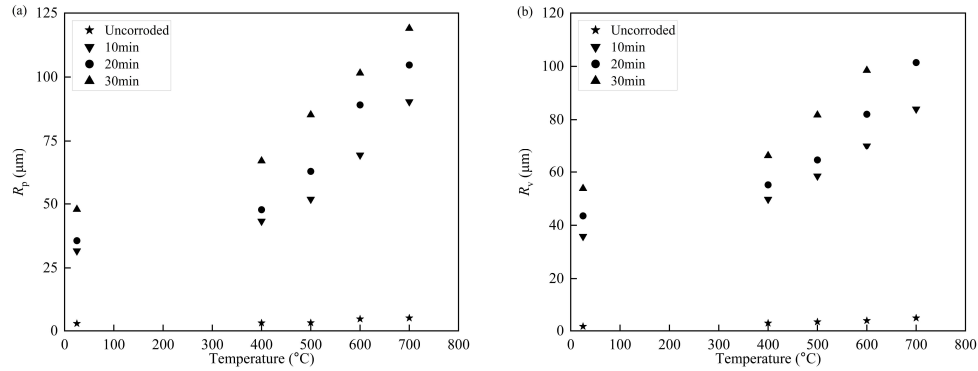


**Fig. 3.10** Variation of maximum peak height and maximum valley depth with corrosion time and temperature: (a)  $R_p$ ; and (b)  $R_v$ .

### 3.3.1.5 Skewness ( $R_{sk}$ ) and Kurtosis ( $R_{ku}$ ):

Skewness is a measure of the (a)symmetry of pit/surface topography relative to the profile's mean line. This metric is sensitive to the sporadic occurrence of high peaks or deep valleys. A profile with equal number of hills and dales have zero skewness (Gadelmawla et al., 2002).  $R_{sk}$  is expressed by Equation 2.53 given in section (2.9.3.1).

The Kurtosis of a pit/surface topography is the fourth central moment of the profile density function, measured within the evaluation length. This parameter provides information about the "spiky" characteristics of a profile. The distribution curve is referred to be platykurtic if  $R_{ku} < 3$  and has a limited number of high hills and low dales. The distribution curve is referred to be leptokurtic and features a significant number of high peaks and low valleys if  $R_{ku} > 3$  (Gadelmawla et al., 2002).  $R_{ku}$  is given by Equation 2.54 in section (2.9.3.1). Fig. 3.11 displays the variation in  $R_{sk}$  as a function of corrosion time and temperature. Not only does the  $R_{sk}$



### Fatigue Behavior of Construction Steels Subjected to Pitting Corrosion and Elevated Temperature

value rises 2.75-fold between 25 °C and 600 °C in the absence of corrosion, but it also becomes negative at 700 °C. With increasing temperatures for a given corrosion period,  $R_{sk}$  exhibits increasingly negative values; eventually, for a 30 min exposure, all values are negative. Similar trends can be seen in longer corrosion duration at a constant temperature. Positive values of  $R_{sk}$  imply bulk metal distribution below the mean line, whereas negative values indicate bulk distribution of metal above it. According to Fig. 3.11, the metal tends to accumulate more above the mean line with either increasing corrosion time at a constant temperature or increasing temperature at a set exposure period.

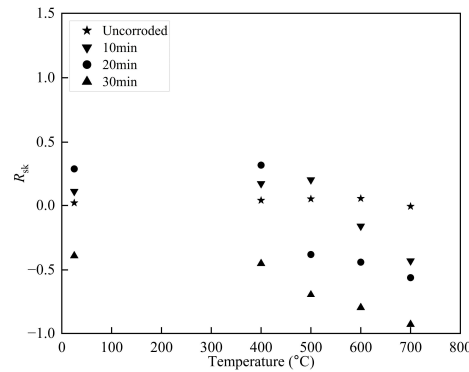


**Fig. 3.11** Variation of  $R_{sk}$  with corrosion time and temperature.

Further, Fig. 3.12 depicts the relation of  $R_{ku}$  with temperature and corrosion period. The values of  $R_{ku}$  for corrosion-free samples increase by 16% as the temperature rises from 25 °C to 700 °C. For corroded samples: (i) for a set temperature,  $R_{ku}$  increases at least 2% and upto 10% with rise in corrosion time from 10 min to 30 min and (ii) for a given corrosion time, trends indicate upto twofold rise in  $R_{ku}$  with increase in temperature from 25 °C to 700 °C. In general, rising  $R_{ku}$  implies that the pit surface will get spikier while falling  $R_{ku}$  indicates that the surface topography will become bumpier. Since all data in Fig. 3.11 show rising trends, pitting corrosion and heat treatment results in pit surface spiking.

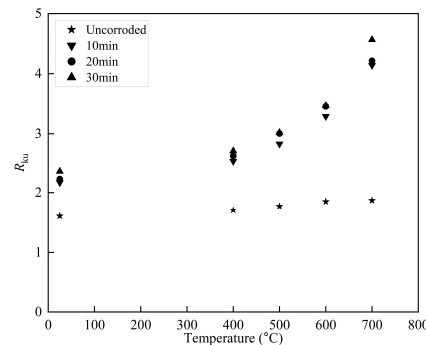


**Fig. 3.12** Relation of  $R_{ku}$  with corrosion time and temperature.

The negative skewness of the measured profile, as shown in Fig. 3.11, indicates a predominance of valleys on the surface. A symmetrical height distribution would result in a skewness value of zero. In this case, the negative skewness signifies a distribution with a greater number of valleys compared to peaks. Additionally, the negative value suggests that most of the sample's material lies above the mean line. This trend of increasing negative skewness further supports the dominance of valleys over peaks. The observed negative skewness can be attributed to the repeated scaling and cracking of oxide layers, a phenomenon typical within the linear kinetics regime. These scaling and cracking processes create surface defects in the material. These defects significantly influence the surface profile, leading to the negative skewness value. In contrast, the rising  $R_{ku}$  value in Fig. 3.12 suggests the surface becoming increasingly spikier. Since all data points in Fig. 3.12 exhibit a rising trend, it can be concluded that both pitting corrosion and heat treatment contribute to the spikier nature of the pit surface. This implies that the thermal oxidation treatments likely modified the surface morphology, resulting in a spikier profile. The results are consistent with the findings reported in the literature (Jia et al., 2021; Omidbakhsh, Ebrahimi, & Sojka, 2013).

### 3.3.2 Spacing parameters:

The spacing parameters are used to access surface deviations in the horizontal characteristics of the pit topography. These parameters give essential information about the surface changes in the pit occurring during corrosion and heat treatment. The spacing parameters are evaluated with respect to the profile element. The spacing parameters include: mean profile element spacing ( $R_{sm}$ ), maximum profile element spacing ( $R_{smx}$ ), standard deviation of profile element spacings ( $R_{smq}$ ), mean profile element height ( $R_{cp}$ ), maximum profile element height ( $R_{cx}$ ), standard deviation of profile element heights ( $R_{cq}$ ), and peak count parameter ( $R_{pc}$ ). While  $R_{sm}$  (mm),  $R_{smx}$  (mm), and  $R_{smq}$  (mm) represent the mean, maximum, and standard deviation of profile element spacings,  $X_s$ ,  $R_{cp}$  ( $\mu\text{m}$ ),  $R_{cx}$  ( $\mu\text{m}$ ), and  $R_{cq}$  ( $\mu\text{m}$ ) represent the mean, maximum, and standard deviation of profile element heights,  $Z_t$ . Finally,  $R_{pc}$  ( $\mu\text{m}$ ) is referred to as the peak count parameter, which is the number of mean spacings of profile elements per unit length. The spacing parameters are expressed using Equations 2.59–2.65 given in section (2.9.3.3). Table 3.4 outline the results of spacing parameters evaluated based on the experiment. In Table 3.4, UC1–UC5 represent uncorroded specimens. For comparison purposes, different specimens serve as controls depending on the control parameter namely, corrosion duration or temperature. Two types of control specimens are used: (i) uncorroded specimens serve as controls for corroded specimens, and (ii) for a given corrosion duration, specimens

## Fatigue Behavior of Constructional Steels Subjected to Pitting Corrosion and Elevated Temperature

corroded at room temperature acts as controls. This study compares uncorroded and corroded specimens, as well as compare corroded specimens within and across multiple sets. It can be observed that the rise in temperature of uncorroded specimens from 25 °C to 700 °C result in: (i) an increase in  $R_{sm}$ ,  $R_{smx}$ , and  $R_{smq}$  by 25%, 48%, and 91%, respectively, (ii) 5–, 10–, and 7–fold rises in  $R_{cp}$ ,  $R_{cx}$ , and  $R_{cq}$ , respectively, and (iii) a decrease of  $R_{pc}$  values by 25%. This indicates that the spacing parameters on the steel surface, except  $R_{pc}$ , increases under heat treatment. In the case of corroded specimens, for a set corrosion time, upto 3.6–, 4.93–, 5.78–, 2.27–, 2.18–, and 2.50–fold increase in  $R_{sm}$ ,  $R_{smx}$ ,  $R_{cp}$ ,  $R_{cx}$ , and  $R_{cq}$ , respectively, are observed for temperature rise from 25 °C to 700 °C. Additionally,  $R_{pc}$  decreases by upto 3.5–fold. Further, for a given temperature,  $R_{sm}$ ,  $R_{smx}$ ,  $R_{cp}$ ,  $R_{cx}$ , and  $R_{cq}$  values are found to rise by upto 1.35–, 1.50–, 2–, 1.4–, 1.45–, and 1.5–fold, respectively, for an increase in corrosion period from 10 min to 30 min. However,  $R_{pc}$  decreases by upto 35%. Thus, with regard to corroded specimens, between the two variables, namely temperature and corrosion duration, the former seems to influence the spacing parameter values more than the latter.

The pitting corrosion—essentially an electrochemical process—progresses by forming electrodes represented by peaks acting as anodes and valleys serving as cathodes (Kandeil & Mourad, 1989). When the electrodes are in close proximity, even a few microns apart, the microcell corrosion process takes precedence (Andrade, 2018). Therefore, microcell corrosion in pits might result in continually changing hills and dales, which would cause  $R_{sm}$  and  $R_{cp}$  values to increase over time as the corrosion progresses. Further, observe that the simultaneous decrease in  $R_{pc}$  indicates a decline in the number of valleys resulting from pit growth. It is important to note that substantial variations in spacing parameters value, such as those found here, might significantly affect the steel's fatigue performance. While corrosion duration may lower fatigue endurance stress, temperature rise makes the material more vulnerable to early micro-crack initiation and propagation, resulting in premature fatigue failure. Amongst various spacing parameters,  $R_{sm}$  has been widely used to assess the influence of surface characteristics on the fatigue strength of metals. By assuming surface roughness as a long crack, a  $\sqrt{area}_R$  parameter model has been proposed to relate surface topographic parameters with fatigue strength. In this study, this model is used to evaluate the equivalent defect size (mm),  $\sqrt{area}_R$ , by considering periodic surface notches on the metal as artificial surface roughness having a depth of  $a$  and a pitch of  $2b$ . Where  $a$  represents the vertical distance between root and peak

while  $2b$  is the horizontal distance of peak–peak. The model is given as by Equation 2.80 and 2.81 in section (2.9.4).

**Table 3.4** Values of profile element based parameters.

Specimen	Temperature (°C)	Corrosion time (min)	Parameters based on profile elements						
			$R_{sm}$ (mm)	$R_{smx}$ (mm)	$R_{smq}$ (mm)	$R_{cp}$ (mm)	$R_{cx}$ (mm)	$R_{cq}$ (mm)	$R_{pc}$ (mm)
UC1	25	–	0.016	0.043	0.011	1.056	1.09	0.51	62.5
UC2	400	–	0.016	0.048	0.015	1.914	2.22	0.85	61.72
UC3	500	–	0.017	0.052	0.017	2.955	3.15	1.42	58.82
UC4	600	–	0.018	0.061	0.019	4.072	7.23	2.72	55.55
UC5	700	–	0.020	0.064	0.021	5.231	10.65	3.59	50.00
SP1	25	10	0.022	0.071	0.0256	28.05	56.04	10.95	45.45
SP2	400	10	0.028	0.095	0.0314	36.34	66.35	14.342	35.71
SP3	500	10	0.037	0.147	0.0574	43.45	85.57	16.84	27.02
SP4	600	10	0.048	0.200	0.0815	51.80	100.86	19.65	20.83
SP5	700	10	0.077	0.328	0.1388	63.95	122.67	25.64	12.98
SP6	25	20	0.025	0.081	0.0258	33.31	64.02	12.39	40.00
SP7	400	20	0.033	0.123	0.0372	40.81	84.40	16.37	30.30
SP8	500	20	0.040	0.169	0.0583	51.67	102.35	20.38	25.0
SP9	600	20	0.053	0.286	0.0839	58.24	123.17	25.25	18.86
SP10	700	20	0.079	0.388	0.0151	69.84	138.68	30.80	12.65
SP11	25	30	0.027	0.087	0.0287	39.03	73.79	15.68	37.03
SP12	400	30	0.034	0.143	0.0416	48.62	96.36	20.43	29.41
SP13	500	30	0.046	0.204	0.0693	58.91	115.10	25.74	21.73
SP14	600	30	0.065	0.301	0.1043	66.86	129.07	29.79	15.38
SP15	700	30	0.099	0.429	0.1659	81.18	144.34	39.27	10.10

The pit surface topography is very uneven; hence, it can be considered as a series of surface notches with an equivalent of  $a$  represented by  $R_t$  and an equivalent of  $2b$  denoted by  $R_{sm}$ . Calculating  $\sqrt{area}_R$  is thus possible by replacing  $R_t$  and  $R_{sm}$  for  $a$  and  $2b$  in Equations 2.80 and 2.81. Fig. 3.13 illustrates the variation of  $\sqrt{area}_R$  with temperature and corrosion time. A 25% increase in the  $\sqrt{area}_R$  is seen when temperature increases from 25 °C to 700 °C for corrosion-free samples. However, in the case of corroded samples: (i) for a given corrosion time, upto a3.6-fold rise in  $\sqrt{area}_R$  is seen for a temperature increase of 25 °C–700 °C, and (ii)

## Fatigue Behavior of Constructional Steels Subjected to Pitting Corrosion and Elevated Temperature

for a given temperature,  $\sqrt{area_R}$  increases by a maximum factor of 1.35 with the corrosion duration. Therefore, it can be concluded that the equivalent defect size of a pit topography increases with the corrosion period and heat treatment.

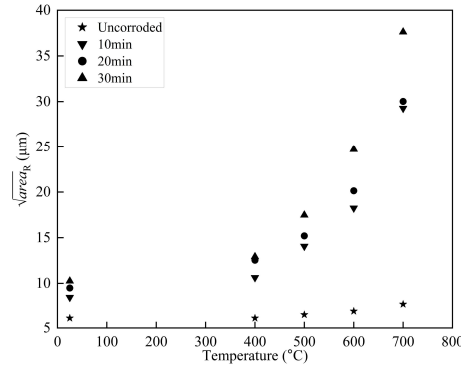


**Fig. 3.13** Variation of  $\sqrt{area_R}$  with corrosion period and temperature.

### 3.3.3 Spatial parameters:

Spatial parameters describe the texture of a pit surface, such as randomness and homogeneity. The most commonly used spatial parameters are autocorrelation length ( $R_{al}$ ) and dominant wavelength ( $\lambda_{max}$ ). The autocorrelation function ( $f_{ACF}$ ) is used to find the correlation of a profile with a shifted (by  $t_x$ ) version of itself. The autocorrelation function returns a value between  $-1$  and  $+1$ , with a value of  $0$  denoting no correlation and a value of  $+1$  representing perfect correlation. The function  $f_{ACF}$  is expressed by Equation 2.57 given in section (2.9.3.2).

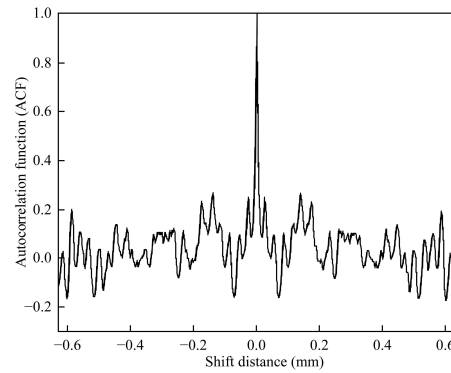


**Fig. 3.14** Illustration of autocorrelation function.

A typical  $f_{ACF}$  is shown in Fig. 3.14. It has been evaluated for a temperature of  $700^\circ\text{C}$  and a corrosion duration of 30 min. As expected, the largest value of  $f_{ACF}$  is observed at the center (for a zero shift). The autocorrelation length (mm),  $R_{al}$  refers to the distance at which  $f_{ACF}$  decays quickly to a specified threshold value  $s$  ( $0 \leq s \leq 1$ ) in any direction. Typical threshold

values are  $1/e$  (natural logarithm), 0.1 or zero (Muralikrishnan & Raja, 2008). For all practical purposes the value of  $s$  can be taken as 0.2 (21920-3:2021, 2021).  $R_{al}$  is explained in section (2.7.3.2).

The relation of  $R_{al}$  with temperature and corrosion duration is illustrated in Fig. 3.15. For uncorroded samples, a 25 °C–700 °C temperature increase results in a 2.5-fold increase in  $R_{al}$ . This indicates that the oxidation reaction during heat treatment, in general, would lead to rise in  $R_{al}$  values. Comparing corroded and uncorroded samples at room temperature shows that  $R_{al}$  rises by 4.5-fold at 10 min exposure but by 9.5-fold at 30 min of corrosion. This implies that the pitting corrosion process would result in a rise of  $R_{al}$  values. Further, for corroded samples, (i)  $R_{al}$  values at a given temperature increase by a factor of upto 2.3 with an increase in corrosion duration of 10 min–30 min, and (ii) at a constant corrosion time,  $R_{al}$  values increase by upto fivefold with a temperature increase of 25 °C–700 °C. In general, a greater value of  $R_{al}$  implies that low spatial frequency dominates the surface, while a lower value of  $R_{al}$  suggests that high spatial frequency dominates the surface (Muralikrishnan & Raja, 2008). In addition,  $R_{al}$  may be used to determine the number of peaks that exceed a specific height in a given profile. A profile with a lower  $R_{al}$  value has a greater likelihood of having a peak than one with a higher  $R_{al}$  value (Zhang & Sundararajan, 2005). Consequently, based on the data shown in Fig. 3.15, it can be inferred that rising values of  $R_{al}$  for various combinations of corrosion time and temperature imply a considerable reduction in number of peaks on the pit surface due to pitting corrosion and heat treatment.

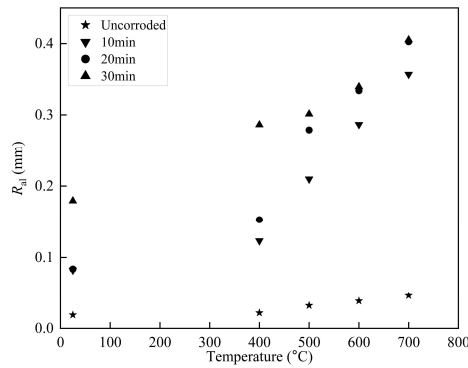


**Fig. 3.15** Relation of  $R_{al}$  with temperature and corrosion period.

The power spectral density function ( $f_{PSD}$ ) can be used to analyze the random nature of the pit surface topography. A pit surface topography comprises of sequences of sine waves with varying amplitude and frequency and  $f_{PSD}$  represents a measure of amplitude of each of the

## Fatigue Behavior of Constructional Steels Subjected to Pitting Corrosion and Elevated Temperature

harmonic component for a given frequency and direction.  $f_{\text{PSD}}$  is derived mathematically by squaring the Fourier transform of the pit surface profile  $z(x)$  of evaluation length expressed by Equation 2.58 given in section (2.9.3.2).

A  $f_{\text{PSD}}$  is illustrated in Fig. 3.16 for a temperature of 700 °C and a corrosion duration of 30 min. As may be seen, a pit's surface topography is dominated by low-frequency waves, indicating that waves with long wavelengths are more prevalent than those with short wavelengths. Furthermore, the figure displays a monotonic downward trend in general, but with more randomized micro geometrical features. The power spectral density of a given pit surface profile has a dominating spatial frequency,  $\omega_{\text{max}}$ , and a dominant wavelength (mm),  $\lambda_{\text{max}}$ . Fig. 3.17 depicts the variation of  $\lambda_{\text{max}}$  with corrosion time and temperature. In uncorroded samples, when the temperature goes up from 25 °C to 700 °C,  $\lambda_{\text{max}}$  rises by 65%. Comparing both corroded and uncorroded samples at room temperature shows that corroded specimens have 2.6-fold rise in  $\lambda_{\text{max}}$  after 10 min and a 4-fold rise after 30 min. For corroded samples: (i) at a constant corrosion time,  $\lambda_{\text{max}}$  grows up to 3.1-fold with an increase in temperature from 25 °C to 700 °C; and (ii) at a fixed temperature,  $\lambda_{\text{max}}$  increases upto 60% with an increase in corrosion duration from 10 min to 30 min. Note that dominant spatial frequency  $\omega_{\text{max}}$  has an inverse relation with  $\lambda_{\text{max}}$ . In practice, surfaces often exhibit a greater spectrum of roughness characteristics, including dominating wavelength roughness patterns that border on waviness (Pfefferkorn et al., 2014). Thus, decreasing  $\omega_{\text{max}}$  indicates the widening of peaks and valleys on the pit surface.

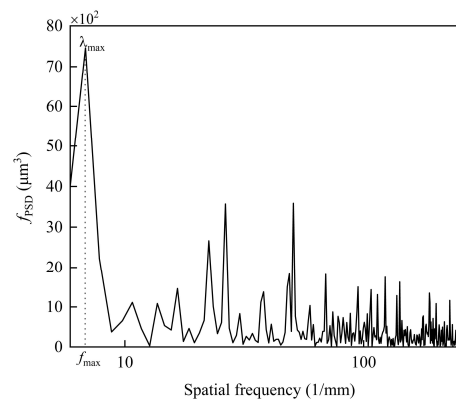


**Fig. 3.16** Illustration of power spectral density function.

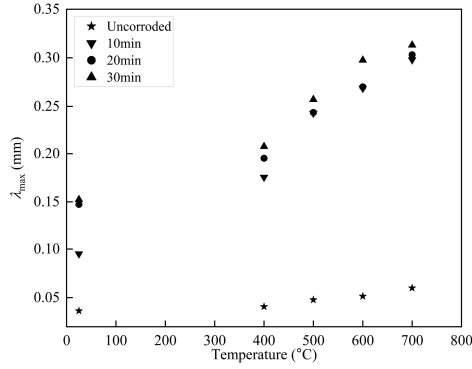


**Fig. 3.17** Variation of  $\lambda_{\max}$  with corrosion time and temperature.

### 3.3.4 Volume parameters:

Volume parameters are classified as functional parameters within the discipline of surface tribology. They assist in examining the surface characteristics of mechanical components concerning frictional wear resistance and fluid retention capacity. However, in the present investigation, these parameters are used to describe the volumetric distribution of metal on the pit surface. The volume parameters are assessed using the Abbott–Firestone curve, commonly known as a material ratio curve. It is a plot that depicts metal ratio distribution from the highest hill to the lowest dale on the corrosion pit profile (Whitehouse, 2002) as explained in section (2.9.3.4). Fig. 3.18 (a) shows the variation of  $R_{\text{vmp}}$  with corrosion time and temperature. For the uncorroded samples, a rise of 90% in  $R_{\text{vmp}}$  values are seen between 25 °C and 700 °C. This behaviour indicates an increase in hill volume with heat treatment caused by metal oxidation. At room temperature,  $R_{\text{vmp}}$  increases by 50% as corrosion time changes from 10 min to 30 min. This indicates that pitting corrosion causes an increase in  $R_{\text{vmp}}$ . In addition, upto 79% increase in  $R_{\text{vmp}}$  has been observed for different combinations of temperature and exposure duration. Thus, it can be inferred that the quantity of metal prone to potential pitting at a specific material ratio increases with corrosion level and temperature.

The volume parameter,  $R_{\text{vmc}}$ , calculates the change in volume of the metal in pit between two material ratios,  $p$  and  $r$ . Fig. 3.18 (b) illustrates the relationship of  $R_{\text{vmc}}$  with temperature and three corrosion levels. For corrosion-free samples, a rise in temperature from 25 °C to 700 °C results in a 45% increase in  $R_{\text{vmc}}$  values. Moreover, for a specified corrosion duration, increase in temperature causes a threefold rise in  $R_{\text{vmc}}$ . Further, for a given temperature, extended corrosion exposure causes  $R_{\text{vmc}}$  values to rise by a maximum of 1.8 times. Note that  $R_{\text{vmc}}$  refers to the quantity of material available for resisting a given load after the removal of



## Fatigue Behavior of Constructional Steels Subjected to Pitting Corrosion and Elevated Temperature

metal surface layers by pitting. In this regard, it can be concluded that the metal available to resist mechanical load decreases for varied pitting corrosion levels and temperatures.

The core void volume parameter,  $R_{vvc}$ , represents the change in void volume between the material ratios  $p$  and  $r$ . Fig. 3.18 (c) depicts the distribution of  $R_{vvc}$  with corrosion time and temperature. As shown, a rise in temperature from 25 °C to 700 °C causes a 70% increase in  $R_{vvc}$  for uncorroded samples. In the case of corroded specimens: (i) at a constant temperature,  $R_{vvc}$  rises by a factor of up to 1.8 when corrosion time increases from 10 min to 30 min, and (ii) at a fixed corrosion time, a temperature shift from 25 °C to 700 °C results in an upto threefold increase in  $R_{vvc}$ . In general, the  $R_{vvc}$  measure represents the volume of the metal's core that is still present after the surface has worn away by pitting. Therefore, a rise in  $R_{vvc}$  indicates that valleys formed during corrosion and heat treatment are becoming deeper. The conclusion is that a rise in corrosion level and temperature increases  $R_{vvc}$ , which causes an increase in dale volume due to metal consumption in the pit.

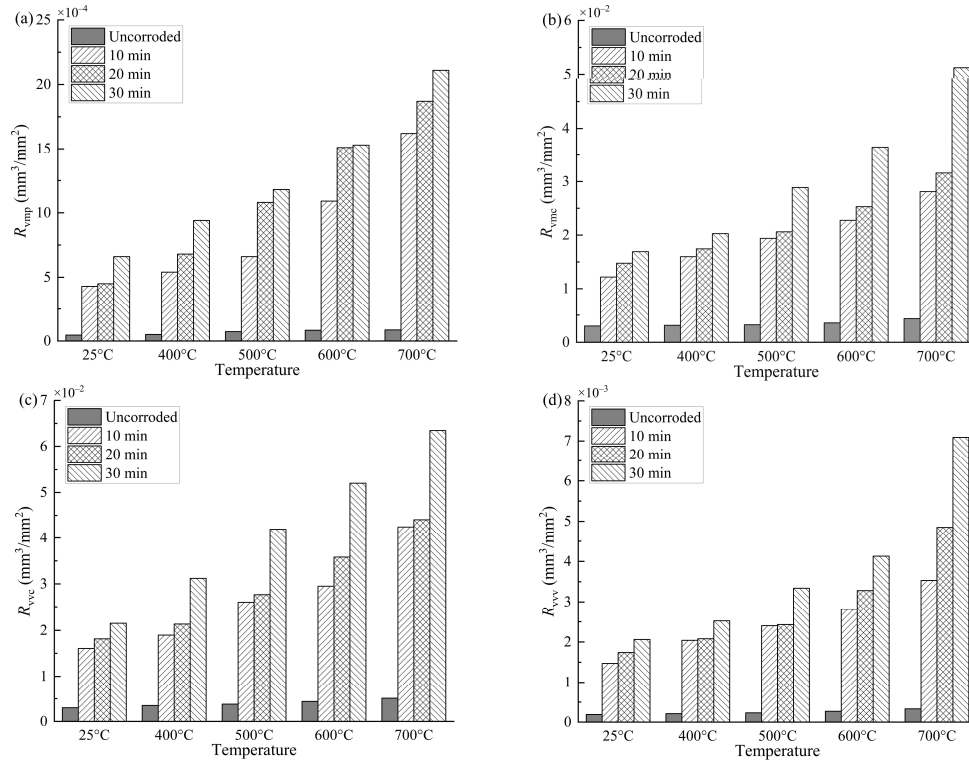


**Fig. 3.18** Variation of volume parameters with corrosion duration and temperature: (a)  $R_{vmp}$ ; (b)  $R_{vmc}$ ; (c)  $R_{vvc}$ ; and (d)  $R_{vvv}$ .

Finally,  $R_{vvv}$  refers to the void volume in the pit surface for a given  $r$ . Fig. 3.18 (d) illustrates the variation of  $R_{vvv}$  with temperature and corrosion period. A rise in temperature

from 25 °C to 700 °C results in a 1.7-fold increase in  $R_{vv}$  values for uncorroded samples. Corroded samples exhibit upto a twofold rise in  $R_{vv}$  values for a given temperature as corrosion time increases from 10 min to 30 min. For a given corrosion duration, an increase in temperature from 25 °C to 700 °C results in a 3.5-fold increase in  $R_{vv}$  values. Note that  $R_{vv}$  represents the void volume available in the pits to accommodate the corrosion products. Thus, it can be concluded that extended corrosion exposure and heat treatment would potentially increase the void volume of dale on the pit surface.

### 3.4 Microstructure investigation

Microstructure investigations are carried out on all specimens using optical and scanning electron microscopes to investigate the pit surface topography further. Following the standard metallographic procedure, the microstructural features of the samples are studied under an inverted optical microscope (Model: Olympus GX 53 series) as shown in Fig. 3.19. The procedure entails cutting the samples, hot mounting them on polymeric material, and polishing them using an automated grinding-polishing machine (Make: METCO) with emery paper grades ranging from P120 to P2000. After every polishing stage, the specimens are rinsed in ethanol solution. Further, to improve the surface quality, the samples are polished using a 1 mm diamond paste placed on a polishing cloth while the machine wheel gently spins. Lastly, the specimens are etched in a solution containing 2 ml nitric acid in 98 ml ethanol. The etched samples are then examined using an optical microscope.

The microstructural features of the steel specimens observed using the optical microscope are shown in Figs. 3.20 (a)–(f). As seen in Fig. 3.20 (a) and Fig. 3.20 (b), samples exposed at room temperature exhibit polygonal and non-polygonal structures of ferrite and pearlite in white and black contrasts, respectively. Equiaxed grains of ferrite and a small quantity of pearlite are observed in the microstructure. In addition, some of the ferritic grain boundaries have thin cementite films. The specimen heated to 400 °C displays a slightly more fine-grained ferrite (Fig. 3.20 (c)). Note that the change in microstructure with temperature is attributed to the solubility of carbon in ferrite. The weight fraction of carbon soluble in ferrite increases from 0.002% at 400 °C to 0.0175% at 700 °C. The iron-carbon phase diagram illustrates that no phase change is conceivable for heat treatments up to 500 °C (Samuels, 1999). However, considerable microstructure changes are seen in specimens heated to 500 °C or higher.

The carbide particles become more noticeable on specimens when heated to 500 °C or above (Figs. 3.20 (d)–(f)). Fine carbide particles are formed at about 500 °C from the excess carbon rejected from the supersaturated solid solution of martensite. At a temperature of around 600 °C, the martensitic structure gets progressively coarsened by continuous removal of carbon

### Fatigue Behavior of Construction Steels Subjected to Pitting Corrosion and Elevated Temperature

from the matrix of martensite and coarsening of the carbide particles. Hence at 600 °C, the ferrite matrix had a large number of non-homogeneously distributed carbide particles (Sk et al., 2017). The transformation of pearlite into austenite takes place in specimens subjected to 700 °C. Consequently, at high temperature, part of the pearlite is transformed into austenite, and as the ferrite cools, a large number of black particles appear in and around it (Qian et al., 2019).

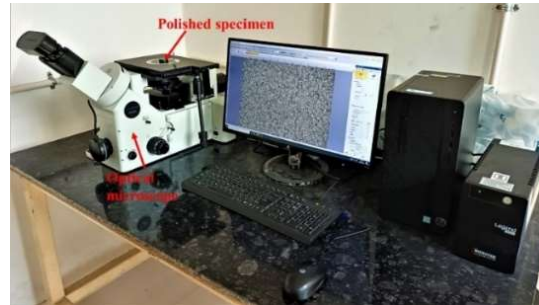


Fig. 3.19. Optical microscope investigation.

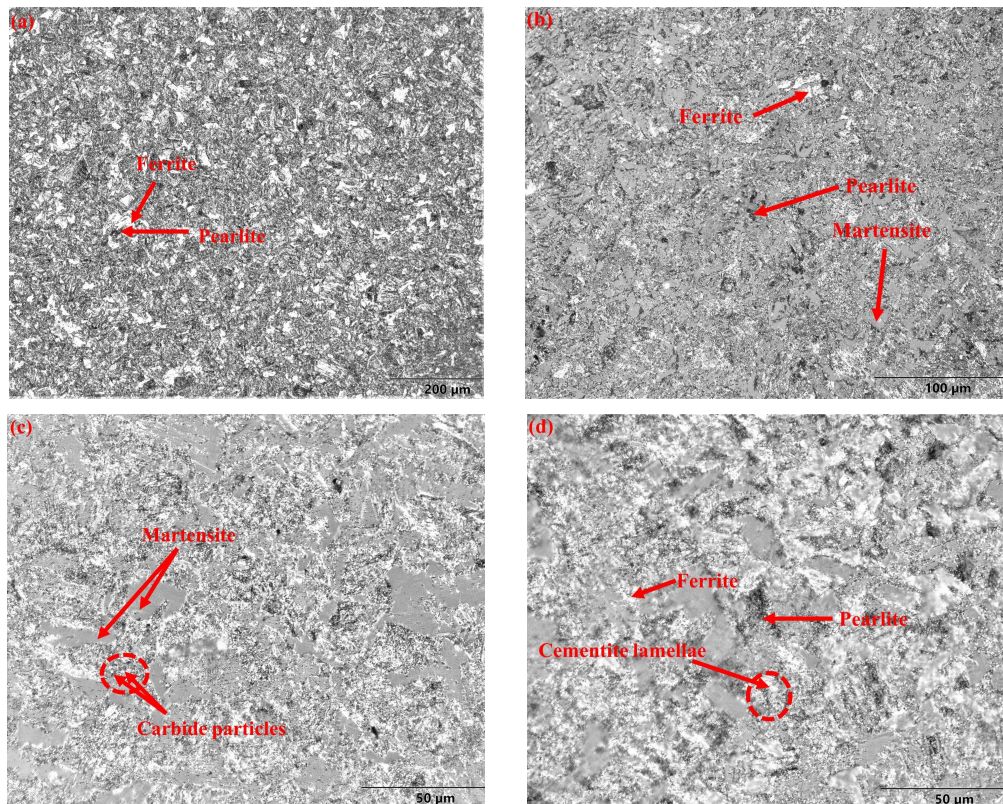


Fig. 3.20 Optical micrographs: (a) and (b) 25 °C; (c) 400 °C; (d) 500 °C; (e) 600 °C; and (f) 700 °C.

The presence of small carbide particles dispersed across the surface, filling the interstices between larger carbide particles. Conversely, the larger carbide particles tend to settle beneath the steel surface due to their inability to occupy the recesses within the pit surface. However, the heat treatments affect the role of carbides in initiating fatigue cracks. Carbides,

being hard and brittle, act as stress concentrators under repeated stress. When stress concentrates around a carbide, it's more likely for a crack to start there. The heat treatment produced coarse and fewer carbides, potentially promoting earlier crack initiation due to the higher stress concentration (Korade et al., 2020a).

To examine the microstructure characteristics of pit surface, further investigations have been conducted using (Model: JEOL JSM-6010LV) SEM and energy dispersive X-ray spectrometry (EDS). Figs. 3.21 (a)–(e) depicts the fractographic images of uncorroded specimens. The solid square marking on the fractographic images represents the region analysed using EDS. At room temperature, polygonal ferrite and lamellar pearlite having axis of approximately the same length were observed. In addition, degenerated pearlite and a small fraction of bainite were also present. At higher temperatures, specifically 500 °C and above, cementite lamellas and films in the pearlite and upper bainite zones fragmented into smaller particles, whereas highly tempered martensite disintegrated into ferrite and carbide (Sk et al., 2017). The particles spheroidize owing to carbon diffusion and curvature effect, where the interface near sub boundary in cementite lamella with a sizeable local curvature and surrounding ferrite causes a fast carbon dissolution leading to a local lamella division (Novikov & Afanasyev, 1978). At a temperature exposure of 500 °C–600 °C, the carbide particles are heterogeneously dispersed.

At high temperatures, the cementite lamellas inside it undergo a transformation. These lamellas first break down into smaller particles, a process called fragmentation. Then, these smaller particles transform into a more energetically favorable, spherical shape through a process called spheroidization. This transformation is driven by the diffusion of carbon atoms, with the goal of minimizing the total energy in the system. This transformation of cementite lamellas has a significant impact on the steel's properties. Originally, the lamellas act like pins that restrict the growth of ferrite grains. However, fragmentation and spheroidization weaken this pinning effect, allowing the ferrite grains to grow larger at high reheating temperatures (Sk et al., 2017). Additionally, the fragmentation and spheroidization lead to a more uniform distribution of the smaller, spherical carbide particles within the steel.



### Fatigue Behavior of Construction Steels Subjected to Pitting Corrosion and Elevated Temperature

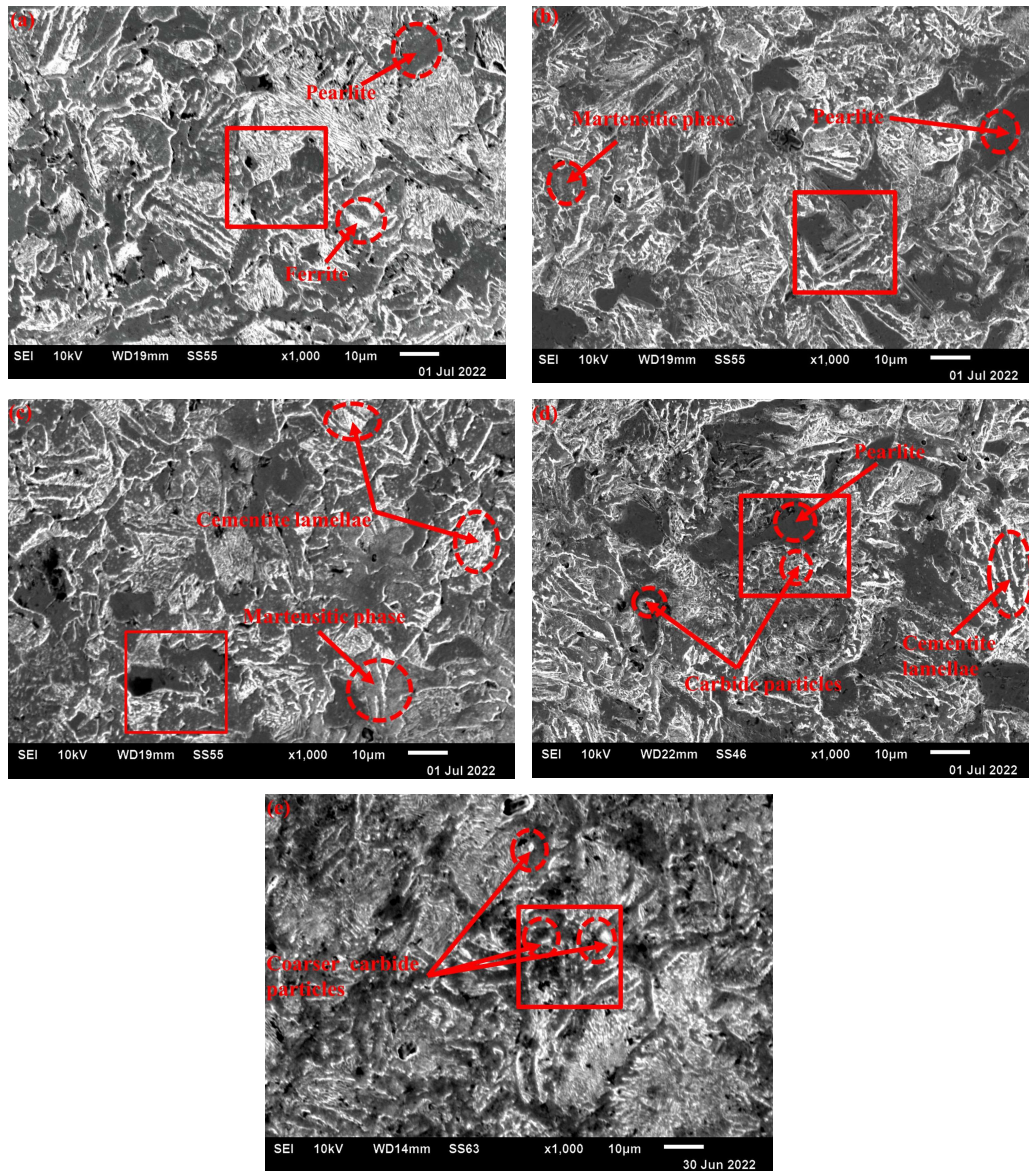


**Fig. 3.21** Fractographic images of uncorroded specimens: (a) 25 °C; (b) 400 °C; (c) 500 °C; (d) 600 °C; and (e) 700 °C.

The pearlitic and bainitic regions have more granular carbides than the ferrite regions. Moreover, ferrite grains and ferritic laths increased owing to the spheroidization and coarsening of fine carbides effects at 600 °C–700 °C. Additionally, the density of granular carbide particles decreased but became coarser at 700 °C. The EDS spectrum of the corrosion-free samples are shown in Fig. 3.22. A notable change in carbon and iron were observed with increasing temperature. The carbon and iron rise and fall by 21– and 2–fold, respectively, with increase in temperature of 25 °C–700 °C, while the oxygen depletes by 2.1–fold.

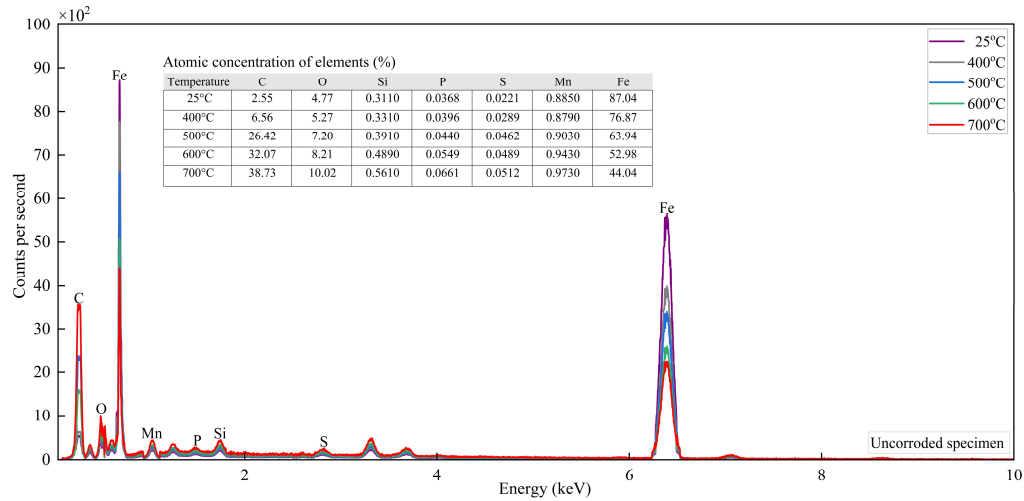
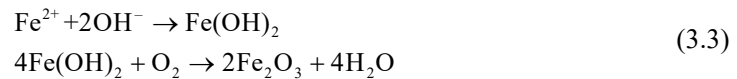


Fig. 3.22 EDS of uncorroded specimen.

The fractographic images of corroded samples for various combinations of corrosion durations and temperatures are illustrated in Figs. 3.23 (a)–(o). All images reveal that the surface features are altered to varying degrees—mild, moderate, and severe—by the electrochemical corrosion process and heat treatment. Surface features of various types manifested as a consequence of chemical reactions between the steel specimen and the 5 wt.% NaCl solution. Oxidation and reduction are typically the two half reactions that make up corrosion given by the following equation as (Nandi et al., 2016; Revie & Uhlig, 2008):



The additional reaction is,



In the presence of an alkaline medium,  $2\text{OH}^-$  forms a stable passive film on the steel surface to protect it. However, this passive film breaks down in chloride-contaminated environments as a result of chlorine adsorption and simultaneous  $\text{O}_2$  deportation from the passive film. Iron dissolution, an anodic reaction, is well defined in terms of charge transfer controlled kinetics. The cathodic reaction, oxygen reduction on iron, is well defined in terms of combination of mass- and charge-transfer controlled kinetics (Cáceres et al., 2009).

At room temperature (Figs. 3.23 (a)–(c)), increasing corrosion time causes progressively bigger pits to emerge. Smaller pits are seen at 10 min exposure and the appearance of identifiable larger pits as dark black spots on the 30 min sample indicates a considerably greater pit depth.

### Fatigue Behavior of Constructional Steels Subjected to Pitting Corrosion and Elevated Temperature

As iron oxide builds up on the surface, pits of varying cross-sections such as circular, elliptical, and irregular shapes continue to form. The observed overall steel surface damage may be attributed to the fact that iron oxide could partly dissolve and permeate the produced iron carbonate. Wide, localized corrosion characteristics were seen as a result of the attack. In addition, the ingress of oxygen into the bulk solution could have also exacerbated the damage to the steel surface.

The fractographic images of corroded and heat-treated specimens are demonstrated in the Figs. 3.23 (d)–(o). During heat treatment, magnetite ( $\text{Fe}_3\text{O}_4$ ) is oxidized, transforming to hematite ( $\alpha\text{-Fe}_2\text{O}_3$ ) at temperatures over 300 °C. Under these conditions, magnetite oxidizes through a topotactic reaction that keeps the original crystal morphology constant. One distinguishing aspect of this transformation is effect of magnetite crystal size on the nature of the corrosion products in crystals smaller than 300 nm, intermediate maghemite ( $\gamma\text{-Fe}_2\text{O}_3$ ) form transforming to hematite at temperatures exceeding 500 °C. Large crystals (>300 nm) bypass maghemite formation and undergo a direct transformation to hematite. Moreover, since oxygen is absorbed during the reaction, the density of starting material decreases and the weight of sample increases (Cornell & Schwertmann, 2003):



Following heat treatment, the pitting corroded surface displays various surface characteristics (Figs. 3.23 (d)–(o)). This could be caused by the uneven thickness development of hematite and magnetite-based oxide scales during heating. At 600 °C–700 °C, hematite-dominated oxide scales occur at various locations and are significantly thinner. Additionally at 600 °C, in regions where the scale remains in contact with the iron, it is rather thick, but in locations where the scale-iron contact has been lost, it is extremely thin (Chen & Yeun, 2003). Figs. 3.23 (d)–(o) also reveals the existence of microcracks, which are found to widen as the temperature rises. Beginning at the grain boundaries of magnetite, microcracks spread into wustite grains. The presence of voids and void coalescence in wustite grains adjacent to the  $\text{Fe}_3\text{O}_4/\text{FeO}$  interface may facilitate crack propagation. Initiation of cracks and localized stress concentration may also be attributed to the volume increase caused by the transition of magnetite into hematite as reported by (Kim, 2003).



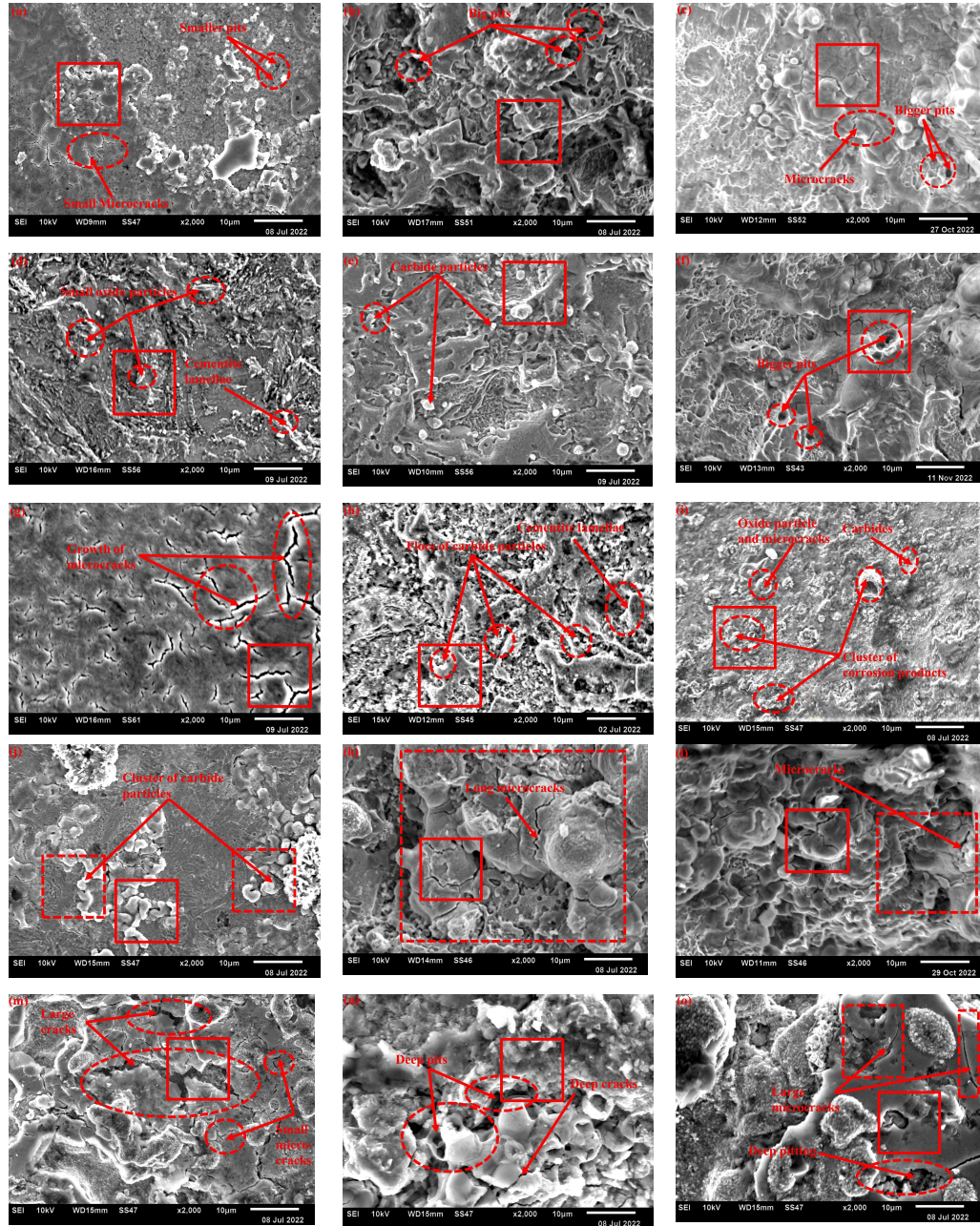


**Fig. 3.23** Fractographic images of corroded pits: (a) 25 °C, 10 min; (b) 25 °C, 20 min; (c) 25 °C, 30 min; (d) 400 °C, 10 min; (e) 400 °C, 20 min; (f) 400 °C, 30 min; (g) 500 °C, 10 min; (h) 500 °C, 20 min; (i) 500 °C, 30 min; (j) 600 °C, 10 min; (k) 600 °C, 20 min; (l) 600 °C, 30 min; (m) 700 °C, 10 min; (n) 700 °C, 20 min; and (o) 700 °C, 10 min.



## Fatigue Behavior of Constructional Steels Subjected to Pitting Corrosion and Elevated Temperature

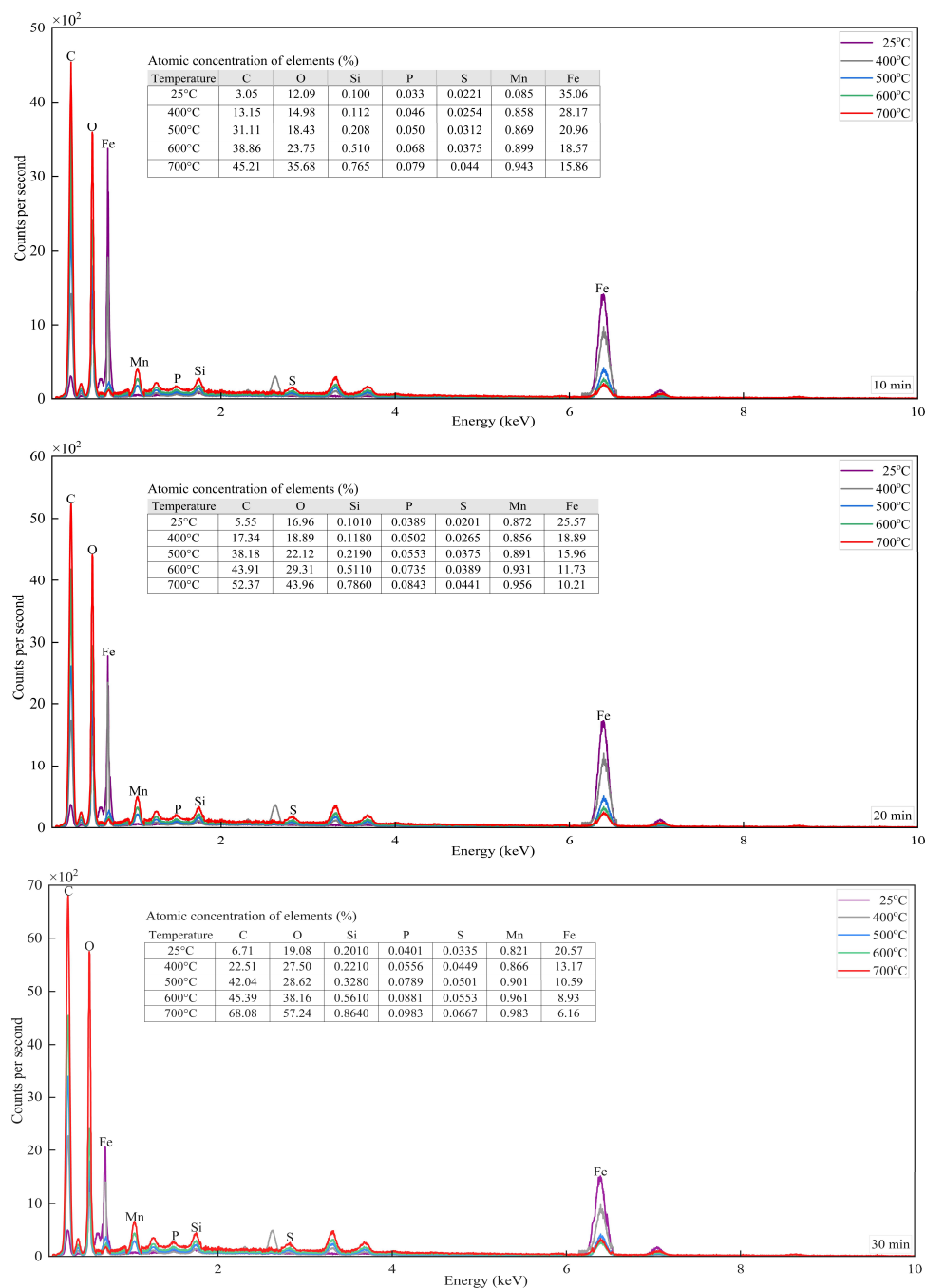


**Fig. 3.24** EDS of corroded pits: (a) 10 min; (b) 20 min; and (c) 30 min.

The EDS patterns of corroded samples exposed to various combinations of corrosion duration and temperature are shown in Figs. 3.24 (a)–(c). As can be seen, the concentrations of three elements, namely carbon (C), oxygen (O), and iron (Fe), undergo significant changes. Compared with uncorroded specimens, corroded samples had typical minimum and maximum carbon reductions of 1.2– and 2.2–fold, oxygen reduction of 2.5–fold, and oxygen rise of upto 3–fold, respectively. In the case of corroded samples: (i) for a set temperature, carbon and

oxygen decrease by upto 2-fold and 3.5-fold, respectively, with increase in corrosion time while oxygen rise by upto 3-fold; (ii) for a set corrosion time, increasing temperature from 25 °C to 700 °C reduces carbon and oxygen by upto 15- and 3-fold, respectively, and increases iron by upto 2.5-fold. Note that carbon oxidation is lower than that of iron oxidation. This may be attributed to insolubility of carbon in adherent and coherent scale forms. The ejected carbon from faster iron oxidation must either stay at the scale-steel contact or infiltrate into the steel, enriching the surface layer of the steel substrate (Plumensi et al., 1969). The microstructural features described in this section are closely related to the significant changes in pit surface roughness parameters discussed in Section 3.3. The surface area and particle size of iron oxides affect the condition of the pit surface.

For instance, faster growth rates at low temperatures may form poorly ordered crystals with a surface area of several hundred  $\text{m}^2\text{g}^{-1}$ . In contrast, slower formation rates at higher temperatures can develop crystals with a small surface area. The surface area of magnetite varies from  $4 \text{ m}^2\text{g}^{-1}$  to  $100 \text{ m}^2\text{g}^{-1}$ , whereas hematites generated at 500 °C to 600 °C have a larger surface area of upto  $200 \text{ m}^2\text{g}^{-1}$  (Cornell & Schwertmann, 2003). Carbides of various sizes and shapes have also been seen in the present investigation from fractographic images. Fine carbides with enhanced density fill the space between coarse carbides and reduce surface roughness. Due to their size, larger carbides cannot fill holes or valleys, increasing their surface roughness. The increased surface roughness indicates an uneven or rough surface that mimics valleys or pits and potentially serves as crack nucleation sites (Korade et al., 2020b). Regardless of whether the carbide particles were initially cracked or uncracked, it can be considered equivalent to a small defect. In general, the initial fracture propagation starts from large carbides on the sub-surface. It spreads to the surface and interior of the samples creating surface spalling, secondary cracks, and internal cracks (Garrison, 1986; Wu et al., 2022).

Based on the obtained results, the potential strategies for mitigating the adverse effects of pitting corrosion and elevated temperature on surface roughness and the practical implications are presented herein. Several surface treatment methods have been employed to prevent/prolong corrosion of reinforcing bar. Higher levels of corrosion and longer exposure durations are associated with increased surface roughness. Corrosion causes steel to become more hydrophilic, which is correlated with an increase in surface roughness. Anticorrosive coatings can be employed as protective measures to prevent corrosion on metal surfaces. These coatings, particularly hydrophobic ones, have the ability to repel saline solutions and hinder the corrosion process. Epoxy and epoxy resin-based surface coatings have been found to effectively prevent corrosion in reinforcing bars (e.g. (Sharma et al., 2022; Swamy & Tanikawa, 1993)). Surface mechanical strengthening techniques are commonly employed to enhance the fatigue resistance of metallic materials through modifications to the microstructure of the surface. Ball-burnishing

## **Fatigue Behavior of Constructional Steels Subjected to Pitting Corrosion and Elevated Temperature**

and shot peening are commonly employed surface treatments for enhancing the performance of structural components made from high-strength steels. These treatments aim to improve fatigue and corrosion fatigue properties (Mhaede, 2012; Prev y & Cammett, 2004). Recently, ultrasonic surface rolling processing at nano-, micro-, and macro-scale are employing ultrasonic energy rather than force as the primary means to treat the surface of a sample, distinguishing it from traditional rolling methods are used (Cao et al., 2010; Zhao et al., 2019). It's important to note that the choice of mitigation strategies depends on factors such as the application, environmental conditions, and materials used. A comprehensive approach that integrates multiple strategies is often the most effective in mitigating the adverse impacts of pitting corrosion and elevated temperature on surface roughness. The practical implications of the findings are:

- i. Pitting corrosion and elevated temperature drastically change the surface characteristics of the reinforcing bar. These changes determine to a large extent, the mechanical and physical properties of the bar, such as adhesion, fatigue, friction, oxidation, wear, etc.
- ii. The surface characteristics of steel are strongly correlated with its residual capacity. Thus, based on the data obtained, it is possible to achieve realistic artificial mimicking of surface profiles for varying degrees of pitting corrosion and temperature. This facilitates performance prediction of existing steel elements.
- iii. In seismic engineering applications, stable cyclic ductility is necessary for the dissipation of seismic energy. The ductility performance of corroded steel depends on its surface characteristics. The presence of an uneven surface on corroded steel leads to stress concentration, which, when subjected to loading conditions, causes early yield and ultimately premature failure of the corroded steel member.

### **3.5 Conclusions**

This work performed experimental investigations including microstructural examinations to explore the surface roughness properties of thermo-mechanically treated rebars subjected to pitting corrosion and elevated temperatures. The following conclusions are drawn from this study:

- i. The amplitude parameters  $R_a$ ,  $R_q$ ,  $R_t$ ,  $R_{ku}$ , and  $R_{sk}$  showed a significant rise with increased corrosion exposure duration and elevated temperature. An increase in corrosion duration results in a rise of valleys and peaks. Further, the metal tends to continue to accumulate above the mean line either with increasing corrosion time at constant temperature or with increasing temperature at a fixed exposure time.

- ii. The spacing parameters  $R_{sm}$ ,  $R_{smx}$ ,  $R_{smq}$ ,  $R_c$ ,  $R_{cx}$ ,  $R_{cq}$ , and  $R_{pc}$  showed considerable changes with extended corrosion and increasing temperature. The equivalent defect size of a pit topography increased with corrosion period and temperature.
- iii. The spatial parameters  $R_{al}$  and  $\lambda_{max}$  demonstrated significant variations with temperature and corrosion level. Rising values of  $R_{al}$  for various combinations of corrosion time and temperature imply a considerable reduction in number of peaks on the pit surface.
- iv. The volume parameters  $R_{vmp}$ ,  $R_{vmc}$ ,  $R_{vvc}$ , and  $R_{vvv}$  varied considerably with corrosion duration and exposure temperature. The quantity of metal prone to potential pitting at a specific material ratio increased with corrosion level and temperature. Further, quantity of metal available to resist mechanical load decreased with pitting corrosion levels and temperature exposures.
- v. Considerable microstructural changes are seen in specimens heated to 500 °C or higher. Specifically, the density of granular carbide particles decreased but became coarser at 700 °C. In general, the initial fracture propagation could begin from the large carbides present on the steel sub-surface.



## Chapter 4

# Fatigue life estimation of TMT rebar exposed to pitting corrosion and elevated temperature impacted surface topography

---

### 4.1 Introduction

High-strength deformed reinforcing bars are extensively utilized in reinforced concrete for their superior structural strength and economic advantages. Despite these benefits, the reinforcing has shown shortcomings in fatigue resistance, prompting thorough investigation. Fatigue initiation, occurring when applied loads exceed the plastic deformation threshold, leads to gradual damage accumulation and crack formation. Surface topography plays a pivotal role in steel's mechanical behavior, especially under cyclic loading, and pitting corrosion emerges as a significant factor altering topography, initiating fatigue-induced cracks through localized metal loss.

Elevated temperatures, a consequence of fire incidents in transportation structures, further exacerbate the impact on topography. Microstructural changes at 500 °C or higher and the formation of thinner hematized oxide layers at 600–700 °C contribute to cracking and localized stress concentrations. The combined effects of pitting corrosion and temperature exposure significantly alter the surface features of steel, subsequently influencing its fatigue performance. Surprisingly, there is a dearth of comprehensive studies examining these combined effects on topographical features. Critical surface topographic parameters, including arithmetic mean height and total height, exhibit a strong correlation with the fatigue stress concentration factor. Additionally, the defect size parameter in the high-cycle fatigue life model, strongly influenced by pitting corrosion, lacks existing models relating to affected parameters.

This study aims to bridge these gaps by conducting experiments, including microstructural examinations. Employing multiple linear regression methods, the research seeks to develop models that comprehensively relate surface topographic feature parameters (such as arithmetic mean height, total height, ten-point height, and profile mean spacing) to the combined effects of pitting corrosion and elevated temperature. Furthermore, MLR models will be developed for a surface topographic feature variable in stress concentration factor and the defect size parameter. The main objective is to propose a comprehensive framework for estimating the high-cycle fatigue life, incorporating these models. Validation involves comparing the estimated fatigue life, incorporating these models, with experimental data sourced from the existing literature, contributing valuable insights to the understanding of steel's performance under complex conditions.

## **4.2 Corrosion–fatigue life**

The total fatigue life ( $N_f$ ) comprises crack initiation life ( $N_{ci}$ ) and crack propagation life ( $N_{cp}$ ):

$$N_f = N_{ci} + N_{cp} \quad (4.1)$$

$N_{ci}$  can be evaluated based on the dislocation dipole accumulation model (Tanaka & Mura, 1981, 1982) expressed as:

$$N_{ci} = \frac{9 \Delta k_{th}^2 G}{2 E (S - S_e)^2 a_0} \quad (4.2)$$

The variable  $\Delta k_{th}$  is expressed as:

$$\Delta K_{th} = 7.03(1 - 0.85 R) \quad (4.3)$$

$S_e$  can be expressed as:

$$S_e = \frac{0.65 f_u + 14.48}{k_t} \quad (4.4)$$

where  $f_u$  represents ultimate tensile strength of steel (MPa) and  $k_t$  is SCF and is computed as:

$$k_t = 1 + \frac{n}{\rho} F_s \quad (4.5)$$

where

$$F_s = R_a \left( \frac{R_t}{R_{10Z}} \right) \quad (4.6)$$

where  $F_s$  ( $\mu m$ ) signifies the effect of surface topography waviness on roughness depends on roughness parameters. (Arola & Ramulu, 2016),  $n$  is stress state factor (=2 for uniform tension (Arola & Williams, 2002)), which takes into account material dependencies such as microstructure, heterogeneity etc., and  $\rho$  is profile valley radius (mm). A schematic representation of surface topographic feature parameters is shown in Fig. 4.1. The analytic solution of Paris law integral gives fatigue crack propagation life,  $N_{cp}$  can be expressed as:

$$N_{cp} = \frac{a_0^{\left(1-\frac{m}{2}\right)} - a_{sc}^{\left(1-\frac{m}{2}\right)}}{C S^m \kappa^m \pi^{\frac{m}{2}} \left(\frac{m}{2} - 1\right)} \quad (4.7)$$

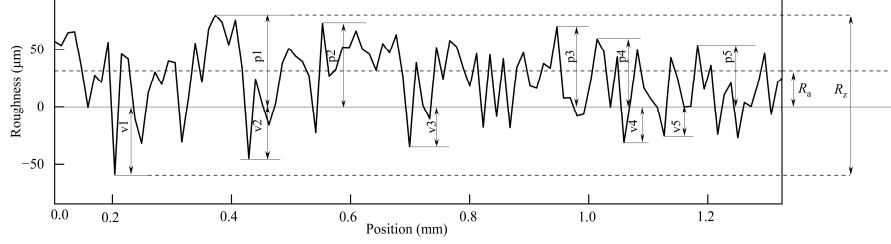


**Fig. 4.1** A schematic of surface topographic feature parameters.

where  $\kappa = 0.5\sqrt{\pi}$  is geometry constant,  $a_{sc}$  represents critical crack size,  $C$  and  $m$  are the fatigue crack growth parameters listed in Table 4.1. According to Equation 4.1, total fatigue life can be expressed as:

$$N_f = \frac{9\Delta k_{th}^2 G}{2E(S - S_e)^2 a_0} + \frac{a_0^{\left(1-\frac{m}{2}\right)}}{C S^m \kappa^m \pi^{\frac{m}{2}} \left(\frac{m}{2} - 1\right)} \quad (4.8)$$

**Table 4.1** Fatigue crack growth properties (Barsom & Rolfe, 1999; Stephens et al., 2000).

$C$	$m$	$\kappa$
$3.6 \times 10^{-10}$	3	0.8862

Assuming surface roughness to be a long crack, a  $\sqrt{area_R}$  model relating surface topographic feature parameters with fatigue strength has been proposed in (Murakami, 2002). In the current study, this model is employed to determine the equivalent defect size,  $\sqrt{area_R}$ . This model is given by Equation 2.80 and 2.81 as explained in section (2.9.4).

## 4.3 Experimental procedure

### 4.3.1 Material and samples preparation:

The steel samples used in this study are made from commercially available hot-rolled high-strength, deformed TMT reinforcement bars of grade Fe 500D confirming to IS 1786:2008. The outer ribbed steel layer is removed by lathe machining and smoothened to achieve a highly polished finish. The finished samples are 10 mm in diameter and 100 mm in length. A total of 15 such samples are prepared and exposed to pitting corrosion and high temperatures. Accelerated corrosion technique is employed for inducing pitting corrosion in samples. Each sample has two pit sites that are 50 mm apart. The entire surface of the sample



## Fatigue Behavior of Constructional Steels Subjected to Pitting Corrosion and Elevated Temperature

is wrapped with an insulating tape except for the two marked pits, each with a diameter of 5 mm (Fig. 4.2 (a)). A hot melt glue is used to seal the ends of the wire tightly. The sample, acting as the anode and the stainless steel as and the stainless steel acting, as the cathode are completely immersed in a tray filled with 5% NaCl solution (Fig. 4.2 (b)). Further, samples are subjected to electrochemically accelerated corrosion using an external direct current source with a constant current of 0.5 A for three different time intervals of 10–, 20– and 30– min. To examine the effect of temperature on surface topography, corroded samples are heated to different target temperatures of 400 °C, 500 °C, 600 °C, and 700 °C in a muffle furnace at 10 °C/min. The target temperatures are selected to represent real fire exposure conditions. For a uniform temperature distribution, the samples were soaked in the muffle furnace at target temperatures for 20 minutes before cooling. Further, all samples are then stored in a desiccator for subsequent investigation.

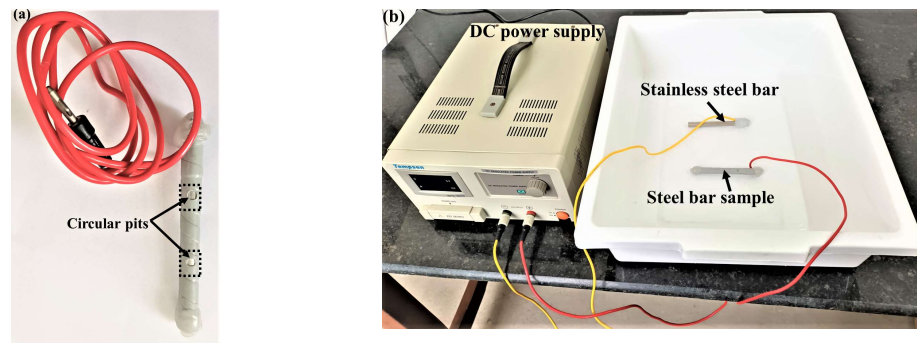


**Fig. 4.2** Experiment: (a) sample preparation; and (b) accelerated corrosion setup.

A high-resolution three-dimensional (3D) laser scanner is used to measure the corrosion pit dimensions such as length ( $l$ ), depth, and width ( $w$ ). During the scanning process, complete geometry of the pit is captured with a scan density of 5 million points per scan with an accuracy of 10  $\mu$ m at a fixed field of view of 100 mm. Following this process, pit geometry is recreated. Figs. 4.3 (a–c) shows pit geometry obtained from accelerated corrosion along with its image recreated by 3D laser scanning. Critical cross-sectional area loss which is often employed criteria to assess the severity of pitting corrosion, while evaluating corrosion-fatigue behaviour. The critical cross-sectional area loss can be estimated as:

$$\eta_{\text{cri}} = (1 - A_{\text{m}}/A_{\text{n}}) \times 100\% \quad (4.9)$$

where  $A_{\text{n}}$  and  $A_{\text{m}}$  represent sample's nominal and minimum cross-sectional area ( $\text{mm}^2$ ). The severity of pitting corrosion has been categorized into three levels: mild, moderate, and severe, based on the range of  $\eta_{\text{cri}}$  values. For instance,  $\eta_{\text{cri}}$  less than 5% is categorized as mild,

whereas  $\eta_{cri}$  between 5% and 10% and higher than 10% are categorized as moderate and severe, respectively. Thus, in this study, the three corrosion durations (i.e., 10–, 20–, and 30–min) are selected to achieve the three levels of corrosion severity.

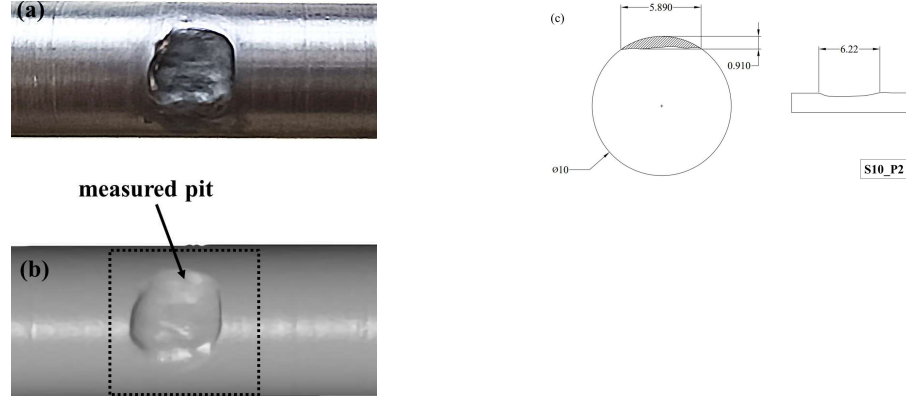


**Fig. 4.3** Corroded pit: (a) sample; (b) 3D laser scan image; and (c) geometry (unit: mm).

#### 4.3.2 Pitting corrosion:

Pitting corrosion is a form of localized corrosion in which the reinforcing bar experience a significant loss of cross-sectional area in localized regions. The result summary of corrosion pit geometry for various combinations of corrosion duration and exposure temperatures obtained from 3D laser scanning are given in Table 4.2. In Table 4.2,  $p_d^{max}$  (mm) denotes maximum corrosion penetration depth, which quantifies loss of steel section and is time-variant. Further,  $w$  (mm) and  $l$  (mm) represent width and length of a corrosion pit. As seen in Table 4.2, the values  $p_d^{max}$  vary significantly with corrosion time and temperature. At room temperature, an 83% increase in  $p_d^{max}$  is observed when corrosion duration increases from 10 to 30 min. Further, 20 min exposure rises  $p_d^{max}$  value by 50% compared to 10 min. However, compared to 20 min exposure, 30 min exposure raises  $p_d^{max}$  by only 23%. This implies rate of corrosion is decreasing over time.

The effects of high temperatures on corrosion pits can also be observed from Table 4.2. When compared to corroded samples exposed at room temperature for similar durations, an increase in temperature from 400 °C to 700 °C results in 25%, 42%, and 45% increases in  $p_d^{max}$  values for 10–, 20–, and 30–min exposures, respectively. At a given temperature, an increase in corrosion time causes a 71% increase in  $p_d^{max}$  values. In addition, at a given corrosion time, an increase in temperature between 400 °C and 700 °C causes a 21% increase

## Fatigue Behavior of Constructional Steels Subjected to Pitting Corrosion and Elevated Temperature

in  $p_d^{\max}$  values among samples subjected to high temperatures. Overall, it can be observed that  $p_d^{\max}$  increases significantly with rising temperatures. This is attributed to oxidation, reduction, and thermal decomposition reactions that occurs at high temperatures in dense layer of corrosion products and in remaining uncorroded part of the steel (Chitty et al., 2005). The dense layer of corrosion products is majorly composed of derived minerals of oxides such as goethite ( $\alpha$ -FeOOH), akageneite ( $\beta$ -FeOOH), and lepidocrocite ( $\gamma$ -FeOOH). At higher temperatures, the thermal decomposition of these minerals leads to an expansion of micropores into increased cylindrical spherical mesopores and macropores (Naono & Fujiwara, 1980). The uncorroded part of the steel in the corroded pit undergoes different degrees of oxidation resulting in the formation of oxide scales primarily composed of magnetite ( $\text{Fe}_3\text{O}_4$ ) and hematite ( $\text{Fe}_2\text{O}_3$ ) layers that are brittle in nature. Further, separation of oxide layers from the base metal results in the formation of craters of voids and deep cracks (Sneha, 2016). Thus, it can be stated that the combined effects of oxidation, reduction, and thermal decomposition reactions may lead to increase in  $p_d^{\max}$  with rising temperatures.

The values of  $\eta_{\text{cri}}$  for all samples are also given in Table 4.2. It can be observed that  $\eta_{\text{cri}}$  values ranging 3.02–4.89, 7.38–9.99, and 11.11–14.77 are obtained for 10–, 20–, and 30–min exposures, respectively. Thus, based on  $\eta_{\text{cri}}$  values, the severity of pitting corrosion can be classified into three levels: mild ( $\eta_{\text{cri}} \leq 5\%$ ), moderate ( $5\% < \eta_{\text{cri}} \leq 10\%$ ), and severe. Table 4.2 shows that when compared to samples corroded at room temperature and having similar exposure period, a rise in temperature from 400 °C to 700 °C leads to an increase in  $\eta_{\text{cri}}$  values upto 55%, which is significant.

The findings of 3D laser scanning of corrosion pits reveal  $p_d$  values vary at each position along length and breadth. The distribution trend of  $p_d$  along the circumference of the bar, specifically about  $p_d^{\max}$ , is of great interest to the researchers because it can assist in quantifying the maximum reduction in cross-sectional area of the steel, which is the parameter most commonly used to evaluate the deterioration of its structural strength due to corrosion. Hence, data points concerning distributions of  $p_d$  about  $p_d^{\max}$  along entire circumference of the steel bar are extracted from 3D scans. Amongst the various forms of mathematical equations employed to fit the data points, such as Gaussian, linear, elliptical, and semi-elliptical, a flipped Gaussian function of the following form is found to be more appropriate to describe  $p_d$  distribution along the circumference of the steel bar:

$$p_d = -\frac{\psi_1}{\psi_2 \sqrt{2\pi}} e^{-\left(\frac{\theta - \psi_3}{\psi_2 \sqrt{2}}\right)^2} \quad (4.10)$$

where  $\psi_1$ ,  $\psi_2$ , and  $\psi_3$  are curve fitting parameters and  $\theta$  is the angle subtended between center of the bar and a point located along its circumference (radians).

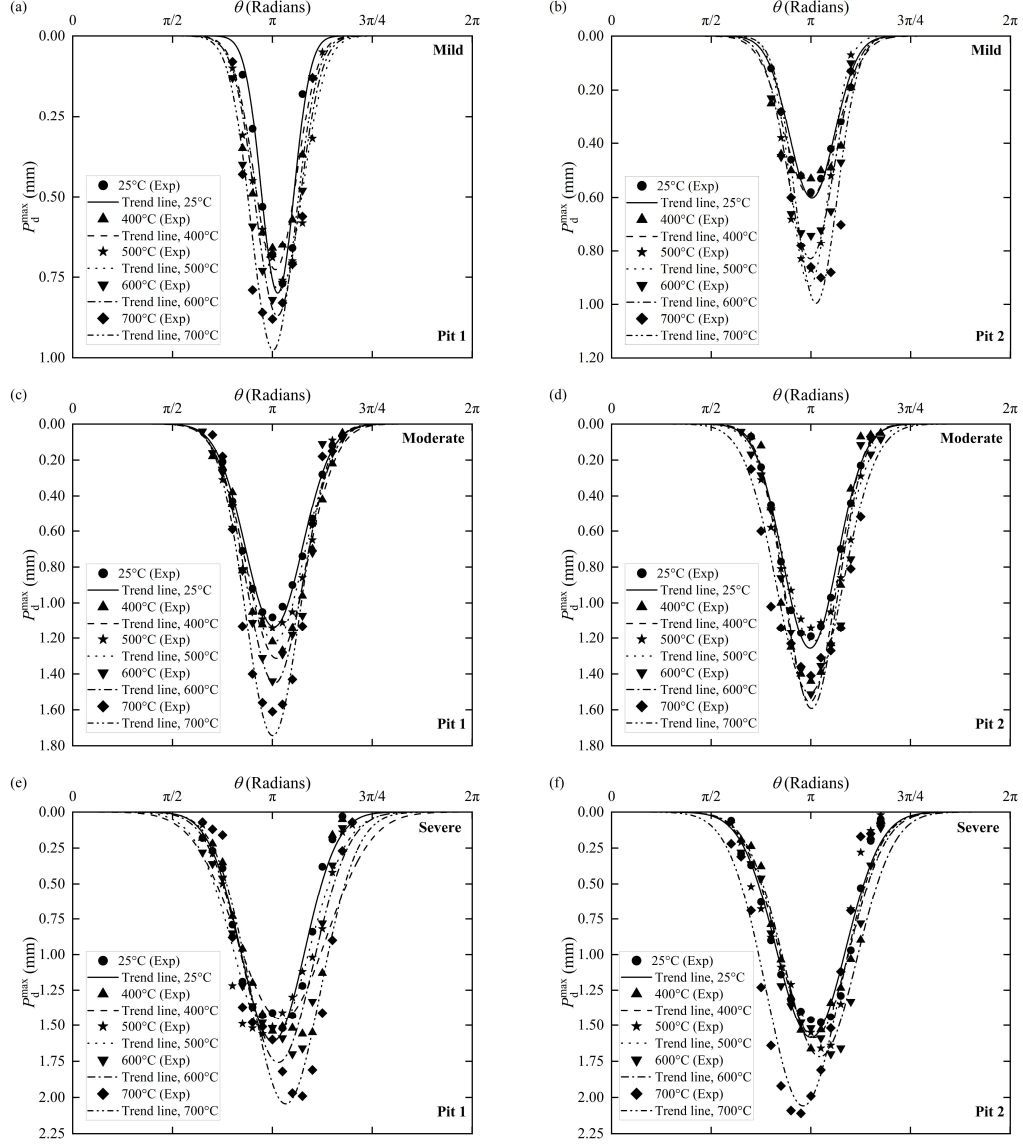


**Fig. 4.4** Experimental data and trends based on flipped Gaussian model.

The fitting parameters  $\psi_1$ ,  $\psi_2$ , and  $\psi_3$  signify different features of  $p_d$  distribution. That is,  $\psi_1$  correlates to the non-uniformity in  $p_d$ ,  $\psi_2$  to the spread of  $p_d$  along the circumference of the steel bar, and  $\psi_3$  to the polar angle at which  $p_d$  becomes equal to  $p_d^{\max}$ . Note that proposed Equation 4.10 is similar to that reported in (Muthulingam, 2019); but, differs in two

## Fatigue Behavior of Constructional Steels Subjected to Pitting Corrosion and Elevated Temperature

important aspects: (i) while Equation 4.10 is a three-parameter model, but the one presented in (Muthulingam, 2019) is a two-parameter model, for  $\psi_3$ , which accounts for the polar angle at which  $p_d$  equals  $p_d^{\max}$ , is introduced here and (ii) Equation 4.10 is proposed here for pitting corrosion, while the equation suggested in (Muthulingam, 2019) represents a type of non-uniform corrosion in which  $p_d$  is completely or partly distributed along the steel bar circumference. In this regard, model suggested in this study is new, according to the authors' best knowledge.

A comparison between the experimental values of  $p_d^{\max}$  along with trendlines based on the proposed flipped Gaussian equation is shown in Figs. 4.4 (a)–(f). Further, estimated values of curve fitting parameters are given in Table 4.3. As observed, minimum and maximum R-Square values obtained are 0.9310 and 0.9937, respectively, with 94% of samples having R-Square values greater than 0.95. This implies proposed flipped Gaussian model best represents the distribution of  $p_d$  along the bar circumference.

Table 4.3 shows that at a given temperature, increasing the corrosion level from mild to moderate increases  $\psi_1$  by a factor of upto 2.6, whereas moderate to severe increases  $\psi_1$  by a factor of upto 1.6 only. This suggests that degree of non-uniformity reduces as corrosion progresses. In addition, Table 4.3 indicates that for a given corrosion level, a rise in temperature from 25 °C to 700 °C causes  $\psi_1$  values to increase by a factor of 1.57, 1.44, and 1.39 for mild, moderate, and severe corrosion, respectively. Concerning  $\psi_2$ , for a given temperature, a rise in corrosion level from mild to severe leads to an increase in  $\psi_2$  by a factor of upto 1.73. Additionally, for a given corrosion level, increase in temperature from 25 °C to 700 °C results in an increase in  $\psi_2$  by a factor of 1.20. Based on these observations, it could be stated that temperature has a greater impact on the spread parameter  $\psi_2$  than corrosion levels. Further, it can also be observed from Table 4.3 that  $p_d^{\max}$  locations range between  $0.96\pi$  and  $1.08\pi$ , which are proximal to  $\pi$ .

**Table 4.2** Result summary of corrosion pit geometry from 3D laser scanning.

Sample	Temperature (°C)	Corrosion time (min)	Pit geometry from 3D laser scanning			
			$p_d^{\max}$ (mm)	$w$ (mm)	$l$ (mm)	$\eta_{\text{cri}}$ (%)
S1_P1	25	10	0.77	5.90	5.42	3.02
S1_P2	25	10	0.76	5.78	5.75	3.22
S2_P1	25	20	1.15	6.59	5.78	7.38
S2_P2	25	20	1.14	6.53	5.80	7.38
S3_P1	25	30	1.42	6.65	5.92	11.11
S3_P2	25	30	1.39	6.56	5.99	11.94
S4_P1	400	10	0.8	5.90	5.68	3.57
S4_P2	400	10	0.81	5.96	5.73	3.62
S5_P1	400	20	1.22	6.75	6.01	8.07
S5_P2	400	20	1.21	6.69	5.83	8.07
S6_P1	400	30	1.49	6.78	6.11	11.92
S6_P2	400	30	1.43	6.33	5.89	11.92
S7_P1	500	10	0.86	5.99	6.87	4.28
S7_P2	500	10	0.87	6.05	6.59	4.13
S8_P1	500	20	1.27	6.68	5.72	8.71
S8_P2	500	20	1.28	6.73	5.91	8.69
S9_P1	500	30	1.6	6.45	5.91	11.92
S9_P2	500	30	1.61	6.79	5.90	12.53
S10_P1	600	10	0.89	5.80	6.08	4.51
S10_P2	600	10	0.91	5.89	6.22	4.46
S11_P1	600	20	1.44	6.55	6.22	9.16
S11_P2	600	20	1.45	6.60	6.52	9.16
S12_P1	600	30	1.7	6.30	5.92	13.15
S12_P2	600	30	1.68	6.26	6.01	13.55
S13_P1	700	10	0.95	5.40	6.99	4.89
S13_P2	700	10	0.96	5.35	6.87	4.77
S14_P1	700	20	1.61	6.42	5.99	9.99
S14_P2	700	20	1.65	6.58	6.22	9.99
S15_P1	700	30	1.99	6.30	6.11	14.77
S15_P2	700	30	2.09	6.41	6.23	14.77

**Table 4.3** Curve fitting parameters of flipped Gaussian model.

Sample	$\psi_1$	$\psi_2$	$\psi_3$	R-square
S1_P1	0.515	0.257	3.224	0.973
S1_P2	0.540	0.358	3.155	0.974
S2_P1	1.283	0.452	3.163	0.987
S2_P2	1.350	0.429	3.128	0.994
S3_P1	2.028	0.502	3.146	0.981
S3_P2	2.176	0.548	3.143	0.981
S4_P1	0.603	0.331	3.186	0.957
S4_P2	0.615	0.412	3.137	0.940
S5_P1	1.558	0.473	3.204	0.989
S5_P2	1.582	0.405	3.126	0.984
S6_P1	2.180	0.701	3.412	0.931
S6_P2	2.217	0.558	3.193	0.968
S7_P1	0.724	0.365	3.250	0.974
S7_P2	0.701	0.300	3.121	0.975
S8_P1	1.429	0.467	3.169	0.976
S8_P2	1.474	0.467	3.148	0.976
S9_P1	2.388	0.590	3.125	0.960
S9_P2	2.335	0.560	3.202	0.967
S10_P1	0.751	0.344	3.218	0.958
S10_P2	0.757	0.364	3.132	0.961
S11_P1	1.628	0.448	3.174	0.985
S11_P2	1.657	0.408	3.152	0.976
S12_P1	2.433	0.552	3.232	0.970
S12_P2	2.476	0.575	3.285	0.962
S13_P1	0.842	0.344	3.152	0.960
S13_P2	0.823	0.330	3.221	0.952
S14_P1	1.862	0.426	3.145	0.985
S14_P2	1.953	0.517	3.122	0.964
S15_P1	2.843	0.555	3.351	0.956
S15_P2	3.015	0.584	3.020	0.968

#### 4.3.3 Surface topography:

The 3D surface topographies of all corrosion pits are evaluated employing a non-contact 3D optical profiler (Model: BRUKER Contour GT-K). Using white light interferometry, the

profiler evaluates surface geometry. The pits are scanned using a lens with a magnification of 5X, a back scan length of 25 mm and a laser beam of 1  $\mu\text{m}$  diameter. The samples are held in position on a moveable platform illuminated by a profiler light pointing into the pit. Corrosion pits are scanned three times each in longitudinal and transverse directions: once along the center and once on each side equidistant from the center. Figs. 4.5 (a–h) shows surface topography of corrosion pits measured by the 3D profiler for different combinations of corrosion duration and temperature.

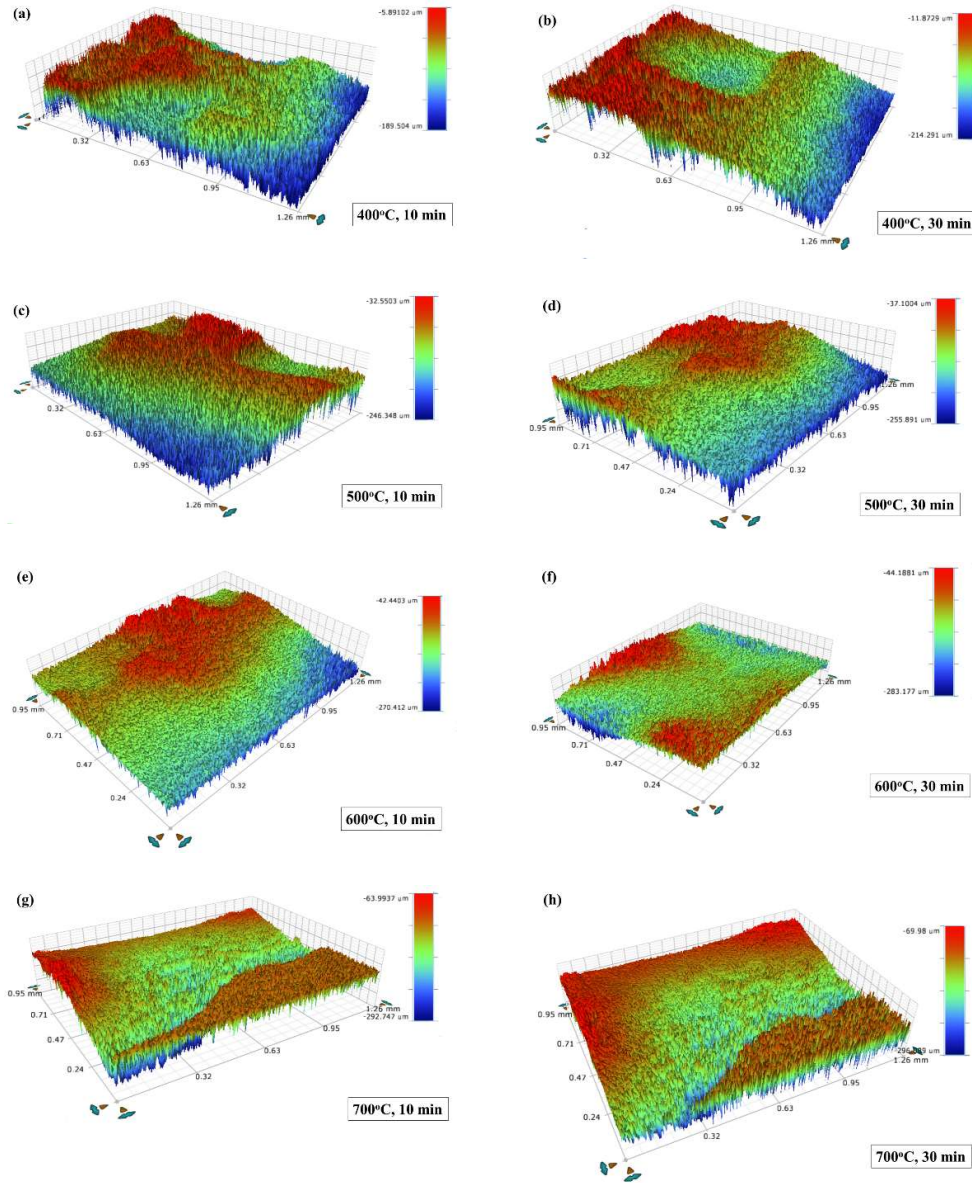


**Fig. 4.5** 3D surface topography of corroded pits.

The following observations can be made from the figures: (i) corroded surfaces have a random distribution of peaks (typically in red contrast) and valleys (typically in blue contrast),



## **Fatigue Behavior of Constructional Steels Subjected to Pitting Corrosion and Elevated Temperature**

thus exhibiting pitting characteristics, (ii) in general, the concentration of peak and valley change significantly with temperature and corrosion duration, and (iii) for a given temperature, pitting becomes deeper like needles and wider with increasing corrosion duration.

SEM and EDS is used to investigate microstructural features of corrosion pit surfaces. SEM images of corroded samples for different combination of corrosion levels and temperatures are shown in Figs. 4.6 (a)–(o). All images demonstrate electrochemical corrosion process and temperature exposure affects pit surface characteristics to varying degrees. Figs. 4.6(a)–(c) show SEM images from samples corroded at room temperature. It can be observed that increase in corrosion level from mild to severe leads to appearance of larger and deeper corrosion pits. Moreover, small microcracks and corrosion voids can be seen under mild exposure conditions, while globular clusters of corrosion products along with deeper pits appear as dark black spots on moderate and severe exposure samples.

A dense layer of corrosion products primarily composed of  $\alpha$ -FeOOH,  $\beta$ -FeOOH, and  $\gamma$ -FeOOH is formed. In most cases, corrosion pit originates from the metal's surface at multiples sites and propagates over time. Once pit formation reaches a stable state, it develops localized corrosion products at its mouth, which then spread and cover the pit completely (Melchers, 2020). After pit reaches a particular depth and enters the propagation phase, oxygen concentration cells begin to develop, with the pit's interior functioning as an anode and its exterior as a cathode. It is important to note that pit growth follows the autocatalytic process since it continues to grow itself (Wranglen, 1974). SEM images of pitting corroded and high temperature exposed samples are shown in Figs. 4.6 (d)–(o). Observe that corroded surface exhibits different surface characteristics. This could be due to non-homogeneous formation and growth of  $\text{Fe}_3\text{O}_4$  – and  $\text{Fe}_2\text{O}_3$  –based oxide scales during temperature exposure. A two-layer oxide scale consisting of  $\text{Fe}_3\text{O}_4$  (inner layer) and  $\text{Fe}_2\text{O}_3$  (outer layer) exists in the temperature range of 200 °C–570 °C. However, at temperatures above 570 °C, an additional oxide, namely wüstite ( $\text{FeO}$ ) exists due to increased oxidation of iron. Further, Figs. 4.6 (d)–(o) also show presence of larger voids at higher temperatures. This might be the result of iron ions diffusing outward. At elevated temperatures, outward diffusion of iron ions inhibits the formation of  $\text{FeO}$  and  $\text{Fe}_3\text{O}_4$  whereas the inward diffusion of iron ions inhibits the formation of  $\text{Fe}_2\text{O}_3$  (Chang & Wei, 1989; Krzyzanowski et al., 2010). Thus, the former process might result in the formation of larger voids as visible in SEM images.

SEM images Figs. 4.6(d)–(o) show the presence of microcracks that progressively widen with increasing temperature. The microcracks originate at the inter grain boundaries of  $\text{Fe}_3\text{O}_4$

and progresses into FeO grain boundaries. Further propagation of microcracks is assisted by the presence of voids and voids coalescence in FeO grains adjacent to Fe<sub>3</sub>O<sub>4</sub>/FeO interface.

Note that crack initiation and stress concentration at local scale may also be attributable to the volume increase caused by Fe<sub>3</sub>O<sub>4</sub> to Fe<sub>2</sub>O<sub>3</sub> transition (Kim, 2003). Further, as shown in Figs. 4.6(d)–(o) also show the presence of slit shaped micropores. This could be attributed to the transformation reactions occurring in the corrosion products at elevated temperatures. Thermal decomposition of  $\beta$ -FeOOH produces slit-shaped micropores with average pore sizes ranging 1.1 and 1.3 nm between 200 °C and 400 °C, but at 500 °C produces irregular macropores with average pore sizes more than 15 nm. Additionally, thermal decomposition causes structural changes in  $\gamma$ -FeOOH, which also leads to the formation of slit shaped micropores having a size 0.9 nm width (Naono et al., 1982; Naono & Nakai, 1989).

The size and surface area of iron oxides have a significant impact on pit surface conditions. Figs. 4.6 (d–o)) show the presence of carbide particles of varying size and shape. In general, images show small carbide particles that are widely spread and occupy the space between larger carbide particles. Large carbide particles, however, settle at the steel sub-surface because they are unable to fill the valleys in the pit surface. Large carbide particles are equivalent to surface defects and thus serve as potential sites for fatigue crack nucleation and propagation (Korade et al., 2020). Further, the temperature also influences the growth rate of iron oxides. The slower and faster growth rates of iron oxides, respectively, lead to the formation of poorly ordered crystals with a large surface area and well-formed crystals with a smaller surface area (Cornell & Schwertmann, 2003).

The EDS spectrums of corrosion pits obtained for different combinations of corrosion level and high temperature are depicted in Figs. 4.7 (a–c). As noted, the concentrations of carbon (C), oxygen (O), and iron (Fe) exhibit significant changes with respect to both parameters. For a given corrosion level, when the temperature rises from 400 °C to 700 °C, C and O increase by a factor of upto 10.7 and 2.9, respectively, while Fe decreases by a factor of upto 5.2. Further, for a given temperature, when the corrosion level changes from mild to severe, C and O increase by a factor of upto 2.1 and 1.6, respectively, while Fe decreases by a factor of upto 2.8. Thus, in comparison to the change in corrosion levels, exposure to high temperatures has a considerable effect on the concentrations of C, O, and Fe. It can be observed oxidation of C is lower than the oxidation of Fe. This is due to carbon's insolubility in adherent and coherent scale forms. The carbon ejected by quicker iron oxidation must either remain at the scale-steel interface or permeate the steel, thus enriching the surface layer of the steel substrate (Plumensi et al., 1969).

## Fatigue Behavior of Constructional Steels Subjected to Pitting Corrosion and Elevated Temperature

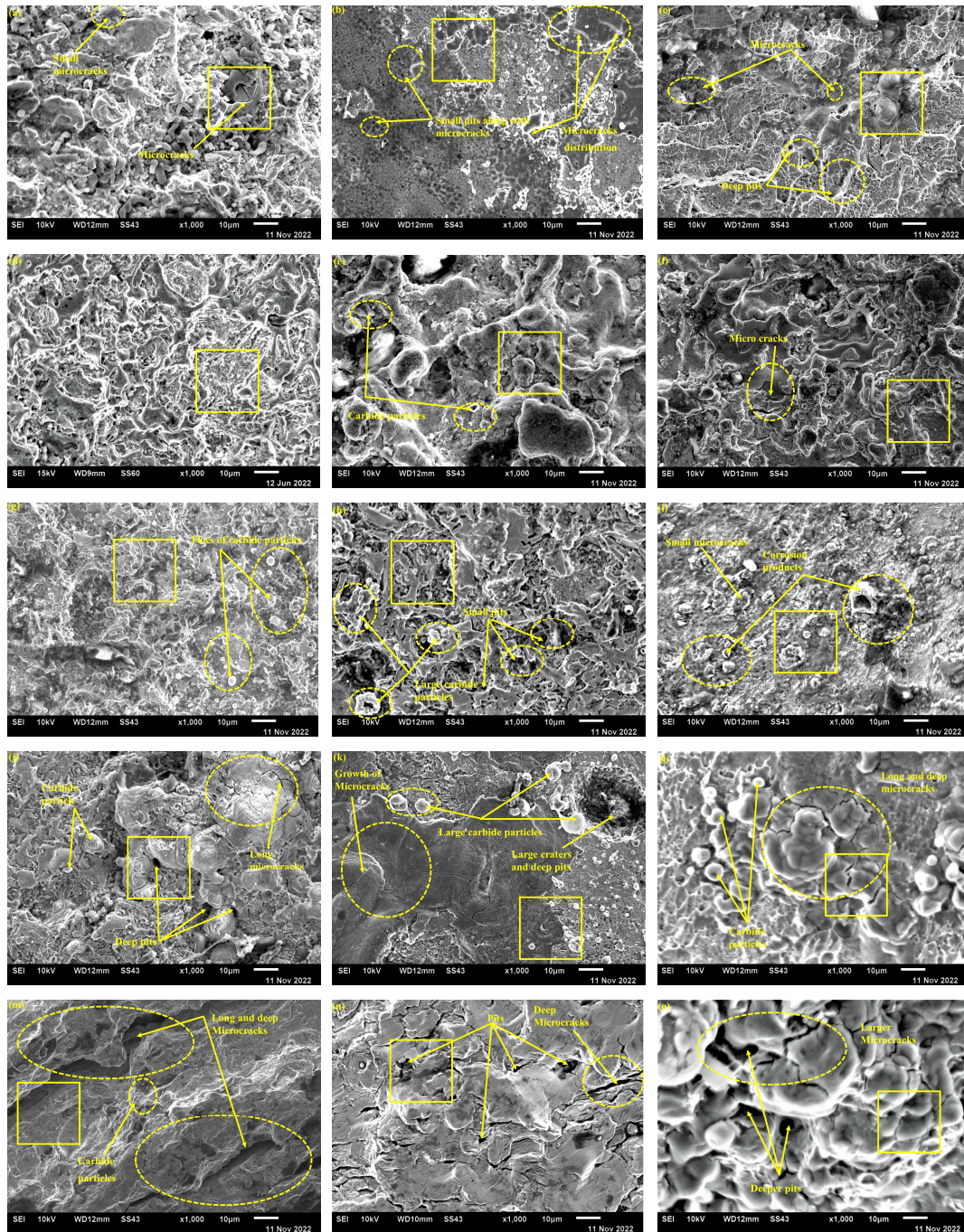


**Fig. 4.6** SEM images of pitting corroded samples: (a) S1\_P1; (b) S4\_P1; (c) S7\_P1; (d) S10\_P1; (e) S13\_P1; (f) S2\_P1; (g) S5\_P1; (h) S8\_P1; (i) S11\_P1; (j) S14\_P1; (k) S3\_P1; (l) S6\_P1; (m) S9\_P1; (n) S12\_P1; and (o) S15\_P1.

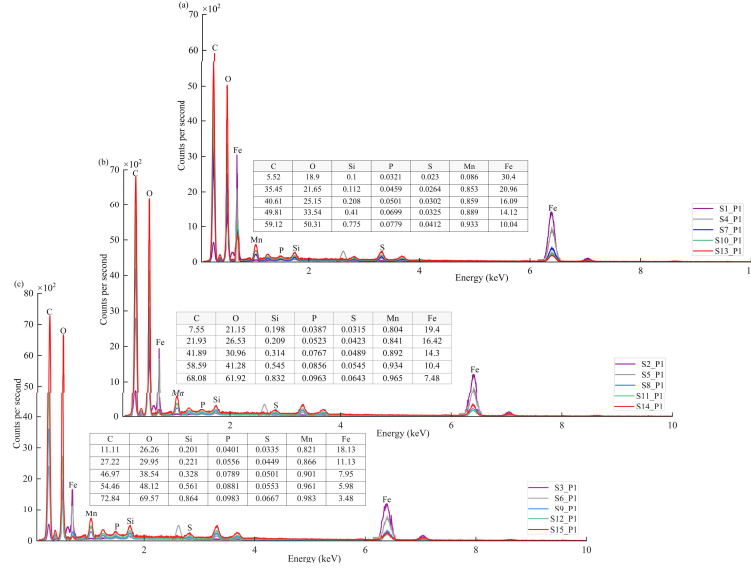


Fig. 4.7 EDS spectrum of corroded pits: (a) 10 min; (b) 20 min; and (c) 30 min.

#### 4.4 Prediction models

The pit surface topographic feature parameters are independently evaluated from 3D optical profiler data and their average values are summarized in Table 4.4. Note that each value in the Table 4.4 is estimated from the average of six 3D profile scans performed on each corrosion pit surface. In this section, prediction models for surface topographic parameters, namely  $R_a$ ,  $R_t$ ,  $R_{10z}$ , and  $R_{sm}$  are developed. In addition, prediction model for  $F_s$  and  $a_0$  are also developed. In this study, multiple linear regression (MLR) method is employed for developing the prediction models.

MLR is a simplest and most widely used statistical technique to relate a set of two or more variables. The relationship between two or more independent/explanatory variables and dependent/response variable can be modelled by fitting a linear equation of the following form to the data (Andrews, 1974):

$$Y = \{X\}^T \{\beta\} + \sigma\{e\} = \beta_0 + x_1\beta_1 + x_2\beta_2 + \dots + x_k\beta_k + \sigma\{e\} \quad (4.11)$$

where  $Y$  is the dependent variable,  $\{X\}^T = (1, x_1, x_2, \dots, x_k)$  represents a column vector of explanatory variables,  $\{\beta\} = (\beta_0, \beta_1, \dots, \beta_k)$  represents a row vector of unknown regression coefficients,  $\sigma$  is an unknown scale parameter,  $\{e\}$  represents the residual and  $k$  denotes the number of explanatory variables. Amongst others, MLR approach is based on three key assumptions: (i) normal distribution of the residuals, (ii) homoscedasticity, and (iii) absence of autocorrelation between the residuals.

**Table 4.4** Values of surface topographic feature parameters.

Sample	Average values of surface topographic feature parameters				
	$R_a$	$R_t$	$R_{10z}$	$R_{sm}$	$F_s$
	( $\mu\text{m}$ )	( $\mu\text{m}$ )	( $\mu\text{m}$ )	( $\mu\text{m}$ )	( $\mu\text{m}$ )
S1_P1	16.28	94.72	84.40	24.34	18.27
S1_P2	16.38	94.38	84.75	24.04	18.31
S2_P1	19.39	109.47	95.38	37.62	22.25
S2_P2	19.53	109.54	96.17	37.50	22.43
S3_P1	24.80	126.41	111.64	49.52	28.08
S3_P2	24.82	126.35	112.10	48.97	28.09
S4_P1	16.88	98.62	89.53	25.57	18.60
S4_P2	17.02	98.83	89.78	25.44	18.74
S5_P1	19.92	112.03	98.37	39.41	22.69
S5_P2	19.96	112.88	98.61	39.55	22.84
S6_P1	25.61	129.97	117.11	54.33	28.42
S6_P2	25.68	130.14	117.09	54.41	28.54
S7_P1	20.15	118.25	106.21	27.31	22.44
S7_P2	20.14	117.39	108.58	27.54	21.77
S8_P1	23.77	137.36	121.91	41.60	26.78
S8_P2	24.15	136.92	127.67	41.54	25.98
S9_P1	29.79	168.10	140.79	59.36	35.57
S9_P2	30.05	168.66	142.11	58.99	35.67
S10_P1	24.21	142.17	130.39	30.32	26.40
S10_P2	24.03	141.93	128.07	30.42	26.63
S11_P1	28.72	167.22	145.27	45.67	33.02
S11_P2	28.28	165.82	142.27	45.44	32.96
S12_P1	35.26	192.31	168.75	64.03	40.18
S12_P2	35.11	191.87	170.83	64.17	39.44
S13_P1	28.12	165.42	147.17	33.87	31.61
S13_P2	28.02	164.27	147.24	34.06	31.27
S14_P1	33.41	184.52	167.02	49.26	36.91
S14_P2	33.70	185.77	167.93	49.23	37.28
S15_P1	45.27	211.23	201.18	69.82	47.53
S15_P2	45.34	210.88	199.23	69.91	47.99

A violation of these assumptions, particularly homoscedasticity, means prediction model could become inefficient, rendering the hypothesis testing procedure dubious. The presence of the heteroscedasticity indicates variance of the residual conditional on the explanatory variables is not a constant. One approach to removing heteroscedasticity in the residual is to transform the dependent and/or explanatory variables through algebraic transformations (Gujarati, 2022). Further, MLR method estimates regression coefficients of statistical significance through backward elimination based on confidence interval bounds, backward elimination based on the correlation coefficient, forward selection based on the sum of square errors, or combinations of explanatory variables (Pires et al., 2008).

In the current study,  $R_a$ ,  $R_t$ ,  $R_{10Z}$ , and  $R_{sm}$ ,  $F_s$ , and  $a_0$  are dependent variables in the prediction models. The three explanatory variables considered here include  $p_d^{\max}/w$ ,  $\eta_{cr}$ , and  $T$ ,  $\eta_{cr}$  is a pit severity parameter represented by aspect ratio of the pit,  $\eta_{cr}$  is a corrosion severity parameter represented by critical cross-sectional loss in the steel bar, and  $T$  accounts for the effect of temperature. It is understood from the preceding sections that the surface topographic features parameters are significantly impacted by the chosen three explanatory variables. MLR evaluates regression coefficients corresponding to each explanatory variable by considering the experimentally measured values given in Table 4.4 as sampling data. To evaluate the accuracy of the developed prediction models, the commonly used metrics, namely mean absolute error (MAE), mean squared error (MSE), root mean square error (RMSE), mean absolute percentage error (MAPE), R-Square ( $R^2$ ), and adjusted R-Square ( $R^2$  Adj.) are estimated.

#### 4.4.1 Model development of $R_a$ :

The average values of  $R_a$  for all samples are given in Table 4.4. It can be noted that, for a given temperature, rise in corrosion level from mild to severe results in a upto 1.6-fold increases in  $R_a$ . Further, for a given corrosion level, compared with the room temperature, increase in temperature from 25 °C to 700 °C results in a upto 1.8-fold increases in  $R_a$ . Particularly at 700 °C, the difference in  $R_a$  is very significant (by upto 83%). With regard to surface topography, increase in  $R_a$  with corrosion level meant rise in hills and dales on the pit surface.

The effect of corrosion level and temperature on  $p_d^{\max}$  has been discussed in Section 4.2.2. Thus, in a first approximation, a prediction model of the following form is considered:



$$R_a = \xi'_1 + \xi'_2 \eta_{\text{cri}} + \xi'_3 \left( p_d^{\text{max}} / w \right) + \xi'_4 T \quad (4.12)$$

where  $\xi'_1$ ,  $\xi'_2$ ,  $\xi'_3$ , and  $\xi'_4$  represent regression coefficients. By performing MLR analysis, the regression coefficients are estimated as  $-7.029$ ,  $-1.197$ ,  $205.4$ , and  $4.272 \times 10^{-3}$ , respectively.

Note that MLR analysis is conducted on the entire data set (=180 nos.) and not on the average values. However, for certain combinations of explanatory variables (e.g.,  $p_d^{\text{max}}/w = 0.1$  and  $\eta_{\text{cri}} = 15\%$ ) Equation 4.12 could result in non-positive values of  $R_a$ , which is unacceptable since it is always positive. Thus, Equation 4.12 must be modified and the simple approach is to perform algebraic transformation of variables. From many such transformations performed to arrive at a suitable equation, model of the following form is proposed for  $R_a$  prediction:

$$\sqrt{R_a} = \xi_1 + \xi_2 \eta_{\text{cri}} + \xi_3 \left( \sqrt{p_d^{\text{max}} / w} \right) + \xi_4 T \quad (4.13)$$

where  $\xi_1$ ,  $\xi_2$ ,  $\xi_3$ , and  $\xi_4$  are regression coefficients of the modified equation. Note that Equation 4.13 introduces a square root algebraic transformation in the variables  $R_a$  and  $p_d^{\text{max}}/w$  of Equation 4.12. The regression performed on the data using Equation 4.13 resulted in the coefficient values of  $\xi_1 = -1.958$ ,  $\xi_2 = -0.11$ ,  $\xi_3 = 17.369$ , and  $\xi_4 = 4.97 \times 10^{-4}$ . Comparison between the experimental values of  $\sqrt{R_a}$  and that estimated by the model (i.e., Equation 4.13) is depicted in Fig. 4.8.

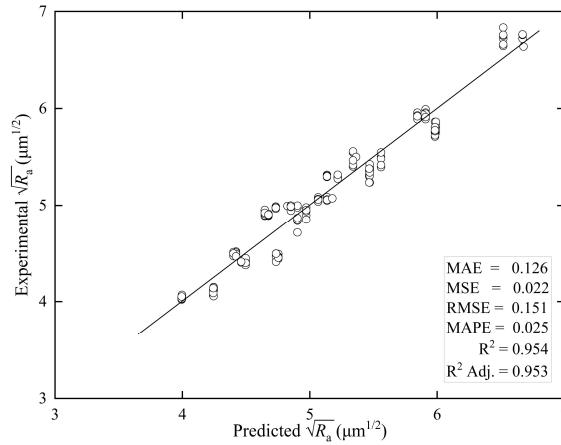


**Fig. 4.8** Comparison between experimental and predicted values of  $\sqrt{R_a}$ .

As seen, the adjusted  $R^2$  obtained is 0.953, which indicates that, when taken as a set  $\sqrt{p_d^{\text{max}}/w}$ ,  $\eta_{\text{cri}}$  and  $T$  account for 95.3% of the variance in  $\sqrt{R_a}$ . Thus, values predicted by the developed model correlate well with the experimental values. From regression, Durbin–Watson statistic measure is estimated as 2.047, which indicates the absence of first-order autocorrelation

between the residuals thus confirming the appropriateness of the developed prediction model. Further, Table 4.5 lists Pearson correlations between the dependent and explanatory variables. It is observed that dependent and explanatory variables have positive correlations.  $\sqrt{p_d^{\max}/w}$  has the highest correlation coefficient (0.926) with  $\sqrt{R_a}$  and is therefore the most statistically significant explanatory variable, followed by  $\eta_{\text{cri}}$  (0.778) and  $T$  (0.654). This meant, as compared to  $\eta_{\text{cri}}$  and  $T$ , changes in  $\sqrt{p_d^{\max}/w}$  have a more significant effect on  $\sqrt{R_a}$ . Strong correlations among explanatory variables can also be observed in Table 4.5. For instance, correlation between  $\eta_{\text{cri}}$  and  $\sqrt{p_d^{\max}/w}$  (0.943) is comparable with that exists between  $\sqrt{R_a}$  and  $\sqrt{p_d^{\max}/w}$  (0.944). Further, the weakest correlation is observed between  $\eta_{\text{cri}}$  and  $T$  (0.215).

**Table 4.5** Pearson correlation matrix for  $R_a$ .

Pearson Correlation	$\sqrt{R_a}$	$\eta_{\text{cri}}$	$\sqrt{p_d^{\max}/w}$	$T$
$\sqrt{R_a}$	1.00	0.778	0.926	0.654
$\eta_{\text{cri}}$	0.778	1.00	0.943	0.215
$\sqrt{p_d^{\max}/w}$	0.926	0.943	1.00	0.439
$T$	0.654	0.215	0.439	1.00

The developed regression model is based on the assumption that residuals are normally distributed and the same needs to be validated. This validation can be verified from the histogram distribution and probability–probability plot of regression standardized residual. These plots are depicted in Fig. 4.9 (a–c). The normal distribution of the residuals is corroborated by the absence of outliers in the histogram of the dependent variable (Fig. 4.9 (a)), which has a bell-shaped distribution with a zero-centered centre in a range between –3.0 and 3.0. The normality assumption can further be effectively verified with the normal probability–probability plot shown in Fig. 4.9 (b). It can be seen data are very closely distributed with the straight line, which indicates assumption of normality is satisfied. Yet another assumption in MLR approach is homoscedasticity, which stipulates constant variance between experimental and predicted values of  $\sqrt{R_a}$ . This assumption also needs to be verified. A scatter plot between standardized regression residuals and the standardized regression predicted values of the dependent variable  $\sqrt{R_a}$  is shown in Fig. 4.9 (c). It can be observed that variation around the regression line is almost same across  $R_a$  values; it neither increases nor decreases as  $\sqrt{R_a}$  varies, thus satisfying the homoscedasticity assumption. Furthermore,



the Breusch–Pagan estimate obtained 0.2685, which is higher than the significant value of 0.05, thereby accepting the null hypothesis of no heteroscedasticity (Breusch & Pagan, 1979). Thus, since the proposed model satisfies the assumptions of MLR method, it can be said to be highly capable of providing confidence estimates of  $\sqrt{R_a}$ .

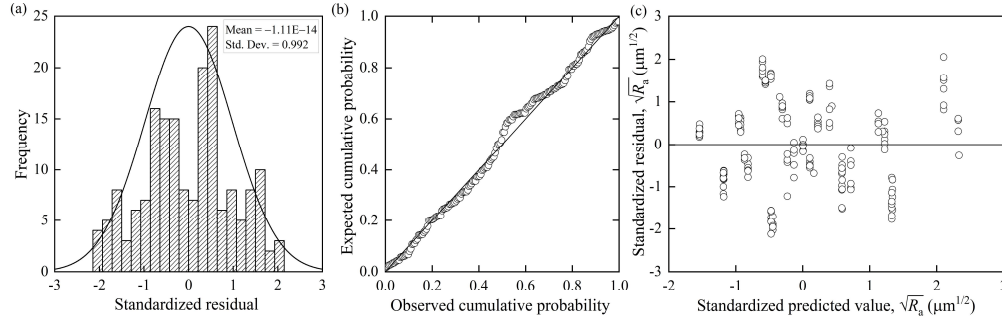


**Fig. 4.9** Residual plots for  $\sqrt{R_a}$  model: (a) histogram; (b) normal probability–probability; (c) standardized residual–predicted value.

To examine the impact of regression coefficients  $\xi_1$ ,  $\xi_2$ ,  $\xi_3$ , and  $\xi_4$  on the proposed predictive model for  $\sqrt{R_a}$ , a sensitivity analysis is performed by considering regression coefficients as sensitivity parameters. Sensitivity analysis is performed by comparing  $\sqrt{R_a}$  estimated by the actual values of the parameters to that estimated by perturbing each parameter by  $\pm 5\%$ . The outcome of the sensitivity study is illustrated in Fig. 4.10. Estimates of  $\sqrt{R_a}$  ranged between 1.4% and 2.4% when  $\xi_1$  was perturbed by  $+5\%$ , and between  $-1.4\%$  and  $-2.4\%$  when  $\xi_1$  was perturbed by  $-5\%$ . Further,  $\sqrt{R_a}$  values increased and decreased by 0.4% to 1.4%, respectively, with  $\pm 5\%$   $\xi_2$  perturbations. Furthermore,  $\pm 5\%$  changes in  $\xi_3$  resulted in  $\sqrt{R_a}$  deviations of  $\pm 7.0\%$  to  $8.4\%$ . Finally,  $\pm 5\%$  perturbations in  $\xi_4$  lead to  $\pm 0.01\%$  to  $0.3\%$  changes in  $\sqrt{R_a}$ . The sensitivity analysis shows that  $\sqrt{R_a}$  is relatively more affected by changes in  $\xi_3$ , the one associated with  $\sqrt{p_d^{\max}/w}$ , than other parameters. Nevertheless, it can be concluded that the margin of error is well within the acceptable limits.

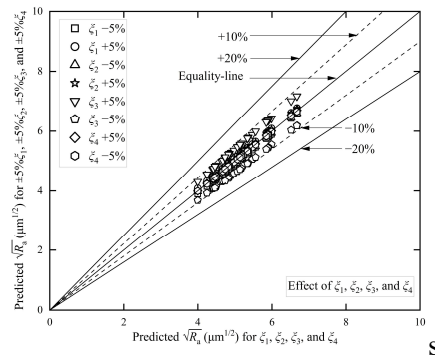


**Fig. 4.10** Sensitivity analysis for  $\sqrt{R_a}$  model.

#### 4.4.2 Model development of $R_t$ :

The variations in average values of  $R_t$  with corrosion level and temperature are given in Table 4.4. As observed, for a given temperature, an increase in corrosion level from mild to severe results in an increase in  $R_t$  of upto 43%. Further, for a given corrosion level, an increase in temperature results in an increase in  $R_t$  of upto 69%. These trends indicate a significant change in the surface topography of pits caused first by the corrosion process itself followed by exposure to high temperatures. Substantial changes in  $R_t$  may be attributed to pit growth occurring due to considerable differences in constantly changing surfaces between two differently reacting surface regions (Burstein et al., 2004). In addition, the linear oxidation kinetics change the surface topography significantly when exposed to high temperatures (Omidbakhsh et al., 2013).

A MLR prediction model for  $R_t$  of the following form is investigated as a first approximation:

$$R_t = \chi'_1 + \chi'_2 \eta_{\text{cri}} + \chi'_3 \left( p_d^{\text{max}} / w \right) + \chi'_4 T \quad (4.14)$$

where  $\chi'_1$ ,  $\chi'_2$ ,  $\chi'_3$ , and  $\chi'_4$  represent the regression coefficients. Though the model performed well with good statistical parameters, resulted in a significant value of 0.00 which is less than 0.05 thereby rejecting the null hypothesis of no heteroscedasticity. In order to increase the confidence estimates of the prediction model and to remove heteroscedasticity, algebraic transformations of dependent and explanatory variables are performed. As an outcome of the transformation operations, the following prediction model for  $R_t$  is proposed:

$$\sqrt{R_t} = \chi_1 + \chi_2 \eta_{\text{cri}} + \chi_3 \left( p_d^{\text{max}} / w \right) + \chi_4 T \quad (4.15)$$

where  $\chi_1$ ,  $\chi_2$ ,  $\chi_3$ , and  $\chi_4$  are regression coefficients. Note that  $R_t$  in Equation 4.14 is transformed to  $\sqrt{R_t}$ . From regression, the values of respective regression coefficients are estimated as 6.287, -0.1516, 29.277, and  $2.25 \times 10^{-3}$ . Comparison between the experimental and predicted values of  $\sqrt{R_t}$  is shown in Fig. 4.11. The regression analysis yielded an adjusted R-Square value of 0.919, signifying that, when taken collectively,  $p_d^{\text{max}} / w$ ,  $\eta_{\text{cri}}$  and  $T$  account for 92% of variance in  $\sqrt{R_t}$ . Hence, the values predicted by the developed model correspond well with the experimental values. Further, the regression yielded a Durbin-Watson statistical measure of 2.056, indicating absence of first-order autocorrelation between the residuals. The Pearson correlations between the dependent and explanatory

## Fatigue Behavior of Constructional Steels Subjected to Pitting Corrosion and Elevated Temperature

variables are given in Table 4.6. Positive correlations are observed between the explanatory and dependent variables.  $p_d^{\max}/w$  has the strongest correlation (0.858) with  $\sqrt{R_t}$  making it the most statistically significant explanatory variable, followed by  $\eta_{\text{cri}}$  (0.678) and  $T$  (0.752). This implies, relative to  $\eta_{\text{cri}}$  and  $T$ , changes in  $p_d^{\max}/w$  have a greater impact on  $\sqrt{R_t}$  values. In addition, Table 4.6 also reveals the presence of correlations between explanatory variables. Strong correlations among explanatory variables can also be observed from Table 4.6. For example, correlation between  $\eta_{\text{cri}}$  and  $p_d^{\max}/w$  (0.933) is even higher than that between  $\sqrt{R_t}$  and  $p_d^{\max}/w$  (0.858). Moreover, the correlation among  $\eta_{\text{cri}}$  and  $T$  is the least significant (0.215).

The three key assumptions of MLR need to be validated with regard to the developed prediction model  $\sqrt{R_t}$ . The frequency distribution Fig. 4.12 (a) of the residual follows normal distribution having zero mean and unit standard deviation. Further, observed and cumulative probability distributions Fig. 4.12 (b) of the residual are closely aligned with the 1:1 straight line. Therefore, it is stated that normality assumption of the standard residual is satisfied. Further, the hypothesis representing the absence of heteroscedasticity is also satisfied since the estimated Breusch–Pagan value of 0.1225 is greater than the significant value of 0.05. In addition, it can be seen from the scatter plot between regression residuals and regression predicted values (Fig. 4.12 (c)) that the residuals distributions are random and do not follow any trend. Thus, the assumption of heteroscedasticity is also fulfilled. As a result, it can be stated proposed model is capable to provide confidence estimates of  $\sqrt{R_t}$  as it satisfies the assumptions of MLR method.

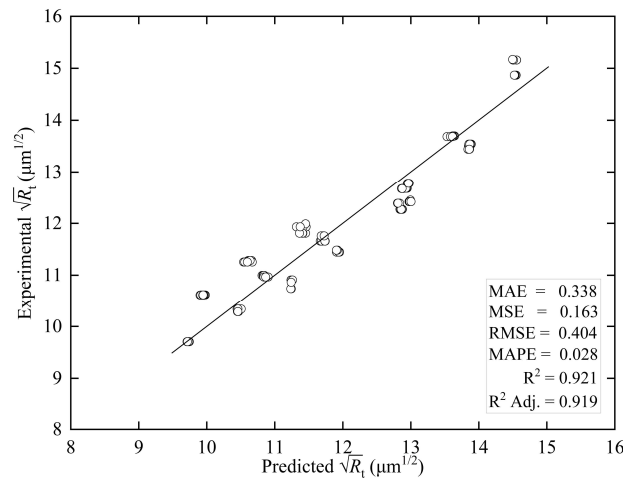


**Fig. 4.11** Comparison between experimental and predicted values of  $\sqrt{R_t}$ .

**Table 4.6** Pearson correlation matrix for  $R_t$ .

Pearson Correlation	$\sqrt{R_t}$	$\eta_{\text{cri}}$	$p_d^{\text{max}}/w$	$T$
$\sqrt{R_t}$	1.00	0.678	0.858	0.752
$\eta_{\text{cri}}$	0.678	1.00	0.933	0.215
$p_d^{\text{max}}/w$	0.858	0.933	1.00	0.443
$T$	0.752	0.215	0.443	1.00

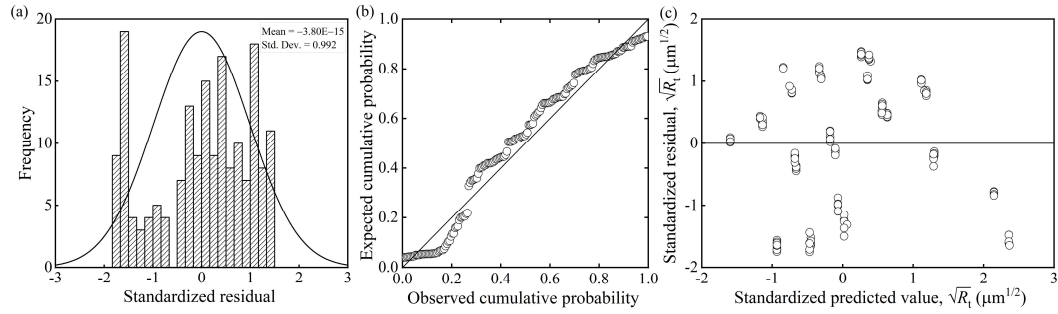


**Fig. 4.12** Residual plots for  $\sqrt{R_t}$  model: (a) histogram; (b) normal probability–probability; (c) standardized residual–predicted value.

Estimating the sensitivities of the regression coefficients, namely  $\chi_1$ ,  $\chi_2$ ,  $\chi_3$ , and  $\chi_4$  on  $\sqrt{R_t}$  is essential to understand the relative significance of the four coefficients influencing  $\sqrt{R_t}$ . The sensitivity estimates are obtained by perturbing each regression coefficient individually by  $\pm 5\%$  and assessing the effects on  $\sqrt{R_t}$ . Fig. 4.13 depicts the comparison between the predicted values of  $\sqrt{R_t}$  with those obtained from perturbing the regression coefficients by  $\pm 5\%$ .  $\sqrt{R_t}$  changed by  $\pm 2.0\%$  to  $\pm 3.2\%$  with  $\pm 5\%$  changes in  $\chi_1$ , while  $\sqrt{R_t}$  changed by  $\mp 0.2\%$  to  $\mp 0.8\%$  with  $\pm 5\%$  changes in  $\chi_2$ . Further,  $\pm 5\%$  perturbation in  $\chi_3$  led to  $\pm 1.7\%$  to  $3.1\%$  changes in  $\sqrt{R_t}$ , whereas  $\pm 5\%$  perturbation in  $\chi_4$  leads to  $\pm 0.1\%$  to  $0.6\%$  changes in  $\sqrt{R_t}$ . Amongst the regression coefficients,  $\chi_1$  that is associated with  $\eta_{\text{cri}}$  is found to be the most sensitive albeit not being significant. Nevertheless, margin of error is thus well within the acceptable range.

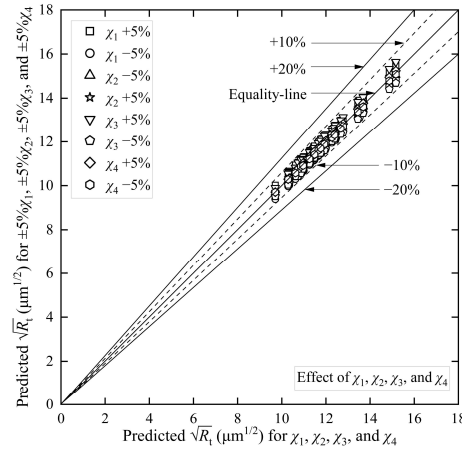


**Fig. 4.13** Sensitivity analysis for  $\sqrt{R_t}$  model.

#### 4.4.3 Model development of $R_{10Z}$ :

The effects of varying corrosion levels and temperature on  $R_{10Z}$  can be observed from Table 4.4. For a given corrosion level, compared to samples exposed at room temperature, an increase in temperature from 400 °C to 700 °C caused a 79% increase in  $R_{10Z}$  values. In addition, at a given temperature, an increase in corrosion severity from mild to severe led to a 32% increase in  $R_{10Z}$  values. Note that an increase in  $R_{10Z}$  reflects the propagation of corrosion pit growth.

As a first approximation, an MLR prediction model for  $R_{10Z}$  of the following form is considered:

$$R_{10Z} = \varepsilon'_1 + \varepsilon'_2 \eta_{\text{cri}} + \varepsilon'_3 \left( p_d^{\text{max}} / w \right) + \varepsilon'_4 T \quad (4.16)$$

where  $\varepsilon'_1$ ,  $\varepsilon'_2$ ,  $\varepsilon'_3$ , and  $\varepsilon'_4$  represent regression coefficients. The regression was effective, yielding an adjusted R-Square value of 0.967 and satisfying the normality condition of the residuals. However, regression resulted in a significance value of 0.00 (i.e., <0.05), failing the homoscedasticity assumption. To fulfill this assumption, which would lead to high confidence estimates of  $R_{10Z}$ , algebraic transformations are performed. Based on many transformation attempts, a predictive model for  $R_{10Z}$  is proposed of the following form:

$$R_{10Z} = \varepsilon_1 + \varepsilon_2 \eta_{\text{cri}} + \varepsilon_3 \left( p_d^{\text{max}} / w \right)^2 + \varepsilon_4 T \quad (4.17)$$

where  $\varepsilon_1$ ,  $\varepsilon_2$ ,  $\varepsilon_3$ , and  $\varepsilon_4$  are regression coefficients. From the regression analysis,  $\varepsilon_1$ ,  $\varepsilon_2$ ,  $\varepsilon_3$ , and  $\varepsilon_4$  are obtained as 66.953, -2.313, 1316.05, and 0.0542, respectively. Comparison between the experimental values of  $R_{10Z}$  and that estimated by the model (i.e., Equation 4.17)

is depicted in Fig. 4.14. In addition, the regression resulted in an adjusted R–Square value of 0.930, meaning explanatory variables (i.e.,  $(p_d^{\max}/w)^2$ ,  $\eta_{\text{cri}}$ , and  $T$ ) account for 93% of variance in  $R_{10Z}$ . Further, the obtained Durbin–Watson value of 2.044 reflects the absence of first–order autocorrelation between the residuals. The correlations (Pearson) amongst the predictive model variables are given in Table 4.7. Note that dependent and explanatory variables have positive correlations between them. The strongest correlation (0.869) is observed between  $R_{10Z}$  and  $(p_d^{\max}/w)^2$ , while the weakest (0.655) is observed between  $R_{10Z}$  and  $\eta_{\text{cri}}$ . Moreover, strong correlations are also observed amongst the explanatory variables. Notably, correlation between  $\eta_{\text{cri}}$  and  $(p_d^{\max}/w)^2$  is significant (0.898) amongst all the variables.

**Table 4.7** Pearson correlation matrix for  $R_{10Z}$ .

Pearson Correlation	$R_{10Z}$	$\eta_{\text{cri}}$	$(p_d^{\max}/w)^2$	$T$
$R_{10Z}$	1.00	0.655	0.869	0.752
$\eta_{\text{cri}}$	0.655	1.00	0.898	0.215
$(p_d^{\max}/w)^2$	0.869	0.898	1.00	0.448
$T$	0.752	0.215	0.448	1.00

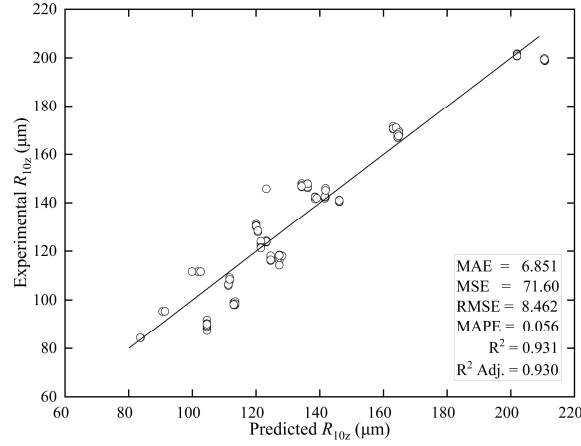


**Fig. 4.14** Comparison between experimental and predicted values of  $R_{10Z}$ .

In order to have higher confidence in  $R_{10Z}$  estimates, the prediction model must meet three main assumptions, which were listed in the beginning of Section 4.4. In this regard, Fig. 4.15 (a) shows distribution frequency of the residuals. It can be observed that histogram follows normal distribution (zero mean and unit standard deviation), with zero positioned at the center of curve ranging between  $-3$  and  $3$ , with insignificant outliers. Further, probability–probability scatter plot Fig. 4.15 (b) shows residuals are closely aligned with the

## Fatigue Behavior of Constructional Steels Subjected to Pitting Corrosion and Elevated Temperature

1:1 line. Both of these observations suggest residuals satisfy normality distribution. Moreover, scatterplot shown in Fig. 4.15 (c) depicts the relation between standardized predicted value and residual. It can be inferred distribution is random and does not follow any specific increasing/decreasing trend. Further, regression resulted in a Breusch–Pagan value of 0.0732, which is greater than the significance level of 0.05, indicating the absence of heteroscedasticity. Thus, the proposed prediction model satisfies the assumptions of regression.

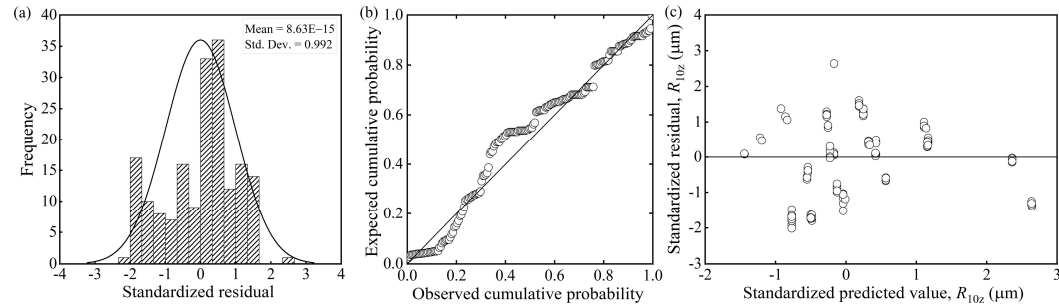


**Fig. 4.15** Residual plots for  $R_{10Z}$  model: (a) histogram; (b) normal probability–probability; (c) standardized residual–predicted value.

Assessing the sensitivities of the prediction model's regression coefficients can assist in determining the relative significance of the coefficients affecting the dependent variable. This evaluation is performed by considering the regression coefficients (i.e.,  $\varepsilon_1$ ,  $\varepsilon_2$ ,  $\varepsilon_3$ , and  $\varepsilon_4$ ) as sensitivity parameters and perturbing each of them and evaluating the value of the dependent variable  $R_{10Z}$ . The outcome of the sensitivity study is illustrated in (Fig. 4.16). From the sensitivity study, it is observed that  $\pm 5\%$  perturbations in  $\varepsilon_1$  result in  $\pm 1.6\%$  to  $4.0\%$  changes in  $R_{10Z}$ . Further,  $\pm 5\%$  perturbations of  $\varepsilon_2$  result in  $\mp 0.4\%$  to  $1.4\%$  changes in  $R_{10Z}$  while the same perturbations of  $\varepsilon_3$  result in  $\pm 1.1\%$  to  $3.3\%$  changes in  $R_{10Z}$ . Furthermore,  $\pm 5\%$  perturbations in  $\varepsilon_4$  result in  $\pm 0.06\%$  to  $1.4\%$  changes in  $R_{10Z}$ . Although the proposed prediction model is relatively more sensitive to the constant (i.e.,  $\varepsilon_1$ ), the margin of error is within acceptable limits.

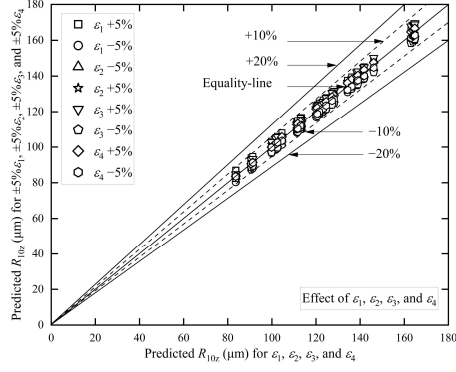


**Fig. 4.16** Sensitivity analysis for  $R_{10Z}$  model.

#### 4.4.4 Model development of $R_{sm}$ :

The values of spacing parameter,  $R_{sm}$  for various combinations of corrosion level and temperature are given in Table 4.4. At a given temperature, increasing the level of corrosion from mild to severe results in upto a 2.2-fold increase in  $R_{sm}$  values. Compared to the samples exposed at room temperature, an increase in the level of corrosion from mild to severe with a corresponding temperature increase from 400 °C to 700 °C results in an increase in  $R_{sm}$  values of upto 42%. In addition, at a given temperature, a progressive increase in the level of corrosion from mild to severe results in  $R_{sm}$  values increasing upto 55%.

In order to establish a relation between  $R_{sm}$  and the explanatory variables, a mathematical equation of the following form is considered as a first approximation:

$$R_{sm} = \mu'_1 + \mu'_2 \eta_{cri} + \mu'_3 \left( p_d^{\max} / w \right) + \mu'_4 T \quad (4.18)$$

where  $\mu'_1$ ,  $\mu'_2$ ,  $\mu'_3$ , and  $\mu'_4$  are the regression coefficients. An MLR is performed on the data using the proposed equation. The evaluated regression coefficients are 5.004, 2.721, 70.04, and  $2.87 \times 10^{-3}$ , respectively. The regression also resulted in an adjusted R-Square value of 0.967 indicating a good fit over the data. However, significance value of the obtained regression is 0.00 ( $< 0.05$ ), indicating the presence of heteroscedasticity and thus failing one of the assumptions of regression. Therefore, the model needs to be modified to satisfy the homoscedastic assumption. By employing algebraic transformations, a prediction model of the following form is proposed:

$$\sqrt{R_{sm}} = \mu_1 + \mu_2 \eta_{cri} + \mu_3 \left( \sqrt{p_d^{\max} / w} \right) + \mu_4 \sqrt{T} \quad (4.19)$$



## Fatigue Behavior of Constructional Steels Subjected to Pitting Corrosion and Elevated Temperature

where  $\mu_1$ ,  $\mu_2$ ,  $\mu_3$ , and  $\mu_4$  are regression coefficients of the modified model. The MLR results in the coefficient values of  $\mu_1=3.3$ ,  $\mu_2=0.28$ ,  $\mu_3=7.5$ , and  $\mu_4=8.15 \times 10^{-3}$ . Comparison between the experimental values of  $\sqrt{R_{sm}}$  and those estimated by the model (i.e., Equation 4.19) is depicted in Fig. 4.17. This regression results in an adjusted R-Square value of 0.992, indicating a very high 99.2% variance in  $\sqrt{R_{sm}}$  is attributable to  $\eta_{cri}$ ,  $\sqrt{p_d^{max}/w}$ , and  $\sqrt{T}$  together. In addition, a Durbin-Watson value of 2.079 indicates absence of first-order autocorrelation between the residuals. Table 4.8 gives Pearson's correlation coefficients of the regression variables. It is observed that  $\sqrt{R_{sm}}$  has a very strong correlation with  $\eta_{cri}$  (0.988) and  $\sqrt{p_d^{max}/w}$  (0.973). In addition, there is also a strong correlation between a few explanatory variables. For instance, between  $\eta_{cri}$  and  $\sqrt{p_d^{max}/w}$ , a correlation coefficient of 0.943 is observed. The weakest correlation (0.199) exists between  $\eta_{cri}$  and  $\sqrt{T}$ .

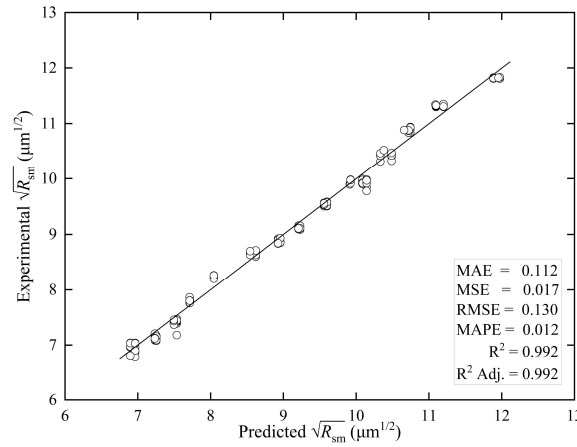


**Fig. 4.17** Comparison between experimental and predicted values of  $\sqrt{R_{sm}}$ .

**Table 4.8.** Pearson correlation matrix for  $R_{sm}$ .

Pearson Correlation	$\sqrt{R_{sm}}$	$\eta_{cri}$	$\sqrt{p_d^{max}/w}$	$\sqrt{T}$
$\sqrt{R_{sm}}$	1.00	0.988	0.973	0.299
$\eta_{cri}$	0.988	1.00	0.943	0.199
$\sqrt{p_d^{max}/w}$	0.973	0.943	1.00	0.390
$\sqrt{T}$	0.299	0.199	0.390	1.00

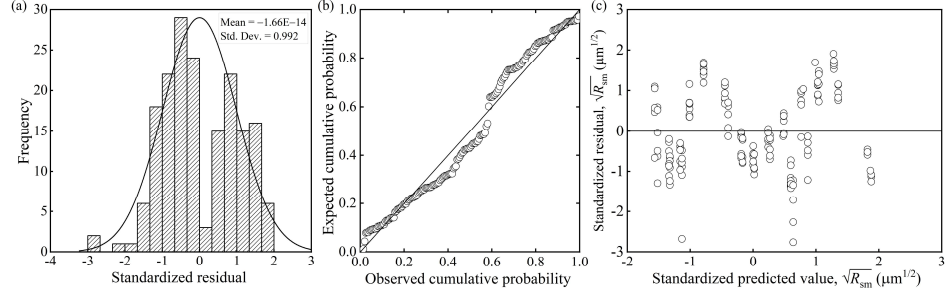


**Fig. 4.18** Residual plots for  $\sqrt{R_{sm}}$  model: (a) histogram; (b) normal probability–probability; (c) standardized residual–predicted value.

#### 4.4.5 Prediction of $k_t$ and $a_0$ :

As indicated by Equation 4.5,  $k_t$  is dependent on surface topographic feature parameters, namely  $R_a$ ,  $R_t$ , and  $R_{10Z}$ . Studying the relationship between the parameters and  $k_t$  can help in defining the surface topography effects on metal strength in terms of  $k_t$ . Table 4.4 lists the variations of  $F_s$  with corrosion severity and temperature. As observed, at a set temperature, an increase in corrosion level from mild to severe leads to an increase in  $F_s$  values of upto 61%. Further, at a set corrosion level, an increase in temperature from 25 °C to 700 °C leads to an increase in  $F_s$  values of upto 72%. These two observations indicate  $F_s$  values are significantly affected by corrosion level and temperature. Thus, based on algebraic transformation, a prediction model for  $F_s$  of the following form is proposed:

$$F_s = \gamma_1 + \gamma_2 \eta_{cr}^2 + \gamma_3 \left( p_d^{\max} / w \right) + \gamma_4 T \quad (4.20)$$

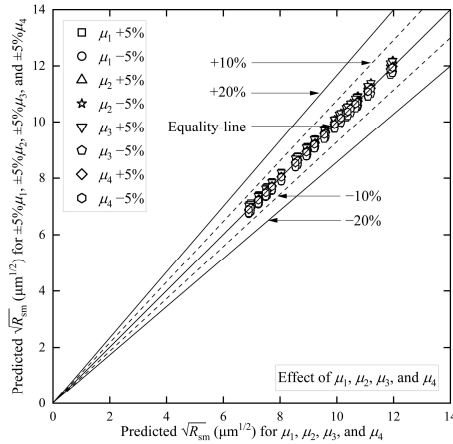


**Fig. 4.19** Sensitivity analysis for  $\sqrt{R_{sm}}$  model.

where  $\gamma_1$ ,  $\gamma_2$ ,  $\gamma_3$ , and  $\gamma_4$  are regression coefficients and performing MLR gives their values as  $-5.146$ ,  $-0.0311$ ,  $167.993$ , and  $7.07 \times 10^{-3}$ , respectively. Additionally, regression resulted in an

adjusted R-Square value of 0.948, indicating that, taken as a set,  $\eta_{\text{cri}}^2$ ,  $p_d^{\text{max}}/w$ , and  $T$  account for 94.8% of variation in  $F_s$ . Further, a Durbin-Watson value of 2.019 means no first-order autocorrelation between the residuals.

Pearson correlation coefficients of the prediction model are given in Table 4.9. All variables show positive correlations with each other. Maximum (0.942) and minimum (0.630) correlations are observed between  $F_s$  and  $p_d^{\text{max}}/w$ , and between  $F_s$  and  $T$ . Further, strong correlations between explanatory variables are also observed, e.g.,  $\eta_{\text{cri}}^2$  and  $p_d^{\text{max}}/w$  (0.941). The basic assumptions of MLR can be verified using Fig. 4.20 (a–c). From the Fig. 4.20 (a), it can be seen residual histogram follows a normal distribution, with the curve centered at zero and varying between  $-3$  and  $3$ . Fig. 4.20 (b) shows probability–probability plot of the residual, and it can be seen residuals are closely aligned with the straight line. These two observations suggest that residuals satisfy the normality assumption. Fig. 4.20 (c) shows random distribution data between standardized predicted values and residuals and follows neither an increasing nor a decreasing trend. Further, Breusch–Pagan value of 0.06 is greater than the significance value of 0.05. Thus, these two observations satisfy the homoscedasticity assumption of the residuals. By substituting the surface topographic feature parameters prediction models, namely Equations 4.13, 4.15, and 4.17 into Equation 4.6, an additional equation thus becomes available for  $F_s$  estimation. It is given as:

$$F_s = \left( \xi_1 + \xi_2 \eta_{\text{cri}} + \xi_3 \left( p_d^{\text{max}}/w \right) + \xi_4 T \right)^2 \left( \frac{(\chi_1 + \chi_2 \eta_{\text{cri}} + \chi_3 (p_d^{\text{max}}/w) + \chi_4 T)^2}{\varepsilon_1 + \varepsilon_2 \eta_{\text{cri}} + \varepsilon_3 (p_d^{\text{max}}/w)^2 + \varepsilon_4 T} \right) \quad (4.21)$$

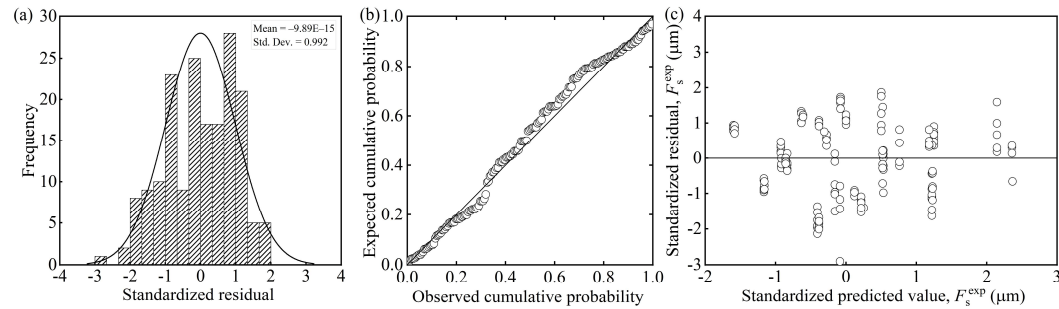


**Fig. 4.20** Residual plots for  $F_s$  model: (a) histogram; (b) normal probability–probability; (c) standardized residual–predicted value.

**Table 4.9** Pearson correlation matrix for  $F_s$ .

Pearson Correlation	$F_s$	$\eta_{\text{cri}}^2$	$p_d^{\text{max}}/w$	$T$
$F_s$	1.00	0.819	0.942	0.630
$\eta_{\text{cri}}^2$	0.819	1.00	0.941	0.228
$p_d^{\text{max}}/w$	0.942	0.941	1.00	0.443
$T$	0.630	0.228	0.443	1.00

A comparison between the values of  $F_s$  estimated from experiment and those based on the prediction model (i.e., Equation 4.20) and Equation 4.21 is shown in Fig. 4.21. Compared to experimentally evaluated  $F_s$ ,  $F_s$  based on the prediction model deviates between 6% and 5% on an average. Further, compared to experimentally evaluated  $F_s$ ,  $F_s$  based on Equation 4.21 deviates between 6% and 4% on average. Since the difference in the deviation between the prediction model and Equation 4.21 is insignificant, it can be stated that either the prediction model or Equation 4.21 can be used to estimate  $F_s$  values. As stated in Section 4.2, an equivalent surface defect  $\sqrt{\text{area}_R}$  model given by Equations 2.80 and 2.81 is used for  $a_0$  evaluation. Because ratio  $a/2b$  that is equivalent to ratio  $R_t/R_{\text{sm}}$  is greater than 0.195 for all combinations of corrosion level and temperature, Equation 2.81 in section (2.9.4) is thus applicable for  $a_0$  evaluation. Hence,  $a_0$  can be expressed as:

$$a_0 \approx \sqrt{a_R} \approx 0.38 R_{\text{sm}} \quad (4.22)$$

By substituting  $R_{\text{sm}}$  prediction model (i.e., Equation 4.19) into Equation 4.22  $a_0$  can be approximated as:

$$a_0 \approx 0.38 \left( \mu_1 + \mu_2 \eta_{\text{cri}} + \mu_3 \left( \sqrt{p_d^{\text{max}}/w} \right) + \mu_4 \sqrt{T} \right)^2 \quad (4.23)$$

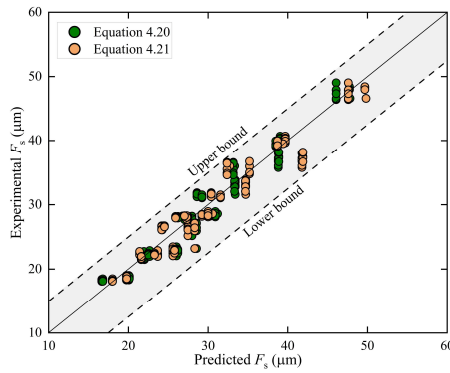


**Fig. 4.21** Comparison of experimental values of  $F_s$  with prediction model and Equation 4.21.

## Fatigue Behavior of Constructional Steels Subjected to Pitting Corrosion and Elevated Temperature

Thus, Equation 4.23 relates  $a_0$  to pitting corrosion parameters and temperature. Equation 4.23 implies that  $a_0$ 's relation with corrosion and temperature is comparable to that of  $R_{sm}$  and applies a reduction factor to  $R_{sm}$ . When evaluated using experimental values of  $R_{sm}$ , values of  $a_0$  range from 17.5 mm to 53.1 mm, while the values evaluated based on Equation 4.23 range from 18.0 mm to 54.4 mm. This confirms  $a_0$  predictions are comparable to those estimated from experiments. To better understand relative influence of the explanatory variables of Equation 4.23 on  $a_0$  estimates, the variation of  $a_0$  is compared to  $p_d^{\max}/w$  and  $\eta_{cri}$  individually. Fig. 4.22 (a) shows the relation between  $a_0$  and  $p_d^{\max}/w$  for selected ranges of  $\eta_{cri}$  (5%, 10%, and 15%) and temperatures (25 °C, 400 °C, 500 °C, 600 °C, and 700 °C). Three characteristic bands can be observed, each corresponding to a value of  $\eta_{cri}$ . For a given  $p_d^{\max}/w$ , increasing  $\eta_{cri}$  from 5% to 15% results in upto 2-fold increase in  $a_0$  values. Moreover, for a given  $\eta_{cri}$ , increasing  $p_d^{\max}/w$  from 0.1 to 0.3 results in upto 1.3-fold increase in  $a_0$  values. These two observations suggest that variations in  $\eta_{cri}$  relative to  $p_d^{\max}/w$  have more impact on  $a_0$ . In practical terms, this means that prolonged exposure of the steel rebar to corrosion would significantly affect its surface defects. Furthermore, it can be observed that for a given  $p_d^{\max}/w$  and  $\eta_{cri}$ , variation of  $a_0$  with temperatures are relatively less significant. The relationship of  $a_0$  with  $\eta_{cri}$  for selected values of  $p_d^{\max}/w$  (i.e., 0.1, 0.2, and 0.3) and temperatures are depicted in Fig. 4.22 (b). The trend between  $a_0$  and  $\eta_{cri}$  is found to be directly proportional to each other. For a given  $p_d^{\max}/w$ , increasing  $\eta_{cri}$  from 5% to 15% results in upto 44% increase in  $a_0$  values. Moreover, for a given  $\eta_{cri}$ , increasing  $p_d^{\max}/w$  from 0.1 to 0.3 results in upto 55% increase in  $a_0$  values. Thus, in conclusion, it can be stated that both  $p_d^{\max}/w$  and  $\eta_{cri}$  affect  $a_0$  values significantly.

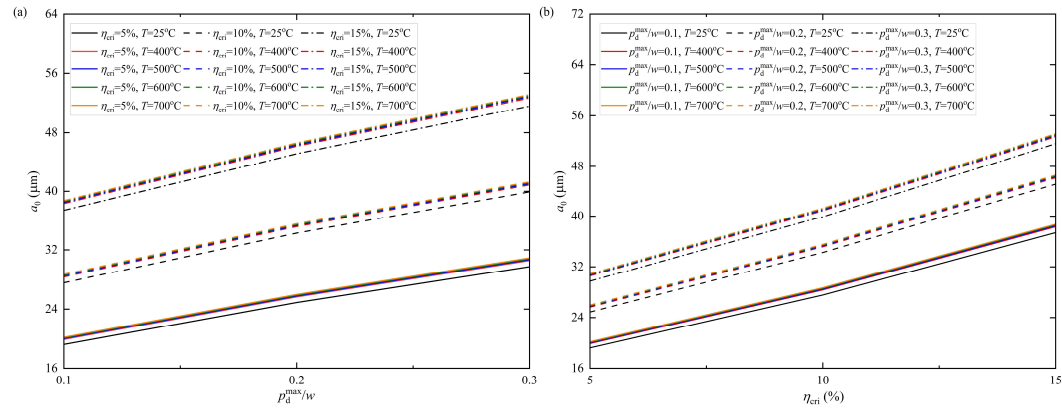


**Fig. 4.22** Variations in  $a_0$  : (a)  $a_0$  Vs  $p_d^{\max}/w$ ; (b)  $a_0$  Vs  $\eta_{cri}$ .

## 4.5 Fatigue life estimation

A procedure for estimating the fatigue life of steel bars subjected to pitting corrosion and temperature has been described in Section 4.2. In particular, Equation 4.8 can be used to express fatigue life as a function of pitting and corrosion severity parameters along with temperature. By substituting the developed predictions models for  $a_0$  (i.e., Equation 4.23) and  $F_s$  (i.e., Equation 4.20) into Equation 4.8,  $N_f$  can be expressed as:

$$N_f = \left\{ \frac{444.78 (1 - 0.85R)^2 G}{2E \left( S - (0.65f_u + 14.48) \left[ 1 + \frac{2}{\rho} (\gamma_1 + \gamma_2 \eta_{\text{cri}}^2 + \gamma_3 (p_d^{\text{max}}/w) + \gamma_4 T) \right]^{-1} \right)^2 \left( 0.38 [\mu_1 + \mu_2 \eta_{\text{cri}} + \mu_3 (\sqrt{p_d^{\text{max}}/w}) + \mu_4 \sqrt{T}]^2 \right)} \right. \\ \left. + \frac{\left( 0.38 [\mu_1 + \mu_2 \eta_{\text{cri}} + \mu_3 (\sqrt{p_d^{\text{max}}/w}) + \mu_4 \sqrt{T}]^2 \right)^{\left( 1 - \frac{m}{2} \right)}}{CS^m \beta^m \pi^2 \left( \frac{m}{2} - 1 \right)} \right\} \quad (4.24)$$

In the current study, Equation 4.24 is used to estimate the fatigue life of steel bars. The overall procedure for estimating  $N_f$  from surface topographic feature parameters proceeds as follows:

- i. Evaluate the material and mechanical properties of steel such as  $E$ ,  $G$ , and  $f_u$
- ii. Determine corrosion pit geometry parameters such as  $p_d^{\text{max}}/w$  and  $\eta_{\text{cri}}$  along with temperature.
- iii. Choose fatigue test parameters such as  $R$ ,  $S$ , and maximum stress level ( $S_m$ ).
- iv. Evaluate the values of  $k_t$  from Equation 4.5 by obtaining the values of  $F_s$  from either Equation 4.20 or Equation 4.21 using the values of pit geometry parameters and temperature.
- v. Estimate the values of  $a_0$  from Equation 4.23 by substituting the values of the pit geometry parameters and temperature.
- vi. Evaluate fatigue life  $N_f$  from Equation 4.24 using the values of various parameters obtained in steps i to v above.

### 4.5.1 Effect of $p_d^{\text{max}}/w$ :

The effect of  $p_d^{\text{max}}/w$  on  $N_f$  for various combinations of  $\eta_{\text{cri}}$ ,  $R$ , and  $S_m$  are shown in Fig. 4.23 (a–c). It can be seen that each of the figures shows three distinctive bands each corresponding to a value of  $\eta_{\text{cri}}$ . The general observation from all three figures is that  $N_f$  decreases significantly with  $p_d^{\text{max}}/w$ . For example, at room temperature and for a given value

## Fatigue Behavior of Constructional Steels Subjected to Pitting Corrosion and Elevated Temperature

of  $\eta_{\text{cri}}$  (Fig. 4.23 (a)), an increase in  $p_d^{\text{max}}/w$  from 0.1 to 0.3 results in a maximum 20% decrease in  $N_f$ . In addition, a maximum decrease in  $N_f$  of upto 12% between successive values of  $p_d^{\text{max}}/w$  is observed. These two observations can be seen at all temperatures. Further, it can be seen from Fig. 4.23 (a) that for a given value of  $p_d^{\text{max}}/w$ , increasing  $\eta_{\text{cri}}$  from 5% (i.e. mild) to 15% (i.e. severe) leads to a maximum of 28% reduction of  $N_f$ . In addition, between any two consecutive values of  $\eta_{\text{cri}}$ , a maximum reduction in  $N_f$  of upto 16% is observed. These two observations can also be seen across all temperatures.

The effect of  $R$  on  $N_f$  as  $p_d^{\text{max}}/w$  changes is shown in Fig. 4.23 (b). For illustration, the value of  $R$  is assumed to be 0.4 while all values of other parameters are held constant. Similar variation of  $p_d^{\text{max}}/w$  as observed in Fig. 4.23 (a). are also found in Fig. 4.23 (b). In addition, as expected,  $N_f$  is higher in Fig. 4.23 (b) than in Fig. 4.23 (a). Precisely, a 29% increase in  $N_f$  values is observed. Remarkably, it is observed that this deviation of 29% is almost a constant for any two consecutive values of  $\eta_{\text{cri}}$  between Fig. 4.23 (a). and Fig. 4.23 (b). Referring to Fig. 4.23 (a)., the effect of changing  $S_m$  on fatigue life is examined and the same is shown in Fig. 4.23 (c). As expected,  $N_f$  shows a significant reduction compared to Fig. 4.23 (a) due to the change in  $S_m$  from  $0.5 f_y$  to  $0.8 f_y$ . In fact, not only is this reduction found to be 4-fold, but it is also observed to be constant for any two consecutive values of  $\eta_{\text{cri}}$ .

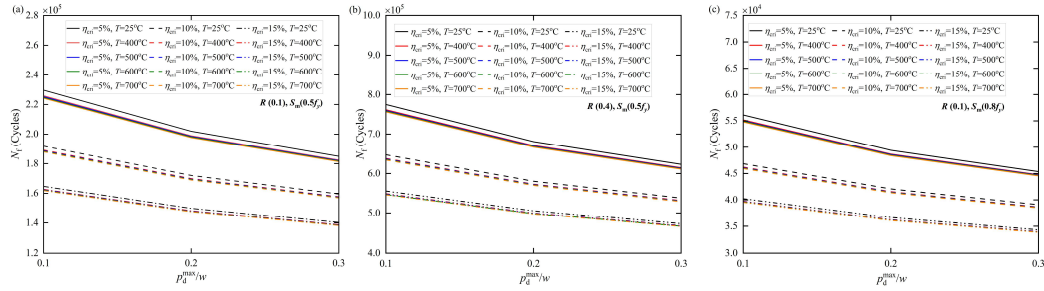


**Fig. 4.23** Effect of  $p_d^{\text{max}}/w$  on  $N_f$ : (a)  $R(0.1)$  and  $S_m(0.5f_y)$ ; (b)  $R(0.4)$  and  $S_m(0.5f_y)$ ; (c)  $R(0.1)$  and  $S_m(0.8f_y)$ .

### 4.5.2 Effect of $\eta_{\text{cri}}$ :

Fig. 4.24 (a–c) show the influence of  $\eta_{\text{cri}}$  on  $N_f$  for various combinations of  $\eta_{\text{cri}}$ ,  $R$ , and  $S_m$ . Each of the figures exhibits three separate bands, each of which corresponds to a different value of  $p_d^{\text{max}}/w$ .  $N_f$  reduces significantly with  $\eta_{\text{cri}}$ , as is evident from all three plots. For instance, an increase in  $\eta_{\text{cri}}$  from 5% to 15% leads to a maximum 28% reduction in  $N_f$  at

room temperature and for a given value of  $p_d^{\max}/w$  (Fig. 4.24 (a)). Moreover, a maximum reduction in  $N_f$  of upto 16.5% is observed between subsequent values of  $\eta_{\text{cri}}$ . Both observations are evident at all temperature values. Additionally, as shown in Fig. 4.24 (a), for a given value of  $\eta_{\text{cri}}$ , increasing  $p_d^{\max}/w$  from 0.1 to 0.3 results in a maximum 19.5% decrease in  $N_f$ . Between any two successive  $p_d^{\max}/w$  values, a maximum 12% decrease in  $N_f$  is seen. These two observations hold true at all temperatures.

To examine the effect of changing  $R$  on  $N_f$  as  $\eta_{\text{cri}}$  varies, the value of  $R$  is changed from 0.1 to 0.4 and the  $N_f$  values are estimated. Note that Fig. 4.24 (b) and Fig. 4.24 (a) show similar trends in  $\eta_{\text{cri}}$ . However, as expected, the values of  $N_f$  in Figure 4.24 (b) are about 29% higher than in Fig. 4.24 (a). Notably, this deviation of 29% is seen to be almost constant for any two successive values of  $p_d^{\max}/w$  between Fig. 4.24 (a) and Figure Fig. 4.24 (b). The effect of changing  $S_m$  on  $N_f$  is examined by changing  $S_m$  from  $0.5 f_y$  to  $0.8 f_y$  Fig. 4.24 (c) and comparing the values of  $N_f$  to those shown in Fig. 4.24 (a). A quadrupling of the values is observed, which remains constant for any two consecutive values of  $p_d^{\max}/w$ .

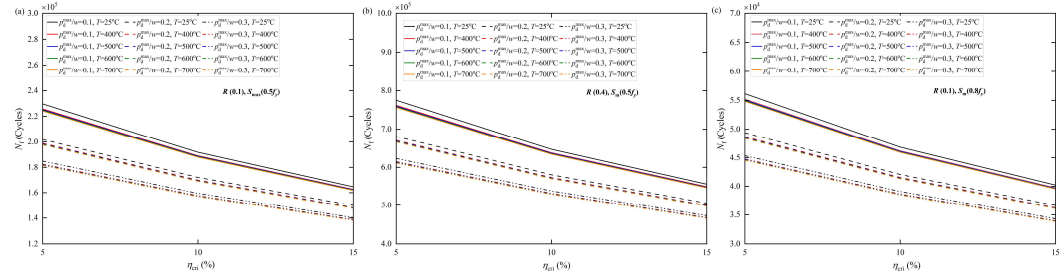


**Fig. 4.24** Effect of  $\eta_{\text{cri}}$  on  $N_f$ : (a)  $R(0.1)$  and  $S_m(0.5f_y)$ ; (b)  $R(0.4)$  and  $S_m(0.5f_y)$ ; (c)  $R(0.1)$  and  $S_m(0.8f_y)$ .

## 4.6. Fatigue life Estimation using prediction models

The fatigue life evaluated with the developed prediction models is compared with numerous experimental results from the literature. Due to unavailability of high cycle fatigue data under combined corrosion and temperature, validations are performed using corroded and uncorroded data at room temperature. Fernandez et al. (Fernandez et al., 2015) performed high cycle fatigue tests on 10 mm/12 mm diameter B500SD steel with 0.22% carbon content. Table 4.10 lists values of the experimental variables of Ref. (Fernandez et al., 2015) along with the values estimated based on the prediction models developed. Note that since the experimental values of  $\eta_{\text{cri}}$  are greater than 10%, they belong to a severe level of corrosion. The values of surface topographic feature parameters estimated using the developed prediction models are



## Fatigue Behavior of Constructional Steels Subjected to Pitting Corrosion and Elevated Temperature

also tabulated. As observed, the estimated errors between predicted and experimental values of  $N_f$  are within about 15% for all comparisons except one comparison where the error is 23%.

The effects of pitting geometries on the fatigue behavior of the steel bars were reported by (Ma et al., 2017). High cycle fatigue testing was performed on 9 mm diameter HPB300 steel by introducing notches of different geometries into the steel to simulate different pitting corrosion geometries. The details of the experimental samples and values reported are given in Table 4.10. A comparison between these experimental values and the values predicted by the developed models are given in Table 4.10. As observed, the errors between the experimental and predicted values of  $N_f$  range from 0.49% to 14.96%. In addition,  $K_t$  values estimated by the model agree well with those reported in the experiment. This indirectly confirms the correctness of surface topographic parameters  $R_a$ ,  $R_t$ , and  $R_{10z}$  estimated based on the prediction models. Zhang et al. (Zhang et al., 2021) conducted high cycle fatigue tests on pitting corroded 8 mm diameter HRB400 steel at a constant maximum stress of  $0.7 f_u$ . Pitting corrosion was performed at room temperature using an electrochemically accelerated process. The electro-hydraulic servo fatigue testing system with a constant load frequency of 5 Hz was used to carry out the fatigue tests. A comparison, between experimental (Zhang et al., 2021) and predicted values of  $N_f$  is given in Table 4.10. As can be observed, the error between them is upto 40%.

To examine the prediction accuracy of the predicted models in the case of uncorroded samples, validations are performed on some fatigue tests data reported in the literature. Paul et al. (Paul et al., 2014) conducted high cycle fatigue tests on 8 mm diameter TMT bars (Fe500) having a carbon content of 0.2%. The tests were carried out using a servo-hydraulic testing machine with test frequency of 30 Hz. A comparison between experimental and predicted values of  $N_f$  is given in Table 4.10. As can be observed, the error between them ranges from 0.79% to 10.9%. Further, Zhang et al. (Zhang et al., 2020) performed high cycle fatigue tests on 14 mm diameter HRB400 steel using an electro-hydraulic servo fatigue testing machine with a sine waveform at a frequency of 2 Hz. A comparison between experimental values of  $N_f$  with those obtained from predictive models is given in Table 4.10. As observed, the errors between them range from 3.7% to 19.6%. These observations imply developed model can also predict  $N_f$  values for uncorroded samples.

Thus, the values of  $N_f$  predicted based on the developed models are comparable to those reported from experiments for both corroded and uncorroded samples. For few comparisons, a relatively higher percentage of error is observed. This may be attributed to the system errors in the experiment, micromorphological features of the samples, interference effects during the

experiment, or sensitivity of the samples to surface roughness, stress amplitude and loading conditions (Wang et al., 2016). Nevertheless, the developed models are capable of predicting  $N_f$  values. Unfortunately, the developed models could not be validated with experimental data under combined pitting corrosion and high temperature. This is not only because such tests data are unavailable, but also because such tests require special equipment to perform. In the absence of such data, the developed predictive models are very useful and can be used for estimation of unknown parameters and preventive maintenance decisions.

**Table 4.10.** Comparison between predicted and experimental values of  $N_f$ .

Reference	Yield stress /Ultimate stress (MPa)	Stress range (MPa)	$k_t$	$\eta_{cri}$ (%)	Experimental $N_f$ (cycles)	Predicted values						Error (%)
						$R_a$	$R_t$	$R_{10Z}$	$R_{sm}$	$k_t$	$N_f$	
						(mm)	(mm)	(mm)	(mm)		(cycles)	
Fernandez et al., 2015	542.56/649.50	300	—	10.70	82,951	15.69	92.25	80.08	88.37	1.45	73,405	−11.50
		200	—	12.50	2,54,568	19.72	106.28	92.03	104.00	1.56	2,28,045	−10.41
		300	—	12.70	60,355	28.47	137.90	121.18	113.41	1.80	64,934	7.59
		200	—	15.10	1,67,236	25.71	129.49	115.63	128.21	1.71	2,05,392	22.81
		300	—	11.60	91,536	8.49	68.06	62.03	85.45	1.23	74,594	−18.50
Yafei Ma et al., 2017	446/495	217.70	1.67	12.27	2,05,791	24.16	121.91	105.84	106.65	1.69	1,74,994	−14.96
		215.40	1.73	12.43	1,67,112	27.44	133.92	117.12	110.69	1.78	1,77,524	6.22
		268.9	1.54	14.60	86,707	25.00	126.43	112.12	123.84	1.70	87,136	0.49
		275.3	1.67	15.89	70,545	26.61	133.59	120.65	135.04	1.73	78,060	10.65
		232.7	1.76	18.72	1,09,326	26.12	134.36	125.25	156.98	1.70	1,18,725	8.59
Zhang et al., 2021b	418/584	358.2	—	7.620	79,241	16.85	96.14	83.32	71.42	1.46	51,881	−34.52
		358.2	—	5.820	93,867	14.27	88.36	78.59	59.63	1.40	56,276	−40.04
Paul et al., 2014	551/649	328	—	—	1,65,861	3.78	40.31	68.30	11.16	1.05	1,57,495	−5.04
		252	—	—	3,19,253	3.78	40.31	68.30	11.16	1.05	3,48,277	9.09
		200	—	—	7,64,096	3.78	40.31	68.30	11.16	1.05	6,93,640	−9.22
		181	—	—	10,68,470	3.78	40.31	68.30	11.16	1.05	9,51,923	−10.90
		140	—	—	20,59,100	3.78	40.31	68.30	11.16	1.05	20,59,110	−0.79
Zhang et al., 2020b	425.17/581.20	290.60	—	—	2,82,566	3.78	40.31	68.30	11.16	1.05	2,82,567	−19.63
		319.66	—	—	1,77,239	3.78	40.31	68.30	11.16	1.05	1,77,240	−3.69
		348.72	—	—	1,45,077	3.78	40.31	68.30	11.16	1.05	1,45,078	−9.31

## 4.7 Conclusions

This study presents, based on experimental results including microstructural investigations, a model for pitting corrosion penetration depth distribution and prediction models for surface topographical feature parameters such as arithmetic mean height, total height, ten-point height, mean profile spacing as a function of pitting severity, corrosion level severity, and temperature. The MLR method is employed for developing the prediction models. Further, using similar parameters, prediction models for a surface topographic feature variable in stress concentration factor and defect size parameter are also presented. Each of the prediction models is validated to meet the key assumptions of the MLR method, namely normality and homoscedasticity. Further, a sensitivity analysis of each of the prediction models is performed by considering model coefficients as sensitivity parameters. A framework for fatigue life estimation is proposed incorporating the developed models considering pitting corrosion and high temperature exposure. Further, the effect of pitting corrosion and high temperature on the fatigue life of reinforcing bar is investigated. Furthermore, the proposed framework is validated by comparing the fatigue life estimated by incorporating the developed models with the experimental data available in the literature. The following conclusions can be drawn from this study:

- i. A flipped Gaussian function is more appropriate to describe the distribution of pitting corrosion penetration depth along the circumference of the reinforcing bar.
- ii. In samples exposed to 500 °C or higher, carbide particles became progressively coarser. Large carbide particles are potential sites for initial fatigue crack propagation.
- iii. The prediction models developed indicate surface topographic features of steel are significantly affected by pitting corrosion and high temperatures. Correlation studies from MLR analyses show the existence of strong relationships between the dependent and explanatory variables. The sensitivity study of each developed models found margin of error to be within acceptable limits.
- iv. The prediction models developed for a surface topographic feature variable in stress concentration factor and defect size parameter show presence of a strong dependence on pitting severity, corrosion level severity, and temperature.
- v. The fatigue life of steel reinforcing bar decreases with increasing pitting severity, corrosion level severity, and temperature. The fatigue life values predicted based on the developed models are comparable to those reported from experiments for both corroded and uncorroded samples.



**LCF behaviour of pitting corroded high-strength TMT rebars exposed to high temperatures considering Gaussian morphology**

---

**5.1 Introduction**

High-strength and ductile reinforcing bars, particularly TMT rebars, are gaining popularity in the construction industry for two key reasons. (i) they exhibit superior performance compared to mild steel bars, leading to cost savings, smaller structural components, and visually appealing structures. (ii) design standards allow for the full utilization of their enhanced strength. However, these bars may experience challenges in fatigue performance due to the high-stress levels they endure, primarily attributed to cyclic softening under fatigue loading.

During seismic events, reinforcing bars are susceptible to LCF, potentially resulting in bar rupture, premature member failure, or even the collapse of entire structures. Particularly, when exposed to aggressive environments like marine atmospheres and deicing salts, leading to corrosion and a significant reduction in service life. Pitting corrosion, a form of localized corrosion, further compromises the mechanical strength of the bars.

Corrosion pits, taking various geometries such as elliptical, semi-elliptical, linear, and circular, act as stress concentrators during cyclic loading. The SCF plays a pivotal role in influencing fatigue life. While numerical methods like the FE analysis are commonly used to estimate SCF, analytical solutions reported in the literature, particularly for limited undulated surfaces, also provide valuable insights.

Reinforcing bars face the challenge of exposure to high temperatures during their service life, especially during fire incidents in reinforced concrete structures. Transportation structures, like bridges and tunnels, constructed with these bars, can experience fire incidents over time, causing significant damage and prolonged disruption of traffic flow. The mechanical strength of reinforcing bars significantly decreases at temperatures ranging from 600 °C to 800 °C, with notable decreases in yield strength, ultimate strain, failure strain, and ductility observed in certain high-strength bars.

Various approaches, categorized as stress-, strain-, and energy-based models, have been widely utilized for determining the fatigue strength of structural members. Energy-based models, which consider both stress and strain behaviors, have gained attention for providing a more comprehensive description of fatigue behavior. For instance, the Coffin-Manson relationship has been employed to estimate LCF behavior at large strain amplitudes. Predictions based on energy dissipated on average cycles are found to better predict fatigue life than those based on the first cycle, and total energy dissipated to failure is even more accurate. Recently,

an average SED based approach successfully estimated the fatigue strength of corroded high strength cables.

Despite the significant impact of high-temperature exposure on the LCF of pitting corroded reinforcing bars, there is limited research on the combined effects of pitting corrosion and high temperature on high-strength, TMT bars. Analytical and numerical models, particularly those analyzing stress distribution parameters, are essential, considering the Gaussian representation of corrosion pits and temperature effects. It is also crucial to verify the applicability of the SED approach for fatigue life prediction of reinforcing bars under these specific conditions. This comprehensive understanding is vital for preserving large-scale infrastructures, preventing economic losses, and guiding the development of improved design approaches for engineers and scientists.

The novelty and knowledge contribution of this study are: (i) LCF tests are performed on high-strength high-ductile reinforcing bars considering pitting corrosion and high-temperature exposure conditions; (ii) proposes a two-parameter Gaussian function for corrosion depth distribution along the perimeter of the reinforcing bar; (iii) develops analytical model for estimating SCF based on Gaussian function and verifies it numerically using the FE method; (iv) relates experimental cycles to failure and energy dissipation capacity with corrosion and temperature; (v) develops/estimates temperature-dependent stress distribution parameters/values, including pit sensitivity, average SED, and pit opening angle, based on Gaussian representation of corrosion pit; (vi) compares experimental cycles to failure with that estimated based on SED approach; and conducts a comprehensive fractographic analysis of fracture surfaces.

## **5.2 Experimental work**

### **5.2.1 *Material and specimen preparation:***

The specimens used in this study are commercially obtained from hot-rolled high-strength high-ductile, deformed thermo-mechanically treated ductile reinforcing bars of grade Fe 500D, which adhere to the specifications outlined in IS 1786:2008. These reinforcing bars are often used in the construction industry due to their suitability under fire exposure conditions and their ability to retain most of their strength upto temperatures of 500 °C–600 °C. The chemical composition and mechanical properties of the specimens received from the manufacturers are detailed in Tables 5.1 and 5.2.

**Table 5.1** Chemical composition of Fe 500D specimen (in wt.%).

Chemical composition	C	P	S	Mn
Specimen	0.2	0.033	0.020	0.88

**Table 5.2** Mechanical properties of Fe 500D.

Tensile strength (MPa)	Yield strength (MPa)	Tensile strength/Yield strength	Elongation (%)	Young's modulus (MPa)	Poisson's ratio
645	560	1.15	22	$2.1 \times 10^5$	0.28

LCF tests are conducted on a total of 30 specimens. The specimens are prepared following ASTM E606/E606M–12. Fig. 5.1 (a) and (b) display the geometrical details of the specimen. A lathe machine is employed to remove the outer ribs of the bars, and then are polished to achieve a mirror finish with a maximum surface roughness of 0.2 mm. The finished steel specimen has a uniform gauge section of length 16mm with a diameter of 8mm. A transition length of about 16.70 mm and a radius of curvature of 48 mm are provided. The clamping region of the specimen has threads at both ends. The threads are 34.30 mm long and have a diameter of 16 mm.

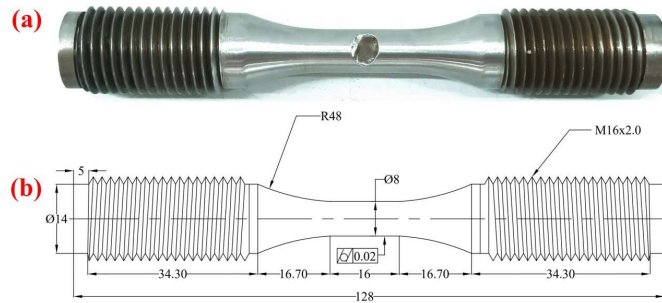


**Fig 5.1** Test specimen: (a) prepared sample; and (b) geometry (unit: mm).

## 5.2 Corrosion procedure:

An electrochemical accelerated corrosion method induces pitting corrosion in specimens at room temperature. (Fig. 5.2 (a) and (b)) shows the experimental setup of the technique. Each specimen has a 5 mm diameter pit site marked at the center of the gauge section. The specimen is fully wrapped with an insulation tape to prevent corrosion at other locations. After attaching a wire to one end, the two ends of the specimens are glued with a hot melt adhesive. Note that stainless steel acts as a cathode, and the bar acts as an anode. The cathode and anode are immersed in a 5% NaCl solution tray. A direct current power source is used to initiate the accelerated corrosion. A constant impressed current of 0.5 A is applied for 20 minutes during



## Fatigue Behavior of Constructional Steels Subjected to Pitting Corrosion and Elevated Temperature

the experiment. Following the accelerated corrosion process, the specimens are gently removed from the tray, and the wire and insulation tape are carefully detached from them. The standard procedure outlined in ISO 8407:2021 is followed to remove both coarse and fine corrosion products from the specimen surface. The procedure involves: cleaning the specimen using deionized water, immersing specimen in a freshly prepared chemical solution containing 3.5 g of hexamethylenetetramine, 500 ml hydrochloric acid, and 500 ml water, and washing with 99% pure ethanol and water.

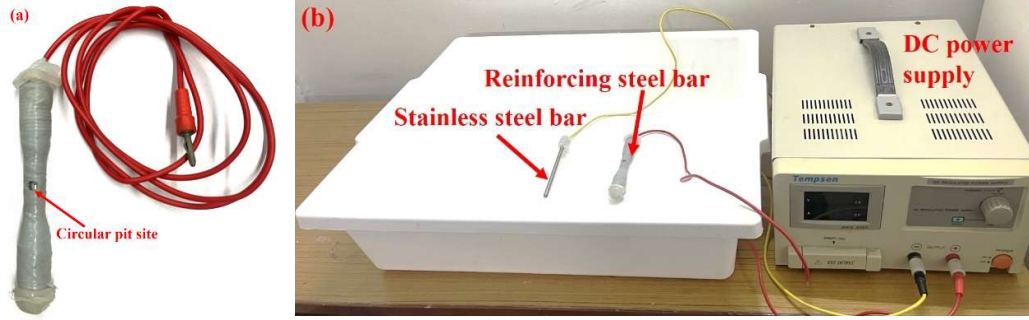


**Fig 5.2** Corrosion experiment: (a) sample preparation; and (b) accelerated corrosion.

### 5.2.3 Pits characterization:

The dimensions of corroded pits, including width ( $w$ ), length ( $l$ ), and depth ( $p_d$ ), are measured using a compact high-definition three-dimensional laser scanner with a precision of 0.2 mm. The pit geometry is scanned using a laser at a density of 5 million points per scan. This is achieved by emitting light pulses onto the pit surface and capturing the reflected light with a sensor, thus enabling the acquisition of pit geometry data. The scanner effectively captures and visualizes the pit, recreating the corroded specimen. The three-dimensional structure of a pit recreated using the laser scanner is illustrated in Figs. 5.3 (a) and (b).

The results summary of the laser scanning can be found in Table 5.3. As can be observed, a three-index nomenclature is used for specimen identification. The first index represents corrosion status: corroded (C) or uncorroded (UC). The second index indicates temperature exposure in °C, and the last index refers to the specimen number (1–3). It is important to highlight that the specimens are not exposed to elevated temperatures at this stage of the experiment. The critical cross-sectional loss ( $\eta_{\text{cri}}$ ) is a widely adopted parameter to assess the pitting severity. It is given as:

$$\eta_{\text{cri}} = (1 - A_m / A_n) \times 100\% \quad (5.1)$$

where  $A_m$  and  $A_n$  represent the specimen's minimum and nominal cross-sectional areas ( $\text{mm}^2$ ), respectively. The values of  $\eta_{\text{cri}}$  also summarized in Table 5.3.

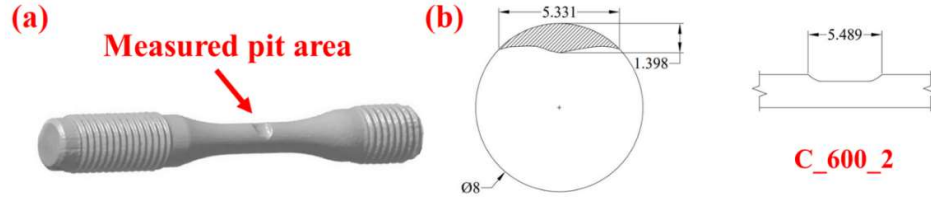


**Fig 5.3** Illustrative 3D image of a specimen: (a) 3D laser scan; and (b) pit morphology and dimensions (unit: mm).

**Table 5.3** Summary of corrosion pit geometry from 3D laser scanning.

Specimen	Temperature (°C)	Corrosion time (min)	Pit geometry from 3D laser scanning			
			$P_d^{\text{max}}$ (mm)	$w$ (mm)	$l$ (mm)	$\eta_{\text{cri}}$ (%)
C_25_1	25	20	1.377	5.641	5.656	13.801
C_25_2	25	20	1.380	5.612	5.551	13.640
C_25_3	25	20	1.382	5.531	5.601	14.030
C_400_1	400	20	1.389	5.357	5.899	14.118
C_400_2	400	20	1.403	5.432	5.743	14.056
C_400_3	400	20	1.408	5.519	5.799	13.706
C_500_1	500	20	1.388	5.235	5.743	13.767
C_500_2	500	20	1.400	5.312	5.784	13.627
C_500_3	500	20	1.399	5.301	5.789	13.593
C_600_1	600	20	1.389	5.289	5.58	13.126
C_600_2	600	20	1.398	5.331	5.489	13.148
C_600_3	600	20	1.400	5.258	5.799	13.702
C_700_1	700	20	1.399	5.129	5.768	13.071
C_700_2	700	20	1.408	5.248	5.784	13.075
C_700_3	700	20	1.398	5.206	5.534	13.134

It is observed that  $\eta_{\text{cri}}$  values for all the specimens are greater than 10%. This corresponds to severe corrosion level as  $\eta_{\text{cri}}$  is greater than 10%.

### 5.2.3 Gaussian representation of pits:

The laser scan results indicate that  $p_d$  varies along  $w$  and  $l$  at different positions. The variation of  $p_d$  along the specimen perimeter interests practicing engineers as it can be used to estimate a decrease in steel cross-sectional area. The  $p_d$  data extracted from laser scans are fitted with various mathematical expressions, including Gaussian, linear, semi elliptical, and elliptical. The following inverted Gaussian expression is found to represent  $p_d$  variation along the specimen perimeter better:

$$p_d = -\nu_1 e^{-\nu_2 \theta^2} \quad (5.2)$$

where  $\nu_1$  and  $\nu_2$  are regression parameters, while  $\theta$  is the angle between the bar's center and a circumferential point (radians). Note that  $\nu_1$  is associated with the uneven distribution of  $p_d$  along the specimen's perimeter, while  $\nu_2$  correlates with  $\theta$  at which  $p_d$  takes the value of  $p_d^{\max}$ . Similar Gaussian expression is reported in (Chauhan & Muthulingam, 2023). However, the mathematical form of Equation 5.2 differs from the equation as reported in literature (Chauhan & Muthulingam, 2023), since it utilizes only two parameters, resulting in a simpler representation. In addition, Equation 5.2 is better suited for developing analytical SCF models, as will be demonstrated in Section 5.3.

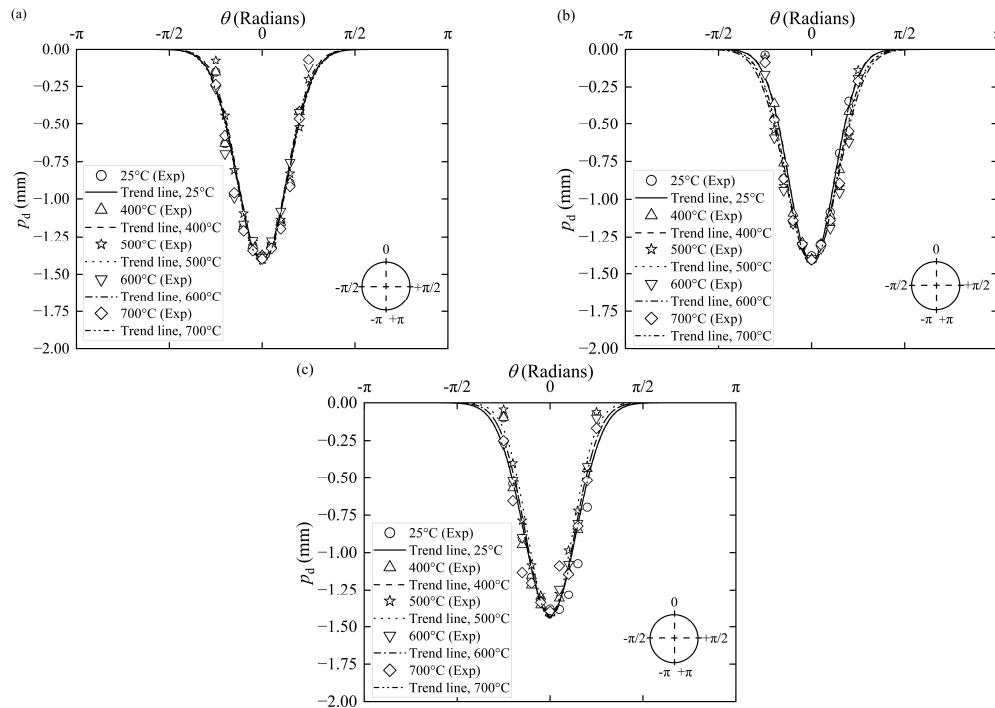


**Fig. 5.4** Experimental data and trends based on flipped Gaussian model.

The variation of  $p_d$  along the perimeters of the specimens, along with the corresponding trendlines based on Equation 5.2 are illustrated in Figs. 5.4 (a)–(c). Additionally, Table 5.4 presents  $\nu_1$ ,  $\nu_2$ , and R-Square values for all specimens. As observed, R-Square values range from 0.967 to 0.990. It is worth mentioning that 60% of the specimens exhibit R-Square values exceeding 0.98. Thus, the inverted Gaussian model is the most suitable representation for the distribution of  $p_d$  along the perimeter of the specimen. Additionally, minor variations in  $\nu_1$  indicate a consistent uneven distribution of corrosion along the specimens' perimeters, confirming the uniformity of the corrosion tests.

**Table 5.4** Fitting parameters of inverted Gaussian model.

Specimen	$\nu_1$	$\nu_2$	R-square
C_25_1	1.40012	2.72986	0.97341
C_25_2	1.41956	3.28119	0.98270
C_25_3	1.41994	2.52873	0.96725
C_400_1	1.41639	2.92588	0.97313
C_400_2	1.42076	3.35532	0.98441
C_400_3	1.43637	2.89765	0.97718
C_500_1	1.43788	2.99496	0.98980
C_500_2	1.43729	2.75004	0.98087
C_500_3	1.42494	3.39922	0.99049
C_600_1	1.42366	2.70971	0.97850
C_600_2	1.42381	2.52904	0.98246
C_600_3	1.44187	2.89809	0.98715
C_700_1	1.42597	2.65785	0.98065
C_700_2	1.43792	2.83172	0.98719
C_700_3	1.42051	2.51024	0.96706

### 5.3 SCF of inverted Gaussian model

The perturbation theory in the context of surface perturbations assumes that the undulating surface is nearly flat, with a small perturbation compared to other length scales of the bulk material, thus allowing it to be treated as an elastic half-plane (Gao, 1991). This perturbation approach can be employed to analytically calculate the SCF for the Gaussian model (Equation 5.2). This approach uses a specific elastic Green's function for perfectly flat elastic surfaces. The undulating surface is considered as a perturbation relative to the flat surface. By applying the perturbation theory, the stress concentration factor ( $k_t$ ) can be expressed as (Gao, 1991; Medina, 2015; Medina & Hinderliter, 2014):

$$k_t(\theta) = \left[ 1 + \frac{2}{\pi} PV \int_{-\infty}^{\infty} \frac{p'_d(\varsigma) d\varsigma}{(\varsigma - \theta)} \right] \quad (5.3)$$

where  $PV$  refers to the principal value in which the integral is evaluated in the Cauchy sense,  $d'_p(\varsigma)$  represents spatial derivative of an arbitrary pitting surface profile  $p_d(\varsigma)$ , and  $\varsigma$  is a dummy variable.

To find the solution to Equation 5.3 Hilbert transform (HT) can be used. Suppose  $\xi(t)$  is the analytic associate of  $u(t)$  (Hahn, 1996; Le Van Quyen et al., 2001)

$$\xi(t) = u(t) + i\tilde{u}(t) = a(t)e^{i\phi(t)} \quad (5.4)$$

where  $\tilde{u}(t)$  is the HT of  $u(t)$ ,  $a(t)$  and  $\phi(t)$  are the instantaneous amplitude and instantaneous phase angle, respectively, given by:

$$a(t) = \{u^2(t) + \tilde{u}^2(t)\}^{1/2} \quad (5.5)$$

$$\phi(t) = \arctan \frac{\tilde{u}(t)}{u(t)} \quad (5.6)$$

Then HT of  $u(t)$  is given in the form of improper integral as:

$$\tilde{u}(t) = H(u(t)) = \frac{1}{\pi} PV \int_{-\infty}^{\infty} \frac{u(\tau)}{\tau - t} d\tau = -\frac{1}{\pi} PV \int_{-\infty}^{\infty} \frac{u(\tau)}{t - \tau} d\tau \quad (5.7)$$

Further, the inverse of HT is given as:

$$u(t) = H^{-1}(\tilde{u}(t)) = \frac{1}{\pi} PV \int_{-\infty}^{\infty} \frac{\tilde{u}(\tau)}{\tau - t} d\tau = -\frac{1}{\pi} PV \int_{-\infty}^{\infty} \frac{\tilde{u}(\tau)}{t - \tau} d\tau \quad (5.8)$$

The convolution kernel function, which is  $h(t) = 1/\pi t$  and is singular at  $t = 0$ , in terms of Cauchy's principal value Equation 5.8 can be expressed as:

$$\tilde{u}(t) = \lim_{\beta \rightarrow 0} \left( \int_{-\infty}^{t-\beta} + \int_{t+\beta}^{\infty} \right) u(\tau) \cdot h(t-\tau) d\tau \quad (5.9)$$

Note that HT can be treated as a phase shifter which introduces a phase lag  $(-i = e^{-i\pi/2})$  and can be also be expressed as (Liu, 2012):

$$U(t)=G(t).(-i\operatorname{sgn}(t)) \quad (5.10)$$

where  $U(t)$  and  $G(t)$  are Fourier transforms of  $\tilde{u}(t)$  and  $g(t)$ , while  $\tilde{u}(t)$  and  $g(t)$  form HT pairs. If the Fourier transforms  $U(t)$  and  $G(t)$  are related by Equation 5.10, then  $\tilde{u}(t)$  is the HT of  $u(t)$ .

$$\tilde{u}(t)=H(u(t)) \quad (5.11)$$

Further, HT can be evaluated by taking the inverse Fourier transform of Equation 5.10 in conjunction with Equation 5.11. A concise expression for HT can be expressed in the form as (Boashash, 2015):

$$H(u(t))=F_{t \leftarrow F}^{-1}\{-i\operatorname{sgn}(t)F_{t \rightarrow F}(u(t))\} \quad (5.12)$$

where  $F_{t \rightarrow F}(u(t))$  is Fourier transform. Applying Equation 5.12 to Equation 5.3,  $k_t$  can be expressed as:

$$k_t(\theta)=1-2H[p_d'(\theta)] \quad (5.13)$$

A property of the HT states that HT of the derivative of a function is equal to the derivative of the HT, that is, if  $u(t)=H(v(t))$  then  $H(v'(t))=u'(t)$ , Equation 5.13 can be expressed as (Medina, 2015):

$$k_t(\theta)=1-2\frac{d[H p_d(\theta)]}{d\theta} \quad (5.14)$$

Applying Equation 5.14 to the proposed inverted Gaussian model (i.e. Equation 5.2),  $k_t$  is evaluated as:

$$k_t(\theta)=1+\frac{4v_1\sqrt{v_2}}{\sqrt{\pi}}\left[1-\theta e^{(-v_2\theta^2)}\sqrt{\pi}\sqrt{v_2}\operatorname{erfi}(\sqrt{v_2}\theta)\right] \quad (5.15)$$

where  $\operatorname{erfi}$  represents imaginary error function. It can be observed from Figs. 5.4 (a)–(c) that  $p_d$  becomes equal to  $p_d^{\max}$  when  $\theta=0$ . Thus, the maximum value of  $k_t$  is obtained by substituting  $\theta=0$  in Equation 5.15.

$$k_t=1+\frac{4v_1\sqrt{v_2}}{\sqrt{\pi}} \quad (5.16)$$

Note that the developed model for  $k_t$  accounts for non-uniformity variation in the inverted Gaussian representation of the corrosion pit. The maximum  $k_t$  values for all specimens are listed in Table 5.5. As observed,  $k_t$  values range between 6.07 and 6.93, showing minimal deviations among the specimens.

**Table 5.5** Stress concentration factor for inverted Gaussian model.

Specimen	$k_t$	Specimen	$k_t$	Specimen	$k_t$
	Analytical /FE		Analytical /FE		Analytical /FE
C_25_1	6.22/6.24	C_25_2	6.80/7.24	C_25_3	6.09/6.98
C_400_1	6.46/7.03	C_400_2	6.87/6.96	C_400_3	6.15/6.83
C_500_1	6.61/6.02	C_500_2	6.37/6.08	C_500_3	6.92/6.35
C_600_1	6.28/6.30	C_600_2	6.10/7.12	C_600_3	6.53/7.02
C_700_1	6.24/6.62	C_700_2	6.46/6.28	C_700_3	6.07/6.94

The variation in  $k_t$  for all specimens based on Equation 5.15 is shown in Figs. 5.5 (a) – (c). As observed, with increase in the root radius of the pit,  $k_t$  decreases. For the axial loading,  $k_t$  are highest at a polar angle value of  $\theta = 0$ , which corresponds to  $p_d^{\max}$  location, then consistently decreases between 0 and  $\pm\pi/4$ , rises from  $\pm\pi/4$  to  $\pm\pi/2$ , and remains almost constant between  $\pm\pi/2$  and  $\pm\pi$ . Note that  $k_t$  between  $\pm\pi/4$  to  $\pm\pi/2$  corresponds to tail ends of the Gaussian representation, where the radius of curvature reverses sign. Further,  $k_t$  between  $\pm\pi/2$  and  $\pm\pi$  stabilizes, which corresponds to constant radius of curvature in the Gaussian representation.

FE analysis is performed to compare SCF with the analytical model. The three-dimensional models are recreated for each specimen from three-dimensional laser scanning. This approach replicates the specimen's exact dimensions, including the pit geometry is shown in Fig. 5.6 (a). The model is directly preprocessed in the FE computational tool to understand the stress distribution in the pit. The element size in the pit is 0.05 mm, while that near the pit is 0.1 mm. In addition, the element size is kept at 0.15 mm in the tapering region and at 0.2 mm in the cylindrical part (Fig. 5.6 (b)). The modulus of elasticity, density, and Poisson's ratio are  $2.1 \times 10^5$  MPa, 7850 kg/m<sup>3</sup>, and 0.3, respectively. At one end of the FE model, translational unrestraint along longitudinal direction and rotation restraints in all three directions are applied as boundary conditions. Additionally, a nominal axial tensile stress of 200 MPa is applied to the opposite end of the model.

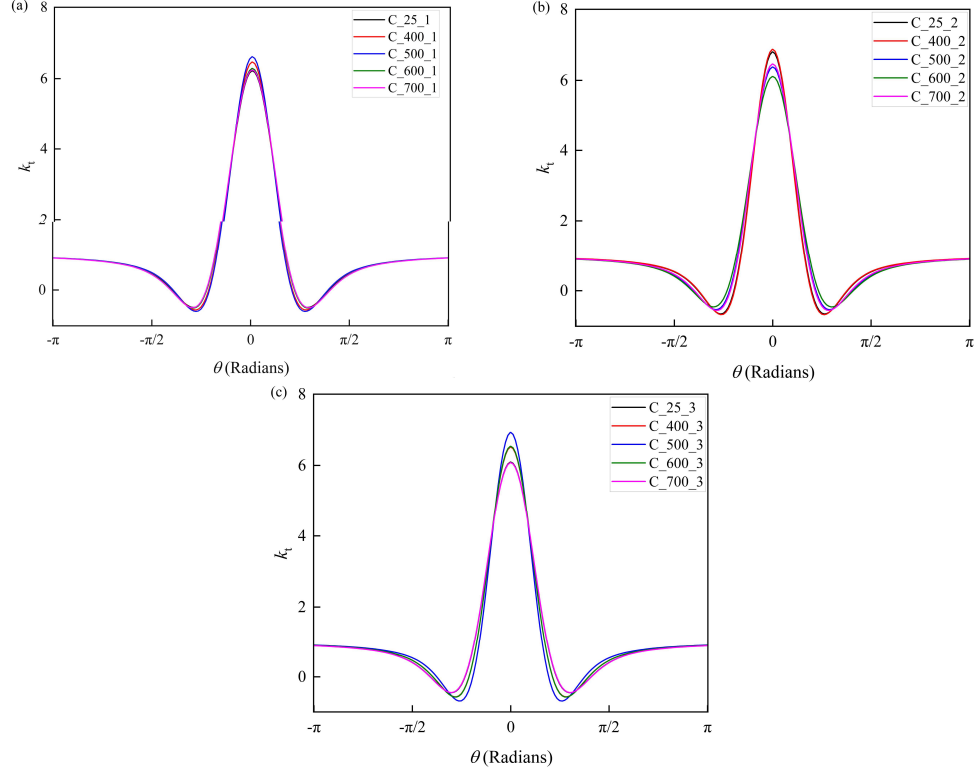


**Fig 5.5** Variation of SCF based on the analytical model.

The stress distribution in entire specimen obtained from FE analysis is shown in Fig. 5.6 (c). Note that the analysis results in a symmetrical stress profile. Further, Fig. 5.6 (d) shows the stress distribution within the corrosion pit. As observed, the corrosion pit exhibits the highest level of stress in comparison to other locations. In addition, the stress within the corrosion pit fluctuates due to the changing profile of the corrosion surface. It can also be observed that the highest stresses occur in the central region of the pit, where the corrosion pit is deepest. In general, SCF can be expressed as a ratio between peak stress and nominal stress:

$$k_t^{FE} = \frac{\sigma_p}{\sigma_n} \quad (5.17)$$

where  $k_t^{FE}$  represents the SCF obtained from FE analysis,  $\sigma_p$  refers to the peak stress (MPa) and  $\sigma_n$  represents nominal stress (MPa). Table 5.5 compares analytical and FE based  $k_t$ . As observed, the average deviation between the two values is 7%, suggesting a strong agreement between the values. Thus, the developed analytical model is suitable for estimating the SCF associated with pitting corrosion, specifically when the corrosion profile follows a Gaussian trend.



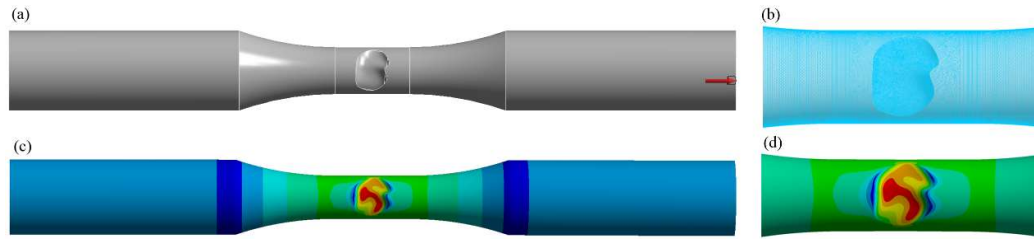


**Fig. 5.6.** Numerical analysis of SCF: (a) 3D laser scan image; (b) FE mesh; (c) stress distribution in the specimen; and (d) stress distribution in the corrosion pit.

## **5.4 LCF experiment**

### **5.4.1 Test procedure:**

LCF tests are performed using a computer-controlled servo-electric universal testing machine (Model: BISS UTM-02-0100) equipped with a 100 kN load cell. The machine features a split-type furnace capable of reaching temperatures ranging from 0 °C to 1000 °C. The furnace has a center-split design for easy access to the specimen and grippers. The temperature of the specimen is regulated using a PID controller. Three K-type thermocouples are used to monitor the temperature in the gauge length region. A cooling system is typically installed to maintain a low temperature and safeguard the test systems from the high heat generated by the furnace. Fig. 5.7 displays the fatigue test machine and furnace.

LCF tests are conducted in controlled environments at both room temperature and elevated temperatures to study the behavior of corroded and uncorroded specimens. Of the 30 specimens tested, 15 are uncorroded, and 15 are corroded. For consistent test results, each test is repeated three times. The test specimens are heated at the rate of 10 °C/min. An automatic temperature controller controls the process of heating the test specimens. Note that the chosen heating rate closely correlates with the fire exposure condition of the reinforcing steel bar in RCC members having a nominal reinforcement cover (Kodur et al., 2004; Lie, 1988). This suggests that, the heating rate in the experiment simulates the heating experienced by the reinforcing bar within a concrete structure when subjected to a fire event. In practical terms, the experimental conditions in the study, such as the rate at which temperature is increased, mimic the conditions that a reinforcing bar would experience if it were part of a concrete structure exposed to a fire. This comparison helps to understand how the steel properties change under such conditions, which is crucial for assessing the structural integrity and safety of reinforced concrete structures in fire situations. This choice also aligns with standard temperature-time curves in ISO standards (ISO 834-13:2019). It is noteworthy that, 10 °C/minute has been utilized in the study as this rate allows for faster testing compared to slower rates in some standard fire curves. The focus of the

study is on understanding how the corroded steel responds to gradual temperature increase, not mimicking an exact fire event.

Before starting LCF loading, the test specimens are heated to the targeted temperature and soaked inside the furnace for 20 minutes to ensure uniform heating. The temperature remained constant throughout the test until the specimen failed. Note that the targeted temperatures are chosen to simulate real fire conditions in steel. Similar heating method have been adopted by many researchers in the past (Hua et al., 2021; Hua, Yang, et al., 2022)

Fatigue tests are performed under load-controlled conditions, applying fully reverse loading cycles to corroded and uncorroded steel specimens throughout the experiment. The cyclic loads are applied to the specimen based on design stress levels. A maximum stress level of  $0.7 f_y$  is adopted in this study. Here,  $f_y$  denotes the yield strength of the reinforcing bar. It is worth pointing out that  $0.7 f_y$  reflects the real-life stress conditions in the rebars of RCC bridges under normal and overloaded service conditions (Fernandez et al., 2015). Distinct fatigue fracture or deformation does not occur in high-strength steel under stress amplitude  $0.5 f_y$ . However, fatigue fractures occur in the steel when subjected to a stress amplitude of  $0.7 f_y$  or greater. The applied stress level remained constant throughout the test, maintaining a stress ratio of -1 at a cyclic frequency of 0.10 Hz. The frequency is chosen based on practical applications in structural engineering. The fatigue tests are conducted till the complete detachment of the specimen.

#### 5.4.2 Hysteresis behaviour:

The cumulative fatigue damage induced in the specimen due to pitting corrosion and elevated temperature can be evaluated from the hysteresis curves under the cyclic loading conditions. Figs. 5.8 (a)–(j) display hysteresis curves for uncorroded and corroded specimens. Hysteresis curves are plotted between load and displacement against stress and strain for two main reasons. Firstly, it allows for a direct comparison of degradation in corroded specimens. Secondly, estimating the state of stress in corroded specimens is a challenging task. Note that only a few hysteresis loops are chosen for better representation. In the case of uncorroded specimens, the loops exhibit similar characteristics as the temperature increases. However, the loops become broader as temperature increases, even with fewer cycles. For instance, at the 500th cycle, the loop in UC\_700\_1 (Fig. 5.8 (e)) is noticeably broader than UC\_25\_1 (Fig. 5.8 (a)). This suggests that for a given cycle, the energy dissipation capacity (defined as energy in a hysteresis loop) in specimens exposed at elevated temperature is higher than that exposed at room temperature. Corroded specimens show similar trends.

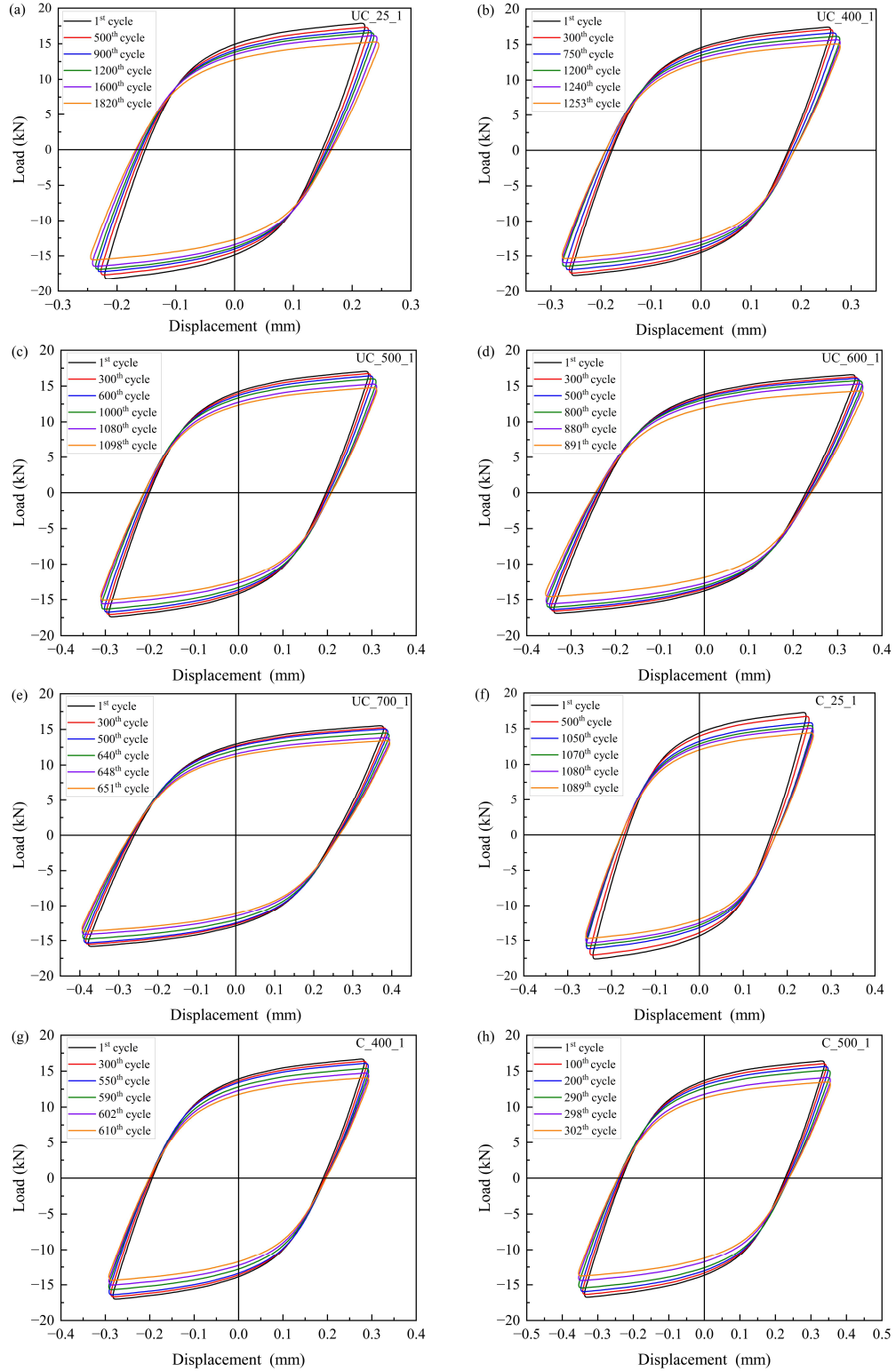
## Fatigue Behavior of Constructional Steels Subjected to Pitting Corrosion and Elevated Temperature

The linear section of the hysteresis loop decreased with increasing cycles in both the corroded and uncorroded specimens. This behavior is known as cyclic softening. With increasing temperature, cyclic softening becomes more pronounced at lower cycles. This is observed in both corroded and uncorroded specimens. However, compared to the uncorroded specimens, progression of cyclic softening in corroded specimens is observed in fewer cycles. Cyclic softening is typically caused by dynamic recovery through dislocation rearrangement. Dislocation wall substructures form through recovery micro-mechanisms, increasing the mean free path for dislocations and favoring cyclic softening (Agnew & Weertman, 1998; Rao et al., 1988; Ye et al., 2006).



**Fig 5.7** Fatigue testing.

Peak loads decrease in specimens with increasing temperature. For instance, at 500 °C, compared to room temperature, a 7.8% reduction in peak load is observed at the 800<sup>th</sup> cycle in uncorroded specimens. However, at the same temperature, corroded specimens show a 6.6% reduction at the 100<sup>th</sup> cycle and an 18.6% reduction at the 300<sup>th</sup> cycle. Thus, peak load decreases significantly in corroded specimens with increasing cycles at a given temperature. This indicates that pitting corrosion considerably reduces the load carrying capacity of the reinforcing bar under LCF. This observation is practically relevant because structures affected by pitting corrosion may not be able to resist design loads, especially in seismically active areas.



## Fatigue Behavior of Constructional Steels Subjected to Pitting Corrosion and Elevated Temperature

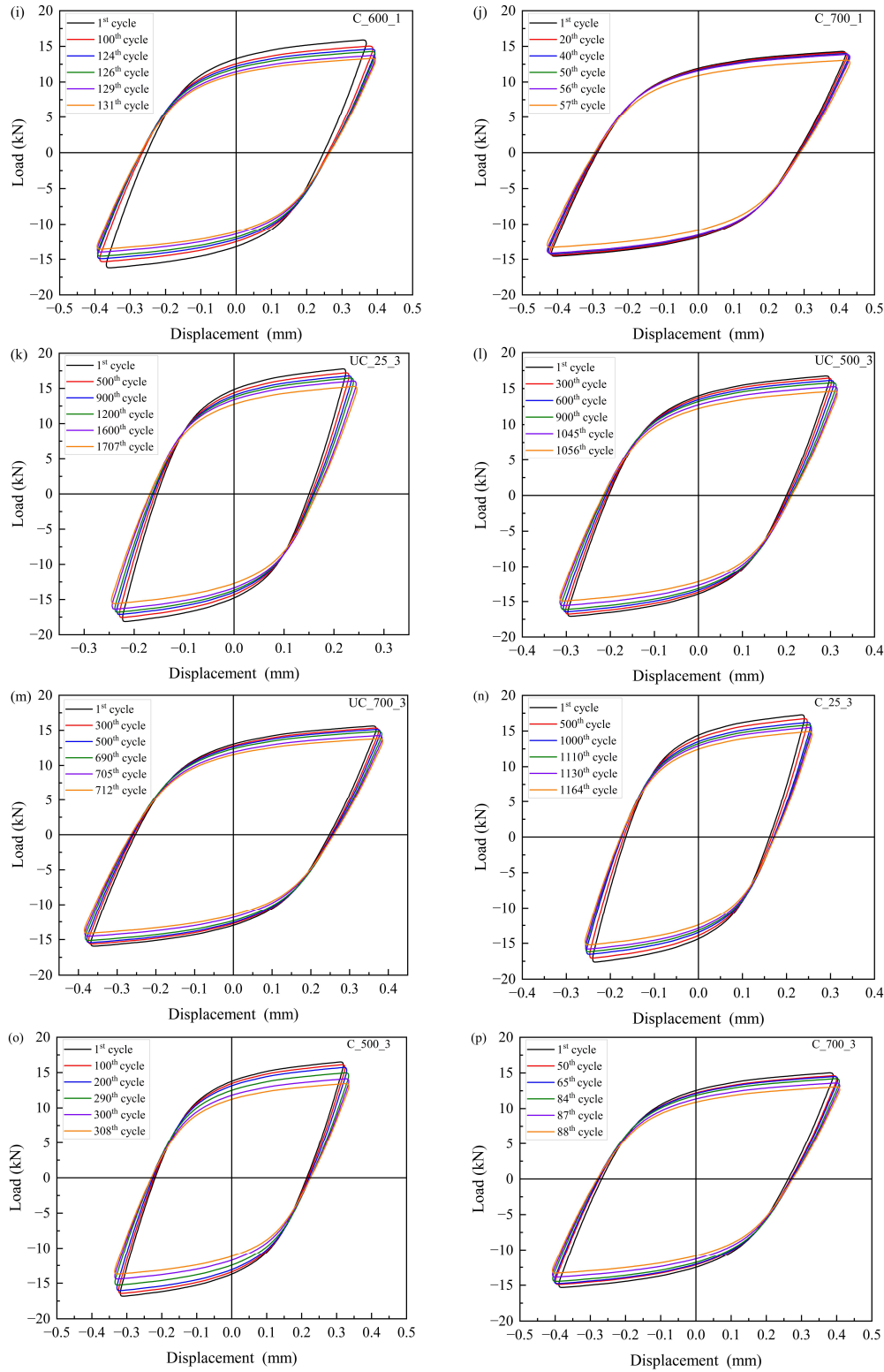


**Fig 5.8** Hysteresis curves: (a) UC\_25\_1; (b) UC\_400\_1; (c) UC\_500\_1; (d) UC\_600\_1; (e) UC\_700\_1; (f) C\_25\_1; (g) C\_400\_1; (h) C\_500\_1; (i) C\_600\_1; (j) UC\_700\_1; (k) UC\_25\_3; (l) UC\_500\_3; (m) UC\_700\_3; (n) C\_25\_3; (o) C\_500\_3 and (p) C\_700\_3.

Peak displacements increase drastically with increasing temperature in corroded and uncorroded specimens. For uncorroded specimens: (i) at 500 cycles, it is 72% higher in the specimen exposed to 700 °C compared to room temperature, (ii) at 800 cycles, it is 54% higher in the specimen exposed to 600 °C compared to room temperature, and (iii) at 1000 cycles, it is 33% higher in the specimen exposed to 500 °C compared to room temperature. For corroded specimens: (i) at 50 cycles, peak displacement at 700 °C is 77% higher than at room temperature, (ii) at 100 cycles, peak displacement at 600 °C is 59% higher than at room temperature, and (iii) at 300 cycles, peak displacement at 500 °C is 44% higher than at room temperature. Thus, corroded specimens experience a faster peak displacement reduction than uncorroded specimens. The practical significance of this observation is increasing temperature reduces the material's ductility, and corrosion exacerbates this effect. This renders the current state of infrastructures unsuitable for service as they do not meet the serviceability condition (Congress, 2020).

#### 5.4.3 Variation in $N_{f,exp}$ :

The number of cycles to failure ( $N_{f,exp}$ ) for uncorroded and corroded specimens in the experiment is summarised in Table 5.6. Significant reductions in  $N_{f,exp}$  values are observed with varying corrosion status and temperature. In the case of uncorroded specimens, an increase in temperature from 25 °C to 700 °C results in 62% reduction in  $N_{f,exp}$ . However, in the case of corroded specimens, an increase in temperature from 25 °C to 700 °C results in a 94% reduction in  $N_{f,exp}$ . Thus, for a given temperature,  $N_{f,exp}$  reduction is more severe in corroded specimen compared to the uncorroded specimen by upto 36%. This can be attributed to the high temperature causing the formation of an oxide layer on steel. Tensile loading during the LCF test opens the crack, allowing oxygen diffusion at the crack tip. Thus, the nucleation of multiple fatigue cracks results in decreased fatigue life (Chauhan et al., 2017).

Table 5.6 also compares  $N_{f,exp}$  values between uncorroded and corroded specimens. Observations indicate that  $N_{f,exp}$  in corroded specimens decreases by a factor of 1.6 at 25 °C, 2.1 at 400 °C, 3.6 at 500 °C, 6.3 at 600 °C, and 9.7 at 700 °C when compared to uncorroded specimens. The reduction is due to the combined effect of temperature and pitting corrosion. Specifically, the decrease in  $N_{f,exp}$  can be attributed to premature crack nucleation caused by the presence of pits (Chlistovsky et al., 2007). Section 5.6 includes further discussions on  $N_{f,exp}$  reduction with the help of fractographic images.

## Fatigue Behavior of Constructional Steels Subjected to Pitting Corrosion and Elevated Temperature

A dimensionless analysis was conducted by comparing the maximum value of  $N_{f, \exp}$  at  $T$  °C to the maximum value at  $N_{f, \exp}$  at 25 °C i.e.  $N_{f, T}^{\max} / N_{f, 25}^{\max} \cdot N_{f, 25}^{\max}$  is considered a benchmark for both corroded and uncorroded specimens. Fig. 5.9 compares  $N_{f, T}^{\max} / N_{f, 25}^{\max}$  of various specimens. The trend reveals that  $N_{f, T}^{\max} / N_{f, 25}^{\max}$  decreases with an increase in temperature.  $N_{f, 400}^{\max}$  is 74.3% of  $N_{f, 25}^{\max}$  and  $N_{f, 700}^{\max}$  is 39.1% of  $N_{f, 25}^{\max}$  for corroded specimens. Whereas for corroded specimens  $N_{f, 400}^{\max}$  is 53.4% compared to  $N_{f, 25}^{\max}$  and  $N_{f, 700}^{\max}$  is only 7.5% of  $N_{f, 25}^{\max}$ . The decrease in  $N_{f, T}^{\max} / N_{f, 25}^{\max}$  with higher exposure temperature is because the pearlite size reduces and becomes more evenly distributed at temperatures above 600 °C. This increases dislocation resistance and contributes to fatigue crack progression (Hua, Wang, et al., 2022).

The data points of  $N_{f, \exp}$  are plotted against temperature in Fig. 5.10. To predict the trend in the data points of  $N_{f, \exp}$ , the following linear polynomial function of first degree is selected:

$$N_{f, \exp} = \eta_1 + \eta_2 T \quad (5.18)$$

where  $\eta_1$  and  $\eta_2$  are the regression coefficients. Linear regression yields  $\eta_1$  (1842.11) and  $\eta_2$  (−1.60) with a R-Square value of 0.976 for the uncorroded specimens, and  $\eta_1$  (1175.25) and  $\eta_2$  (−1.63) with a R-Square value of 0.975 for corroded specimens. The trendlines are shown in Fig. 5.10, and it can be observed that they fit well with the data points.

The stiffness progression of specimens is assessed by analyzing the hysteresis loops as shown in Fig. 5.11 (a)–(c). The stiffness of all specimens gradually decreases from the first cycle and continues to decline consistently until it reaches a point close to failure, where a sudden reduction is observed. Uncorroded specimens demonstrate a range of stiffness reduction, with a maximum decrease of 48% and a minimum decrease of 36%. In the corroded specimens, the respective values are 6% and 30%, respectively. The results indicate that corroded specimens exhibit a notable decrease in stiffness reduction before fracturing compared to uncorroded specimens. One reasonable explanation for this behaviour is cyclic softening, which leads to the formation and propagation of microcracks (Xie et al., 2019).

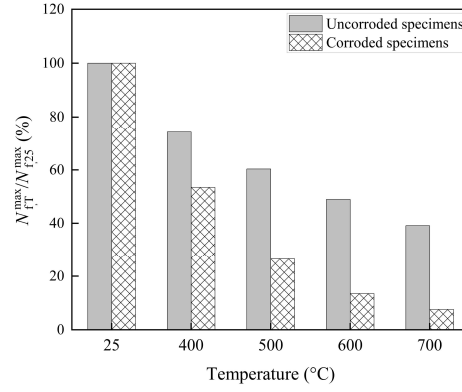


**Fig 5.9** Effect of high temperatures: a dimensionless comparison of  $N_{f,T}^{\max} / N_{f,25}^{\max}$ .

**Table 5.6**  $N_{f,exp}$  of specimens exposed to different temperatures.

Specimen	$N_{f,exp}$	Average of $N_{f,exp}$	Standard deviation of $N_{f,exp}$	Specimen	$N_{f,exp}$	Average of $N_{f,exp}$	Standard deviation of $N_{f,exp}$
UC_25_1	1820	1766	56.62	C_25_1	1089	1120	38.99
UC_25_2	1770			C_25_2	1108		
UC_25_3	1707			C_25_3	1164		
UC_400_1	1253	1281	60.68	C_400_1	610	611	10.53
UC_400_2	1351			C_400_2	601		
UC_400_3	1240			C_400_3	622		
UC_500_1	1098	1058	39.52	C_500_1	302	298	12.49
UC_500_2	1019			C_500_2	284		
UC_500_3	1056			C_500_3	308		
UC_600_1	891	852	33.54	C_600_1	131	136	19.42
UC_600_2	831			C_600_2	119		
UC_600_3	835			C_600_3	157		
UC_700_1	651	688	32.71	C_700_1	57	71	15.82
UC_700_2	702			C_700_2	67		
UC_700_3	712			C_700_3	88		



## Fatigue Behavior of Constructional Steels Subjected to Pitting Corrosion and Elevated Temperature

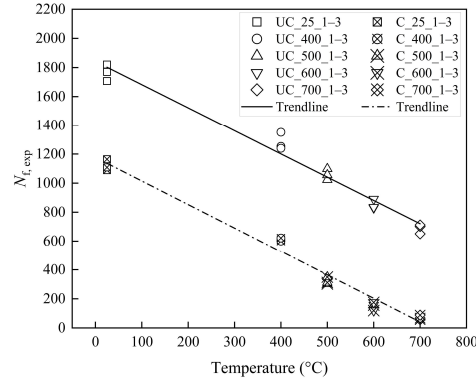


**Fig 5.10** Variation of  $N_{f,exp}$  with temperature.

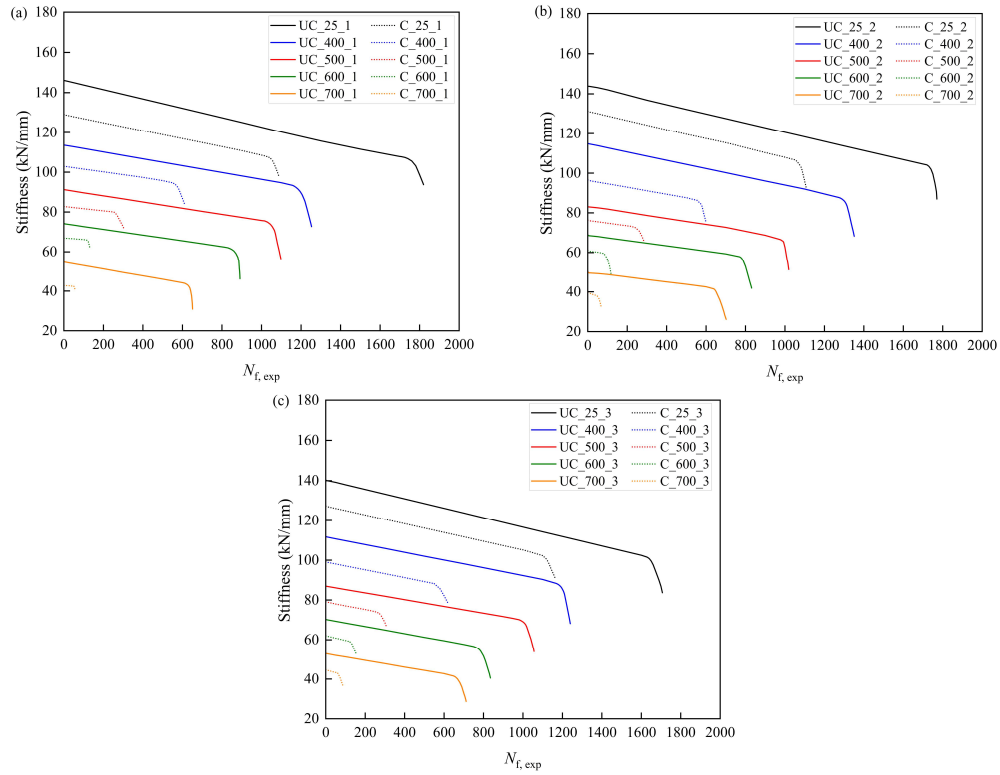


**Fig 5.11** Relation between stiffness and  $N_{f,exp}$ .

### 5.4.4 Energy dissipation capacity:

The integral of the load–displacement curve over one cycle gives the energy dissipation capacity per cycle, which is visualized as the area enclosed by hysteresis loop. Fig. 5.12 (a)–(c) illustrate the relation between energy dissipation capacity ( $W$ , kNmm) and number of cycles to failure,  $N_{f,exp}$ . Each curve demonstrates the presence of two stages in fatigue fracture: crack initiation and crack propagation. In the first stage, cyclic stabilization results in a constant value

of energy. During this stage, crack initiation dominates the majority of the cycle life in LCF testing. In the second stage, there is a significant reduction in energy dissipation capacity due to the growth of macrocracks, which ultimately leads to fracture and a notable decrease in specimen strength (Viswanathan, 1989).

A contrasting behaviour in  $W$  is observed in Fig. 5.12 (a)–(c) for corroded specimens exposed to 500 °C and above. These specimens demonstrate a declining trend in  $W$  from the first cycle, while others exhibit a cyclic stabilization regime. It may be attributed to the fact that corroded specimens tend to experience accelerated cyclic softening right from the initial stages. According to research, the cyclic softening behavior caused by dislocations in the microstructure, cell structure, and slip deformation band is accelerated at high temperatures (Park et al., 2001).

The estimates of total energy dissipation capacity ( $W_t$ , kNmm) are commonly used to assess the fatigue resistance of the reinforcing steel bar. The evaluation involves calculating the cumulative sum of the area under each cycle of a hysteresis curve until fracture occurs. Table 5.7 summarizes the result of  $W_t$  for all specimens, including their average and standard deviation. In uncorroded specimens: (i) compared to room temperature, an increase in temperature from 400 °C to 700 °C leads to a maximum decrease of 43% in  $W_t$  and (ii)  $W_t$  reduces by upto 15% between any two successive temperature values. In corroded specimens: (i) compared to room temperature, an increase in temperature from 400 °C to 700 °C leads to a maximum decrease of 91% in  $W_t$  and (ii)  $W_t$  reduces by upto 52% between any two successive temperature values. Moreover, for a given temperature,  $W_t$  decreases by upto 5.61 times in corroded specimens compared to uncorroded specimens. These observations indicate that corroded steel at high temperatures has significantly lower fatigue resistance than uncorroded steel. The practical importance of these findings is that the structures experiencing these conditions may have a significantly reduced fatigue life and may require immediate remedial intervention to restore their functionality.

A dimensionless analysis is performed to understand further the influence of exposure temperature on  $W_t$ . Fig. 5.13 shows the comparison between  $W_T^{\max} / W_{25}^{\max}$  and exposure temperature for the specimens. Here,  $W_T^{\max}$  refers to the maximum total energy dissipation capacity of the specimens at  $T$  °C. Whereas  $W_{25}^{\max}$  indicates the maximum total energy dissipation capacity of the specimen at 25 °C. As observed,  $W_T^{\max} / W_{25}^{\max}$  decreases with an increase in exposure temperature. For uncorroded specimens,  $W_{400}^{\max}$  is 84.1% of  $W_{25}^{\max}$ , and  $W_{700}^{\max}$

## Fatigue Behavior of Constructional Steels Subjected to Pitting Corrosion and Elevated Temperature

is 57.1% of  $W_{25}^{\max}$ . Whereas for corroded specimens,  $W_{400}^{\max}$  is 60.3% compared to  $W_{25}^{\max}$  and  $W_{700}^{\max}$  is only 10.6% of  $W_{25}^{\max}$ .

To find the mathematical relation between  $W_t$  and  $T$ , a linear regression using polynomial function of first degree is performed:

$$W_t = \varsigma_1 + \varsigma_2 T \quad (5.19)$$

where  $\varsigma_1$  and  $\varsigma_2$  are the regression coefficients. Linear regression yields  $\varsigma_1$  (17345.10) and  $\varsigma_2$  (−10.48) with a R-Square value of 0.953 for uncorroded specimens, and  $\varsigma_1$  (11928.20) and  $\varsigma_2$  (−15.55) with a R-Square value of 0.976 for corroded specimens. The trendlines fitted against the data points are shown in Fig. 5.14, and it can be observed that they are in good agreement.

**Table 5.7**  $W_t$  of specimens exposed to different temperatures.

Specimen	$W_t$ (kNmm)	Average of $W_t$ (kNmm)	Standard deviation of $W_t$ (kNmm)	Specimen	$W_t$ (kNmm)	Average of $W_t$ (kNmm)	Standard deviation of $W_t$ (kNmm)
UC_25_1	16762.71	16287.14	488.43	C_25_1	10640.60	10893.04	326.16
UC_25_2	16311.92			C_25_2	10777.22		
UC_25_3	15786.80			C_25_3	11261.30		
UC_400_1	13205.91	13493.43	528.16	C_400_1	6713.51	6722.56	69.37
UC_400_2	14102.98			C_400_2	6658.15		
UC_400_3	13171.41			C_400_3	6796.01		
UC_500_1	12773.22	12431.25	296.34	C_500_1	3731.67	3752.11	104.20
UC_500_2	12249.73			C_500_2	3659.65		
UC_500_3	12270.79			C_500_3	3865.02		
UC_600_1	11717.82	11023.95	617.94	C_600_1	1785.16	1798.82	231.22
UC_600_2	10532.95			C_600_2	1574.73		
UC_600_3	10821.07			C_600_3	2036.57		
UC_700_1	8942.61	9367.15	367.76	C_700_1	796.50	979.13	206.26
UC_700_2	9571.07			C_700_2	938.05		
UC_700_3	9587.77			C_700_3	1202.84		

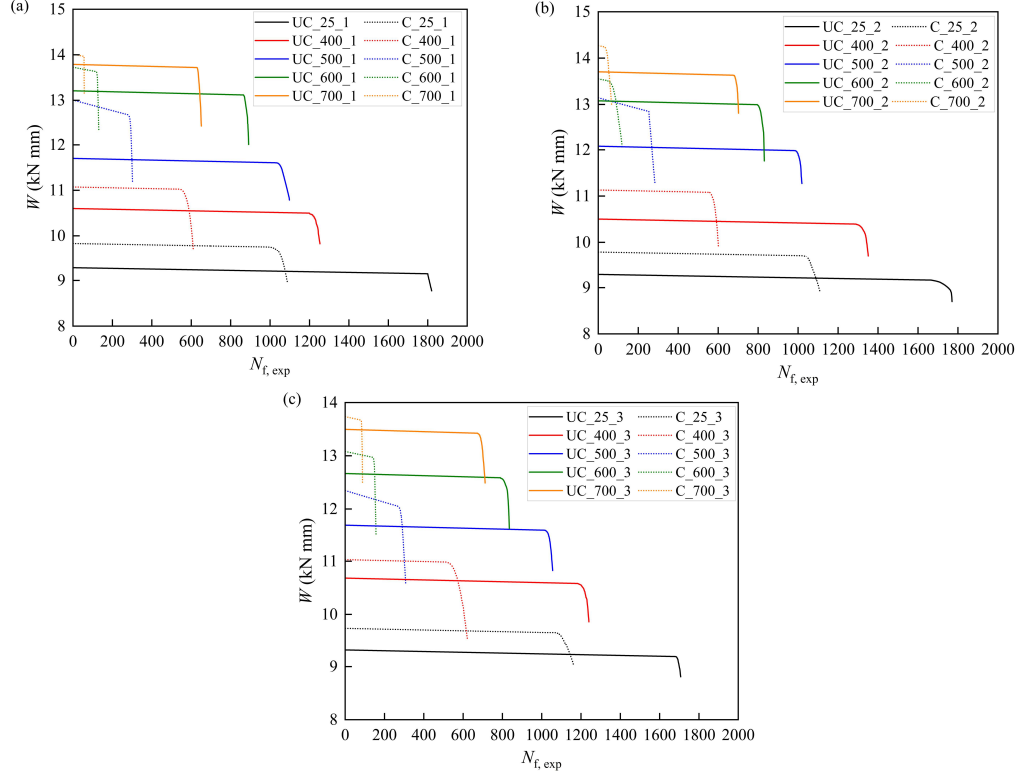


**Fig 5.12** Variation of energy dissipation capacity and number of cycles to failure.

To determine the relation between  $W_t$  and  $N_{f,exp}$ , a regression analysis is performed between the two variables using the values listed in Tables 5.6 and 5.7. A power-law having the following mathematical form is adopted (Callaghan et al., 2010):

$$W_t = C' (N_{f,exp})^{m'} \quad (5.20)$$

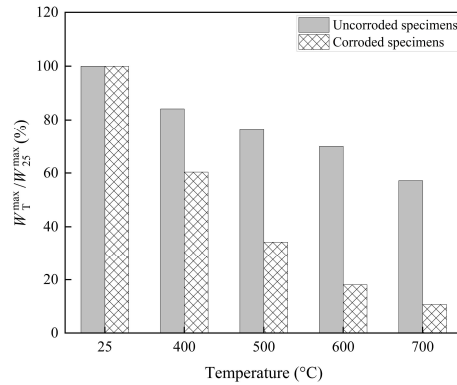


**Fig 5.13** Influence of high temperatures: a dimensionless comparison of  $W_T^{\max} / W_{25}^{\max}$ .

where  $C'$  denotes the fatigue toughness coefficient and  $m'$  represents the fatigue toughness exponent. A regression analysis is performed using Equation 5.20 and  $W_t$  values as data points.

## Fatigue Behavior of Constructional Steels Subjected to Pitting Corrosion and Elevated Temperature

The analysis resulted in coefficient values of  $C'$  (239.44) and  $m'$  (0.564) for uncorroded specimens with an R-Square value of 0.988. Further, values of  $C'$  (33.42) and  $m'$  (0.826) are obtained for corroded specimens with an R-Square value of 0.997. The trendlines based on Equation 5.20 are drawn over the data points of  $W_t$  for uncorroded and corroded specimens in Fig. 5.15 (a) and (b), respectively. It can be observed that the Equation 5.20 fits well with the experimental values of  $N_{f, \exp}$ .

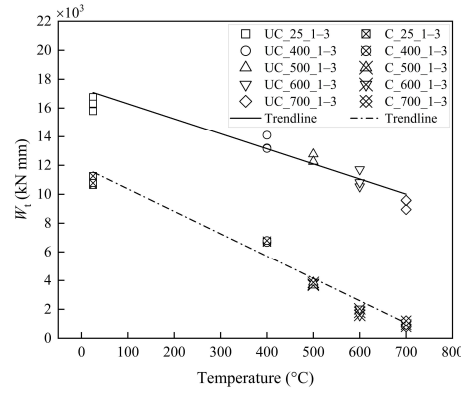


Fig 5.14 Relation between  $W_t$  and temperature.

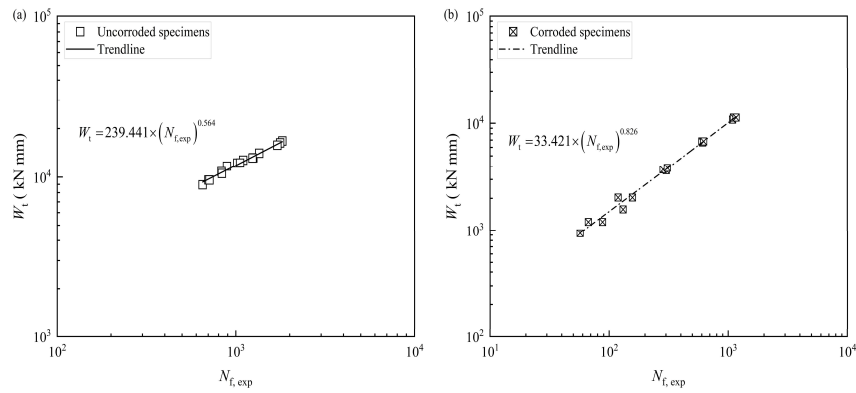


Fig 5.15 Variation of  $W_t$  with  $N_{f, \exp}$  : (a) uncorroded specimens; and (b) corroded specimens.

## 5.5 SED approach

In this section analytical equations are used to estimate SED based on Gaussian representation of corrosion pits. Researchers have adopted the concept of strain energy to evaluate the fatigue behaviour of notches/pits first under uniaxial stress condition and later under multiaxial stress condition (Jie et al., 2020; Molski & Glinka, 1981). With reference to Fig. 5.16, the components of stress in the vicinity of Gaussian shaped pit under Mode I loading can be described by (Filippi & Lazzarin, 2004):

$$\begin{Bmatrix} \sigma_\phi \\ \sigma_r \\ \tau_{r\phi} \end{Bmatrix} = \lambda_1 r^{\lambda_1-1} a_1 \left[ \begin{array}{l} \begin{Bmatrix} (1+\lambda_1)\cos(1-\lambda_1)\phi \\ (3-\lambda_1)\cos(1-\lambda_1)\phi \\ (1-\lambda_1)\sin(1-\lambda_1)\phi \end{Bmatrix} + \chi_{b_1}(1-\lambda_1) \begin{Bmatrix} \cos(1+\lambda_1)\phi \\ -\cos(1+\lambda_1)\phi \\ \sin(1+\lambda_1)\phi \end{Bmatrix} \\ + \frac{q}{4(q-1)} \left(\frac{r}{r_0}\right)^{\mu_1-\lambda_1} \left( \begin{array}{l} \chi_{d_1} \begin{Bmatrix} (1+\mu_1)\cos(1-\mu_1)\phi \\ (3-\mu_1)\cos(1-\mu_1)\phi \\ (1-\mu_1)\sin(1-\mu_1)\phi \end{Bmatrix} \\ + \chi_{c_1} \begin{Bmatrix} \cos(1+\mu_1)\phi \\ -\cos(1+\mu_1)\phi \\ \sin(1+\mu_1)\phi \end{Bmatrix} \end{array} \right) \end{array} \right] \quad (5.21)$$

where  $\sigma_\phi$ ,  $\sigma_r$  and  $\tau_{r\phi}$  are the stress components,  $\lambda_1$  is Williams' eigen value,  $\mu_1$  is additional exponent to express the stress field in the vicinity of the pit tip. Moreover,  $r$  and  $\phi$  are local polar coordinates. Further,  $\chi_{b_1}$ ,  $\chi_{d_1}$  and  $\chi_{c_1}$  are the linearly dependent terms, and are derived by applying local boundary condition on pit free edge. In addition, the parameter  $a_1$  is given as:

$$a_1 = \frac{\sigma_{\max}}{\lambda_1 r^{\lambda_1-1} \left\{ (1-\lambda_1) + \chi_{b_1}(1-\lambda_1) + [(1+\mu_1)\chi_{d_1} + \chi_{c_1}] \left[ \frac{q}{4(q-1)} \right] \right\}} \quad (5.22)$$

where  $\sigma_{\max}$  is the maximum principal stress. Moreover,  $r_0$  is the distance between the origin of the coordinate system and pit tip given by:

$$r_0 = \frac{q-1}{q} \rho \quad (5.23)$$

where  $q = (2\pi - 2\alpha)/\pi$ ,  $2\alpha$  is the notch opening angle, and  $\rho$  is the pit root radius. The total strain energy density for isotropic material and in the linear elastic region is expressed as (Lazzarin & Zambardi, 2001):

$$W_{t,SED} = \frac{1}{2E} \left\{ \sigma_{11}^2 + \sigma_{22}^2 + \sigma_{33}^2 - 2\nu(\sigma_{11}\sigma_{22} + \sigma_{11}\sigma_{33} + \sigma_{22}\sigma_{33}) + 2(1+\nu)\sigma_{12}^2 \right\} \quad (5.24)$$

where  $\sigma_{11}$ ,  $\sigma_{22}$ ,  $\sigma_{33}$ , and  $\sigma_{12}$  are the stress components in the given reference system,  $E$  is the modulus of elasticity of the material and  $\nu$  is Poisson's ratio. Under mode I loading, the critical volume or the control volume is the circle having a radius  $R_c$  which is centered at the pit tip (Fig. 5.16). Moreover, the energy within a small volume near the pit is always finite, regardless of its characteristics. Evidently, over a small volume of material close to the pit tip there is always some finite value of energy. The control radius over which the energy is averaged is a material dependent property such as the fracture toughness and ultimate tensile strength of the material (Lazzarin & Zambardi, 2001).

## Fatigue Behavior of Constructional Steels Subjected to Pitting Corrosion and Elevated Temperature

The radius of curvature for Gaussian profile can be estimated by:

$$R = \left[ 1 + (p'_d)^2 \right]^{3/2} (p''_d)^{-1} \quad (5.25)$$

By substituting the mathematical expression given in Equation 5.2 into Equation 5.25,  $\rho$  for the Gaussian profile is estimated as:

$$\rho = \frac{\left[ 1 + \left( 2\nu_1 \nu_2 \theta e^{-\nu_2 \theta^2} \right)^2 \right]^{3/2}}{2\nu_1 \nu_2 e^{-\nu_2 \theta^2} - 4\nu_1 \nu_2^2 \theta^2 e^{-\nu_2 \theta^2}} \quad (5.26)$$

Further, with reference to Fig. 5.16, following SED approach, the critical radius  $R_c$  of control volume can be expressed in a simplified form as (Yosibash et al., 2004):

$$R_c = \frac{(1+\nu)(5-8\nu)}{4\pi} \left( \frac{K_{IC}}{\sigma_t} \right)^2 \quad (5.27)$$

where  $\sigma_t$  is the fracture stress and equal to yield stress of the material and  $K_{IC}$  is fracture toughness. Note that  $R_c$  for the Gaussian pit is evaluated as given in Table 5.8. Further, with reference to (Fig. 5.16), area of the control volume  $\Omega$  is expressed as:

$$\Omega = \int_{R_1(\phi)}^{R_2} \int_{-\bar{\phi}}^{+\bar{\phi}} r dr d\phi \quad (5.28)$$

where radius  $R_2$  describes the domain that intersects the curvilinear pit tip and  $R_{1(\phi)}$  describe the domain. The elastic strain energy is expressed as:

$$E_1^e = \int_{\Omega} W_{t,SED} d\Omega = \int_{-\bar{\phi}}^{+\bar{\phi}} d\phi \int_{R_1(\phi)}^{R_2} W_{t,SED}(r, \phi) r dr \quad (5.29)$$

where  $R_{1(\phi)}$  and  $R_2$  are as shown in Fig. 5.16. The energy can also be expressed in more explicit form as (Lazzarin & Berto, 2005):

$$E_1^e = \frac{1}{2E} \left[ \frac{\sigma_{\max} \sqrt{2\pi}}{r_0^{\lambda_1-1} (1 + \bar{\omega}_1)} \right]^2 I_1 \quad (5.30)$$

where  $\bar{\omega}_1$  depends on pit opening angle while  $I_1$  depends on Poisson's ratio and pit opening angle. The mean value of strain energy is finally expressed as (Lazzarin & Berto, 2005):

$$\Delta \bar{w} = \frac{1}{E} \left( \frac{I_1}{2\Omega} \right) \sigma_{\max}^2 r_0^{2(1-\lambda_1)} \left[ \frac{\sqrt{2\pi}}{\bar{\omega}_1} \right]^2 \quad (5.31)$$

Under fatigue loading, the average value of strain energy density range over a control volume is expressed as (Gallo & Berto, 2015):

$$\Delta \bar{w} = \varepsilon_w k_t^2 \frac{1}{E} \left( \frac{I_1}{2\Omega} \right) \sigma_{\max}^2 r_0^{2(1-\lambda_1)} \left[ \frac{\sqrt{2\pi}}{\bar{\omega}_1} \right]^2 \quad (5.32)$$

where  $\varepsilon_w$  takes into account the nominal load ratio in SED evaluation:  $\varepsilon_w = 1.0$  for  $R = 0$  and  $\varepsilon_w = 0.5$  for  $R = -1$  (Berto et al., 2014).

### 5.5.1 Pit sensitivity function:

In this section, a temperature-dependent pit sensitivity function is proposed. Firstly, fatigue pit factor ( $P_f$ ), the ratio between the fatigue strength of uncorroded specimens at room temperature and the fatigue strength of corroded specimens at various temperatures is evaluated. To evaluate  $P_f$ , the number of reference cycles needs to be fixed. In the past, the values of 100 cycles or 500 cycles were used in specimens (Sharifi & Rahgozar, 2009; Zhang et al., 2015). In this study, a reference cycle of 100 is used. The temperature-dependent pit sensitivity function is evaluated as follows:

$$P_s(T) = \frac{P_f - 1}{k_t - 1} \quad (5.33)$$

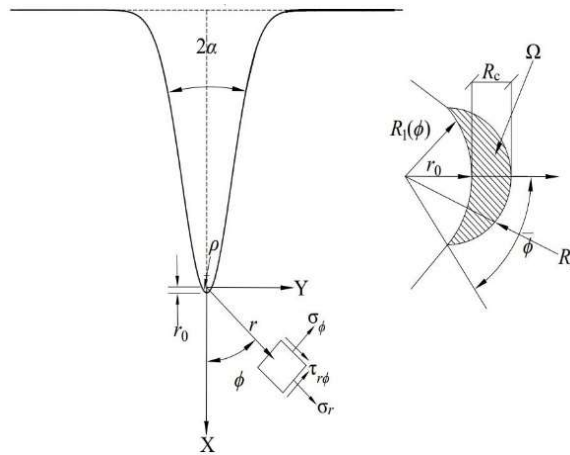


**Fig 5.16** Gaussian pit: reference system, stress components, and control volume.



**Table 5.8** Parameters for the stress distributions of Gaussian model.

Specimen	$2\alpha$ (degrees)	$q$	$I_1$	$\lambda_1$	$\bar{a}_1$	$r_0$ (mm)	$2\Omega$ (mm <sup>2</sup> )	$\rho$ (mm)	$R_c$ (mm)	$r_2$ (mm)
C_25_1	137.00	1.238	0.613	0.684	0.412	0.025	0.013	0.130	0.05	0.077
C_25_2	136.69	1.240	0.061	0.682	0.415	0.020	0.009	0.107	0.042	0.063
C_25_3	136.02	1.244	0.616	0.679	0.422	0.027	0.015	0.139	0.055	0.082
C_400_1	134.44	1.253	0.621	0.671	0.437	0.024	0.011	0.120	0.048	0.072
C_400_2	134.61	1.252	0.621	0.672	0.435	0.021	0.008	0.104	0.042	0.063
C_400_3	135.13	1.249	0.619	0.674	0.430	0.023	0.011	0.120	0.048	0.071
C_500_1	133.48	1.258	0.625	0.668	0.445	0.023	0.011	0.116	0.046	0.070
C_500_2	133.74	1.256	0.624	0.669	0.443	0.025	0.013	0.126	0.050	0.076
C_500_3	133.68	1.257	0.624	0.668	0.444	0.021	0.008	0.103	0.041	0.062
C_600_1	133.89	1.256	0.623	0.669	0.442	0.026	0.013	0.129	0.051	0.078
C_600_2	133.95	1.255	0.623	0.669	0.441	0.028	0.015	0.138	0.055	0.083
C_600_3	133.30	1.259	0.625	0.667	0.447	0.024	0.011	0.119	0.048	0.072
C_700_1	132.25	1.265	0.628	0.663	0.457	0.027	0.014	0.131	0.052	0.080
C_700_2	132.97	1.261	0.626	0.666	0.450	0.025	0.012	0.122	0.049	0.074
C_700_3	133.93	1.261	0.626	0.666	0.451	0.029	0.016	0.140	0.056	0.085

The variation of  $P_s(T)$  with  $T$  has been depicted in Fig. 5.17. A regression analysis is conducted using an exponent growth function over the data points to find the trendline of  $P_s(T)$ . The mathematical function is given as:

$$P_s(T) = \xi_1 + \xi_2 e^{\xi_3 T} \quad (5.34)$$

where  $\xi_1$ ,  $\xi_2$  and  $\xi_3$  are regression parameters. Regression resulted in  $\xi_1 = 4.7 \times 10^{-3}$ ,  $\xi_2 = 3.14 \times 10^{-4}$  and  $\xi_3 = 7.62 \times 10^{-3}$ , respectively. The parameter  $\xi_1$  is the offset term,  $\xi_2$  represents the initial value at  $T = 25^\circ\text{C}$ , and  $\xi_3$  signifies the growth rate, i.e. the rate at which  $P_s(T)$  increases exponentially with temperature.

Regression analysis resulted in a R-Square value of 0.993. Fig. 5.17 also shows the trendline based on Equation 5.34 drawn over the data points. The proposed mathematical function fits the data points well. It is important to point out that temperature significantly affects LCF properties of corroded and uncorroded steel specimens, specifically at temperatures above 500 °C. LCF properties of reinforcing steel bars at temperatures above 500 °C are essential as they reflect real-life exposure conditions.

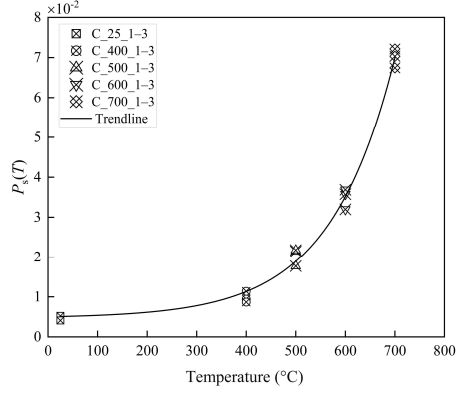


**Fig 5.17** Variation of  $P_s(T)$  with temperature.

Introducing  $P_s(T)$ , Equation 5.32 gets modified as:

$$\Delta \bar{w} = \varepsilon_w P_s(T) k_t^2 \frac{1}{E} \left( \frac{I_1}{2\Omega} \right) \sigma_{\max}^2 r_0^{2(1-\lambda_1)} \left[ \frac{\sqrt{2\pi}}{\bar{\omega}_1} \right]^2 \quad (5.35)$$

### 5.5.2 Variation of average SED:

The variation of average strain energy density,  $\Delta \bar{w}$ , with the temperature has been shown in Fig. 5.18. As observed,  $\Delta \bar{w}$  increases gradually with  $T$  in uncorroded specimens but increases drastically with  $T$  in corroded specimens. In corroded specimens, about a three-fold increase in  $\Delta \bar{w}$  is observed with an increase in temperature from 25 °C to 700 °C. Regression analyses are performed to find the trends of  $\Delta \bar{w}$  with  $T$  for both types of specimens. The mathematical forms of the following types are used:

$$\Delta \bar{w} = \begin{cases} \mathcal{Q}_1 + \mathcal{Q}_2 T & \text{Uncorroded specimens} \\ \psi_1 + \psi_2 e^{\psi_3 T} & \text{Corroded specimens} \end{cases} \quad (5.36)$$

where  $\mathcal{Q}_1$ ,  $\mathcal{Q}_2$ ,  $\psi_1$ ,  $\psi_2$ , and  $\psi_3$  are regression parameters. Note that two different mathematical equations are used to find the trendlines of  $\Delta \bar{w}$ . A linear equation is used for uncorroded specimens. In contrast, an exponential function is used for corroded specimens. The regression coefficients are obtained as  $\mathcal{Q}_1 = 0.1386$  and  $\mathcal{Q}_2 = 0.0170$  for the linear function and  $\psi_1 = 0.1893$ ,  $\psi_2 = 0.0120$ , and  $\psi_3 = 0.0076$  for the exponential function. Fig. 5.18 shows the trendlines based on Equation 5.36; it can be observed that the linear function fits well in uncorroded specimens ( $R^2 = 0.968$ ) while the exponential function fits well in corroded specimens ( $R^2 = 0.991$ ).

## Fatigue Behavior of Constructional Steels Subjected to Pitting Corrosion and Elevated Temperature

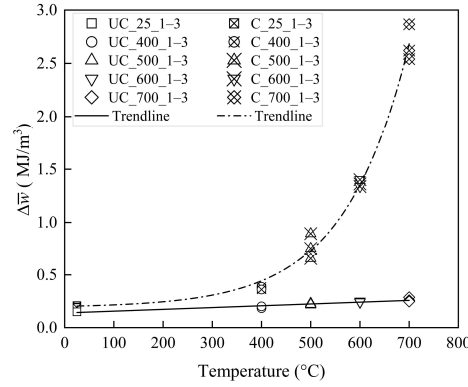


**Fig 5.18** Variation of  $\Delta \bar{w}$  with temperature.

### 5.5.3 Pit opening angle:

The normal stress at the pit tip of a Gaussian profile can be evaluated by using the analytical solution based on the stress distribution around an elliptical hole reported in (CE, 1913). However, to apply the solution to the Gaussian profiled pit an accuracy index of the following form is adopted (Filippi & Lazzarin, 2004):

$$\nabla = \frac{1}{0.4\rho} \int_0^{0.4\rho} [\sigma_{nn} - \sigma_{\phi}]^2 dr \quad (5.37)$$

where  $\sigma_{nn}$  is normal stress for mode I loading and  $0.4\rho$  signifies the distance in the vicinity of pit where pit effect disappears, and crack and pits have similar stress values (Atzori et al., 2001).

The variation in normalized index  $\nabla/\sigma_{\max}^2$  is shown in Fig. 5.19 with pit opening angle  $2\alpha$ . As observed, an increase in  $p_d^{\max}/w$  leads to a decrease in  $\nabla/\sigma_{\max}^2$ . In addition, the minimum value of  $\nabla/\sigma_{\max}^2$  marginally increases. By interpolating numerical data shown in Fig. 5.19, following interpolating law for opening angle of inverted Gaussian function can be derived:

$$2\alpha = 198.59 \left( 1 + 2 \frac{p_d^{\max}}{w} \right)^{-0.934} \quad (5.38)$$

Note that interpolation coefficients obtained in this study (198.59, -0.934) are marginally different from that obtained for an elliptical notch (192.64, -0.916) as reported in literature (Filippi & Lazzarin, 2004). Further, the value of  $2\alpha$  becomes  $71.17^\circ$  when  $p_d^{\max} = w$ , representing a circular pit. This can also be justified based on other theoretical considerations related to free edge effects (Filippi & Lazzarin, 2004).

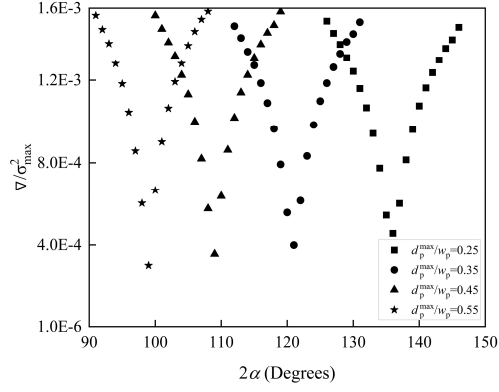


**Fig 5.19** Variation of normalized index with Gaussian pit opening angle.

#### 5.5.4 Evaluation of $N_{f,est}$

To obtain a convenient expression for fatigue life estimation of reinforcing steel bar,  $\Delta\bar{w}$  vs  $N_{f,exp}$  is plotted as shown in Fig. 5.20. The scattered plot is represented on a log-log scale. Note that  $\Delta\bar{w}$  is evaluated using Equation 5.35 and the values are listed in Table 5.9. The plot shows a narrow scatter band. The scatter band in the plot is evaluated for probability of survivals ( $P_s$ ) equal to 2.3% and 97.7%, respectively. The bottom curve ( $P_s = 97.7\%$ ) is obtained by subtracting standard deviation twice from the mean values. The scatter index is  $T_{\Delta w} = 4.566$  with an inverse slope of  $k = 1.501$  and  $\bar{w}_a = 0.123 \text{ MJ/m}^3$ . In the scatter plot  $N_r$  signifies reference cycles to failure used in this study. Note that  $N_r$  is taken as  $5 \times 10^3$  cycles. An appropriate expression for  $\Delta\bar{w}$  vs  $N_{f,exp}$  for reinforcing steel bar subjected to LCF can be represented as (Jie et al., 2020):

$$\Delta\bar{w}^k \times N_{f,est} = \Delta\bar{w}_a^k \times N_r \quad (5.39)$$

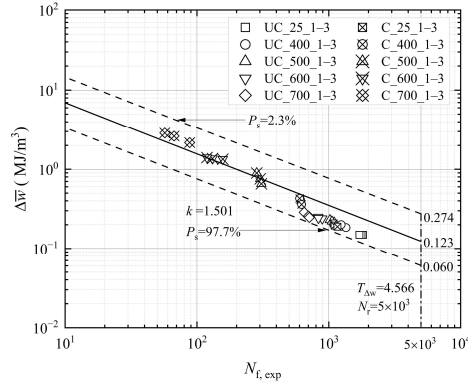


**Fig 5.20** Relation between average SED and  $N_{f,exp}$ .

## Fatigue Behavior of Constructional Steels Subjected to Pitting Corrosion and Elevated Temperature

A comparison between the estimated cycles to failure  $N_{f, \text{ est}}$  and experimental cycles to failure  $N_{f, \text{ exp}}$  is shown in Fig. 5.21. Note that the entire data falls within an error band of 1.5. Thus, it can be stated that utilization of average SED approach is appropriate. Further, from Equation 5.39 estimated cycles to failure can be obtained as:

$$N_{f, \text{ est}} = \frac{\Delta \bar{w}_a^k \times N_r}{\Delta \bar{w}^k} \quad (5.40)$$

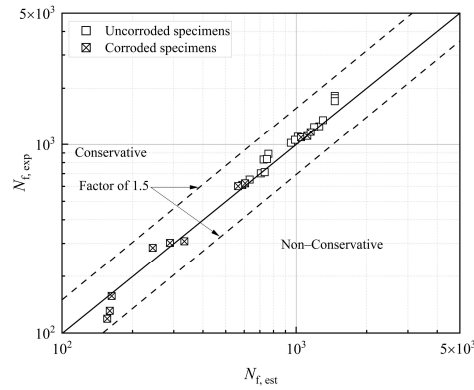


**Fig 5.21** Comparison between experimental and estimated value of  $N_f$ .

**Table 5.9** Comparison between experimental  $N_{f, \text{ exp}}$  and estimated  $N_{f, \text{ est}}$  of specimens.

Specimen	$\Delta \bar{w}$ (MJ/m <sup>3</sup> )	$N_{f, \text{ exp}}$	$N_{f, \text{ est}}$	Error (%)	Specimen	$\Delta \bar{w}$ (MJ/m <sup>3</sup> )	$N_{f, \text{ exp}}$	$N_{f, \text{ est}}$	Error (%)
UC_25_1	0.149	1820	1461	19.73	C_25_1	0.207	1089	1049	3.67
UC_25_2	0.149	1770	1461	17.46	C_25_2	0.195	1108	1116	-0.72
UC_25_3	0.149	1707	1461	14.41	C_25_3	0.189	1164	1153	0.95
UC_400_1	0.174	1253	1255	-0.16	C_400_1	0.370	610	589	3.44
UC_400_2	0.168	1351	1302	3.63	C_400_2	0.386	601	565	5.99
UC_400_3	0.182	1240	1194	3.71	C_400_3	0.361	622	605	2.73
UC_500_1	0.214	1098	1017	7.38	C_500_1	0.756	302	289	4.30
UC_500_2	0.230	1019	949	6.87	C_500_2	0.894	284	244	14.08
UC_500_3	0.221	1056	988	6.44	C_500_3	0.655	308	333	-8.12
UC_600_1	0.287	891	761	14.59	C_600_1	1.361	131	160	-22.14
UC_600_2	0.300	831	726	12.64	C_600_2	1.402	119	156	-31.09
UC_600_3	0.290	835	750	10.18	C_600_3	1.337	157	163	-3.82
UC_700_1	0.344	651	633	2.76	C_700_1	2.866	57	76	-33.33
UC_700_2	0.310	702	706	-0.57	C_700_2	2.620	67	83	-23.88
UC_700_3	0.300	712	734	-3.09	C_700_3	2.164	88	101	-14.77

Thus,  $N_f$  values are comparable for uncorroded and corroded specimens. However, a few specimens have a higher error percentage. Possible reasons for the observed results include specimen sensitivity, system errors during the experiment, and the sensitivity of the specimens to stress range (Wang et al., 2016). Nevertheless, Equation 5.40 is capable of predicting cycles to failure under LCF condition.

## 5.6 Fractographic analysis

In this section, fatigue fracture morphology of the specimens is investigated SEM and EDS. The failure surface of the specimen is depicted in Fig. 5.22 (a). It is observed that fracture is more likely to occur in the minimum area of cross section surrounding a corrosion pit. This is attributed to the presence of high stress concentration, which is the key parameter concerning crack origin. Further, in the figure marked are the fatigue crack sources, fatigue crack initiation site, fatigue crack propagation site and fracture area. Moreover, the fatigue fracture morphology can be identified by dashed lines in red contrast. SEM image of the fatigue failure surface is shown in Fig. 5.22 (b). It can be observed that fracture initiates at multiple sites. In particular, cracks originate from the corrosion pit. Furthermore, smooth failure surface marks the crack initiation area. Note that crack initiation, in general, occurs due to the formation of slip bands resulting from progressive to-and-fro movement of the specimen accompanied by the formation of intrusion and extrusion at the failure surface. Continued cyclic loading induces the formation of the additional slip bands, which subsequently develop into microcracks (Campbell, 2012).

Despite occurring across different microstructural features (grain boundaries or slip bands), the microscopic processes influencing short crack growth exhibit close similarities. These include blunting at the crack tip, branching around the tip, and subsequent dominance of one specific branch for continued growth. The crack path shown in Fig. 5.22 (c) exhibits frequent branching. From the branched crack, a complex pattern emerges as it continued to grow. Meanwhile, another crack formed and assumed the role of the main crack, continuing its own growth. Similar crack branching is also reported in the literature (Korda et al., 2006; Mishnev et al., 2017).

The fatigue failure surfaces of corroded specimens exposed to high temperatures are depicted in Fig. 5.22 (d)–(j). According to Fig. 5.22 (d), transverse or secondary microcracks are formed on the failure surface along with fine striation marks accompanied by smaller voids. The striation marks are an important fractographic feature characterized by parallel, closely spaced marks. At a temperature of 400 °C there are clusters of dimples and microcavities as shown in Fig. 5.22 (e). The dimples, in general, are the indicative of better ductility of the material confirmed by (Li et al., 2014). Exposure to higher temperatures can cause an increase in the size of dimples, resulting in deeper dimples. This is because the interaction forces between

## **Fatigue Behavior of Constructional Steels Subjected to Pitting Corrosion and Elevated Temperature**

the crystal particles increase when the specimen is exposed to high temperature. Subsequently, failure occurs when the specimen experiences higher tensile force or deformation (Ba et al., 2022).

A large number of fine carbide particles are visible at a temperature of 500 °C (Fig. 5.22 (f)). The heating of the specimen causes the additional tempering of martensite phase of steel resulting in release of excess carbon and disintegrating into ferrite. As the temperature is increased to 500 °C tire track marks, having a line profile and deeper voids are visible near the crack propagation area (Fig. 5.22 (g)). The presence of tire track marks is indicative that surface fracture is due to LCF. Similar tire track fractographic features were reported in notched specimens (Attarian et al., 2023). Moreover, the tire track fractographic features are observed in corroded specimen exposed to high temperatures (Fig. 5.22 (g)). The fracture surface constitutes of valleys and ridges in the lower and upper halves of the surface. As the cycling loading continues the two halves will dislocate laterally. Sharp projections protruding on one surface of ridge will make indent on the other surface of the valley leading to the formation of tire track on the surface. These marks are oriented perpendicular to the direction of the crack propagation.

High temperature exposure results in the large number of voids and cracks of irregular shape. As observed in Fig. 5.22 (h), specimen exposed to a temperature of 600 °C reveals stair case pattern, indicating the crack propagation area. Along with stair case pattern, cluster of dimples and deep voids can also be seen. One possible explanation for the development of deeper voids is the occurrence of slip bands during cyclic loading. These slip bands are formed due to tensile forces and promote the growth of corrosion products ( $\text{Fe}_3\text{O}_4$ ). This interaction with the sub-surface steel can lead to irreversible damage (Zhao et al., 2012).

The crack propagation region is also signified by the presence of striation marks, tear ridge and beach marks or clamshell marks. Clamshell marks or beach marks are generally macroscopic feature and are indicative of crack propagation from crack initiation (Fig. 5.22 (i)). The formation of beach marks on the fractured surface is attributed to oxidation and changes in load. This observation is supported by the hysteresis curve, which shows a continuous decrease in the maximum load during cycles to failure under temperature exposure.

At a temperature of 700 °C, there is a notable increase in the occurrence of irregular cracks, as well as the presence of dense microcracks. The deeper voids are results of oxidation of corroded pit surface. The combined effects of elevated temperature and fatigue damage on the interior microstructure of the corroded steel specimen are clearly visible in figure Fig. 5.22 (j). The transverse microcracks expanded even more with temperature exposure. One possible

explanation is that the oxides formed during the corrosion process, such as hematite and magnetite, tend to exhibit a brittle phase, while the wustite behaves in the ductile manner (Gutiérrez-Castañeda et al., 2015). The oxides adhere well to the slip band surface. Magnetite, in particular, has abrasive properties and can easily penetrate the steel surface under cyclic loading. As cyclic loading continues, the oxide layers break and disrupt the steel subsurface, significantly contributing to crack initiation and propagation (Zhao et al., 2012).

The presence of tear-like structures in Fig. 5.22 (j) contributes to a rougher fracture morphology. At elevated temperatures, micro cracks can grow and propagate under cyclic loading, resulting in the formation of metal necking. A sufficient number of metal necking formations can lead to the growth of tear-like structures (Zhang et al., 2021). The final fracture surface shows honeycomb-like dimples and micro voids that increase in depth and volume when exposed to temperatures above 500 °C. The non-uniform distributions of dimples are common fatigue fracture feature found in metallic materials (Zhang et al., 2021).

At room temperature, fine striation marks are visible. To determine the spacing of these marks, ImageJ software was used to analyze samples at specific temperatures: 25 °C, 400 °C, 500 °C, 600 °C, and 700 °C. The spacing between striation marks was measured at different temperatures. At 25 °C, the spacing was found to be 1.28 mm. At 400 °C, it was 1.410 mm, at 500 °C it was 1.775 mm, at 600 °C it was 1.935 mm, and at 700 °C it was 2.455 mm. There is a noticeable 1.7-fold increase in the spacing of striation marks when the temperature rises from 25 °C to 700 °C. Note that the striation spacing measured in this study at 25 °C is comparable to that reported in (Bakkar et al., 2020). Similarly, width of microcracks was also measure. At 25 °C, width of the microcracks was 0.782 mm, at 400 °C it was 1.109 mm, for 500 °C it was 1.4025 mm, at 600 °C it was 1.876 mm, and at 700 °C it was 2.58 mm.



## Fatigue Behavior of Constructional Steels Subjected to Pitting Corrosion and Elevated Temperature

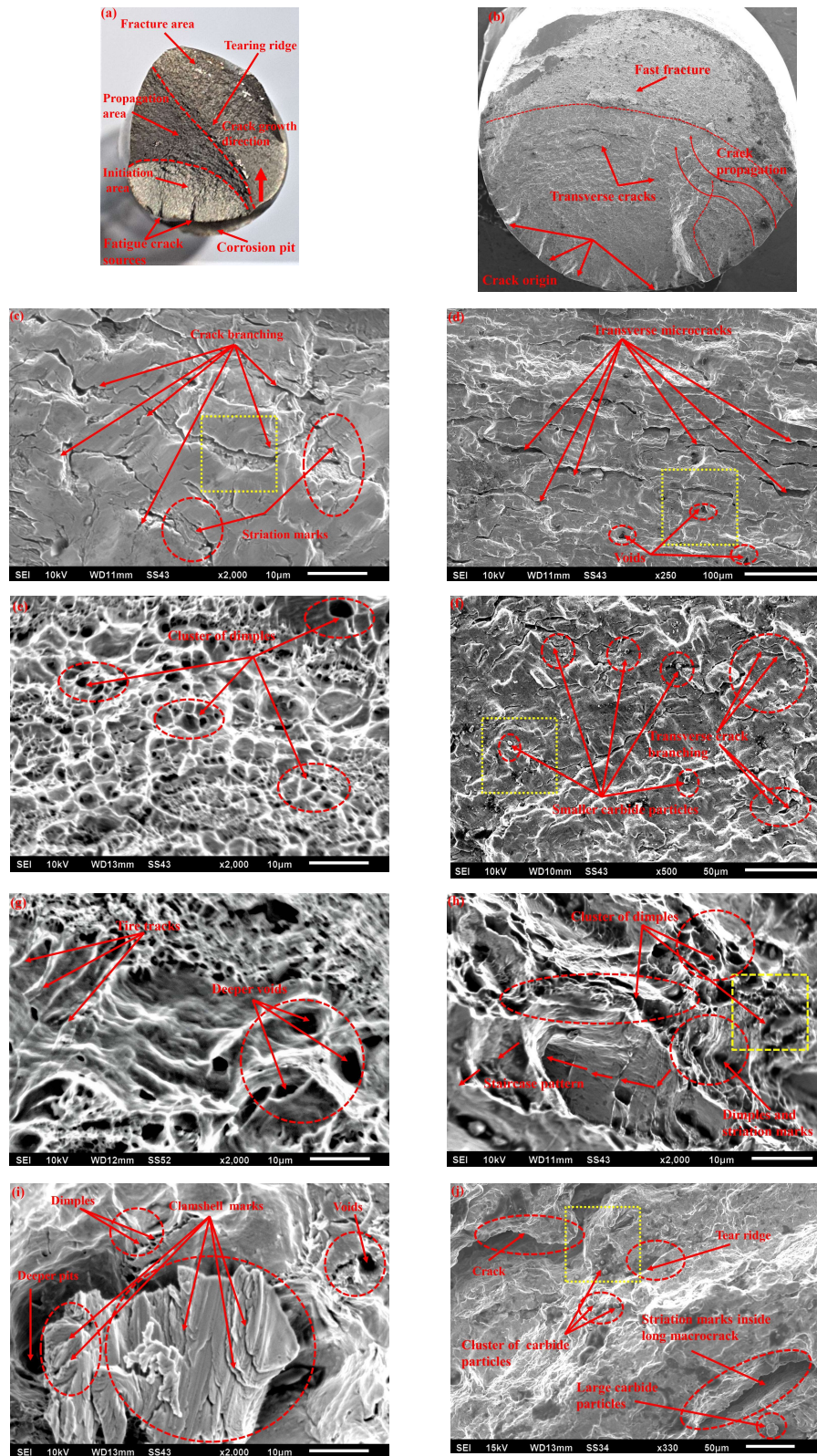


**Fig 5.22** Fractographic analysis of fracture surface: (a) corrosion pit; (b) failure surface; (c) C\_25\_1; (d) C\_400\_1; (e) C\_400\_3; (f) C\_500\_1; (g) C\_500\_3; (h) C\_600\_1; (i) C\_700\_1; and (j) C\_700\_3.

The EDS spectrums of the specimens are illustrated in Fig. 5.23. The dashed line square markings in yellow contrast on the SEM images represent the zone analysed using EDS. Based on the figure, it is evident that as the temperature increases from 25 °C to 700 °C, there is an increase in the concentration of carbon (C) and oxygen (O) by a factor of up to 2.7 and 1.4 respectively. However, iron concentration (Fe) reduces by a factor of 9.0. The increase in the level of O signifies the formation of higher amount of iron oxides. The oxygen level increases by a factor of 1.12 when the temperature rises from 25 °C to 400 °C. From 400 °C to 700 °C, the oxygen level jumps by a factor of 1.3. Similarly, for an increase in temperature from 25 °C to 400 °C carbon level increases by a factor of 1.40 and by a factor of 2.0 for a rise in temperature from 400 °C to 700 °C. The sudden increment in the level of C and O is due to the fact that oxides formed continuously during corrosion process are transformed at high temperature. The dehydroxylation of various form of FeOOH formed during temperature exposure leads to formation of microporosity due to ejection of water. The chemical reaction is expressed as (Cornell & Schwertmann, 2003):

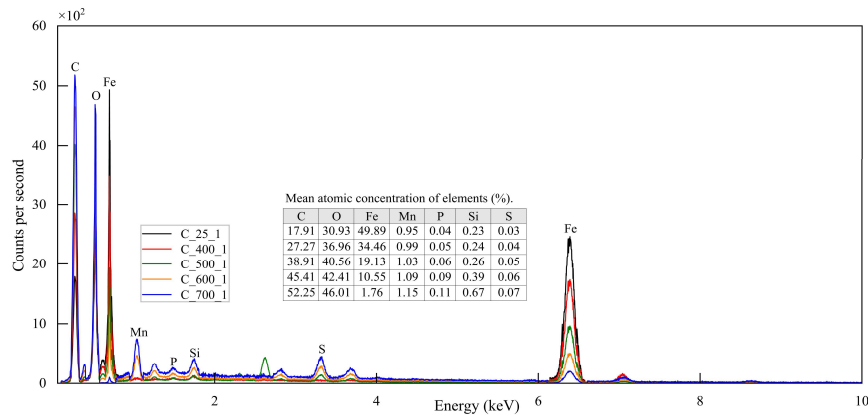


**Fig 5.23** EDS spectrum of the corroded specimens.

High temperature exposure results in micropore clusters that become mesopores, aided by an increase in surface area. At temperatures above 600 °C, hydroxo-bonds convert to oxo-bonds and face sharing between octahedra leads to denser structures (Cornell & Schwertmann, 2003). It can be observed from the figure that concentration of Fe depletes at a higher rate. At temperature less than 700 °C oxidation of carbon is lower than the oxidation of Fe since carbon has very less or no solubility in the scale layer. The ejected carbon present in the layer due to fast oxidation of iron must remain at the interface of scale and steel substrate, results in enrichment of excess carbon (Plumensi et al., 1969). If this excess carbon exceeds the solubility of carbon it leads to precipitation of solid carbon-graphite at the interface of the scale-steel (Caplan et al., 1979).

## **5.7 Conclusions**

The present study investigates the LCF behavior of pitting corroded high-strength ductile reinforcing bars at elevated temperatures (upto 700 °C) under stress-controlled conditions. Based on experimental results, including fractographic analysis of fracture surface, a model for the distribution of pitting corrosion penetration depth and an analytical expression for SCF are proposed. Fatigue tests are performed on corroded and uncorroded specimens at elevated temperatures to analyze the material's LCF strength. Further, prediction equations for corroded and uncorroded specimens are developed to correlate key fatigue parameters, including pit sensitivity function, number of cycles to failure, total energy dissipation capacity, and average SED with temperature. The following are the major conclusions derived from this research.

- i. The distribution of pitting corrosion penetration depth along the perimeter of the reinforcing bar is better represented by the inverted Gaussian function. The proposed analytical equation for calculating the SCF based on the Gaussian function shows a deviation of only 7% compared to the FE analysis.
- ii. While uncorroded bar exhibits a notable cyclic softening behavior under fatigue, this phenomenon occurs significantly faster in corroded specimens, requiring fewer cycles to reach the same softening level. Furthermore, high temperatures exacerbate this behaviour.
- iii. In corroded specimens, total energy dissipation capacity reduces by upto 91% with an increase in temperature from 400 °C to 700 °C. This suggests infrastructures exposed to these conditions may face a substantial drop in fatigue life and require immediate intervention to maintain functionality.
- iv. Comparison between experimental  $N_f$  and that of estimated  $N_f$  obtained based on the average SED approach shows that the values for uncorroded and corroded specimens fall within a narrow error band of 1.5.
- v. Fractographic analysis of fractured corroded specimen surfaces reveals that elevated temperature exposure introduces a larger number of irregularly shaped voids and microcracks, clamshells or beach marks, a significant increase in dimples, and notable increases in the width and spacing of striation marks.

## Chapter 6

# Effect of High Temperature and Strain Amplitude on LCF Behavior of Pitting Corroded Killed E350 BR Structural Steel

---

## 6.1 Introduction

E350 steel, conforming to the Indian Standard IS 2062, widely used for various construction applications due to its advantageous mechanical properties. Additionally, its excellent weldability, facilitated by its controlled chemical composition and microstructure, enables efficient joining in fabrication processes. However, E350 steel exhibits moderate fatigue resistance due to its microstructure, which can be further enhanced through surface finishing techniques. This makes it suitable for applications experiencing cyclic loading, such as bridges and machinery. However, its fire resistance is limited, with significant property degradation above 500°C–600°C.

Corrosion is an inevitable challenge encountered in steel structures exposed to aggressive environments such as marine atmospheres and deicing salts. Despite the implementation of protective measures like coatings, significant corrosion issues persist, impacting both the appearance and mechanical properties of steel components, consequently compromising structural safety and durability. Addressing these concerns is imperative due to the potential consequences on structural integrity. Extensive research has been conducted to understand the corrosion–fatigue behavior of steel structures, focusing on various aspects such as anti–fatigue performance, low–cycle fatigue properties, and fatigue life prediction. However, fundamental research into the LCF properties of corroded structural steel remains limited.

Moreover, structural steels are vulnerable to strength reduction when exposed to fire, necessitating precise evaluation of post–fire structural performance. Studies have examined the mechanical properties of structural steel after fire exposure, with research indicating a significant influence of exposure temperature on residual mechanical properties. Considering the potential seismic events following fire incidents, understanding post–fire LCF properties of structural steel is crucial for assessing structural resilience. Further, studies investigating the LCF behavior of structural steel after high–temperature exposure are scarce lacking post–fire considerations. Fire–induced high temperatures significantly impact the residual tensile properties of structural steel due to microstructural transformations. These alterations can lead to varying degrees of change in the material's mechanical properties, fatigue resistance, and ultimately, its seismic performance. Therefore, investigating post–fire low–cycle fatigue properties of structural steel, particularly after exposure to high temperatures, becomes essential.

The objectives of the study are: (i) to conduct LCF tests on medium–strength hot–rolled structural E350 killed steel under the combined pitting corrosion and elevated temperature

## Fatigue Behavior of Constructional Steels Subjected to Pitting Corrosion and Elevated Temperature

conditions. The tests are performed under strain-controlled loading.; (ii) analyze the shape and characteristics of hysteresis curves for both corroded and uncorroded specimens under different strain amplitude conditions and at various exposure temperatures.; (iii) to quantify the fatigue behavior of E350 structural steel specimens exposed to different elevated temperatures, determining fatigue life and associated properties such as the ratio of fatigue life at elevated temperature to that at 25°C, and the ratio of total strain energy density at elevated temperature to that at 25°C; (iv) study develop a fatigue model to accurately quantify the relationship between applied strain amplitude and fatigue life of corroded E350 structural steel specimens exposed to different elevated temperatures; (v) the study aims to analyse the stress and strain properties at varying exposure temperatures and at different fatigue strain amplitudes; (vi) comparative analysis between experimentally determined fatigue life and that estimated using the average SED approach.

## 6.2 Materials and methods

### 6.2.1 Specimen preparation:

The specimens are made from IS 2062:2011 killed E350 BR steel plate. This steel grade belongs to medium-strength and high-tension types and is prepared by hot-rolling. Killed steel is deoxidized to a high degree, ensuring no gas is released during the solidification process. Aluminum, manganese, and silicon ferroalloys are most commonly used for the deoxidation (Singh, 2020). Table 6.1 provides the chemical composition of the steel, while Table 6.2 gives the mechanical properties of the steel in as-received condition from the manufacturer. The steel is lathed using a computer numerical control machine to achieve the desired geometry of the specimens following ASTM E606/E606M-12 guidelines. Fig. 6.1 depicts the specimen geometry. Each specimen measures 128 mm in total length, with a gauge length of 16 mm and a diameter of 8 mm. A total of 30 such specimens are prepared for conducting LCF tests. After lathing, the specimens are polished to achieve a bright mirror finish, ensuring a surface roughness of no more than 0.2 mm.

**Table 6.1.** Chemical composition of E350 (in wt. %).

Chemical composition	C	Mn	S	P	Si	Al	Cu	V	Nb	Ti	CEQ
Specimen	0.14	1.45	0.0020	0.014	0.31	0.026	0.006	0.002	0.018	0.012	0.38

**Table 6.2.** Mechanical properties of E350.

Tensile strength (MPa)	Yield strength (MPa)	Tensile strength/ Yield strength	Elongation (%)	Young's modulus (MPa)	Poisson's ratio
534	372	1.43	34	$2.1 \times 10^5$	0.30

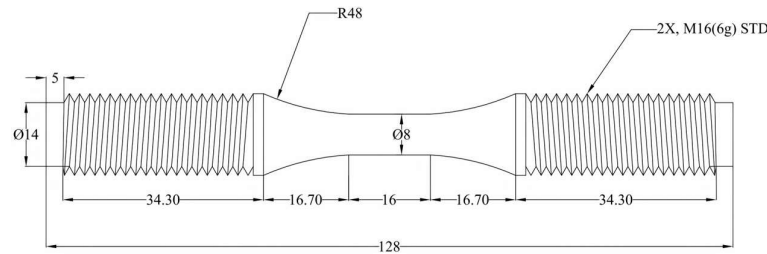


**Fig. 6.1** Specimen for fatigue testing (unit: mm).

### 6.2.2 Corrosion experiment:

This study employs an electrochemical accelerated corrosion technique. Fig. 6.2 depicts the corrosion setup. The specimens are fully insulated, with a 5 mm diameter region left at the center of the gauge length. The specimen is connected to an electrical wire, and both ends are securely sealed with hot melt glue. Then, the specimen is placed in a tray with a 5% solution, acting as the anode, while stainless steel acts as the cathode. An impressed current of 0.5 A is applied directly to accelerate corrosion in the marked region for 20 minutes.

Following accelerated corrosion, the specimen is removed from the tray and cleansed in deionized water. The corrosion products are removed by immersing it in a chemical solution containing 500 ml hydrochloric acid, 500 ml water, and 3.5 g hexamethylenetetramine for 10 minutes. Further, the specimen is carefully washed with 99% pure ethanol by weight. Subsequently, the specimen is dried and kept in a desiccator for subsequent experiments. The procedure described above is repeated for all the specimens.

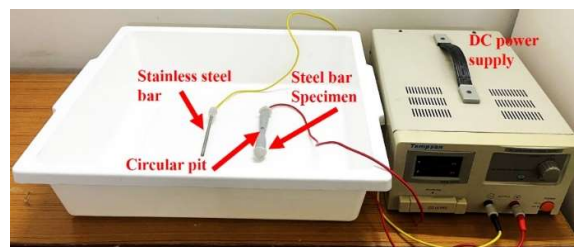


**Fig. 6.2** Corrosion experimental setup.



### 6.2.3 Pit Geometry evaluation:

A high-resolution three-dimensional laser scanner is employed to quantify the pit geometry of the specimens, such as width ( $w$ ), length ( $l$ ), and depth ( $p_d$ ). This technique recreates the specimen accurately, including pit geometry, by laser scanning the entire specimen with a scan density of 5 million points per scan. Fig. 6.3 (a) and (b) illustrate the three-dimensional laser scanned image of a specimen along with its pit dimensions, respectively. As noted, every specimen underwent pitting corrosion, a type of localized corrosion affecting a specific area of the steel bar. This corrosion pit acts as a stress raiser and can contribute to fatigue-induced damage. Further, the summary of pit geometry results for all specimens can be found in Table 6.3.

To quantify the severity of pitting corrosion,  $\eta_{\text{cri}}$  is commonly used.  $\eta_{\text{cri}}$  relates corrosion severity with cross-sectional area loss in the steel relative to the original area.  $\eta_{\text{cri}}$  is evaluated as:

$$\eta_{\text{cri}} = (1 - A_m/A_n) \times 100\% \quad (6.1)$$

where  $A_m$  and  $A_n$  represent specimen's minimum and nominal cross-sectional area ( $\text{mm}^2$ ), respectively.  $A_n$  has a value of  $50 \text{ mm}^2$ , while  $A_m$  is determined from the recreated images of the corrosion pit. The values of  $\eta_{\text{cri}}$  are given in Table 6.3. Further, the level of pitting corrosion can generally be classified as mild, moderate, or severe. According to the data, it has been determined that the pitting corrosion level in all specimens is classified as severe due to the value of  $\eta_{\text{cri}}$  being greater than 10% (Chauhan and Muthulingam, 2023).

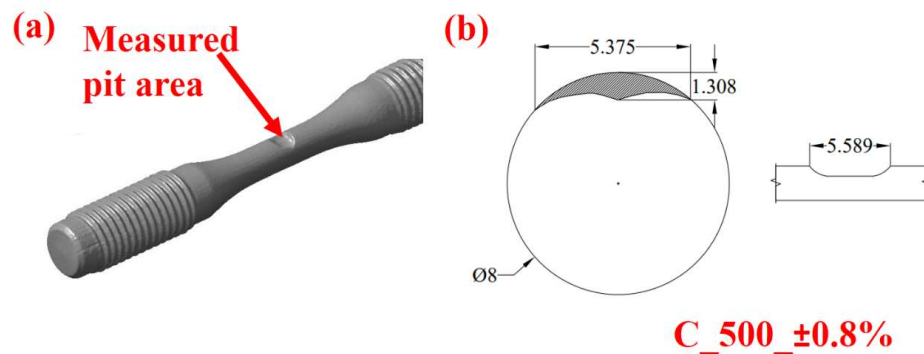


**Fig. 6.3** 3-D image of a specimen (a) 3D laser scan; and (b) pit morphology and dimensions (unit: mm).

**Table 6.3** Result summary of corrosion pit geometry using 3D laser scanning.

Specimen	Temperature (°C)	Pit geometry from 3D laser scanning			
		$p_d^{\max}$ (mm)	$w$ (mm)	$l$ (mm)	$\eta_{\text{cri}}$ (%)
C_25_±0.6%	25	1.343	5.313	5.473	12.242
C_25_±0.8%	25	1.225	5.267	5.584	12.099
C_25_±1.0%	25	1.358	5.419	5.221	12.445
C_400_±0.6%	400	1.223	5.526	5.373	12.523
C_400_±0.8%	400	1.298	5.201	5.399	12.468
C_400_±1.0%	400	1.321	5.209	5.291	12.157
C_500_±0.6%	500	1.276	5.283	5.421	12.212
C_500_±0.8%	500	1.308	5.375	5.589	12.087
C_500_±1.0%	500	1.319	5.431	5.393	12.057
C_600_±0.6%	600	1.321	5.484	5.392	11.643
C_600_±0.8%	600	1.284	5.572	5.543	11.663
C_600_±1.0%	600	1.285	5.285	5.358	12.154
C_700_±0.6%	700	1.318	5.456	5.489	11.594
C_700_±0.8%	700	1.312	5.271	5.692	11.598
C_700_±1.0%	700	1.301	5.191	5.501	11.650

#### 6.2.4 Corrosion depth distribution:

As shown in Fig. 6.3, the corrosion depth varies both along the perimeter and length of the specimen. It is critical to take into account the depth variation along the perimeter, as it can have a substantial effect on the mechanical strength of the specimen. Consequently, assessing the distribution of depth and recognizing any patterns is of considerable importance. In this regard, values of  $p_d$  along the perimeter specifically about the maximum corrosion depth ( $p_d^{\max}$ ) are extracted from the laser scan images. Various mathematical equations, such as linear, elliptical, parabolic, semi-elliptical, and Gaussian, are used to determine the trend of  $p_d$ . After analyzing multiple equations, it is determined an inverted Gaussian equation of the following form is more suitable for representing the trend in  $p_d$  along the perimeter.

$$p_d = -\zeta_1 \exp(-\zeta_2 \theta^2) \quad (6.2)$$

where  $\zeta_1$  and  $\zeta_2$  are fitting parameters, while  $\theta$  represents the polar angle (radians).



## Fatigue Behavior of Constructional Steels Subjected to Pitting Corrosion and Elevated Temperature

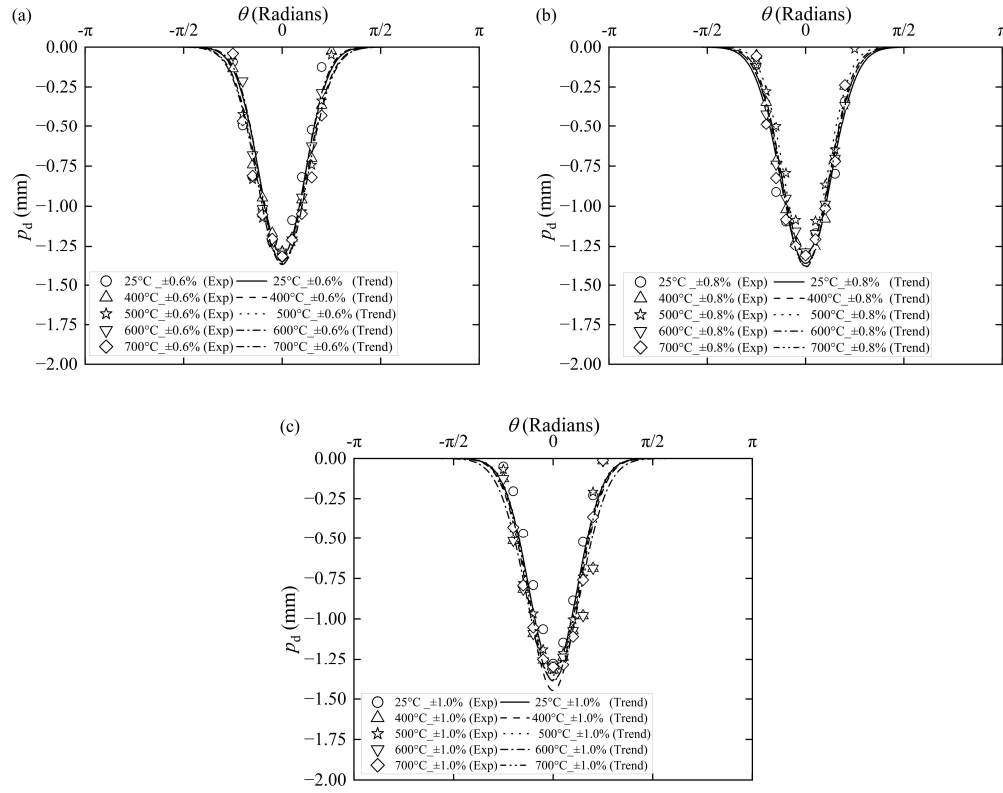


**Fig. 6.4** Experimental data and trends based on inverse Gaussian model.

**Table 6.4.** Regression parameter values from the inverse Gaussian model.

Specimen	$\zeta_1$	$\zeta_2$	R-square
C_25_±0.6%	1.309	3.640	0.968
C_25_±0.8%	1.362	3.052	0.976
C_25_±1.0%	1.323	3.344	0.976
C_400_±0.6%	1.306	3.199	0.989
C_400_±0.8%	1.385	3.625	0.986
C_400_±1.0%	1.345	3.226	0.964
C_500_±0.6%	1.364	3.225	0.984
C_500_±0.8%	1.319	3.067	0.988
C_500_±1.0%	1.353	3.468	0.982
C_600_±0.6%	1.369	3.623	0.991
C_600_±0.8%	1.307	3.300	0.987
C_600_±1.0%	1.381	3.270	0.969
C_700_±0.6%	1.366	3.117	0.980
C_700_±0.8%	1.379	3.354	0.979
C_700_±1.0%	1.388	3.286	0.982

It's important to note that parameters  $\zeta_1$  and  $\zeta_2$  are related to different behaviors of pitting corrosion.  $\zeta_1$  signifies non-uniformity in corrosion pit, while  $\zeta_2$  is associated with the maximum corrosion depth. Figs. 6.4 (a–c) depicts data points of  $p_d$  representing the variation of corrosion depth, along with trend lines based on Equation 6.2. The trends in the data points follow Gaussian equation. Further, the values of  $\zeta_1$  and  $\zeta_2$  are given in Table 6.4. The R-Square values range from 0.964 to 0.991, with a majority of them (60%) exceeding 0.98. This confirms Equation 6.2 better describe the trend in  $p_d$  distribution.

### 6.3 Analytical stress concentration factor

The perturbation theory applied to surface perturbations assumes the surface, although slightly undulating, is almost flat. It considers perturbation is small compared to the other length scales in the bulk material. As a result, the surface composed of elastic half-plane (Gao, 1991). Using this perturbation approach, it becomes possible to analytically determine the stress concentration factor ( $k_t$ ) for Gaussian equation. The method relies on a specific elastic Green's function designed for perfectly flat elastic surfaces, treating the undulating surface as a perturbation in relation to the flat surface. Following perturbation theory,  $k_t$  can be expressed as (Gao, 1991; Medina, 2015; Medina and Hinderliter, 2014):

$$k_t = \left[ 1 + \frac{2}{\pi} PV \int_{-\infty}^{\infty} \frac{p'_d(\kappa) d\kappa}{(\kappa - \theta)} \right] \quad (6.3)$$

where  $PV$  refers to the principal value in which the integral is evaluated in the Cauchy sense,  $p'_d(\kappa)$  represents spatial derivative of an arbitrary pitting surface profile  $p_d(\kappa)$ , and  $\kappa$  is a dummy variable. To find the solution to Equation 6.3 Hilbert transform can be used. It relies on a linear operator that, in contrast to the Fourier transform, preserves the domain of the independent variable. Hilbert transform is defined as (Hahn, 1996; Le Van Quyen et al., 2001):

$$\tilde{u}(t) = H(u(t)) = \frac{1}{\pi} PV \int_{-\infty}^{\infty} \frac{u(\tau)}{\tau - t} d\tau = -\frac{1}{\pi} PV \int_{-\infty}^{\infty} \frac{u(\tau)}{t - \tau} d\tau \quad (6.4)$$

By applying Equation 6.4 to Equation 6.3,  $k_t$  can be given as (Medina, 2015):

$$k_t = 1 - 2 \frac{d[H p_d(\theta)]}{d\theta} \quad (6.5)$$

Further, applying Equation 6.5 to the proposed inverted Gaussian equation,  $k_t$  is evaluated as:

$$k_t(\theta) = 1 + \frac{4\zeta_1\sqrt{\zeta_2}}{\sqrt{\pi}} \left[ 1 - \theta e^{(-\zeta_2\theta^2)} \sqrt{\pi} \sqrt{\zeta_2} \operatorname{erfi}(\sqrt{\zeta_2}\theta) \right] \quad (6.6)$$

where  $\operatorname{erfi}$  represents imaginary error function. It can be observed from the Figs. 6.4(a)–(c) that  $p_d$  becomes equal to  $p_d^{\max}$  when  $\theta = 0$ . Thus, the maximum value of  $k_t$  is obtained by substituting  $\theta = 0$  in Equation 6.6 and expressed as:

$$k_t = 1 + \frac{4\zeta_1\sqrt{\zeta_2}}{\sqrt{\pi}} \quad (6.7)$$

It's worth pointing out the developed analytical model for  $k_t$  consider the effect of non-uniform distribution of corrosion pit along the steel bar perimeter. The  $k_t$  values for all specimens are summarized in Table 6.5. As observed,  $k_t$  range between 6.21 and 7.24.

**Table 6.5.** Stress concentration factor for inverted Gaussian model.

Specimen	$k_t$	Specimen	$k_t$	Specimen	$k_t$
	Analytical /FE		Analytical /FE		Analytical /FE
C_25_±0.6%	6.63/7.24	C_400_±1.0%	6.45/6.84	C_600_±0.8%	6.35/6.62
C_25_±0.8%	6.36/6.61	C_500_±0.6%	6.52/6.56	C_600_±1.0%	6.63/6.48
C_25_±1.0%	6.45/7.02	C_500_±0.8%	6.21/6.54	C_700_±0.6%	6.44/6.64
C_400_±0.6%	6.27/6.64	C_500_±1.0%	6.68/6.43	C_700_±0.8%	6.69/6.85
C_400_±0.8%	6.95/6.14	C_600_±0.6%	6.88/6.60	C_700_±1.0%	6.67/6.74

The analytical method based  $k_t$  values are compared with numerical method, such as the FE analysis. To conduct FE analysis, a three-dimensional computational model is constructed for each specimen based on its laser-scanned recreated image. The model is directly preprocessed using FE tool and subsequently postprocessed to extract stress variations within the corrosion pit. A study to establish mesh independence is conducted, yielding optimal element sizes of 0.05 mm in the pit region, 0.1 mm near the pit, 0.15 mm in the tapering section, and 0.2 mm at the ends. Boundary conditions involve applying a nominal axial stress of 100 MPa to one end of the model, while restraining rotation and axial translation at the other end. Fig. 6.5 (a) depicts the stress within the corrosion pit is highlighted, with the deepest region experiencing the highest and fluctuating stresses due to the varying nature corrosion surface profile. Moreover, Fig. 6.5 (b) illustrates the stress distribution across the entire specimen obtained from FE analysis, showcasing a symmetrical stress profile. Through FE analysis,  $k_t$  is computed as the ratio of maximum stress to nominal stress. The values of  $k_t$  obtained from the

FE analysis are compared in Table 6.5. The average error, found to be 9%, falls within acceptable bounds, thus confirming the validity of the proposed analytical model for  $k_t$ .

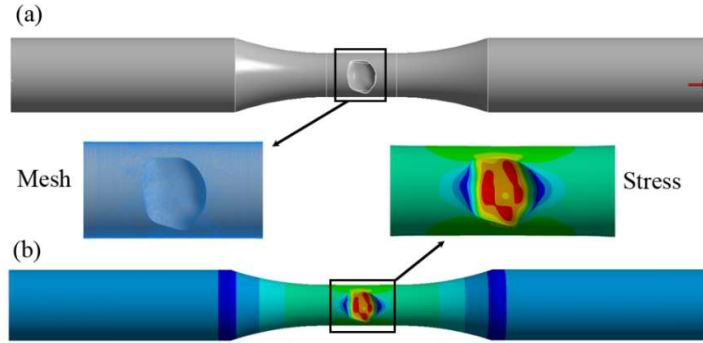


**Fig. 6.5** Numerical analysis of SCF: (a) 3D laser scan image, FE mesh, stress distribution in the corrosion pit; and (b) stress distribution in the specimen.

## 6.4 Fatigue Experiment

### 6.4.1 Testing procedure:

A servo-controlled UTM (Model: BISS UTM-02-0100) having 100 kN load cell and equipped with a split-type furnace, capable of temperatures ranging from 0 °C to 1000 °C is used to perform LCF tests. The furnace has a center-split design for easy specimen access, and temperature regulation is achieved using a PID controller. Three K-type thermocouples monitor the temperature in the gauge length region. The tests are conducted under varying strain amplitude and constant strain rate. Specimens are tested for three strain amplitudes ( $\epsilon_a$ ):  $\pm 0.6\%$ ,  $\pm 0.8\%$ , and  $\pm 1.0\%$ . Moreover, symmetrical triangular waveforms are applied at a strain rate of  $5 \times 10^{-3} \text{ s}^{-1}$ . Similar strain amplitude and rate are reported in the literature (Narendra et al., 2019; Tripathi et al., 2018). Further, a 12.5 mm gauge length extensometer facilitated precise strain measurement.

The specimens are securely clamped at both ends using threaded jaws in the machine. Fatigue tests are performed in both room (25 °C) and elevated temperatures (400 °C, 500 °C, 600 °C, and 700 °C). A total of 30 specimens, comprising 15 uncorroded and 15 corroded, undergo testing. Once a specimen is mounted, the furnace temperature is increased at a ramp rate of 10 °C/min and is then held for 20 minutes at the target temperature to ensure homogeneous heating. Testing proceeds at target temperatures until complete fracture.

## 6.4.2 Cyclic response

### 6.4.2.1 Hysteresis behaviour:

The cyclic stress–strain response of selected uncorroded and corroded specimens are depicted in Figs. 6.6 (a)–(l). For better comprehension of LCF behaviour, a few distinct cycles are chosen and represented. It is important to note that the last cycle corresponds to fatigue failure. In general, cyclic response displays a typical shuttle shape, indicating good energy dissipation capacity. Further, in uncorroded specimens exposed to room temperature, it is clear that the influence of temperature on the cyclic responses appears to be minimal, regardless of the fatigue strain amplitude (Figs. 6.6 (a–f)).

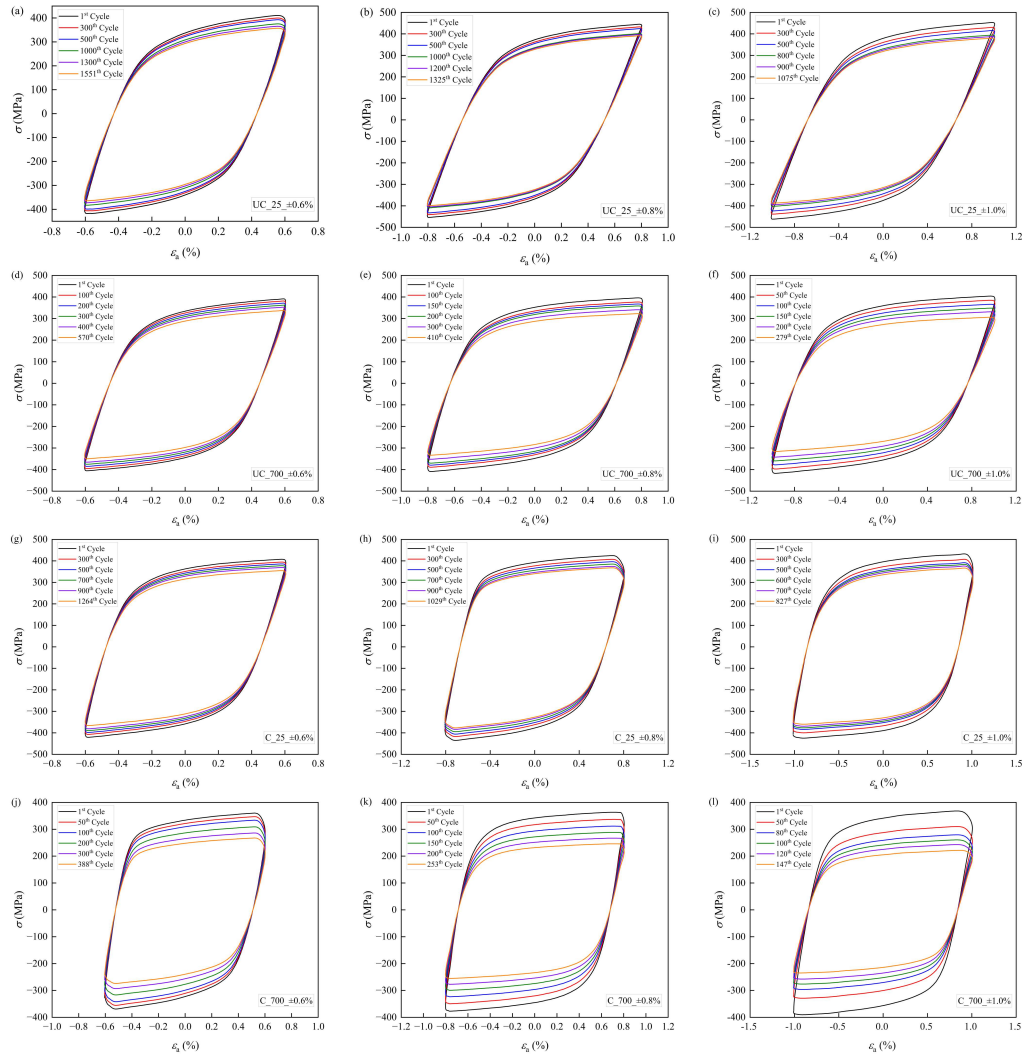


**Fig 6.6** Hysteresis curves: (a) UC\_25  $\pm 0.6\%$ ; (b) UC\_25  $\pm 0.8\%$ ; (c) UC\_25  $\pm 1.0\%$ ; (d) UC\_700  $\pm 0.6\%$ ; (e) UC\_700  $\pm 0.8\%$ ; (f) UC\_700  $\pm 1.0\%$ ; (g) UC\_25  $\pm 0.6\%$ ; (h) UC\_25  $\pm 0.8\%$ ; (i) UC\_25  $\pm 1.0\%$ ; (j) UC\_700  $\pm 0.6\%$ ; (k) UC\_700  $\pm 0.8\%$  and (l) UC\_700  $\pm 1.0\%$ .

However, it is evident that at high temperatures (specifically at 700 °C), there are noticeable changes in cyclic responses as the strain amplitude increases. This may be attributed to the growing fatigue strain amplitude, which causes a greater plastic deformation component. The interaction between increased strain amplitude and stress concentration caused by corrosion accelerates the accumulation of fatigue damage, resulting in a notable decrease in fatigue life. For instance, at a temperature of 25 °C, the specimen fails at the 1364th cycle with a 0.6% amplitude (Fig. 6.6 (g)). However, it fails at the 827th cycle with a 1.0% amplitude (Fig. 6.6 (i)). The decrease in fatigue life can be attributed to uneven weakening of effective cross-section due to corrosion. Additionally, high fatigue stress concentration in the corrosion pit can also lead to a decrease in fatigue life.

#### 6.4.2.2 Variation in peak stress:

The peak stress amplitude in various specimens shows a progressive variation, as observed from the cyclic responses. Figs. 6.7 (a) and (b) illustrate the relationship between peak stress and the number of cycles to failure ( $N_{f,exp}$ ) in uncorroded and corroded specimens, respectively. Each curve exhibits three distinct stages: an initial softening stage, a stable stage, and a final stage, despite the variability in peak stress. In the beginning, peak stress gradually decreases with  $N_{f,exp}$ , and crack initiation is the main factor affecting the cycle life. Therefore, this stage is called the crack initiation stage. During the second stage, there is minimal change in peak stress and  $N_{f,exp}$ , while cracks gradually grow. Therefore, this stage is also known as the crack propagation stage. Large macrocracks form during the third stage, known as the failure stage, ultimately leading to final rupture.

Initial peak stress amplitude changes with increasing strain amplitude and given temperature are minimal (Fig. 6.7 (a and b)). This trend can be seen in both uncorroded and corroded specimens. However, notable variations are observed with increasing temperatures. For instance, in uncorroded and corroded specimens, peak stress amplitude rises by upto 11% and 16%, respectively, when the temperature is raised from 25 °C to 700 °C. When comparing room temperature and 500 °C values, the uncorroded specimen experiences a 6.2% reduction in peak stress amplitude after 800 cycles at  $\pm 0.6\%$ , whereas it endures a 12% reduction after just 500 cycles at  $\pm 1.0\%$ . Regarding corroded specimens, a 6.2% reduction occurs after 100 cycles at  $\pm 0.6\%$  and an 11% reduction after 300 cycles at  $\pm 1.0\%$ . The observations highlight the impact of corrosion on peak stress amplitude.

There is a notable difference in the ratio between the initial and final peak stress amplitude values in uncorroded and corroded specimens. The ratio for a given temperature shows minimal

## Fatigue Behavior of Constructional Steels Subjected to Pitting Corrosion and Elevated Temperature

variation with varying  $\varepsilon_a$ . However, at 700 °C, the ratio increases by 31% compared to 25 °C in uncorroded specimens. The ratio increases significantly, reaching up to 68% at 700 °C, compared to 25 °C, in the case of corroded specimens. These observations have practical significance. One key finding is that amplitude-dependent damage accumulation is accelerated in corroded specimens. This could lead to faster crack propagation rates and a significant decrease in fatigue life.

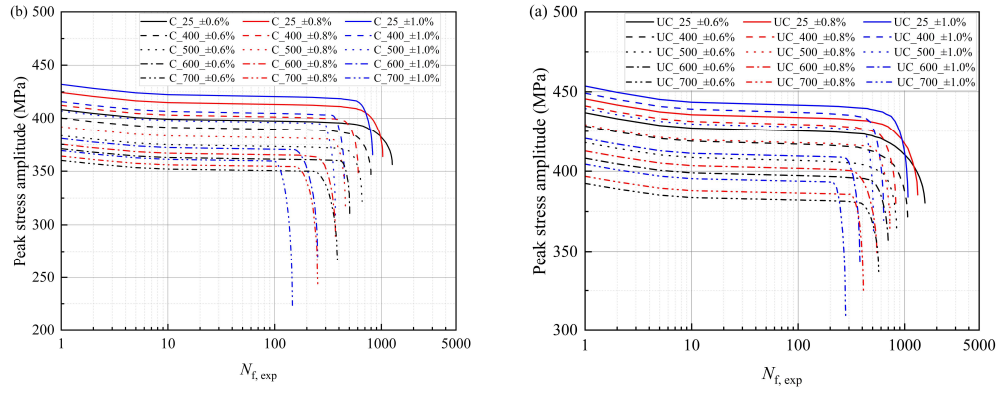


**Fig. 6.7** Variation of peak stress amplitude with  $N_{f,exp}$ .

### 6.4.2.3 Stress softening:

A cyclic softening factor ( $K_\sigma$ ) can be used to analyze cyclic softening discarding the effect of stress levels. In the case of strain-controlled fatigue tests with varying strain amplitude,  $K_\sigma$  is given as (Wu et al., 2015):

$$K_\sigma = \frac{\Delta\sigma - \Delta\sigma_{N_{f,exp}/2}}{\Delta\sigma} \quad (6.8)$$

where  $\Delta\sigma$  represents the stress range of each cycle, while  $\Delta\sigma_{N_{f,exp}/2}$  corresponds to the stress range of  $N_{f,exp}/2$ . For better representation,  $K_\sigma$  variation in corroded specimens for  $\pm 0.6\%$  and  $\pm 1.0\%$  are depicted in Fig. 6.8 (a and b), respectively. For all specimens,  $K_\sigma$  tends to decrease with increasing  $N_{f,exp}$ . In addition, specimens exhibit three distinct stages. The first stage signifies initial softening, during which  $K_\sigma$  decreases gradually with  $N_{f,exp}$ . In the second stage, referred to as steady-state softening,  $K_\sigma$  stabilizes within a relatively constant range. During the last stage, drastic variation in  $K_\sigma$  with  $N_{f,exp}$  is observed. It is worth noting that as  $N_{f,exp}$  approaches fatigue-induced fracture,  $K_\sigma$  experiences a notable decline. The decline becomes more pronounced as the temperature rises, particularly at higher temperatures. These

observations in  $K_\sigma$  behavior emphasize the significant influence of high exposure temperatures on the cyclic softening mechanisms in steel specimens.

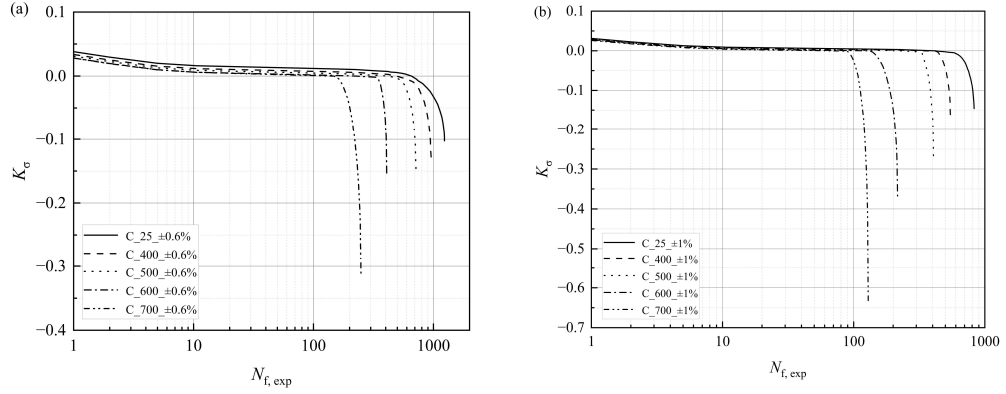


**Fig. 6.8** Variation of  $K_\sigma$  with  $N_{f,exp}$  : (a)  $\epsilon_a = 0.6\%$ ; and (b)  $\epsilon_a = 1.0\%$ .

#### 6.4.2.4 Variation in plastic strain:

The LCF life is greatly affected by plastic strain, which is especially noticeable in steel specimens exposed to high temperatures and pitting corrosion, as shown in Figs. 6.9 (a–c). Notably, plastic strain amplitude increased in response to rising fatigue strain amplitude and accumulating cycles. This aligns with the observation from Section 6.4.2.2, where the number of cycles to failure correlated with a reduction in the maximum stress. Figure 6.9 illustrates three distinct regions based on the plastic strain amplitude variation trend. In Region I, the plastic strain amplitude increases as  $N/N_{f,exp}$  rises.  $N/N_{f,exp}$  is the relative number of cycles. In Region II, there is a noticeable stability in the plastic strain amplitude. However, a significant increase in the plastic strain amplitude with increasing  $N/N_{f,exp}$  is observed in Region III.

Although there is a marginal increase in plastic strain at low  $N/N_{f,exp}$  values ( $<0.5$ ), the amplitude remains relatively constant until 0.8. Beyond 0.9, the plastic strain amplitude significantly increases until fracture, as shown in Fig. 6.9. It is worth mentioning that the plastic strain for corroded specimens is noticeably higher than that of uncorroded specimens, as shown in Fig. 6.9. This corroborates with the observed decreases in cycles to failure in corroded specimens. Similar observations are reported in (Hua et al., 2022; Hua et al., 2021).



## Fatigue Behavior of Constructional Steels Subjected to Pitting Corrosion and Elevated Temperature

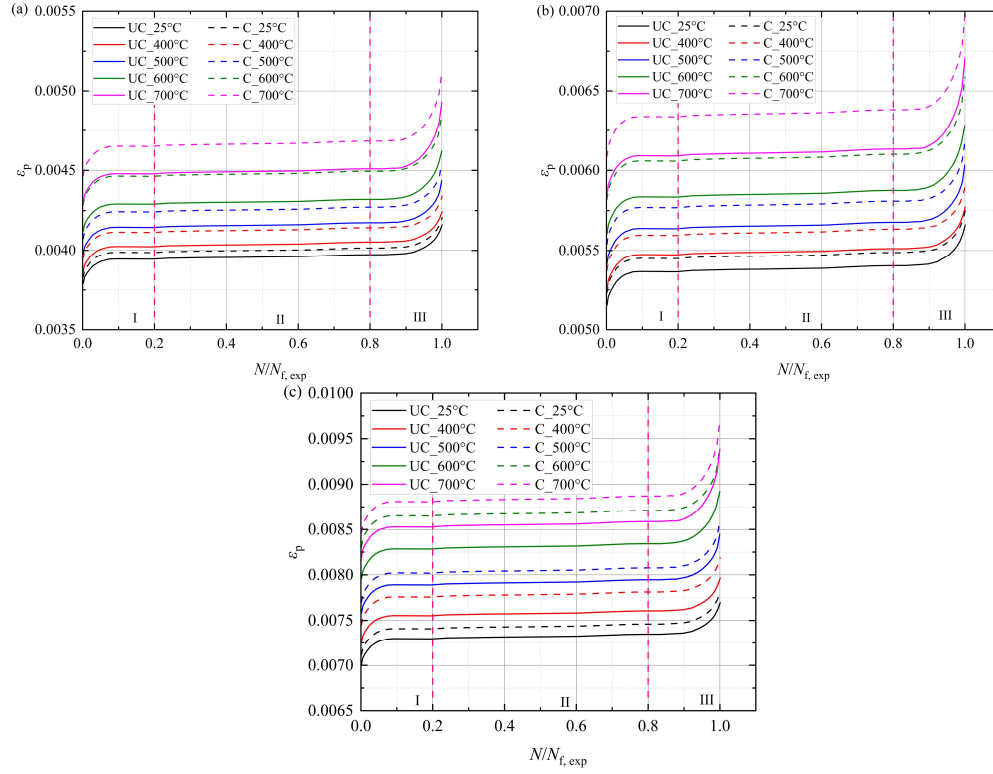


**Fig. 6.9** Variation of  $\varepsilon_p$  with  $N/N_{f,exp}$  : (a)  $\varepsilon_a = 0.6\%$ ; (b)  $\varepsilon_a = 0.8\%$ ; and (c)  $\varepsilon_a = 1.0\%$ .

### 6.4.2.5 Variation in modulus:

One way to assess the modulus ( $E_t$ ) reduction of specimens is by analyzing the hysteresis loops, as illustrated in Figs 6.10 (a) and (b). The modulus of all specimens progressively diminishes from the first cycle and continues to fall steadily until it approaches a point near failure, at which a rapid decrease is seen. In particular, the reduction in initial modulus becomes more noticeable at temperatures of 600 °C and higher. Uncorroded specimens in this higher temperature range show a smaller spread in modulus reduction (9–14%) compared to their corroded counterparts (12–39%). Notably, corroded specimens at 600–700 °C undergo a significantly larger reduction in the elastic modulus, specifically at fatigue strain amplitudes of  $\pm 0.8\%$  and  $\pm 1.0\%$ . One reasonable explanation likely arises from the combined influence of fatigue strain amplitude, corrosion exposure, elevated temperature, and the final softening stage at failure (Xie et al., 2019).

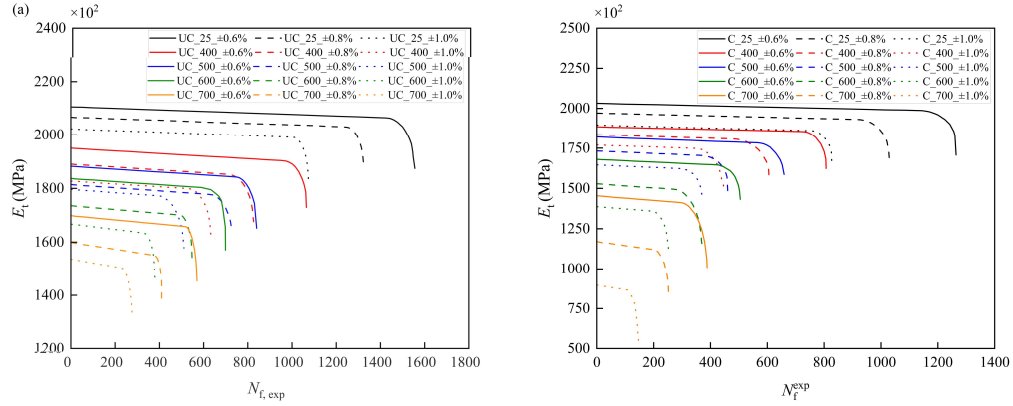


**Fig. 6.10** Variation of  $E_t$  with  $N_{f,exp}$ .

#### 6.4.3 Variation in $N_{f,exp}$ :

The fatigue life, expressed in terms of number of cycles to failure ( $N_{f,exp}$ ), is summarized in Table 6.6 for both uncorroded and corroded specimens. In uncorroded specimens, at a given temperature,  $N_{f,exp}$  reduces by upto 47% between any two successive strain amplitudes. However, in corroded specimens, this reduction reaches a significant 72%. Further, when comparing uncorroded and corroded specimens, it is observed that corroded specimens experience a considerable reduction of 90%  $N_{f,exp}$ . The drastic decrease in fatigue resistance can be attributed to the synergetic effects of temperature and pitting corrosion. In particular, one factor contributing to the reduction of  $N_{f,exp}$  is the early development of cracks caused by corrosion pits.

To investigate the effect of high temperature on fatigue life, a dimensionless analysis is conducted. The number of cycles to failure at a given exposure temperature of  $T$  °C ( $N_{f,T}$ ) is compared to  $N_{f,25}$  at 25 °C ( $N_{f,T}/N_{f,25}$ ) for both uncorroded and corroded specimens. Note that  $N_{f,25}$  serves as the reference for comparative analysis across different temperatures. Fig. 6.11 presents the trends in  $N_{f,T}/N_{f,25}$  for various specimens. A consistent decrease in  $N_{f,T}/N_{f,25}$  is observed with increasing temperatures. In uncorroded specimens,  $N_{f,400}$  is 80 % of  $N_{f,25}$  at  $\pm 0.6\%$  strain amplitude. In addition, 79% and 72% drops are observed at  $\pm 0.8\%$  and  $\pm 1.0\%$  strain amplitudes, respectively.  $N_{f,700}$  drops to 29%, 25% and 22% of its  $N_{f,25}$  counterpart for  $\pm 0.6\%$ ,  $\pm 0.8\%$  and  $\pm 1.0\%$  strain amplitudes, respectively. In contrast, corroded specimens exhibit a significantly steeper decline in  $N_{f,T}/N_{f,25}$ .  $N_{f,400}$  retains 77% compared to  $N_{f,25}$  at  $\pm 0.6\%$  strain amplitude. In addition, 76 % and 67 % drops are observed for  $\pm 0.8\%$  and  $\pm 1.0\%$

## Fatigue Behavior of Constructional Steels Subjected to Pitting Corrosion and Elevated Temperature

strain amplitudes, respectively.  $N_{f,700}$  is just 20%, 14% and 9% of  $N_{f,25}$  at  $\pm 0.6\%$ ,  $\pm 0.8\%$  and  $\pm 1.0\%$  strain amplitudes, respectively. These pronounced reductions in fatigue life underscore the enhanced detrimental effect of pitting corrosion, which introduces stress concentrations and facilitates premature crack initiation, further exacerbating the temperature-induced weakening of the material.

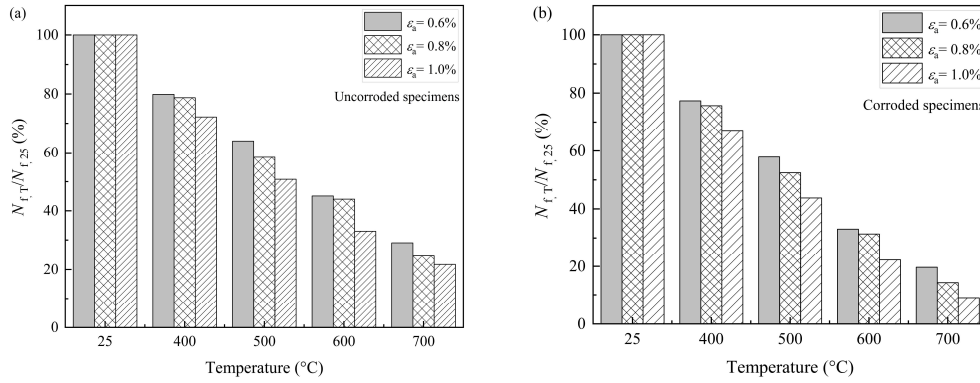


**Fig 6.11** Effect of high temperatures: a dimensionless comparison of  $N_{f,T}/N_{f,25}$ .

**Table 6.6** Test result summary of  $N_{f,exp}$  and  $\bar{W}_{T,exp}$  values.

Specimen	$N_{f,exp}$	$\bar{W}_{T,exp}$	Specimen	$N_{f,exp}$	$\bar{W}_{T,exp}$
		(MPa)			(MPa)
UC_25_±0.6%	1551	6039	C_25_±0.6%	1264	3452
UC_25_±0.8%	1325	5519	C_25_±0.8%	1029	3110
UC_25_±1.0%	1075	4877	C_25_±1.0%	827	2698
UC_400_±0.6%	1065	4795	C_400_±0.6%	807	2670
UC_400_±0.8%	826	4160	C_400_±0.8%	606	2222
UC_400_±1.0%	635	3609	C_400_±1.0%	449	1794
UC_500_±0.6%	840	4253	C_500_±0.6%	659	2347
UC_500_±0.8%	727	3797	C_500_±0.8%	461	1827
UC_500_±1.0%	511	3185	C_500_±1.0%	370	1579
UC_600_±0.6%	699	3802	C_600_±0.6%	505	1976
UC_600_±0.8%	548	3307	C_600_±0.8%	371	1591
UC_600_±1.0%	380	2653	C_600_±1.0%	253	1229
UC_700_±0.6%	570	3359	C_700_±0.6%	388	1640
UC_700_±0.8%	410	2788	C_700_±0.8%	253	1231
UC_700_±1.0%	279	2237	C_700_±1.0%	147	857

It is of engineering importance to predict the relation between  $N_{f,exp}$  and temperature. In this regard,  $N_{f,exp}$  values are plotted in Figs. 6.12 (a) and (b) as data points considering the variation in temperature for uncorroded and corroded specimens, respectively. To find the trend of these data points, a curve fitting analysis is conducted using a first-degree linear polynomial function expressed as:

$$N_{f,exp} = \nu_1 + \nu_2 T \quad (6.9)$$

where  $\nu_1$  and  $\nu_2$  are curve fitting coefficients. The values of coefficients are listed in Table 6.7. The calculated R-squared value of 0.99 suggests a strong fit between the model and the observed data. Further, Fig. 6.12 also displays the trendlines based on the equation over the data points. It can be observed that the proposed equation fits well with the data.

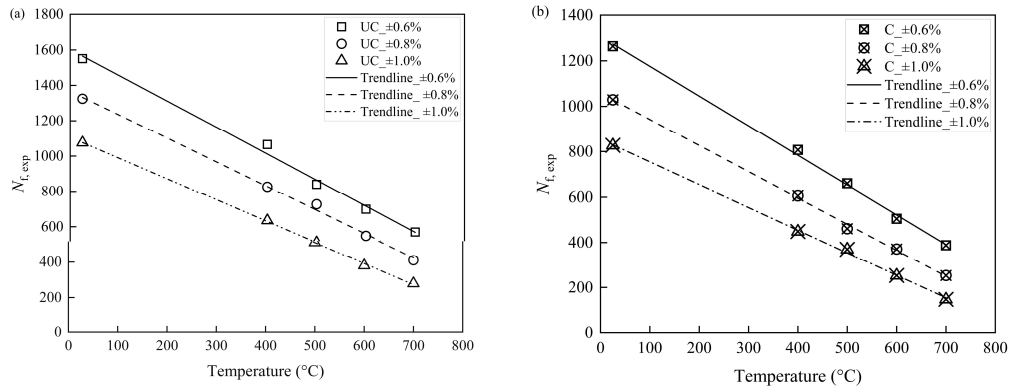


**Fig 6.12** Relation between  $N_{f,exp}$  and temperature.

**Table 6.7.** Regression coefficients used to find the relation between  $N_{f,exp}$  and  $T$

Uncorroded Specimens				Corroded Specimens			
$\varepsilon_a$	$\nu_1$	$\nu_2$	R-square	$\varepsilon_a$	$\nu_1$	$\nu_2$	R-square
±0.6%	1602.135	-1.476	0.99	±0.6%	1306.53	-1.307	0.99
±0.8%	1366.33	-1.346	0.99	±0.8%	1057.4	-1.153	0.99
±1.0%	1105.59	-1.19	0.99	±1.0%	854.19	-0.999	0.99

#### 6.4.4 Relation between $\varepsilon_a$ and $N_{f,exp}$ :

This section examines the applicability of the Coffin–Manson model in determining the relationship between  $\varepsilon_a$  and  $N_{f,exp}$  for uncorroded and corroded specimens exposed to high temperatures. Here is the equation that quantifies the relationship

# **Fatigue Behavior of Constructional Steels Subjected to Pitting Corrosion and Elevated Temperature**

$$\varepsilon_a = \beta (2N_{f,exp})^\alpha \quad (6.10)$$

where  $\beta$  represents the fatigue ductility coefficient, while  $\alpha$  signifies the fatigue ductility exponent. The independent variable,  $\varepsilon_a$ , and the dependent variable,  $2N_{f,exp}$ , are represented as data points in Figs. 6.13 (a) and (b). The data points on the graph correspond to the values provided in Table 6.8. Trendlines are drawn over the data points for every temperature value through curve fitting analysis using Equation 6.10. As anticipated, negative correlations between  $\varepsilon_a$  and  $2N_{f,exp}$  suggest that fatigue life decreases as strain amplitude increases. The results of the curve fitting analysis can be found in Table 6.8. It can be noted that the R-Square values for uncorroded and corroded specimens range from 0.97 to 0.99 and 0.98 to 0.99, respectively. Based on these observations, the Coffin–Manson model can be utilized to establish the relationship between  $\varepsilon_a$  and  $2N_{f,exp}$ .

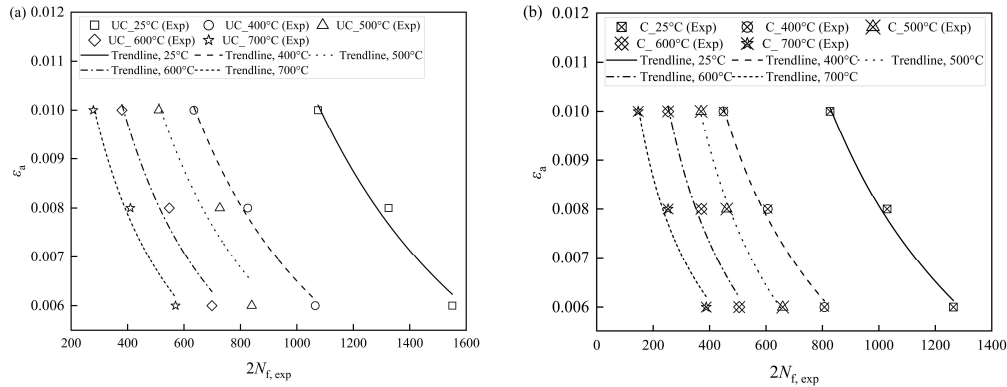


**Fig 6.13** Relation between  $\varepsilon_a$  and  $2N_{f,exp}$

**Table 6.8** Regression coefficients and exponents used in fatigue model.

Temperature	$\beta$	$\alpha$	R-square	Temperature	$\beta$	$\alpha$	R-square
25°C	0.7016	−0.831	0.97	25°C	0.4644	−0.767	0.99
400°C	0.5047	−0.763	0.99	400°C	0.25932	−0.648	0.99
500°C	0.2684	−0.694	0.92	500°C	0.1096	−0.594	0.99
600°C	0.1044	−0.578	0.96	600°C	0.0522	−0.405	0.98
700°C	0.04853	−0.687	0.98	700°C	0.01232	−0.501	0.98

It is also of engineering importance to determine relation of coefficients  $\beta$  and  $\alpha$  with  $T$ . An effective approach to achieve this is by introducing dimensionless coefficients,  $\beta_T/\beta_{25}$  and  $\alpha_T/\alpha_{25}$ , which can objectively demonstrate the variation in the trends of  $\beta$  and  $\alpha$ . The

dimensionless coefficient indicates the relationship between its value at the specified temperature and room temperature. It is observed that  $\beta_T/\beta_{25}$  and  $\alpha_T/\alpha_{25}$  decrease as the temperature increases as depicted in Figs. 6.14. Further, a linear equation is utilized to establish the relationship between the dimensionless coefficient and temperature. Curve fitting analyses are then conducted. The following mathematical equations are derived:

$$\begin{aligned} \text{Uncorroded specimens} & \begin{cases} \beta_T/\beta_{25} = 1.04 - 1.33 \times 10^{-3} T \\ \alpha_T/\alpha_{25} = 1.01 - 5.15 \times 10^{-4} T \end{cases} \\ \text{Corroded specimens} & \begin{cases} \beta_T/\beta_{25} = 1.04 - 1.15 \times 10^{-3} T \\ \alpha_T/\alpha_{25} = 1.02 - 7.26 \times 10^{-4} T \end{cases} \end{aligned} \quad (6.11-6.14)$$

The R-Square values obtained from curve fitting analysis range between 0.97 and 0.99, suggesting a strong fit between the data points and the linear equation.

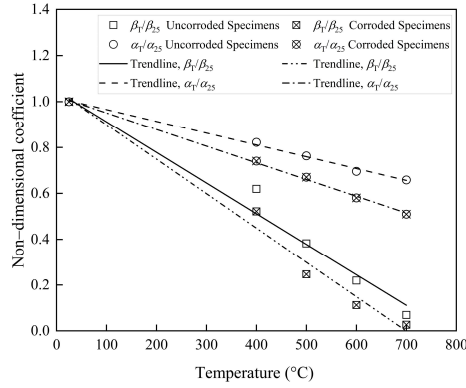


**Fig 6.14** Relation between coefficients and temperature.

#### 6.4.5 Total dissipated energy density:

This study utilizes the concept of total dissipated energy density,  $\bar{W}_{t,exp}$ , to assess the impact of pitting corrosion, exposure temperature, and fatigue strain amplitude on the LCF behavior of steel specimens. Note that  $\bar{W}_{t,exp}$  represents the cumulative sum of envelope areas of stress-strain hysteresis curves. The estimated values of  $\bar{W}_{t,exp}$  are presented in Table 6.6, highlighting their dependency on both exposure temperature and fatigue strain amplitude.

When the temperature is raised from 400 °C–700 °C, the  $\bar{W}_{t,exp}$  values in uncorroded specimens decrease by upto 38% at  $\pm 1.0\%$  compared to room temperature. Further,  $\bar{W}_{t,exp}$  reduces by upto 20%, 31%, and 34% between any two consecutive temperature levels at  $\pm 0.6\%$ ,  $\pm 0.8\%$ , and  $\pm 1.0\%$ , respectively. On the contrary, when the temperature is raised from 400 °C

## Fatigue Behavior of Constructional Steels Subjected to Pitting Corrosion and Elevated Temperature

to 700 °C in corroded specimens, there is a significant decrease in  $\bar{W}_{t,exp}$  values of upto 52.2% at  $\pm 1.0\%$  compared to room temperature. In addition, there is a considerable drop in  $\bar{W}_{t,exp}$  of upto 22% and 41% between any two consecutive temperature levels as the strain amplitude increases from  $\pm 0.6\%$  to  $\pm 1.0\%$ . Further, it is worth noting that at a specific temperature and strain amplitude,  $\bar{W}_{t,exp}$  in corroded specimens decreases by a factor of 2.61 compared to uncorroded specimens. These observations suggest corroded steel exposed to high temperatures exhibits significantly diminished fatigue resistance compared to its uncorroded counterpart.

To investigate the effect of exposure temperature on  $\bar{W}_{t,exp}$  further, a dimensionless analysis is conducted. Fig. 6.15 illustrates the comparison between  $\bar{W}_{t,T}/\bar{W}_{t,25}$  and temperature for specimens exposed to different strain amplitude. Here,  $\bar{W}_{t,T}$  denotes the maximum total energy dissipation capacity at a specific temperature of  $T$  °C, while  $\bar{W}_{t,25}$  represents the value at 25°C. The figure reveals a decreasing trend in  $\bar{W}_{t,T}/\bar{W}_{t,25}$  with increasing temperature. Notably, for uncorroded specimens,  $\bar{W}_{t,400}$  corresponds to 79%, 75%, and 74% of  $\bar{W}_{t,25}^{exp}$  at  $\pm 0.6\%$ ,  $\pm 0.8\%$ , and  $\pm 1.0\%$ , respectively. Whereas,  $\bar{W}_{t,700}$  falls to 56%, 51%, and 46% of  $\bar{W}_{t,25}$  at  $\pm 0.6\%$ ,  $\pm 0.8\%$ , and  $\pm 1.0\%$ , respectively. These observations signify a substantial decline in energy dissipation capacity at elevated temperatures with increasing strain amplitude. Conversely, corroded specimens  $\bar{W}_{t,400}$  correspond to 77%, 71%, and 67% of  $\bar{W}_{t,25}$  at  $\pm 0.6\%$ ,  $\pm 0.8\%$ , and  $\pm 1.0\%$ , respectively. Whereas,  $\bar{W}_{t,700}$  falls to 47%, 40%, and 32% of  $\bar{W}_{t,25}$  at  $\pm 0.6\%$ ,  $\pm 0.8\%$ , and  $\pm 1.0\%$ , respectively.

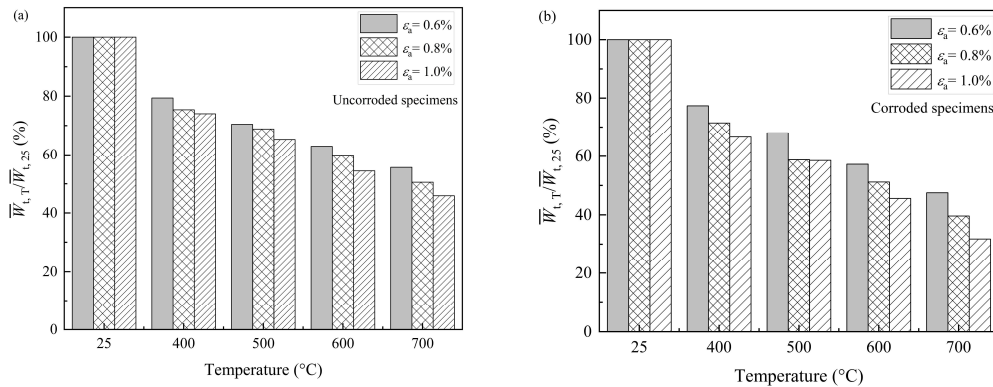


**Fig 6.15** Effect of high temperatures: a dimensionless comparison of  $\bar{W}_{t,T}/\bar{W}_{t,25}$ .

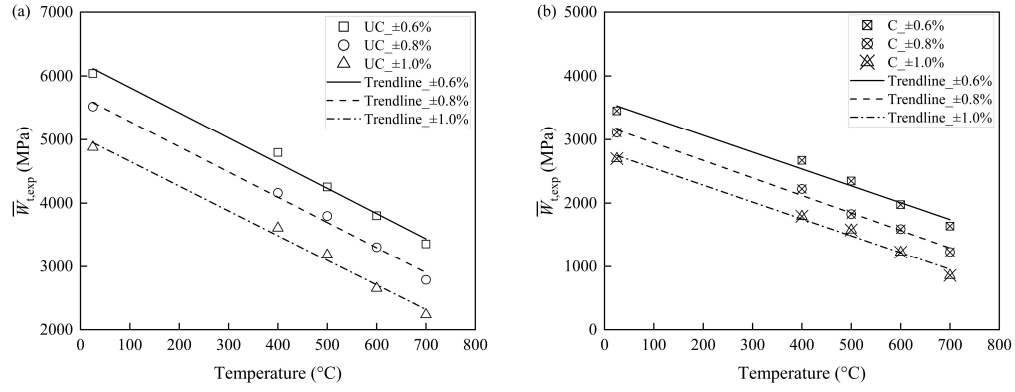


**Fig 6.16** Relation between  $\bar{W}_{t,exp}$  and temperature.

To quantitatively characterize the relationship between  $\bar{W}_{t,exp}$  and  $T$ , a linear regression analysis is performed. This analysis utilizes a first-degree polynomial function, essentially a linear equation, to model the underlying trend

$$\bar{W}_{t,exp} = \delta_1 + \delta_2 T \quad (6.15)$$

where  $\delta_1$  and  $\delta_2$  are regression coefficients. The values of regression coefficients are provided in Table 6.9 for various strain amplitudes. The regressions yield R-Square values of 0.99. Additionally, Fig. 6.16 illustrates the trendlines that have been fitted to the data points. The close alignment with the data indicates a strong agreement between model and observed data.

**Table 6.9.** Regression coefficients used to find the relation between  $\bar{W}_{t,exp}$  and  $T$

Uncorroded Specimens				Corroded Specimens			
$\varepsilon_a$	$\delta_1$	$\delta_2$	R-square	$\varepsilon_a$	$\delta_1$	$\delta_2$	R-square
$\pm 0.6\%$	6213.95	-3.96	0.99	$\pm 0.6\%$	3595.74	-2.64	0.97
$\pm 0.8\%$	5679.93	-3.90	0.99	$\pm 0.8\%$	3222.32	-2.75	0.99
$\pm 1.0\%$	5046.17	-3.89	0.99	$\pm 1.0\%$	2813.18	-2.65	0.98

#### 6.4.6 Strain energy density approach:

Strain energy density (SED) approach posits fracture initiation in the vicinity of the pit occurs when average SED at the control volume at pit apex exceeds the threshold value governed by the material property. In this section, SED approach is utilized to derive analytical model for estimating average SED at the corrosion pit following Gaussian distribution.



**6.4.6.1 Analytical model:**

The Gaussian corrosion pit representation and accompanying stress components are depicted in Fig. 6.17. The stress components in the neighborhood of the pit under Mode-I load is given as (Filippi and Lazzarin, 2004):

$$\begin{Bmatrix} \sigma_\phi \\ \sigma_r \\ \tau_{r\phi} \end{Bmatrix} = \lambda_1 r^{\lambda_1-1} a_1 \left[ \begin{array}{l} \begin{Bmatrix} (1+\lambda_1)\cos(1-\lambda_1)\phi \\ (3-\lambda_1)\cos(1-\lambda_1)\phi \\ (1-\lambda_1)\sin(1-\lambda_1)\phi \end{Bmatrix} + \chi_{b_1}(1-\lambda_1) \begin{Bmatrix} \cos(1+\lambda_1)\phi \\ -\cos(1+\lambda_1)\phi \\ \sin(1+\lambda_1)\phi \end{Bmatrix} \\ \begin{Bmatrix} (1+\mu_1)\cos(1-\mu_1)\phi \\ (3-\mu_1)\cos(1-\mu_1)\phi \\ (1-\mu_1)\sin(1-\mu_1)\phi \end{Bmatrix} \\ \begin{Bmatrix} \cos(1+\mu_1)\phi \\ -\cos(1+\mu_1)\phi \\ \sin(1+\mu_1)\phi \end{Bmatrix} \end{array} \right] + \frac{q}{4(q-1)} \left( \frac{r}{r_0} \right)^{\mu_1-\lambda_1} \begin{Bmatrix} \begin{Bmatrix} (1+\mu_1)\cos(1-\mu_1)\phi \\ (3-\mu_1)\cos(1-\mu_1)\phi \\ (1-\mu_1)\sin(1-\mu_1)\phi \end{Bmatrix} \\ \begin{Bmatrix} \cos(1+\mu_1)\phi \\ -\cos(1+\mu_1)\phi \\ \sin(1+\mu_1)\phi \end{Bmatrix} \end{Bmatrix} \quad (6.16)$$

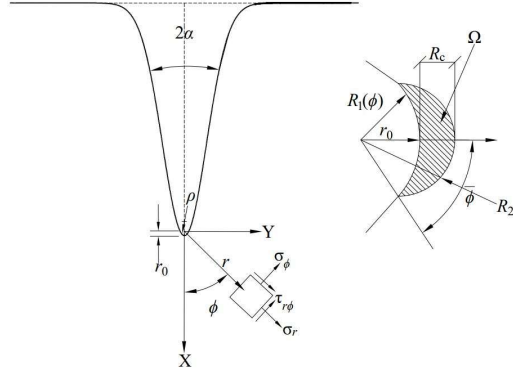


**Fig 6.17** Gaussian pit: reference system, stress components, and control volume.

where  $\sigma_\phi$ ,  $\sigma_r$  and  $\tau_{r\phi}$  represent stress components,  $\lambda_1$  represents Williams' eigen value,  $\mu_1$  signifies supplementary exponent expressing stress field in the neighborhood of pit apex. Further,  $r$  and  $\phi$  represent local polar coordinates. Additionally,  $\chi_{b_1}$ ,  $\chi_{d_1}$  and  $\chi_{c_1}$  are linearly dependent terms obtained through the application of local boundary conditions on the edge free from pits. The total SED in the linear elastic region of an isotropic material is defined as (Lazzarin and Zambardi, 2001):

$$W_{t,SED} = \frac{1}{2E} \left\{ \sigma_{11}^2 + \sigma_{22}^2 + \sigma_{33}^2 - 2\nu(\sigma_{11}\sigma_{22} + \sigma_{11}\sigma_{33} + \sigma_{22}\sigma_{33}) + 2(1+\nu)\sigma_{12}^2 \right\} \quad (6.17)$$

where  $\sigma_{11}$ ,  $\sigma_{22}$ ,  $\sigma_{33}$ , and  $\sigma_{12}$  are the stress components in the given reference system,  $E$  is modulus of elasticity of the material and  $\nu$  is Poisson's ratio. Further, the average SED in the neighborhood of corrosion pit can be expressed as (Lazzarin and Berto, 2005):

$$\Delta \bar{W} = \frac{1}{E} \left( \frac{I_1}{2\Omega} \right) \sigma_{\max}^2 r_0^{2(1-\lambda_1)} \left[ \frac{\sqrt{2\pi}}{1+\bar{\omega}_1} \right]^2 \quad (6.18)$$

where  $\sigma_{\max}$  represents the maximum principal stress,  $\bar{\omega}_1$  signifies pit opening angle ( $2\alpha$ ) dependent parameter while  $I_1$  is dependent on  $2\alpha$  and Poisson's ratio. In addition,  $r_0$  represents the distance from coordinate system origin to pit apex.

$$r_0 = \left( 1 - \frac{1}{q} \right) \rho \quad (6.19)$$

where  $q = (2\pi - 2\alpha)/\pi$ , and  $\rho$  is the pit root radius. Further, the radius of curvature ( $R$ ) of the corrosion pit having a Gaussian profiled can be calculated as:

$$R = \left( \frac{\partial^2 d}{\partial \theta^2} \right)^{-1} \left[ 1 + \left( \frac{\partial d}{\partial \theta} \right)^2 \right]^{3/2} \quad (6.20)$$

By substituting Equation 6.2 into Equation 6.20,  $\rho$  for Gaussian profile corrosion pit can be estimated as:

$$\rho = \frac{e^{\zeta_2 \theta^2} \left[ 1 + \left( 2\zeta_1 \zeta_2 \theta e^{-\zeta_2 \theta^2} \right)^2 \right]^{3/2}}{2\zeta_1 \zeta_2 [1 - 2\zeta_2 \theta^2]} \quad (6.21)$$

By substituting Equation 6.21 into Equation 6.19,  $r_0$  for the Gaussian profiled pit can be expressed as:

$$r_0 = \left( 1 - \frac{\pi}{(2\pi - 2\alpha)} \right) \left( \frac{e^{\zeta_2 \theta^2} \left[ 1 + \left( 2\zeta_1 \zeta_2 \theta e^{-\zeta_2 \theta^2} \right)^2 \right]^{3/2}}{2\zeta_1 \zeta_2 [1 - 2\zeta_2 \theta^2]} \right) \quad (6.22)$$

Finally, the average SED value in the control volume for the corrosion pit following Gaussian profile can be expressed as:

$$\Delta \bar{W} = \varepsilon_w k_t^2 \left( \frac{I_1}{2\Omega} \right) \frac{\sigma_{\max}^2}{E} r_0^{2(1-\lambda_1)} \left[ \frac{\sqrt{2\pi}}{1+\bar{\omega}_1} \right]^2 \quad (6.23)$$

## Fatigue Behavior of Constructional Steels Subjected to Pitting Corrosion and Elevated Temperature

where  $\varepsilon_w$  takes considers nominal load ratio in SED evaluation, taking a value of 1.0 for  $R=0$  and 0.5 for  $R=-1$  (Berto et al., 2014). It is worth pointing out here that Equation 6.22 is valid for room temperature only. Further, the values of different parameters governing average SED analytical model are provided in Table 6.10.

**Table 6.10.** Parameters for the stress distributions of Gaussian model.

Specimen	$2\alpha$ (degrees)	$q$	$I_1$	$\lambda_1$	$\bar{\alpha}_1$	$r_0$ (mm)	$2\Omega$ (mm <sup>2</sup> )	$\rho$ (mm)	$R_c$ (mm)
C_25_±0.6%	132.166	1.266	0.629	0.663	0.458	0.026	0.126	0.050	0.076
C_25_±0.8%	132.572	1.263	0.628	0.664	0.454	0.022	0.103	0.041	0.063
C_25_±1.0%	134.511	1.253	0.622	0.672	0.436	0.027	0.134	0.053	0.080
C_400_±0.6%	135.062	1.250	0.620	0.674	0.431	0.023	0.116	0.046	0.070
C_400_±0.8%	132.072	1.266	0.630	0.662	0.459	0.021	0.101	0.040	0.062
C_400_±1.0%	131.390	1.270	0.632	0.660	0.465	0.025	0.115	0.046	0.071
C_500_±0.6%	133.451	1.259	0.625	0.668	0.446	0.023	0.112	0.045	0.068
C_500_±0.8%	133.136	1.260	0.626	0.666	0.449	0.025	0.122	0.049	0.074
C_500_±1.0%	133.220	1.260	0.626	0.667	0.448	0.020	0.099	0.040	0.060
C_600_±0.6%	133.563	1.258	0.625	0.668	0.445	0.026	0.125	0.050	0.075
C_600_±0.8%	135.404	1.248	0.619	0.676	0.428	0.026	0.133	0.054	0.080
C_600_±1.0%	133.172	1.260	0.626	0.667	0.449	0.024	0.115	0.046	0.070
C_700_±0.6%	133.444	1.259	0.625	0.668	0.446	0.026	0.127	0.051	0.077
C_700_±0.8%	132.183	1.266	0.629	0.663	0.458	0.025	0.118	0.047	0.072
C_700_±1.0%	131.892	1.267	0.630	0.662	0.461	0.028	0.135	0.054	0.083

### 6.4.6.2 Pit sensitivity factor:

A temperature-variant pit sensitivity factor  $P_s(T)$  is introduced here. It is given as:

$$P_s(T) = \frac{P_f - 1}{k_t - 1} \quad (6.24)$$

Note that fatigue pit factor ( $P_f$ ) quantifies the impact of corrosion on fatigue strength at different temperatures and different strain amplitudes by comparing the fatigue strength of uncorroded specimens at room temperature to that of corroded specimens at various elevated temperatures. In this context,  $P_f$  represents the ratio between two strengths. However, evaluating the pit factor requires fixing the number of reference cycles to failure. Previous studies have used 100 or 500 cycles (e.g. (Sharifi and Rahgozar, 2009; Zhang et al., 2015)).

Following the precedent, a reference cycle of 100 is adopted in this study for calculating  $P_f$ .

Fig. 6.18 depict the variation of  $P_s(T)$  with temperature for different strain amplitude.

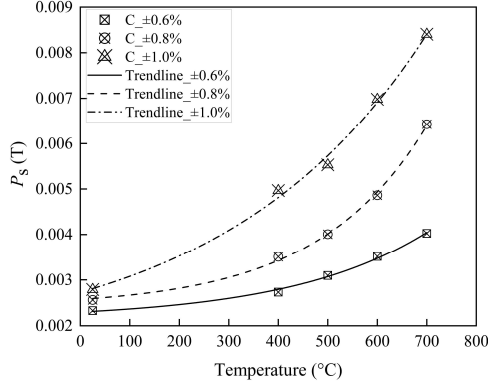


**Fig 6.18** Variation of  $P_s(T)$  with temperature.

For a given strain amplitude, increase in temperature from 25 °C–700 °C results in upto three-fold increase in  $P_s(T)$ . Further, for a given temperature,  $P_s(T)$  values are found to increase by upto 60% between successive strain amplitudes. In particular,  $P_s(T)$  variation is significantly influence by temperature. Hence, it is of engineering interest to develop a mathematical relation between  $P_s(T)$  and  $T$ . To find the relation, an exponential growth function is fitted to the data points of  $P_s(T)$ . The specific mathematical model employed as:

$$P_s(T) = \varsigma_1 + \varsigma_2 e^{\varsigma_3 T} \quad (6.25)$$

where  $\varsigma_1$ ,  $\varsigma_2$  and  $\varsigma_3$  are fitting parameters. Note that  $\varsigma_1$  represent the offset term representing the value of  $P_s(T)$  at room temperature;  $\varsigma_2$  is a conditional constant, and  $\varsigma_3$  represents the growth rate. The results of curve fitting analysis are listed in Table 6.11.

$$\Delta \bar{W} = \varepsilon_w P_s(T) k_t^2 \left( \frac{I_1}{2\Omega} \right) \frac{\sigma_{\max}^2}{E} r_0^{2(1-\lambda_1)} \left[ \frac{\sqrt{2\pi}}{1 + \bar{\omega}_1} \right]^2 \quad (6.26)$$

**Table 6.11.** Regression coefficients used to find the relation between  $P_s(T)$  and  $T$

$\varepsilon_a$	$\varsigma_1$	$\varsigma_2$	$\varsigma_3$	R-square
$\pm 0.6\%$	0.0021	$1.55 \times 10^{-4}$	0.0035	0.99
$\pm 0.6\%$	0.0024	$1.65 \times 10^{-4}$	0.0045	0.99
$\pm 1.0\%$	0.0014	0.0012	0.0024	0.99

## Fatigue Behavior of Constructional Steels Subjected to Pitting Corrosion and Elevated Temperature

Note that the analysis resulted in R-Square values of 0.99. Fig. 6.18 shows the trendlines over the data points based on Equation 6.24. A strong agreement seen between the model and the observed data, further supporting the suitability of the proposed mathematical function. By introducing Equation 6.25 into Equation 6.26, the average SED values considering the impact of high temperatures can be evaluated as:

### 6.4.6.3 Pit opening angle:

To estimate pit opening angle in the Gaussian profiled corrosion pit, the analytical solution for elliptical pit can be extended with a suitable accuracy index (CE, 1913; Filippi and Lazzarin, 2004). The accuracy index is expressed as :

$$\nabla = \frac{1}{0.4p} \int_0^{0.4p} [\sigma_{nn} - \sigma_{\phi}]^2 dr \quad (6.27)$$

where  $\sigma_{nn}$  represents normal stress under mode I loading and  $0.4p$  implies distance near the pit where the pit effect diminishes, and both cracks and pits experience comparable stress levels (Atzori et al., 2001).

Fig. 6.19 shows the relation between  $2\alpha$  and  $\nabla/\sigma_{\max}^2$  for varying values of  $p_d^{\max}/w$ . As observed, with increasing  $p_d^{\max}/w$ ,  $\nabla/\sigma_{\max}^2$  progressively diminishes. In addition,  $\nabla/\sigma_{\max}^2$  shows upward trend with increasing  $p_d^{\max}/w$ . To mathematically model this relationship, a regression of the data points in Fig 6.14 yields the following interpolating law for  $2\alpha$  :

$$2\alpha = 195.11 \left( 1 + 2 \frac{p_d^{\max}}{w} \right)^{-0.963} \quad (6.28)$$

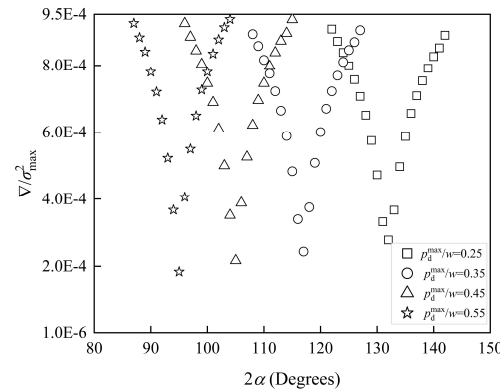


**Fig 6.19** Variation of normalized index with Gaussian pit opening angle.

To validate Equation 6.28, the regression coefficients, 195.11 and  $-0.963$ , are compared with the values reported for elliptical notch, 192.64,  $-0.916$  (Filippi and Lazzarin, 2004). As observed, the values are comparable. Moreover,  $2\alpha$  assumes a value of  $67.73^\circ$  for  $p_d^{\max} = w$ , representing a circular corrosion pit. This can also be justified based on other theoretical considerations related to free edge effects (Filippi and Lazzarin, 2004).

#### 6.4.6.4 Variation of $\Delta\bar{w}$ :

The values of  $\Delta\bar{w}$  are calculated using Equation 6.29 for different temperatures. Fig. 6.20 shows the variation of  $\Delta\bar{w}$  with temperature. In corroded specimens: (i) for a given strain amplitude, increase in temperature from  $25^\circ\text{C}$  to  $700^\circ\text{C}$  results in upto 2.8-fold increase in  $\Delta\bar{w}$ ; upto 31% increase in  $\Delta\bar{w}$  between successive strain amplitude for a given temperature; and a growth rate of 16% between successive strain amplitude. Meanwhile in corroded specimens, for a given strain amplitude, increase in temperature from  $25^\circ\text{C}$  to  $700^\circ\text{C}$  results in upto 4.1-fold increase in  $\Delta\bar{w}$ ; upto 46% increase in  $\Delta\bar{w}$  between successive strain amplitude for a given temperature; and a growth rate of 32% between successive strain amplitude. Further, comparing  $\Delta\bar{w}$  of uncorroded and corroded specimens at a given strain rate leads to upto 68% increase in  $\Delta\bar{w}$  from  $25^\circ\text{C}$ – $700^\circ\text{C}$ . These observations underscore the effects of pitting corrosion and high temperature in  $\Delta\bar{w}$ .

To establish a mathematical relation between  $\Delta\bar{w}$  and  $T$  for varying strain amplitude, a following model is used as:

$$\Delta\bar{w} = \psi_1 + \psi_2 e^{\psi_3 T} \quad (6.29)$$

where  $\psi_1$ ,  $\psi_2$ , and  $\psi_3$  are fitting parameters and are listed in Table 6.12. Figure 6.20 displays the fitted trendlines generated using Equation 6.29, for both uncorroded and corroded specimens, an exponential function provides a significantly best fit, as reflected by an R-squared value of 0.99.

**Table 6.12.** Regression coefficients used to find the relation between  $\Delta\bar{w}$  and  $T$ .

Uncorroded specimens					Corroded specimens				
$\varepsilon_a$	$\psi_1$	$\psi_2$	$\psi_3$	R-square	$\varepsilon_a$	$\psi_1$	$\psi_2$	$\psi_3$	R-square
$\pm 0.6\%$	0.416	0.033	0.004	0.998	$\pm 0.6\%$	0.455	0.042	0.004	0.995
$\pm 0.8\%$	0.347	0.049	0.003	0.994	$\pm 0.8\%$	0.493	0.066	0.004	0.987
$\pm 1.0\%$	0.322	0.176	0.002	0.979	$\pm 1.0\%$	0.562	0.004	0.005	0.993

## Fatigue Behavior of Constructional Steels Subjected to Pitting Corrosion and Elevated Temperature

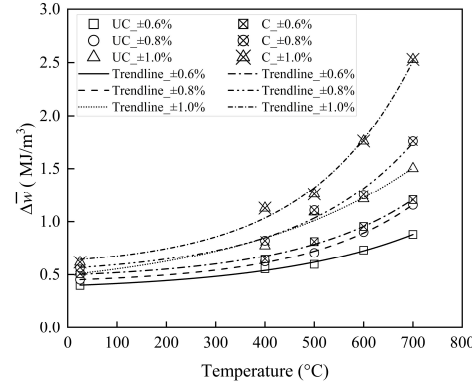


**Fig 6.20** Variation of  $\Delta \bar{w}$  with temperature.

### 6.4.6.5 Estimation of $N_{f, \text{est}}$ :

Fig. 6.21 presents a log–log scatter plot between  $\Delta \bar{w}$  and  $N_{f, \text{exp}}$  based on the estimated values of  $\Delta \bar{w}$  listed in Table 6.13. The plot displays a narrow scatter band having 2.3% and 97.7% probability of survival limits. The lower curve in the plot represents the mean  $\Delta \bar{w}$  minus two standard deviations, defining the scatter index ( $T_{\Delta w}$ ) with an inverse slope of  $(\bar{k})=1.500$ . Using this approach, an appropriate relation between  $\Delta \bar{w}$  and  $N_{f, \text{exp}}$  for LCF behaviour of the high–strength structural steel bars can be represented as:

$$\Delta \bar{w}^{\bar{k}} \times N_{f, \text{est}} = \Delta \bar{w}_a^{\bar{k}} \times N_r \quad (6.30)$$

Considering the reference number of cycles,  $N_r$ , equal to  $5 \times 10^3$ , Fig. 6.22 compares the  $N_{f, \text{est}}$  based on Equation 6.30 with  $N_{f, \text{exp}}$ . Notably, all data points fall within an error band of  $\pm 1.5$ . This validates the effectiveness of using the average SED approach for evaluating the LCF behaviour of structural steel exposed to pitting corrosion and elevated temperature. Further, Equation 6.30, can be rewritten as:

$$N_{f, \text{est}} = \frac{\Delta \bar{w}_a^{\bar{k}} \times N_r}{\Delta \bar{w}^{\bar{k}}} \quad (6.31)$$

The values of  $N_{f, \text{est}}$  estimated from Equation 6.31 are compared with  $N_{f, \text{exp}}$  in Table 6.17. Analysis of Table 6.13 reveals individual error percentages for  $N_{f, \text{est}}$  range from 0.97 % to 23.42%, with 20 out of 30 specimens showing errors below 15%. This validates the applicability of average SED approach for estimating the LCF behaviour of the structural steel. It's worth pointing out here a few estimates exceed 15% threshold. This may be attributed to inherent

specimen sensitivity, experimental system errors, and individual sensitivity to stress range (Wang et al., 2016). Nevertheless, Equation 6.31 demonstrates sufficient accuracy in predicting  $N_{f,exp}$  under LCF conditions in structural steel exposed to pitting corrosion and high temperatures.

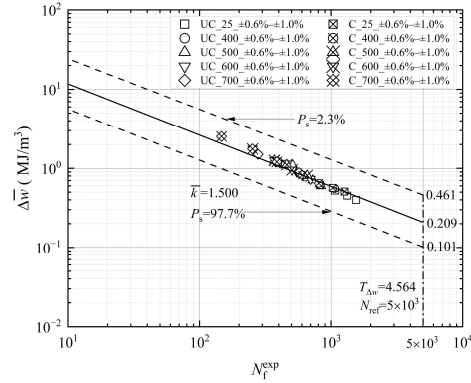


**Fig 6.21** Relation between average SED and  $N_{f,exp}$ .

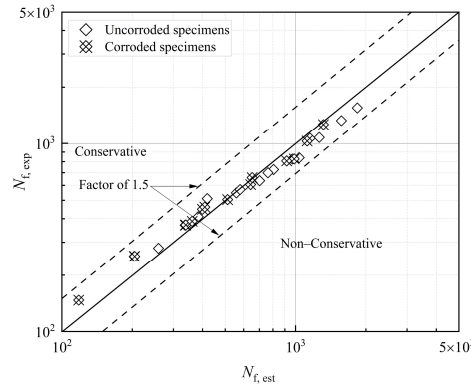


**Fig 6.22** Comparison between experimental and estimated value of  $N_f$ .



**Table 6.13.** SED approach for comparison between  $N_{f,exp}$  and  $N_{f, est}$  of specimens.

Specimen	$\Delta \bar{w}$ (MJ/m <sup>3</sup> )	$N_{f,exp}$	$N_{f, est}$	Error (%)	Specimen	$\Delta \bar{w}$ (MJ/m <sup>3</sup> )	$N_{f,exp}$	$N_{f, est}$	Error (%)
UC_25_ $\pm$ 0.6%	0.399	1551	1838	-18.53	C_25_ $\pm$ 0.6%	0.509	1264	1316	-4.16
UC_25_ $\pm$ 0.8%	0.452	1325	1571	-18.60	C_25_ $\pm$ 0.8%	0.566	1029	1121	-8.96
UC_25_ $\pm$ 1.0%	0.523	1075	1263	-17.50	C_25_ $\pm$ 1.0%	0.617	827	986	-19.27
UC_400_ $\pm$ 0.6%	0.556	1065	1153	-8.34	C_400_ $\pm$ 0.6%	0.648	807	916	-13.57
UC_400_ $\pm$ 0.8%	0.624	826	969	-17.36	C_400_ $\pm$ 0.8%	0.821	606	642	-6.04
UC_400_ $\pm$ 1.0%	0.774	635	702	-10.57	C_400_ $\pm$ 1.0%	1.127	449	399	11.03
UC_500_ $\pm$ 0.6%	0.597	840	1036	-23.42	C_500_ $\pm$ 0.6%	0.812	659	652	0.97
UC_500_ $\pm$ 0.8%	0.706	727	805	-10.76	C_500_ $\pm$ 0.8%	1.108	461	409	11.11
UC_500_ $\pm$ 1.0%	1.091	511	419	17.97	C_500_ $\pm$ 1.0%	1.260	370	337	8.70
UC_600_ $\pm$ 0.6%	0.733	699	762	-9.01	C_600_ $\pm$ 0.6%	0.954	505	512	-1.49
UC_600_ $\pm$ 0.8%	0.901	548	558	-1.90	C_600_ $\pm$ 0.8%	1.255	371	339	8.39
UC_600_ $\pm$ 1.0%	1.214	380	357	6.00	C_600_ $\pm$ 1.0%	1.759	253	204	19.05
UC_700_ $\pm$ 0.6%	0.879	570	579	-1.62	C_700_ $\pm$ 0.6%	1.205	388	361	6.96
UC_700_ $\pm$ 0.8%	1.157	410	383	6.42	C_700_ $\pm$ 0.8%	1.757	253	205	18.93
UC_700_ $\pm$ 1.0%	1.502	279	259	6.95	C_700_ $\pm$ 1.0%	2.529	147	118	19.21

## 6.5 Conclusions

The influence of elevated temperatures and pitting corrosion on the LCF properties of the medium-strength and high-tension type killed E350 structural steel is experimentally investigated. Fire exposure can significantly impact the structural performance of structural steel, particularly its LCF properties. This is especially crucial for the medium-strength steels, where fire-induced changes in LCF behavior directly influence post-fire seismic performance. Additionally, pitting corrosion, further exacerbates fatigue crack initiation and propagation under repeated loading, compromising structural durability and safety. The present study experimentally investigates the LCF behavior of structural steel subjected to pitting corrosion and elevated temperatures. Specimens undergo strain-controlled fatigue testing with strain amplitudes ranging from  $\varepsilon_a = \pm 0.6\%$  to  $\pm 1.0\%$  and exposure temperatures from 25 °C to 700 °C. The key findings of this investigation are presented as follows.

- i. Corroded steel subjected to  $\pm 1.0\%$  strain amplitude experiences a significant reduction in total dissipated energy density by 52% when exposed to elevated temperatures ranging from 400 °C to 700 °C. This significant decrease suggests a marked decline in fatigue resistance of corroded steel at elevated temperatures.
- ii. The reduction in modulus is particularly evident at temperatures of 600°C and 700°C. Uncorroded specimens in this range experience a 9–14% decrease in modulus, whereas corroded specimens show a larger reduction of 12–39%. This reduction signifies a weakening of the material's structural integrity, increasing its vulnerability to deformation and failure.
- iii. The decline in peak stress amplitude, with number of cycles to failure, denotes the initiation of cracks in the early testing stages. Notably, corroded specimens exhibit significant reduction, approximately 6.2% after 100 cycles at  $\pm 0.6\%$  and approximately 11% after 300 cycles at  $\pm 1.0\%$ . This decline suggests an increased risk of structural failure due to material deterioration and intensified crack susceptibility.
- iv. The cyclic softening factor tends to decrease with increasing strain amplitude for all specimens. The decline becomes more pronounced with increasing temperature, particularly at higher temperatures.
- v. The Coffin–Manson equation describes the relationship between strain amplitude and cycles to failure for structural steel subjected to pitting corrosion and elevated temperature. Analysis reveals  $N_f$  decreases with increasing  $\varepsilon_a$ . Further, the temperature-dependent trends in model coefficients, decreases as exposure temperature rises. Equations are proposed to predict these temperature-dependent coefficients for fire exposure scenarios.



**High-cycle fatigue behavior of structural steel subjected to pitting corrosion at multiple sites under elastic stress conditions**

---

**7.1 Introduction**

Structural steel is increasingly used in long-span bridges due to its strength, and ductility. However, these structures often face harsh environments with high humidity and salt spray, leading to cracking. Consequently, corrosion becomes a major concern, reducing the effective cross-section and introducing stress concentrations. The presence of corrosion weakens the material, increasing the susceptibility of corroded structures to fatigue crack initiation and propagation under repeated loading. This significantly reduces their long-term load-carrying capacity and structural integrity. Both generalized and pitting corrosion affect steel behavior, with the latter introducing stress concentrations and non-uniform load distribution.

Numerous researchers have extensively studied the fatigue and corrosion properties of structural steel. However, there's a need to investigate the influencing factors of multiple pits, which significantly exacerbate steel's susceptibility to fatigue failure. Multiple pits on steel surfaces act as stress concentrators, intensifying cyclic loading and accelerating fatigue crack initiation and propagation. When pits are close, their combined effects exacerbate, creating overlapping stress fields that amplify crack growth. The sharp edges of pits provide ideal sites for crack initiation, leading to a complex network of propagating cracks that compromise structural integrity. This network can rapidly lead to catastrophic failure, significantly reducing the fatigue life of steel structures.

While numerous studies have examined the impact of corrosion on static properties, fewer have focused on low-cycle and high-cycle fatigue behavior. This study aims to comprehensively address this gap by investigating the impact of corrosion level and maximum stress levels on the fatigue properties of E350 BR grade structural steel. Each steel specimen underwent electrochemical accelerated corrosion before axial tensile fatigue tests. The HCF behavior of structural steel with multiple pit sites has been experimentally determined. Stress-cycle ( $S-N_f$ ) curves for different corrosion levels have been determined and establish the relationship between the fatigue life and maximum stress levels. Additionally, the study investigates the resulting macroscopic and microscopic morphological changes in structural steel specimens. The findings demonstrate that one or multiple located pits play a dominant role in determining the fatigue life of corroded plain reinforcing bars.

## 7.2 Materials and test arrangements

### 7.2.1 Specimen preparation:

The study investigates the HCF behaviour of E350 hot rolled structural steel, commonly used in bridge and industrial structures. These specimens were machined from IS2062 E350 BR grade steel plates with a thickness of 27 mm having a dimension of 27 mm × 2000 mm × 12000 mm. The specimens utilized in this study feature a 50 mm long fatigue section with a 10 mm gauge diameter and a surface roughness of 0.2  $\mu\text{m}$  (Fig. 7.1). Smooth transitions connect this section to the grip sections at each end, which have a length of 16.70 mm and a radius of curvature of 48 mm. The grip sections themselves have a diameter of 20 mm and a combined length of 70 mm. Table 7.1 details the chemical composition of the material, while Table 7.2 summarizes the acquired mechanical properties in the as-received condition from the manufacturer.

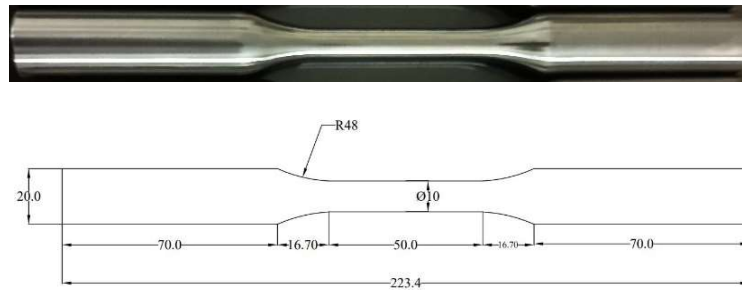


**Fig 7.1** Fatigue testing specimen (unit: mm).

**Table 7.1.** Chemical composition of E350 (in wt. %).

Chemical composition	C	Mn	S	P	Si	Al	Cu	Ni	Cr	CEQ
Specimen	0.14	1.45	0.0020	0.014	0.31	0.026	0.006	0.009	0.013	0.38

**Table 7.2.** Mechanical properties of E350

Tensile strength (MPa)	Yield strength (MPa)	Tensile strength/Yield strength	Elongation (%)	Young's modulus (MPa)	Poisson's ratio
534	372	1.43	34	$2.1 \times 10^5$	0.30

### 7.2.2 Corrosion procedure:

The present study employed an electrochemical technique to accelerate the corrosion. The fatigue tests are conducted with single pit site on one set of specimens and multiple pit sites on the other set of specimens. For both sets, the entire specimen surface, except for designated

circular areas 5 mm in diameter, is covered with insulating tape to localize pitting. One end of each specimen is connected to a wire, and both ends are sealed with hot melt glue to prevent solution ingress.

The specimen act as the anode and are fully immersed in a tray containing a 5% NaCl solution alongside a stainless-steel bar acting as a cathode. For the single-pit specimens, A constant direct current of 0.5 A is applied for 10 minutes to accelerate corrosion within the designated area. For the multiple-pit specimens, the same initial corrosion procedure is performed on one designated pit. Subsequently, an additional pit on the same specimen undergoes further accelerated corrosion for another 10 minutes, resulting in one pit exposed to 20 minutes of corrosion and another to 10 minutes. (Fig. 7.1 (a) and (b)) shows the specimens with single pit site and with multiple pit sites.

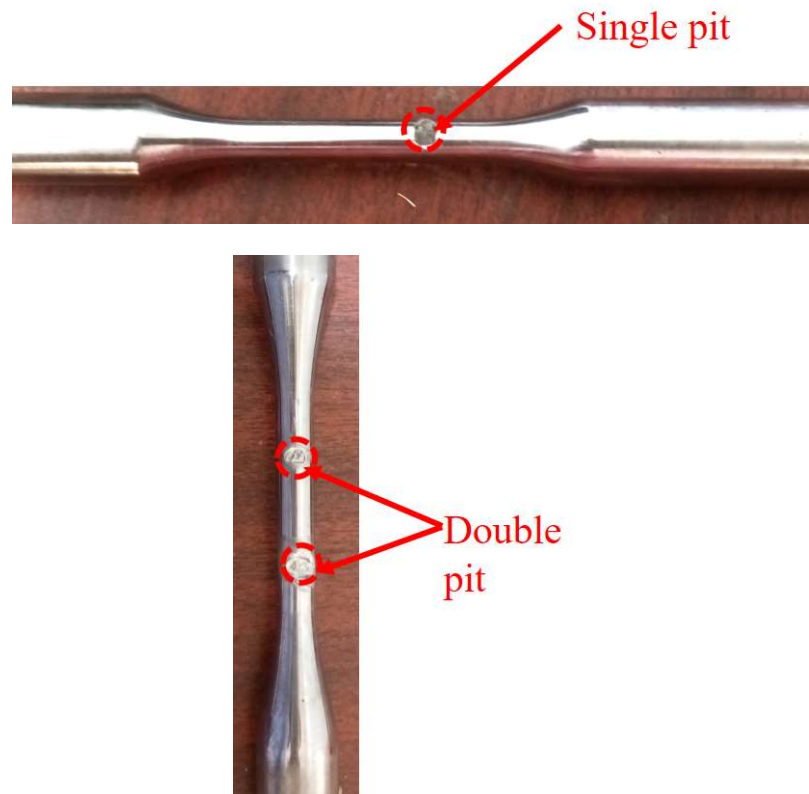


**Fig 7.2** Specimen with corrosion pit: (a) single pit; (b) multiple pits.

### 7.2.3 Characterization of Pitting corrosion:

The dimensions of corroded pits, including width ( $w$ ), length ( $l$ ), and depth ( $p_d$ ), are measured with a precision of 0.2 mm using a compact, high-definition three-dimensional laser scanner. The laser scans the pit geometry at a density of 5 million points, achieving this by

## Fatigue Behavior of Constructional Steels Subjected to Pitting Corrosion and Elevated Temperature

emitting light pulses onto the surface and capturing the reflected light with a sensor. This process acquires detailed data on the pit geometry, effectively capturing and visualizing the pit and recreating the corroded specimen. The results of the laser scanning are summarized in Table 7.3. The critical cross-sectional area loss can be estimated as:

$$\eta_{\text{cri}} = (1 - A_{\text{m}}/A_{\text{n}}) \times 100\% \quad (7.1)$$

where  $A_{\text{n}}$  and  $A_{\text{m}}$  represent sample's nominal and minimum cross-sectional area ( $\text{mm}^2$ ).

**Table 7.3** Result summary of corrosion pit geometry.

Specimen	Corrosion time (min)	Pit geometry from 3D laser scanning							
		$p_{\text{d}}^{\text{max}}$ (mm) Pit_1	$p_{\text{d}}^{\text{max}}$ (mm) Pit_2	$w$ (mm) Pit_1	$w$ (mm) Pit_2	$l$ (mm) Pit_1	$l$ (mm) Pit_2	$\eta_{\text{cri}}$ (%) Pit_1	$\eta_{\text{cri}}$ (%) Pit_2
SC_1	10	0.81	—	5.58	—	5.84	—	3.31	—
SC_2	10	0.83	—	5.49	—	5.72	—	3.38	—
SC_3	10	0.79	—	5.34	—	6.52	—	3.27	—
SC_4	10	0.78	—	5.5	—	6.46	—	3.28	—
DC_1	10/20	1.28	0.79	6.01	5.72	5.92	6.51	7.71	3.28
DC_2	10/20	1.26	0.80	5.89	5.61	5.99	6.42	7.64	3.30
DC_3	10/20	1.31	0.84	6.72	6.39	5.68	5.77	7.94	3.40
DC_4	10/20	1.33	0.79	6.66	5.72	5.73	5.83	8.12	3.29

Table 7.3 presents the  $\eta_{\text{cri}}$  values for both single and multiple pits corroded specimens. It can be observed that for single corroded specimens (SC\_1–SC\_4) exposed for 10 minutes, the  $\eta_{\text{cri}}$  values fall less than 5%, indicating mild exposure. Conversely, double corroded specimens (DC\_1–DC\_4) exposed for 20 minutes of corrosion duration exhibit  $\eta_{\text{cri}}$  of more than 5% but less than 10%, corresponding to moderate exposure.

### 7.2.4 Fatigue testing:

The HCF behavior of the specimens was conducted on a servo-hydraulic fatigue testing machine (Instron 8802, 250 kN), as shown in Fig. 7.3. The fatigue tests employed load control, applied directly to the specimens through a load cell positioned on top of the hydraulic jack. The stress level ranged from 0.70 to 1.0 times the material's yield strength, while maintaining a constant stress ratio of 0.1. The specimens were subjected to tensile fatigue tests under ambient air conditions at room temperature, using a sinusoidal load with a frequency of 20 Hz. The applied load was constant during testing, resulting in varying actual stress ranges due to

differences in their minimum cross-sectional areas caused by corrosion. Table 4 details the applied loads and fatigue life results for each specimen. These stress levels were chosen to reflect those experienced by reinforcing bars in RC bridges under typical service and overload conditions (Fernandez et al., 2015). While the chosen loading frequency of 20 Hz exceeds that of typical vehicle loads on bridge decks, previous studies suggest a minimal impact on test results (Laman and Nowak, 1996). The fatigue testing was terminated in two scenarios: specimen fracture or reaching a predefined cycle limit of 1 million cycles. However, a fracture at the grip section rendered the test invalid.



Fig 7.3 HCF test setup.

## 7.3 Fatigue testing results

### 7.3.1 $S_r - N_{f,exp}$ development based on fatigue data:

In order to assess the influence of stress range and corrosion damage on the fatigue behavior of E350 steel, this study follows the approach of a previous investigation (Zhang and Yuan, 2014) by employing a fatigue  $S_r - N_{f,exp}$  model which is mathematically expressed as:

$$N_{exp} = A' S_r^{m'} \quad (7.2)$$



## Fatigue Behavior of Constructional Steels Subjected to Pitting Corrosion and Elevated Temperature

where  $A'$  and  $m'$  are the material's constant.

The study builds upon a general fatigue  $S_r - N_{f,exp}$  curve for corroded steel developed in, considering the pitting corrosion effects (Hahin, 1994) expressed as:

$$N_{exp} = AS_r^m \quad (7.3)$$

where  $A$  and  $m$  are influenced by the level of corrosion in the reinforcing bars. Equation 7.3 can be transformed into a linear relationship as follows:

$$\log N_{exp} = A - m \log S_r \quad (7.4)$$

Fig. 7.4 presents the fatigue test results from Table 7.3 plotted in a linear format for clarity. The figure reveals a clear linear relationship between stress range (logarithmic scale) and fatigue life for both single and double corroded specimens. Notably, as corrosion severity increases, fatigue life progressively decreases at any given stress range. Drawing on these combined data, Equations 7.5 and 7.6 provide  $S_r - N_{f,exp}$  curves for single and double corrosion respectively.

$$\log N_{exp} = 19.04 - 5.40 \log S_r, \quad R^2 = 0.98 \quad (7.5)$$

$$\log N_{exp} = 21.78 - 6.74 \log S_r, \quad R^2 = 0.98 \quad (7.6)$$

### 7.3.2 Relation between fatigue life and maximum stress levels:

The fatigue testing results, applied loads, and fatigue life of the specimens are detailed in Table 7.4. All fatigue tests were conducted until failure, defined as the complete separation of the specimen. To establish a relationship between fatigue life and maximum stress levels, the fatigue life versus maximum stress is illustrated in Fig. 7.5. A log-linear relation between fatigue life and maximum stress levels is evident, with a notable decrease in life as the maximum stress level increases.

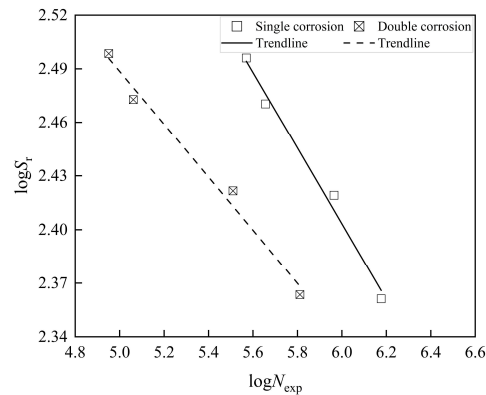
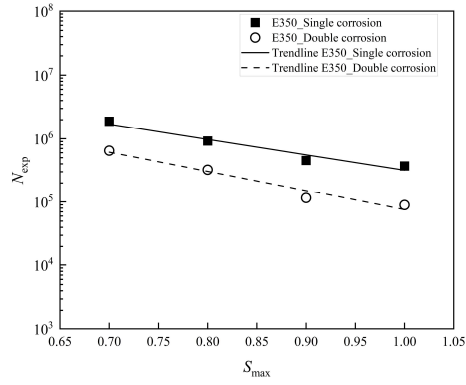


Fig 7.4  $S_r - N_{f,exp}$  curves for corroded E350 structural steel.



**Fig 7.5** Relation between fatigue life and maximum stress levels.

**Table 7.4** Result summary of fatigue testing.

Specimen No.	Specimen corrosion type	Maximum stress levels	Maximum load (kN)	Minimum load (kN)	Cycles to failure
SC_1	Single	$1 f_y$	27.48	2.74	3,71,356
SC_2	Single	$0.9 f_y$	24.73	2.47	4,53,273
SC_3	Single	$0.8 f_y$	21.99	2.19	9,21,977
SC_4	Single	$0.7 f_y$	19.24	1.92	14,79,108
DC_1	Double	$1 f_y$	27.48	2.74	89,370
DC_2	Double	$0.9 f_y$	24.73	2.47	1,15,183
DC_3	Double	$0.8 f_y$	21.99	2.19	3,23,474
DC_4	Double	$0.7 f_y$	19.24	1.92	6,47,649

Equations 7.7 and 7.8 provide relation between the fatigue life and maximum stress levels for single and double corrosion respectively.

$$\log N_{exp} = 7.93 - 2.43 S_{max}, \quad R^2 = 0.95 \quad (7.7)$$

$$\log N_{exp} = 7.90 - 3.02 S_{max}, \quad R^2 = 0.95 \quad (7.8)$$

## 7.4 Fractography analysis

The fracture surface, shown in Fig. 7.5 (a), exhibits both transverse microcracks and fine striation marks. These striations originate from the repeated opening and closing of the fatigue crack during each load cycle, as explained by (Schijve, 2009). Electron microscopy reveals that the striations exist in pairs with a smaller spacing within each pair (Fig. 7.5 (b)). Fewer striation marks have been observed as shown in Fig. 7.5 (a). A significant presence of honeycomb-like dimples and microvoids, exhibiting diverse sizes and shapes, is evident from Fig. 7.5 (c).

## **Fatigue Behavior of Constructional Steels Subjected to Pitting Corrosion and Elevated Temperature**

Previous studies such as Li et al., (2020); Paul et al., (2014) highlight the random distribution of nucleation, resulting in non-uniform sizes and depths of dimples. The emergence of macro-cracks as illustrated in Fig. 7.5 (d) and Fig. 7.5 (e) indicates a shift from gradual fatigue crack growth to an abrupt transition into rapid tensile fracture.

The crack propagation zone of specimens in the as-received state is characterized by the presence of macrocracks, clamshell marks, (Campbell, 2012; Li et al., 2020). Clamshell marks, also known as beach marks, serve as indicators of crack propagation originating from the crack initiation zone (Fig. 7.5 (g)). A large number of irregular and deeper voids are also present in this zone. The crack path depicted in Fig. 7.5 (g) displays branching, and as the branched crack progresses, it gives rise to a complex pattern. Simultaneously, another crack initiates and assumes the role of the principal crack, independently advancing in its own growth trajectory. Furthermore, there is a notable increase in dimple depth as the corrosion exposure increases as shown in Fig. 7.5 (g). In general, the presence of uniform and deep dimples signifies higher plasticity in the specimen, while a limited number of shallow dimples suggests apparent brittleness. The dimples observed serve as confirmation that the region experienced rapid tensile fracture, resulting from the forward branch of the last loading cycle.

Tear ridges are formed on the fracture surface as shown in Fig. 7.5 (e) and Fig. 7.5 (h). This observation can be attributed to the enhanced reaction between steel and the corrosive medium as the corrosion level increases, making the material more susceptible to fracture (Guo et al., 2020). A greater number of deeper microcracks and dimples are predominant in 20 min exposure duration compared to 10 min exposure. Larger tear ridges are indicative of enhanced resistance to material fractures (Kim and Hartt, 2006). The tear ridge formed in Fig. 7.5 (e) exhibited significantly larger dimensions compared to Fig. 7.5 (h).

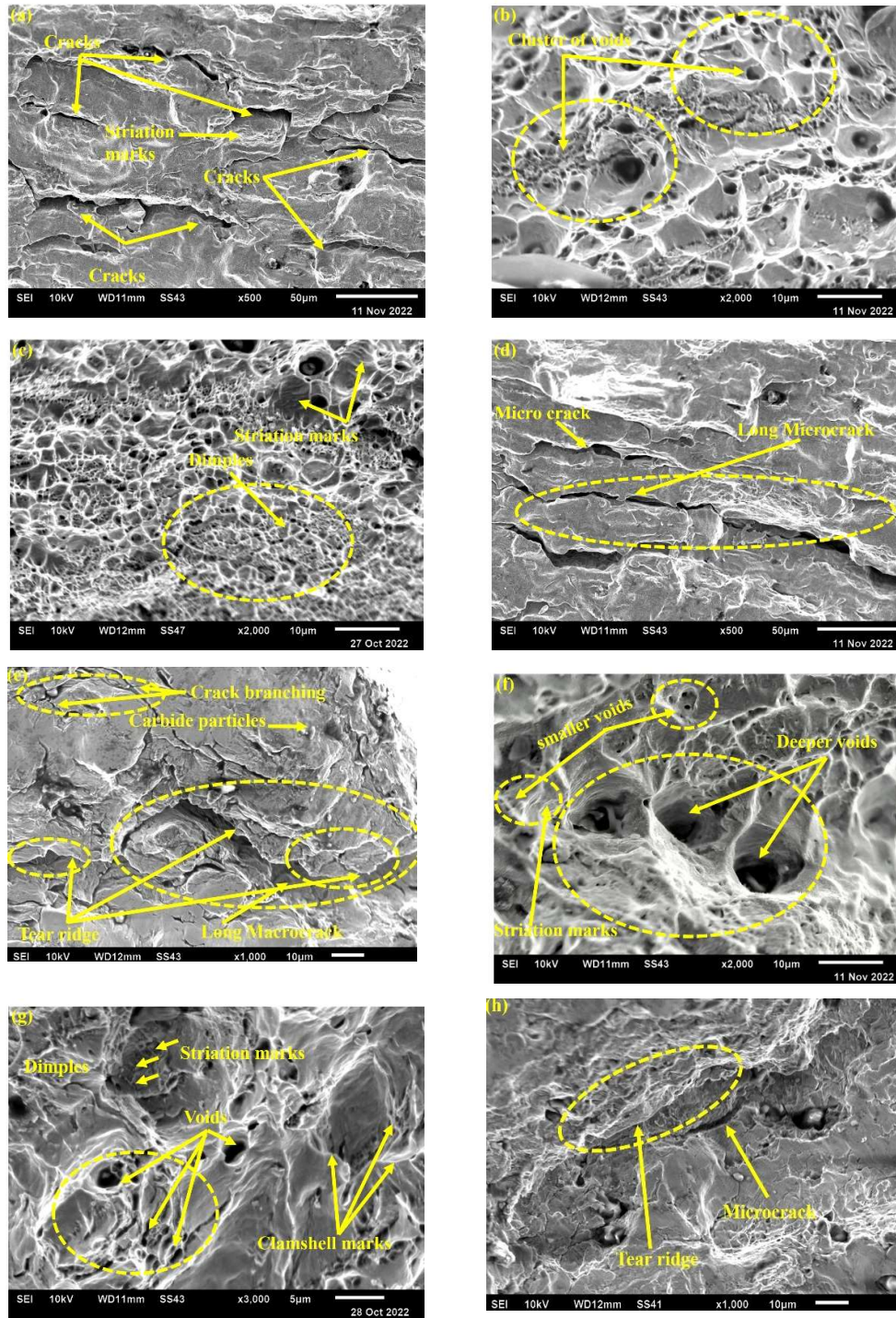


**Fig 7.6** Fractographic images of corroded pits: (a) SC\_1; (b) SC\_2 (c) SC\_3; (d) SC\_4; (e) DC\_1; (f) DC\_2; (g) DC\_3; and (h) DC\_4.

## 7.5 Conclusions

1. Fatigue testing revealed a substantial decrease in the fatigue life of corroded structural steel as both the corrosion level and maximum stress level increased. This indicates a

## **Fatigue Behavior of Constructional Steels Subjected to Pitting Corrosion and Elevated Temperature**

- strong negative relation between fatigue life and both corrosion severity and applied stress.
2. The fatigue test results revealed a clear correlation between stress range and fatigue life for structural steel. This relationship was linear on a logarithmic scale, indicating that a significant decrease in fatigue life occurred with an increase in stress range. Furthermore, the study conclusively demonstrated that corrosion severity had a detrimental effect on fatigue life. Specimens subjected to higher corrosion levels exhibited a shorter fatigue life at any given stress range. These findings are significant for understanding the fatigue behavior of E350 steel in corrosive environments and can inform engineering practices to ensure the durability of structures made from this steel.
  3. The fatigue test revealed a clear inverse relationship between fatigue life and maximum stress levels for structural steel in both single and double corrosion conditions. This relationship followed a log-linear trend, signifying a significant reduction in fatigue life with increasing maximum stress. These findings are crucial for design considerations, as they emphasize the importance of minimizing stress levels to ensure the structural integrity of structural steel exposed to fatigue loads in corrosive environments.
  4. The fractographic analysis revealed a clear transition from fatigue crack growth to rapid fracture in the specimens. The presence of striations, microvoids, and clamshell marks indicated the fatigue crack propagation mechanism. The observed increase in dimple size and tear ridge with increasing corrosion exposure suggested a progressive loss of material ductility and a rise in susceptibility to fracture. These findings highlight the detrimental effect of corrosion on the fracture resistance of the material.
  5. Corroded steel with multiple pits exhibited a significantly shorter fatigue life compared to specimens with single pits. This highlights the detrimental effect of numerous corrosion pits, each acting as a stress concentration point and accelerating fatigue failure.

## **8.1 Introduction**

The study investigated the combined effect of pitting corrosion and elevated temperatures on the fatigue behavior of constructional steels. It focused on comprehensively evaluating the fatigue response under these conditions, offering unprecedented depth in quantifying surface roughness changes induced by pitting and temperature exposure. Predictive models are developed to relate the surface topographic parameters to the severity of corrosion and temperature exposure. The research conducted an extensive experimental investigation of the LCF behavior of pitting-corroded reinforcing bars at elevated temperatures under stress control. Detailed fractographic analysis of fracture surfaces in these corroded specimens at high temperatures provided valuable insights. Further, LCF tests were performed on structural steel under strain control conditions, analysing both corroded and uncorroded specimens. This led to the development of various parameters and predictive models to understand the influence of pitting corrosion and elevated temperature on LCF behavior. Additionally, the study experimentally investigated the HCF behavior of constructional steel containing multiple corrosion pits. This approach provided valuable insights into the fatigue response of the material under these complex and realistic conditions.

## **8.2 Research conclusions and contributions**

The following are the major conclusions and contributions derived from the study:

1. Surface characteristics, including amplitude, spacing, spatial, and volume parameters, exhibit a notable increase with prolonged corrosion exposure and elevated temperatures. These parameters significantly influence the mechanical and physical properties of the reinforcing bar. Realistic artificial mimicking of surface profiles for varying degrees of pitting corrosion and temperature is achievable based on the obtained data.
2. Substantial microstructural changes occur in specimens heated to 500°C or higher, notably a decrease in granular carbide density at 700°C. Fractographic images reveal carbides of varying sizes. Enhanced-density fine carbides reduce surface roughness by filling interstitial spaces between coarse carbides. Larger carbides, constrained by size, contribute to increased roughness by failing to fill voids. This elevated roughness creates an uneven surface resembling valleys or pits, potentially acting as sites for crack initiation.
3. An analysis of the pitting corrosion penetration depth along the circumference of the reinforcing bar revealed that it follows a flipped Gaussian distribution. This model

## **Fatigue Behavior of Constructional Steels Subjected to Pitting Corrosion and Elevated Temperature**

- demonstrates a high degree of agreement with experimental data, as evidenced by the R-squared values ranging from 0.9310 to 0.9937 (minimum and maximum, respectively). Notably, 94% of the specimens exhibited R-squared values exceeding 0.95, indicating a strong fit between the model and the observed data.
4. Pitting corrosion and elevated temperature significantly impact the surface topography. Existing models fail to consider the combined effects of pitting corrosion and high temperatures on surface topography, which significantly impacts fatigue life. This study presents novel models that correlates surface roughness parameters to both corrosion severity and temperature. Through rigorous statistical analysis, the study validates robust relationships between these variables. Moreover, the evaluation of these models demonstrates satisfactory margins of error, affirming their reliability. Notably, the findings reveal that stress concentration factors and defect sizes are intricately linked to the severity of corrosion and temperature variations, providing valuable insights for fatigue life estimation of TMT reinforcing steel bars under challenging environmental conditions.
  5. The study proposes a framework for high-cycle fatigue life estimation, built upon developed models for surface topography features. Validation against existing data confirms its effectiveness. Notably, the framework reveals decreasing fatigue life in steel reinforcing bars with higher pitting severity, corrosion level, and temperature. Predicted fatigue life aligns well with both corroded and uncorroded experimental values.
  6. The study proposes an analytical expression for the stress concentration factor based on the inverted Gaussian distribution of pitting corrosion penetration depth along the reinforcing bar's perimeter. Notably, the proposed analytical equation, derived using the Gaussian function, exhibits a minimal deviation of only 7% from the results of finite element analysis, demonstrating its accuracy and efficiency.
  7. The experimental investigation of the LCF behavior of pitting corroded reinforcing bars at elevated temperatures shows that uncorroded reinforcing bars soften significantly under LCF at elevated temperatures. Corroded bars experience this even faster, reaching the same level of softening in fewer cycles. Higher temperatures worsen this effect. In corroded bars, energy dissipation capacity reduces significantly by 91% between 400°C and 700°C. This suggests urgent intervention is needed for infrastructure exposed to such conditions to prevent significant fatigue life reduction and potential failure.
  8. The fatigue life of reinforcing steel bar considering the combined effects of pitting corrosion and high-temperature exposure have been estimated using average SED approach. Further, a temperature-dependent pit sensitivity function, varying exponentially in corroded specimens, was proposed. Moreover, establishing a

temperature-dependent relation between experimental cycles to failure and energy dissipation capacity under corrosion conditions has been analysed to understand LCF behavior under the influence of pitting corrosion and elevated temperature.

9. The experimental investigation of LCF test on corroded structural steel under strain-controlled conditions revealed a fuller rhombus hysteresis curve expanding with increasing temperature. A significant reduction in fatigue life, with an 82% decrease in cycles to failure observed between 25°C and 700°C. Additionally, the energy dissipation density of corroded specimens declined by 52% within the same temperature range, highlighting reduced energy absorption capacity. Additionally, the stress softening factors reveal the impact of exposure temperature and fatigue strain amplitude on the stress response, while the Coffin-Manson equation provides predictive models for temperature-dependent coefficients. Experimental and estimated cycles to failure closely align, affirming the reliability of the average SED approach. These findings offer crucial insights for engineering applications and structural integrity assessments.
10. SEM analysis revealed a distinct dependency of fatigue fracture morphology on temperature. At room temperature, fine and closely spaced striation marks dominated the fracture surface. As the temperature increased, the striation marks became coarser and additional features like tear-like structures and clamshell marks emerged. Furthermore, microcrack size and spacing increased significantly with rising temperature, indicating faster and more extensive crack growth. EDS analysis confirmed this trend, showing an increase in oxygen and carbon content with temperature, which suggests the formation of iron oxides and enrichment of carbon at the fracture surface.
11. Experimental investigations into HCF behavior of constructional steel containing multiple pit sites revealed that corrosion significantly reduces the fatigue life of structural steel, and this reduction is exacerbated by higher levels of corrosion and applied stress. The fatigue test results demonstrate a clear inverse relationship between fatigue life and both corrosion severity and maximum stress levels. Additionally, the study highlights the importance of minimizing stress levels to ensure structural integrity, particularly in corrosive environments. Fractographic analysis reveals that corrosion leads to a transition from fatigue crack growth to rapid fracture, indicating a loss of material ductility and increased susceptibility to fracture. Furthermore, the presence of multiple corrosion pits accelerates fatigue failure, emphasizing the detrimental effect of corrosion on the structural performance of steel. These findings underscore the importance of considering corrosion effects in engineering design and maintenance practices to ensure the durability and safety of structures made from structural steel, particularly in corrosive environments.



### **8.3 Recommendations for future work**

The present study provides recommendations for future investigations as follows:

1. This study focused on the influence of pitting corrosion on the fatigue behavior of constructional steel. Future research could be expanded to investigate other corrosion types, such as crevice corrosion or stress corrosion cracking, in conjunction with elevated temperatures. Future research might involve testing different bar diameters, different lengths, different grades, different manufacturers, and alkaline and acidic conditions to see if the fatigue life results vary significantly.
2. It is important to note that the current research utilized accelerated corrosion process that did not consider factors like water-to-binder ratio, cement composition, and temperature. This may limit long-term durability insights, especially for combined pitting and elevated temperatures. Future studies should consider these factors for more robust findings.
3. Experimental investigations could be extended to conduct creep-fatigue tests on corroded constructional steel specimens under elevated temperature conditions. Microstructural investigation can be conducted on the creep-fatigue behavior induced by both corrosion and elevated temperature.
4. To further enhance understanding and prediction, developing empirical and analytical models to evaluate the fatigue behavior of structural members experiencing combined pitting corrosion and elevated temperature can be taken up.
5. Exploring surface engineering techniques, such as coatings, treatments, or modifications, holds potential for improving the corrosion resistance and maintaining the surface integrity of steel rebar under elevated temperature conditions. Research in this area can contribute to optimizing the performance and durability of reinforced concrete structures.
6. Implementing advanced corrosion monitoring techniques, such as electrochemical impedance spectroscopy or corrosion potential measurements, could provide valuable insights into the progression of pitting corrosion. Correlating these measurements with changes in surface topography and fatigue life will help establish quantitative relationships for improved damage assessment and prediction.

## Bibliography

---

- Agnew, S. R., & Weertman, J. R. (1998). Cyclic softening of ultrafine grain copper. *Materials Science and Engineering: A*, 244(2), 145-153.
- Andrade, C. (2018). Propagation of reinforcement corrosion: principles, testing and modelling. *Materials and Structures*, 52(1), 2.
- Andrews, D. F. (1974). A Robust Method for Multiple Linear Regression. *Technometrics*, 16(4), 523-531.
- Apostolopoulos, C. A. (2007). Mechanical behavior of corroded reinforcing steel bars S500s tempcore under low cycle fatigue. *Construction and Building Materials*, 21(7), 1447-1456.
- Apostolopoulos, C. A., & Papadopoulos, M. (2007). Tensile and low cycle fatigue behavior of corroded reinforcing steel bars S400. *Construction and Building Materials*, 21(4), 855-864.
- Arola, D., & Ramulu, M. (2016). An Examination of the Effects from Surface Texture on the Strength of Fiber Reinforced Plastics. *Journal of Composite Materials*, 33(2), 102-123.
- Arola, D., & Williams, C. L. (2002). Estimating the fatigue stress concentration factor of machined surfaces. *International Journal of Fatigue*, 24(9), 923-930.
- Attarian, M., Pelaseyed, S. S., & Hayatian, R. (2023). Metallurgical evaluation and failure analysis of turbo expander Tie-bolt. *Engineering Failure Analysis*, 151, 107392.
- Atzori, B., Lazzarin, P., & Filippi, S. (2001). Cracks and notches: analogies and differences of the relevant stress distributions and practical consequences in fatigue limit predictions. *International Journal of Fatigue*, 23(4), 355-362.
- Ba, G., Zhou, J., Dong, M., Liu, C., & Ma, Z. (2022). Residual behaviour of corroded reinforcements after high temperature exposure. *Structures*, 45, 2162-2172.
- Bakkar, M. A., Saha, R., & Das, D. (2020). Low Cycle Fatigue Performance and Failure Analysis of Reinforcing Bar. *Metals and Materials International*, 27(12), 4952-4966.
- Bannantine, J. A., Comer, J. J., & Handrock, J. L. (1990). Fundamentals of metal fatigue analysis.
- Barsom, J. M. (1974). Fatigue behavior of pressure vessel steels. *Welding research council bulletin* (194).
- Barsom JM, Rolfe ST. Fracture and fatigue control in structures—applications of fracture mechanics. *Englewood Cliffs, NJ: Prentice Hall Inc*; 1977.
- Berto, F., Gallo, P., & Lazzarin, P. (2014). High temperature fatigue tests of un-notched and notched specimens made of 40CrMoV13.9 steel. *Materials & Design*, 63, 609-619.
- Bhushan, B. (2013). *Introduction to tribology*. John Wiley & Sons.
- Boashash, B. (2015). *Time-frequency signal analysis and processing: a comprehensive reference*. Academic press.
- Breusch, T. S., & Pagan, A. R. (1979). A Simple Test for Heteroscedasticity and Random Coefficient Variation. *Econometrica*, 47(5), 1287-1294.
- Burstein, G. T., Liu, C., Souto, R. M., & Vines, S. P. (2004). Origins of pitting corrosion. *Corrosion Engineering, Science and Technology*, 39(1), 25-30.
- Cáceres, L., Vargas, T., & Herrera, L. (2009). Influence of pitting and iron oxide formation during corrosion of carbon steel in unbuffered NaCl solutions. *Corrosion Science*, 51(5), 971-978.

## Fatigue Behavior of Constructional Steels Subjected to Pitting Corrosion and Elevated Temperature

- Callaghan, M. D., Humphries, S. R., Law, M., Ho, M., Bendeich, P., Li, H., & Yeung, W. Y. (2010). Energy-based approach for the evaluation of low cycle fatigue behaviour of 2.25Cr–1Mo steel at elevated temperature. *Materials Science and Engineering: A*, 527(21), 5619-5623.
- Callaghan, M. D., Humphries, S., Law, M., Ho, M., Bendeich, P., Li, H., & Yeung, W. (2010). Energy-based approach for the evaluation of low cycle fatigue behaviour of 2.25 Cr–1Mo steel at elevated temperature. *Materials Science and Engineering: A*, 527(21-22), 5619-5623.
- Campbell, F. C. (2012). *Fatigue and fracture: understanding the basics*. ASM International.
- Cao, X. J., Pyoun, Y. S., & Murakami, R. (2010). Fatigue properties of a S45C steel subjected to ultrasonic nanocrystal surface modification. *Applied Surface Science*, 256(21), 6297-6303.
- Caplan, D., Sproule, G., Hussey, R., & Graham, M. (1979). Oxidation of Fe-C alloys at 700° C. *Oxidation of Metals*, 13, 255-272.
- CE, I. (1913). Stresses in a plate due to the presence of cracks and sharp corners. *Trans Inst Naval Archit*, 55, 219-241.
- Chang, Y. N., & Wei, F. I. (1989). High temperature oxidation of low alloy steels. *Journal of Materials Science*, 24(1), 14-22.
- Chauhan, A., Hoffmann, J., Litvinov, D., & Aktaa, J. (2017). High-temperature low-cycle fatigue behavior of a 9Cr-ODS steel: Part 1 - pure fatigue, microstructure evolution and damage characteristics. *Materials Science and Engineering: A*, 707, 207-220.
- Chauhan, S., & Muthulingam, S. (2023). Fatigue life estimation of TMT reinforcing steel bar considering pitting corrosion and high temperature impacted surface topography. *International Journal of Fatigue*, 175.
- Chen, E., Berrocal, C. G., Löfgren, I., & Lundgren, K. (2020). Correlation between concrete cracks and corrosion characteristics of steel reinforcement in pre-cracked plain and fibre-reinforced concrete beams. *Materials and Structures*, 53(2).
- Chen, J., Diao, B., He, J., Pang, S., & Guan, X. (2018). Equivalent surface defect model for fatigue life prediction of steel reinforcing bars with pitting corrosion. *International Journal of Fatigue*, 110, 153-161.
- Chen, R. Y., & Yeun, W. Y. D. (2003). Review of the High-Temperature Oxidation of Iron and Carbon Steels in Air or Oxygen. *Oxidation of Metals*, 59(5), 433-468.
- Chitty, W.-J., Dillmann, P., L'Hostis, V., & Lombard, C. (2005). Long-term corrosion resistance of metallic reinforcements in concrete—a study of corrosion mechanisms based on archaeological artefacts. *Corrosion Science*, 47(6), 1555-1581.
- Chlistovsky, R. M., Heffernan, P. J., & DuQuesnay, D. L. (2007). Corrosion-fatigue behaviour of 7075-T651 aluminum alloy subjected to periodic overloads. *International Journal of Fatigue*, 29(9), 1941-1949.
- Coffin Jr, L. F. (1954). A study of the effects of cyclic thermal stresses on a ductile metal. *Transactions of the American Society of Mechanical engineers*, 76(6), 931-949.
- Congress, I. R. (2020). IRC 112: Code of Practice for Concrete Road Bridges. In *Indian Roads Congress* (pp. 1-89).
- Cornell, R. M., & Schwertmann, U. (2003). *The iron oxides: structure, properties, reactions, occurrences, and uses* (Vol. 664). Wiley-vch Weinheim.
- Darmawan, M. S., & Stewart, M. G. (2007). Spatial time-dependent reliability analysis of corroding pretensioned prestressed concrete bridge girders. *Structural safety*, 29(1), 16-31.
- Dowling, N. E., Kampe, S. L., & Kral, M. V. (1999). Mechanical behavior of materials: engineering methods for deformation, fracture, and fatigue.

- Elsener, B., Andrade, C., Gulikers, J., Polder, R., & Raupach, M. (2003). Half-cell potential measurements—Potential mapping on reinforced concrete structures. *Materials and Structures*, 36(7), 461-471.
- Fernandez, I., Bairán, J. M., & Mari, A. R. (2015). Corrosion effects on the mechanical properties of reinforcing steel bars. Fatigue and  $\sigma$ - $\varepsilon$  behavior. *Construction and Building Materials*, 101, 772-783.
- Filippi, S., & Lazzarin, P. (2004). Distributions of the elastic principal stress due to notches in finite size plates and rounded bars uniaxially loaded. *International Journal of Fatigue*, 26(4), 377-391.
- Forman, R. G., Kearney, V., & Engle, R. (1967). Numerical analysis of crack propagation in cyclic-loaded structures, 459-463.
- Frankel, G. (1998). Pitting corrosion of metals: a review of the critical factors. *Journal of the Electrochemical society*, 145(6), 2186.
- Gadelmawla, E. S., Koura, M. M., Maksoud, T. M. A., Elewa, I. M., & Soliman, H. H. (2002). Roughness parameters. *Journal of Materials Processing Technology*, 123(1), 133-145.
- Gallo, P., & Berto, F. (2015). High temperature fatigue tests and crack growth in 40CrMoV13.9 notched components. *Frattura ed Integrità Strutturale*, 9(34).
- Galvele, J. (1981). Transport processes in passivity breakdown—II. Full hydrolysis of the metal ions. *Corrosion Science*, 21(8), 551-579.
- Gao, H. (1991). Stress concentration at slightly undulating surfaces. *Journal of the Mechanics and Physics of Solids*, 39(4), 443-458.
- Garrison, W. M. (1986). A micromechanistic interpretation of the influence of undissolved carbides on the fracture toughness of a low alloy steel. *Scripta Metallurgica*, 20(5), 633-636.
- Ge, Z., & Kobayashi, F. (2006). High-precision measurement of a fiber connector end face by use of a Mirau interferometer. *Applied optics*, 45(23), 5832-5839.
- Gujarati, D. N. (2022). *Basic econometrics*. Prentice Hall.
- Gutiérrez-Castañeda, E., Salinas-Rodríguez, A., Deaquino-Lara, R., & Márquez-Torres, F. (2015). High Temperature Oxidation and Its Effects on Microstructural Changes of Hot-Rolled Low Carbon Non-oriented Electrical Steels During Air Annealing. *Oxidation of Metals*, 83(3), 237-252.
- Hahn, S. L. (1996). Hilbert transforms. *The transforms and applications handbook*, 463-629.
- Halford, G. (1966). The energy required for fatigue (Plastic strain hysteresis energy required for fatigue in ferrous and nonferrous metals). *Journal of materials*, 1, 3-18.
- Hawileh, R., Abdalla, J., Oudah, F., & Abdelrahman, K. (2010). Low-cycle fatigue life behaviour of BS 460B and BS B500B steel reinforcing bars. *Fatigue & Fracture of Engineering Materials & Structures*, 33(7), 397-407.
- Hua, J., Fan, H., Yan, W., Wang, N., Xue, X., & Huang, L. (2022). Seismic resistance of the corroded bimetallic steel bar under different strain amplitudes. *Construction and Building Materials*, 319, 126088.
- Hua, J., Wang, F., Xue, X., Ding, Z., Sun, Y., & Xiao, L. (2022). Ultra-low cycle fatigue performance of Q690 high-strength steel after exposure to elevated temperatures. *Journal of Building Engineering*, 57.
- Hua, J., Wang, F., Yang, Z., Xue, X., Huang, L., & Chen, Z. (2021). Low-cycle fatigue properties of bimetallic steel bars after exposure to elevated temperature. *Journal of Constructional Steel Research*, 187, 106959.

## Fatigue Behavior of Constructional Steels Subjected to Pitting Corrosion and Elevated Temperature

Hua, J., Yang, Z., Zhou, F., Hai, L., Wang, N., & Wang, F. (2022). Effects of exposure temperature on low-cycle fatigue properties of Q690 high-strength steel. *Journal of Constructional Steel Research*, 190.

ISO 21920-3:2021: Geometrical product specifications (GPS) — Surface texture: Profile - Part 3: Specification operators, International Organization for Standardization. (2021).

ISO 831-11:2014 Standardization: Fire resistance tests Elements of building construction, in: Specific requirements for the assessment of fire protection to structural steel elements; 2014.

Jie, Z., Berto, F., & Susmel, L. (2020). Fatigue behaviour of pitted/cracked high-strength steel wires based on the SED approach. *International Journal of Fatigue*, 135.

Kandeil, A. Y., & Mourad, M. Y. (1989). Effect of surface texture on corrosion behaviour of steel. *Surface and Coatings Technology*, 37(2), 237-250.

Kim, B.-K. (2003). High Temperature Oxidation of Low Carbon Steel McGill University. Canada.

Kodur, V., Wang, T., & Cheng, F. (2004). Predicting the fire resistance behaviour of high strength concrete columns. *Cement and concrete composites*, 26(2), 141-153.

Koh, S., & Stephens, R. (1991). Mean stress effects on low cycle fatigue for a high strength steel. *Fatigue & Fracture of Engineering Materials & Structures*, 14(4), 413-428.

Korade, D., Ramana, K. V., & Jagtap, K. (2020). Wear and Fatigue Behaviour of Deep Cryogenically Treated H21 Tool Steel. *Transactions of the Indian Institute of Metals*, 73(4), 843-851.

Korda, A. A., Mutoh, Y., Miyashita, Y., Sadasue, T., & Mannan, S. L. (2006). In situ observation of fatigue crack retardation in banded ferrite-pearlite microstructure due to crack branching. *Scripta Materialia*, 54(11), 1835-1840.

Krzyzanowski, M., Beynon, J. H., & Farrugia, D. C. (2010). *Oxide scale behavior in high temperature metal processing*. John Wiley & Sons.

Lazzarin, P., & Berto, F. (2005). Some expressions for the strain energy in a finite volume surrounding the root of blunt V-notches. *International Journal of Fracture*, 135(1-4), 161-185.

Lazzarin, P., & Zambardi, R. (2001). A finite-volume-energy based approach to predict the static and fatigue behavior of components with sharp V-shaped notches. *International Journal of Fracture*, 112(3), 275-298.

Le Van Quyen, M., Foucher, J., Lachaux, J.-P., Rodriguez, E., Lutz, A., Martinerie, J., & Varela, F. J. (2001). Comparison of Hilbert transform and wavelet methods for the analysis of neuronal synchrony. *Journal of neuroscience methods*, 111(2), 83-98.

Lee, K.-O., Hong, S.-G., & Lee, S.-B. (2008). A new energy-based fatigue damage parameter in life prediction of high-temperature structural materials. *Materials Science and Engineering: A*, 496(1-2), 471-477.

Lee, Y.-L. (2005). *Fatigue testing and analysis: theory and practice* (Vol. 13). Butterworth-Heinemann.

Li, M., Pan, Q., Shi, Y., & Wang, Y. (2014). Microstructure dependent fatigue crack growth in Al-Mg-Sc alloy. *Materials Science and Engineering: A*, 611, 142-151.

Lie, T., Fire temperature-time relations. 1988. *SFPE Handbook of Fire Protection Engineering*, 3rd ed.; National Fire Protection Association: Quincy, MA, USA, 2002; pp. 4-201.

Liu, X., Xiao, L., Cai, C., Zhang, J., & Wang, L. (2021). Fatigue properties investigation of corroded high-performance steel specimens. *Journal of Materials in Civil Engineering*, 33(1), 04020410.

- Liu, Y.-W. (2012). Hilbert transform and applications. *Fourier Transform Applications*, 291-300.
- Ma, Y., Wang, Q., Guo, Z., Wang, G., Wang, L., & Zhang, J. (2017). Static and Fatigue Behavior Investigation of Artificial Notched Steel Reinforcement. *Materials (Basel)*, 10(5).
- Ma, Y., Wang, Q., Guo, Z., Wang, G., Wang, L., & Zhang, J. (2017). Static and fatigue behavior investigation of artificial notched steel reinforcement. *Materials*, 10(5), 532.
- Mainsah, E., Greenwood, J. A., & Chetwynd, D. G. (2001). *Metrology and properties of engineering surfaces*. Springer Science & Business Media.
- Manson, S. S. (1953). Behavior of materials under conditions of thermal stress (Vol. 2933). *National Advisory Committee for Aeronautics*.
- Medina, H. (2015). A stress–concentration–formula generating equation for arbitrary shallow surfaces. *International Journal of Solids and Structures*, 69–70, 86–93.
- Medina, H., & Hinderliter, B. (2014). The stress concentration factor for slightly roughened random surfaces: Analytical solution. *International Journal of Solids and Structures*, 51(10), 2012–2018.
- Melchers, R. E. (2020). A Review of Trends for Corrosion Loss and Pit Depth in Longer-Term Exposures. *Corrosion and Materials Degradation*, 1(1), 42-58.
- Mhaede, M. (2012). Influence of surface treatments on surface layer properties, fatigue and corrosion fatigue performance of AA7075 T73. *Materials & Design*, 41, 61-66.
- Montemor, M., Simoes, A., & Ferreira, M. (2003). Chloride-induced corrosion on reinforcing steel: from the fundamentals to the monitoring techniques. *Cement and concrete composites*, 25(4-5), 491-502.
- Morrow, J. (1965). Cyclic plastic strain energy and fatigue of metals. *Internal friction, damping, and cyclic plasticity*. ASTM International.
- Mura, T., & Nakasone, Y. (1990). A theory of fatigue crack initiation in solids. 57.
- Murakami, Y. (2002). *Metal Fatigue*. Elsevier Science Ltd.
- Muralikrishnan, B., & Raja, J. (2008). Computational surface and roundness metrology. Springer Science & Business Media.
- Muthulingam, S. (2019). Space-time Gaussian models for evaluating corrosion-induced damages in reinforcing bars. *Sādhanā*, 44(1), 13.
- Nakamura, S., & Suzumura, K. (2013). Experimental study on fatigue strength of corroded bridge wires. *Journal of Bridge Engineering*, 18(3), 200-209.
- Nandi, S. K., Tewary, N. K., Saha, J. K., & Ghosh, S. K. (2016). Microstructure, mechanical properties and corrosion performance of a few TMT rebars. *Corrosion Engineering, Science and Technology*, 51(7), 476-488.
- Naono, H., & Fujiwara, R. (1980). Micropore formation due to thermal decomposition of acicular microcrystals of  $\alpha$ -FeOOH. *Journal of Colloid and Interface Science*, 73(2), 406-415.
- Naono, H., & Nakai, K. (1989). Thermal decomposition of  $\gamma$ -FeOOH fine particles. *Journal of Colloid and Interface Science*, 128(1), 146-156.
- Naono, H., Fujiwara, R., Sugioka, H., Sumiya, K., & Yanazawa, H. (1982). Micropore formation due to thermal decomposition of acicular microcrystals of  $\beta$ -FeOOH. *Journal of Colloid and Interface Science*, 87(2), 317-332.
- Narendra, P. V., Prasad, K., Krishna, E. H., Kumar, V., & Singh, K. D. (2019). Low–Cycle–Fatigue (LCF) behavior and cyclic plasticity modeling of E250A mild steel. *Structures*, vol. 20, pp. 594-606.

## Fatigue Behavior of Constructional Steels Subjected to Pitting Corrosion and Elevated Temperature

Novikov, I. I., & Afanasyev, V. (1978). *Theory of heat treatment of metals*. Mir Publishers Moscow.

OH Basquin, "The exponential law of endurance tests" American Society of Testing Material, Proc., Vol.10, 1910, pp 625-630.

Omidbakhsh, F., Ebrahimi, A. R., & Sojka, J. (2013). High temperature oxidation effects on surface roughness of Ti-4Al-2V. *Surface Engineering*, 29(4), 322-327.

Otieno, M., Beushausen, H., & Alexander, M. (2016). Chloride-induced corrosion of steel in cracked concrete – Part I: Experimental studies under accelerated and natural marine environments. *Cement and Concrete Research*, 79, 373-385.

Palsson, R., & Mirza, M. S. (2002). Mechanical response of corroded steel reinforcement of abandoned concrete bridge. *Structural Journal*, 99(2), 157-162.

Paris, P., & Erdogan, F. (1963). A critical analysis of crack propagation laws.

Park, J. S., Kim, S. J., & Lee, C. S. (2001). Effect of W addition on the low cycle fatigue behavior of high Cr ferritic steels. *Materials Science and Engineering: A*, 298(1), 127-136.

Paul, S. K., Majumdar, S., & Kundu, S. (2014). Low cycle fatigue behavior of thermo-mechanically treated rebar. *Materials & Design*, 58, 402-411.

Paul, S. K., Rana, P. K., Das, D., Chandra, S., & Kundu, S. (2014). High and low cycle fatigue performance comparison between micro-alloyed and TMT rebar. *Construction and Building Materials*, 54, 170-179.

Peklenik, J. (1967). Paper 24: New developments in surface characterization and measurements by means of random process analysis. *Proceedings of the institution of mechanical engineers*, conference proceedings, Vol. 182, No. 11, pp. 108-126.

Pfefferkorn, F. E., Duffie, N. A., Morrow, J. D., & Wang, Q. (2014). Effect of beam diameter on pulsed laser polishing of S7 tool steel. *CIRP Annals*, 63(1), 237-240.

Pires, J. C. M., Martins, F. G., Sousa, S. I. V., Alvim-Ferraz, M. C. M., & Pereira, M. C. (2008). Selection and validation of parameters in multiple linear and principal component regressions. *Environmental Modelling & Software*, 23(1), 50-55.

Plumensi, J. P., Kohn, A., Vagnard, G., & Manenc, J. (1969). Etude de la solubilité du carbone dans le protoxyde de fer. *Corrosion Science*, 9(5), 309-314.

Poupard, O., L'hostis, V., Catinaud, S., & Petre-Lazar, I. (2006). Corrosion damage diagnosis of a reinforced concrete beam after 40 years natural exposure in marine environment. *Cement and concrete research*, 36(3), 504-520.

Prevéy, P. S., & Cammett, J. T. (2004). The influence of surface enhancement by low plasticity burnishing on the corrosion fatigue performance of AA7075-T6. *International Journal of Fatigue*, 26(9), 975-982.

Qian, G., Hong, Y., & Zhou, C. (2010). Investigation of high cycle and very-high-cycle fatigue behaviors for a structural steel with smooth and notched specimens. *Engineering Failure Analysis*, 17(7-8), 1517-1525.

Qian, H., Yan, D., Chen, S., Chen, G., Tian, Y., & Chen, G. (2019). Effect of High Temperature Exposure and Strain Rate on Mechanical Properties of High-Strength Steel Rebars. *Journal of Materials in Civil Engineering*, 31(11).

Raj, H., Saraf, A., Sangal, S., & Misra, S. (2016). Residual Properties of TMT Steel Bars after Exposure to Elevated Temperatures. *Journal of Materials in Civil Engineering*, 28(2).

Ramberg, W., & Osgood, W. R. (1943). Description of stress-strain curves by three parameters, No. NACA-TN-902.

- Rao, K. B. S., Schiffers, H., Schuster, H., & Nickel, H. (1988). Influence of time and temperature dependent processes on strain controlled low cycle fatigue behavior of alloy 617. *Metallurgical Transactions A*, 19(2), 359-371.
- Ren, C., Wang, H., Huang, Y., & Yu, Q.-Q. (2020). Post-fire mechanical properties of corroded grade D36 marine steel. *Construction and Building Materials*, 263, 120120.
- Revie, R. W., & Uhlig, H. H. (2008). *Corrosion and corrosion control: an introduction to corrosion science and engineering*. John Wiley & Sons, 4th ed., Hoboken, New Jersey, 2008.
- Samuels, L. E. (1999). *Light microscopy of carbon steels*. Asm International, 1999.
- Schijve, J. (2009). *Fatigue of Structures and Materials*. Springer Netherlands, Dordrecht, 2009.
- Sharifi, Y., & Rahgozar, R. (2009). Fatigue Notch Factor in Steel Bridges Due to Corrosion. *Archives of Civil and Mechanical Engineering*, 9(4), 75-83.
- Sharma, N., Sharma, S., Sharma, S. K., Mahajan, R. L., & Mehta, R. (2022). Evaluation of corrosion inhibition capability of graphene modified epoxy coatings on reinforcing bars in concrete. *Construction and Building Materials*, 322, 126495.
- Sheng, G.-M., & Gong, S.-H. (1997). Investigation of low cycle fatigue behavior of building structural steels under earthquake loading. *Acta Metall*, Sin. 10 (1997) 51–55.
- Singh, R. (2020). *Applied welding engineering: processes, codes, and standards*. Butterworth–Heinemann.
- Sk, M. B., Syed, B., Chatterjee, A., Lodh, A., Kundu, S., & Chakrabarti, D. (2017). Effect of Thermal Exposure on the Charpy Impact Properties of Thermo-Mechanically Treated Reinforcement Steel Bar. *steel research international*, 88(5), 1600286.
- Sneha, S. (2016). High-Temperature Oxidation of Metals. In A. Zaki (Ed.), *High Temperature Corrosion* (pp. Ch. 6). IntechOpen.
- Steel, W. H. (1985). *Interferometry* (Vol. 1). Cambridge University Press.
- Stephens, R. I., Fatemi, A., Stephens, R. R., & Fuchs, H. O. (2000). *Metal fatigue in engineering*. John Wiley & Sons.
- Stewart, M. G. (2004). Spatial variability of pitting corrosion and its influence on structural fragility and reliability of RC beams in flexure. *Structural safety*, 26(4), 453-470.
- Stewart, M. G., & Al-Harthy, A. (2008). Pitting corrosion and structural reliability of corroding RC structures: Experimental data and probabilistic analysis. *Reliability engineering & system safety*, 93(3), 373-382.
- Swamy, R. N., & Tanikawa, S. (1993). An external surface coating to protect concrete and steel from aggressive environments [Article]. *Materials and Structures*, 26(8), 465-478.
- Tanaka, K., & Mura, T. (1981). A Dislocation Model for Fatigue Crack Initiation. *Journal of Applied Mechanics*, 48(1), 97-103.
- Tanaka, K., & Mura, T. (1982). A theory of fatigue crack initiation at inclusions. *Metallurgical Transactions A*, 13(1), 117-123.
- Tang, F., Lin, Z., Chen, G., & Yi, W. (2014). Three-dimensional corrosion pit measurement and statistical mechanical degradation analysis of deformed steel bars subjected to accelerated corrosion. *Construction and Building Materials*, 70, 104-117.
- Tariq, F., & Bhargava, P. (2021). Temperature-dependent properties of corroded super ductile TMT steel bars. *Structures*, 33, 4124-4140.
- Tilly, G. (1979). Fatigue of steel reinforcement bars in concrete: a review. *Fatigue & Fracture of Engineering Materials & Structures*, 2(3), 251-268.



## **Fatigue Behavior of Constructional Steels Subjected to Pitting Corrosion and Elevated Temperature**

- Tripathi, M., Dhakal, R. P., Dashti, F., & Massone, L. M. (2018). Low-cycle fatigue behaviour of reinforcing bars including the effect of inelastic buckling. *Construction and Building Materials*, 190, 1226–1235.
- Tuutti, K. (1982). *Corrosion of steel in concrete*. Cement-och betonginst.
- Viswanathan, R. (1989). Damage mechanisms and life assessment of high temperature components. *ASM international*.
- Vu, K. A. T., & Stewart, M. G. (2000). Structural reliability of concrete bridges including improved chloride-induced corrosion models. *Structural Safety*, 22(4), 313–333.
- Wang, J., Zhang, Y., Sun, Q., Liu, S., Shi, B., & Lu, H. (2016). Giga-fatigue life prediction of FV520B-I with surface roughness. *Materials & Design*, 89, 1028-1034.
- Wang, Q., Bathias, C., Kawagoishi, N., & Chen, Q. (2002). Effect of inclusion on subsurface crack initiation and gigacycle fatigue strength. *International Journal of Fatigue*, 24(12), 1269-1274.
- Wang, Q., Berard, J., Rathery, S., & Bathias, C. (1999). Technical note High-cycle fatigue crack initiation and propagation behaviour of high-strength spring steel wires. *Fatigue & Fracture of Engineering Materials & Structures*, 22(8), 673-677.
- Wang, Q., Pidaparti, R., & Palakal, M. (2001). Comparative study of corrosion-fatigue in aircraft materials. *AIAA journal*, 39(2), 325-330.
- Wang, W., Liu, T., & Liu, J. (2015). Experimental study on post-fire mechanical properties of high strength Q460 steel. *Journal of Constructional Steel Research*, 114, 100-109.
- Whitehouse, D. J. (2002). *Handbook of surface and nanometrology*. Taylor & Francis.
- Whitehouse, D. J., & Archard, J. (1970). The properties of random surfaces of significance in their contact. *Proceedings of the Royal Society of London. A. Mathematical and Physical Sciences*, 316(1524), 97-121.
- Wranglen, G. (1974). Pitting and sulphide inclusions in steel. *Corrosion Science*, 14(5), 331-349.
- Wu, D.-L., Zhao, P., Wang, Q.-Q., & Xuan, F.-Z. (2015). Cyclic behavior of 9–12% Cr steel under different control modes in low cycle regime: A comparative study. *International Journal of Fatigue*, 70, 114–122.
- Wu, H. Y., Han, D. X., Du, Y., Gao, X. H., & Du, L. X. (2022). Effect of initial spheroidizing microstructure after quenching and tempering on wear and contact fatigue properties of GCr15 bearing steel. *Materials Today Communications*, 30, 103152.
- Xie, X.-f., Jiang, W., Chen, J., Zhang, X., & Tu, S.-T. (2019). Cyclic hardening/softening behavior of 316L stainless steel at elevated temperature including strain-rate and strain-range dependence: Experimental and damage-coupled constitutive modeling. *International Journal of Plasticity*, 114, 196-214.
- Ye, D., Matsuoka, S., Nagashima, N., & Suzuki, N. (2006). The low-cycle fatigue, deformation and final fracture behaviour of an austenitic stainless steel. *Materials Science and Engineering: A*, 415(1), 104-117.
- Yosibash, Z., Bussiba, A., & Gilad, I. (2004). Failure criteria for brittle elastic materials. *International Journal of Fracture*, 125(3), 307-333.
- Zhang, C., Liu, Y., & Huang, C. (2021). Fatigue performance of Q345 structural steel after natural cooling from elevated temperatures. *Journal of Constructional Steel Research*, 184.
- Zhang, J., Jin, W., Mao, J., Xia, J., & Fan, W. (2020b). Determining the fatigue process in ribbed steel bars using piezomagnetism. *Construction and Building Materials*, 239, 117885.

Zhang, K., Zhang, J., Jin, W., Mao, J., Xu, Y., & Li, Q. (2021a). Characterization of fatigue crack propagation of pitting-corroded rebars using weak magnetic signals. *Engineering Fracture Mechanics*, 257.

Zhang, K., Zhang, J., Jin, W., Mao, J., Xu, Y., & Li, Q. (2021b). Characterization of fatigue crack propagation of pitting-corroded rebars using weak magnetic signals. *Engineering Fracture Mechanics*, 257, 108033.

Zhang, Y., & Sundararajan, S. (2005). The effect of autocorrelation length on the real area of contact and friction behavior of rough surfaces. *Journal of Applied Physics*, 97(10), 103526.

Zhang, Y., Lockwood, K. T., Bates, P. J., & DuQuesnay, D. L. (2015). Fatigue properties of vibration-welded postindustrial waste nylon with glass fibers at room and elevated temperatures. *Polymer Engineering & Science*, 55(4), 799-806.

Zhao, W., Liu, D., Zhang, X., Zhou, Y., Zhang, R., Zhang, H., & Ye, C. (2019). Improving the fretting and corrosion fatigue performance of 300M ultra-high strength steel using the ultrasonic surface rolling process. *International Journal of Fatigue*, 121, 30-38.

Zhao, W., Wang, Y., Zhang, T., & Wang, Y. (2012). Study on the mechanism of high-cycle corrosion fatigue crack initiation in X80 steel. *Corrosion Science*, 57, 99-103.

Zhou, R., Cheng, H. S., & Mura, T. (1989). Micropitting in rolling and sliding contact under mixed lubrication. *Journal of Tribology*, 605–613.



### International Journals

1. Chauhan, S., & Muthulingam, S. (2023). Surface roughness characteristics of high-ductile thermo-mechanically treated steel rebar exposed to pitting corrosion and elevated temperature. *Construction and Building Materials*, 404, 133210.
2. Chauhan, S., & Muthulingam, S. (2023). Fatigue life estimation of TMT reinforcing steel bar considering pitting corrosion and high temperature impacted surface topography. *International Journal of Fatigue*, 175, 107810.
3. Chauhan, S., & Muthulingam, S. (Under Review). High-Temperature LCF Behaviour of Gaussian-Pitted High-Strength High-Ductility Steel Rebars. *Engineering Fracture Mechanics*.
4. Chauhan, S., Muthulingam, S & SC Roy. (To be submitted). Effect of High Temperature and Strain Amplitude on LCF Behavior of Pitting Corroded Killed E350 BR Structural Steel.